Multimodal Spectroscopy: Real-time Diagnosis of Breast Cancer during Core Needle Biopsy
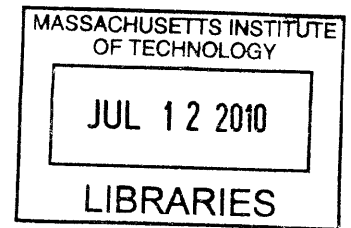
by

Zoya Volynskaya

S.B., Electrical Engineering and Computer Science
University of North Carolina at Charlotte (2003)

S.M., Electrical Engineering and Computer Science
Massachusetts Institute of Technology (2005)

Submitted to the Department of Electrical Engineering and Computer Science
in partial fulfillment of the requirements for the degree of

Doctor of Philosophy in Electrical Engineering and Computer Science

at the

MASSACHUSETTS INSTITUTE OF TECHNOLOGY

June 2010

Author. . . . .
Department of Electrical Engineering and Computer Science
February 23, 2010

Certified by. . . . .
Michael S. Feld
Professor of Physics and Director of G. R .Harrison Spectroscopy Laboratory
Thesis Supervisor

Accepted by . . . .
Terry P. Orlando
Chairman, Department Committee on Graduate Students

Multimodal Spectroscopy: Real-time Diagnosis of Breast Cancer during Core Needle Biopsy

by

Zoya Volynskaya

Submitted to the Department of Electrical Engineering and Computer Science
on February 23rd, 2010, in partial fulfillment of the requirements for the degree of
Doctor of Philosophy in Electrical Engineering and Computer Science

Abstract

Early detection of breast cancer is critical for improved survival. Currently, breast abnormalities are diagnosed based on a histopathological evaluation of tissue removed during core needle biopsy. Microcalcifications are used as targets to position biopsy devices, as they may indicate the presence of malignancy. Despite stereotactic guidance, needle biopsy fails to retrieve target microcalcifications in up to 15% of patients. Optical techniques may help clinicians accurately diagnose and treat patients by providing important diagnostic information in real time in a minimally invasive manner. This thesis describes the results of several studies we performed to evaluate the potential of Raman, reflectance, and intrinsic fluorescence spectroscopy to provide biochemical and morphological information for discriminating breast lesions. Each modality was evaluated individually, as well as in combination, using a technique known as multimodal spectroscopy (MMS). For the first part of this project we conducted a clinical study in which spectra were acquired from excised tissue in 99 patients and physically meaningful parameters were extracted by modeling the data. The goals of the study were as follows: 1) To prospectively validate previously developed diagnostic algorithms on the data from these patients; 2) To develop a new algorithm to evaluate additional histopathology diagnoses. Diffuse reflectance (DRS) spectra were modeled using diffusion theory and provided information about tissue absorbers and scatterers. Intrinsic fluorescence (IFS) spectra were extracted from the combined fluorescence and DRS spectra and analyzed using multivariate curve resolution. Raman spectroscopy data were fit using a linear combination of Raman active components (e.g. collagen, calcium, adipose) found in breast tissue. Prospective validation of Raman spectroscopy resulted in sensitivity and specificity and negative predictive value (NPV) of 78%, 98%, and 98%, respectively. An MMS system was developed to evaluate the benefit of combining information from all three spectroscopic modalities. We found that using new 3D Raman algorithm we could discriminate among 6 histopathology categories as compared to 4 categories previously diagnosed with Raman spectroscopy. For the second part of this project, we designed and developed a portable, miniature Raman clinical spectroscopy system to evaluate the potential of spectroscopy to guide the retrieval of microcalcifications during core needle biopsies. We focused specifically on the use of Raman spectroscopy for this application, as it is particularly sensitive to calcium-containing minerals. The system employs a side-viewing Raman probe that can be used in conjunction with commercial stereotactic needle biopsy devices. Prior to core needle excision, the Raman probe was inserted into the core needle biopsy device and spectra were acquired and analyzed in real time (<1s).

The results from our work indicate that spectroscopy has the potential to accurately diagnose breast lesions and enable targeted biopsies of diseased tissue and retrieval of microcalcifications.

Thesis supervisor: Michael S. Feld
Title: Professor of Physics and Director of G. R. Harrison Spectroscopy Laboratory

Acknowledgments

This research would not have been possible without the strong support of my advisors, colleagues, friends and family. I would like to thank my advisor, Prof. Michael Feld, for his guidance, vision and support throughout my career at MIT. Michael, because of you I grew as an engineer and as a person. I would also like to thank Dr. Ramachandra Dasari for improving my skills in the arts of negotiation and diplomacy.

I thank members of my thesis committee, Prof. Erich Ippen, Prof. Cardinal Warde, and Dr. Maryann Fitzmaurice, for providing great comments that made my research stronger. Maryann, I am very grateful for your support and guidance. Those endless weeks at Cleveland were truly fun while they were one of the most extreme experiences of my PhD work. You are a true believer in Raman spectroscopy and in the rough times you taught me how to make sense of hundreds of spectra.

I would like to thank my colleagues at the Spec Lab for being helpful and supportive: Kate Bechtel, Luis Galindo, Abigail Haka, Condon Lau, Sasha McGee, Jason Motz, Jelena Mirković, and Obrad Šćepanović. Obrad, thanks for being such a great inspiration and for always being there for me. I still cannot believe that you were able to drag me out to MetroWest before 6 am. Kate, thanks for keeping me busy and positive, especially after you left MIT; and thanks for all of the "a" and "the" correctly placed in my paperwork. Dr. McGee, you are an awesome person and thank you for much needed support during last months. Condon, thanks a lot for the ability to always spin any situation in a positive direction. Jelena, thank you for your support and friendship; and thanks a lot for always keeping 'Jelena Café' open 24/7.

I thank all my friends for support throughout my life. Paolo, we got teamed up by complete luck/mistake and now, years later you are just like family to me. And thank you for inspiring me to explore new hobbies. I would like to thank Dr. Jared Schwartz for being a great mentor during the last ten years of my life in the US. Finally, I would like to thank all my family and friends here and overseas for their love and support.

Table of Contents

Chapter 7: *Ex vivo* clinical application of the MMS system   127

Chapter 8: New prognostic algorithms   147

Chapter 9: Apparatus for guiding core needle biopsy   157

Chapter 10: Accomplishments and future directions   181

List of Abbreviations

Acronym	Meaning
BSE	Breast Self-Examination
CARS	Coherent anti-Stokes Raman scattering
CBE	Clinical Breast Examination
CCD	Charge Coupled Device
CLS	Classical Least Squares
CT	Computed tomography
DCIS	Ductal Carcinoma In Situ
DEH	Ductal Epithelial Hyperplasia
DOT	Diffuse Optical Tomography
DNA	Deoxyribonucleic Acid
DRS	Diffuse Reflectance Spectroscopy
EEM	Excitation-Emission Matrix
Ex vivo study	Study performed on a freshly excised tissue
FDA	Food and Drug Administration
FN	False negative
FP	False positive
FT	Fourier Transform
FWHM	Full Width at Half Maximum
H&E	Hematoxylin and Eosin
IDC	Invasive Ductal Carcinoma
IFS	Intrinsic Fluorescence Spectroscopy
ILC	Invasive Lobular Carcinoma
In vitro study	Study performed on frozen tissue
In vivo study	Study performed inside a patient
IR	Infrared
LCIS	Lobular Carcinoma In Situ
MCR	Multivariate Curve Resolution
MMS	Multimodal spectroscopy

MRI	Magnetic Resonance Imaging
NA	Numerical Aperture
NAD(P)H	Nicotinamide Adenine Dinucleotide (Phosphate)
NIR	Near-Infrared
NPV	Negative predictive value
OCT	Optical Coherence Tomography
OLS	Ordinary Least Squares
OR	Operating Room
PBS	Phosphate Buffered Saline
PC	Principal Component
PCA	Principal Component Analysis
PCR	Principal Component Regression
PET	Positron Emission Tomography
PLS	Partial Least-Squares
PPV	Positive predictive value
ROC	Receiver Operator Characteristic
Std	Standard Deviation
SNR	Signal-to-Noise Ratio
TN	True negative
TP	True positive
UV	Ultraviolet

List of Figures

List of Tables

CHAPTER 1

Introduction

The work in this thesis describes the development and evaluation of Raman spectroscopy, diffuse reflectance spectroscopy and intrinsic fluorescence spectroscopy, as well as combination of the three methods, as techniques for the diagnosis of breast cancer. Here we introduce the motivation and the overall goal of the work that was done in this dissertation. This chapter describes the goals of this thesis as well as provides information about thesis content.

1.1 Motivation

1.1.1 Mortality and survival

Breast cancer is the leading cause of non-preventable cancer death among American women. More than 175,000 new cases are diagnosed each year, and more than 40,000 women die annually from breast malignancy. An American woman has a one in eight (12.3%) chance of developing breast cancer during her lifetime [American Cancer Society Breast Cancer Facts and Figures 2007-2008]. However, numerous studies have shown that survival from breast cancer can be improved through early detection and intervention [1].

1.1.2 Current diagnostic procedures and their challenges

The current management of breast cancer involves periodic screening (either by self palpation or mammography) followed by a diagnostic procedure (core needle biopsy or surgical biopsy) in the event that an abnormality is detected.

1.1.2.1 Mammography

Women over the age of 40 should have a clinical breast exam and mammogram annually. Mammography is the current gold standard for screening for non-palpable, highly curable breast cancer [2, 3]. This X-ray technique images tissue based on differences in tissue density either with or without the aid of a contrast agent. This technique is widely used for anatomic (structural) imaging, but provides no biochemical information. Because anatomic changes do not uniquely correlate with breast cancer, abnormalities identified with mammography must be further investigated with biopsy. Therefore, while valuable for screening, it is not diagnostic, and a definitive diagnosis must be rendered by pathologic examination of a biopsied tissue specimen. Thus each year, a large number of breast biopsies are performed on benign lesions. Only 10 to 25 percent of suspicious lesions found during mammography are diagnosed as malignant upon biopsy [4]. Independent of the biopsy procedure employed, the biopsy and wait for diagnosis is a stressful

experience, both physically and mentally, even for those who are not diagnosed with breast cancer.

1.1.2.2 Core needle biopsy

If the radiologist identifies an abnormality during mammography, the patient is then scheduled to undergo breast biopsy in order to diagnose the suspicious lesion. Diagnostic breast biopsy is performed by biopsy procedures such as stereotactic and ultrasound guided core needle biopsy [5]. In order to correctly diagnose a suspicious lesion, five to ten cores of different sizes (depending on the choice of needle devices) are extracted during biopsy. Unfortunately, a significant percentage of core needle biopsies are non-diagnostic and require follow up surgical biopsy [6]. Therefore, there is a clinical need for improved core needle biopsy procedures to minimize patient trauma and expedite diagnosis of the suspicious lesion.

1.1.2.3 Surgical biopsy

Breast cancer surgery has changed dramatically over the past several decades, and continues to evolve. With the emergence of partial mastectomy (also known as lumpectomy or breast conservation surgery), during which a tumor is surgically removed, women may now preserve their breast without compromising survival [7]. To ensure that all malignant tissue is removed, a small margin of non-cancerous breast tissue surrounding the lesion is excised. In order to verify that the surgeon has removed the entire malignant lesion, the margins are examined by a pathologist [8-11]. Negative resection margins, typically defined as the absence of either invasive or intraductal cancer at the tissue margin – within 1 -2 mm from the edge of the tumor, are associated with lower rates of local recurrence following partial mastectomy [12-16]. Positive or unknown margins usually prompt re-excision surgery, since they are associated with a higher risk of local recurrence, even when radiation therapy is administered to the surgical cavity post-operatively [7, 17]. Determining the status of the margins based on a histopathological assessment can take several hours or even longer. Furthermore, in the case of positive margins, the

patient has to undergo a second surgery. In clinical practice, as many as 20-60% of patients undergoing partial mastectomy require a second surgical procedure due to positive margins (incomplete cancer resection) [18]. The complete diagnostic work up, from start to finish, may take weeks and include multiple biopsies. Thus, there is a clinical need for techniques that can accurately assess margins intra-operatively and provide real-time feedback to enable immediate re-excision of positive margins. Reducing the number of unnecessary biopsies and re-excision surgeries will significantly lower the cost associated with breast cancer diagnosis and treatment.

1.2   Thesis goals

Spectroscopic techniques can noninvasively provide information about tissue composition, such as the presence and amount of microcalcification, collagen, fat, and blood. Therefore, spectroscopy has the potential to provide clinically relevant information for diagnosing breast lesions. The goal of this thesis is to develop a real-time clinical diagnostic tool based on reflectance, fluorescence and Raman spectroscopy, as well as combination of these techniques, which accurately classifies breast lesions. The specific aims are as follows:

1) To perform clinical studies to evaluate the diagnostic capabilities of individual modalities (listed above) and the combination of all three – multimodal spectroscopy (MMS);

2) To design and develop a new MMS system (instrument and probe);

3) To evaluate the performance of the MMS system in identifying breast lesions;

4) To prospectively evaluate Raman and DRS/IFS diagnostic algorithms;

5) To expand and improve the capabilities of MMS-based diagnostic algorithms to diagnose additional benign and malignant lesions, discriminate between tumor grades, identify calcifications and correlate with biomarkers; and

6) To design, and test a side-viewing Raman probe that can be used during core needle biopsies.

1.3   Thesis overview

This dissertation is organized as follows:

Chapter 2: This chapter provides the necessary background information on breast anatomy and breast cancer.

Chapter 3: This chapter describes different optical approaches that are currently being investigated to detect breast cancer. It provides extensive background information on the spectroscopic modalities and instrumentation that were used during the course of the work presented in this thesis.

Chapter 4: This chapter focuses on the application of Raman spectroscopy to diagnose breast lesions during *ex vivo* and *in vivo* clinical studies. It describes the development of a Raman diagnostic algorithm, as well as the prospective application of the algorithm. It concludes with the application of this spectroscopic-based diagnostic technique to assess the status of surgical margins. This final study is significant in that it is the first ever *in vivo* study of Raman spectroscopy for this application.

Chapter 5: This chapter gives an overview of the clinical *ex vivo* work that was done using diffuse reflectance and intrinsic fluorescence spectroscopy. After presenting these results, we describe the motivation for combining the three spectroscopic modalities (diffuse reflectance, intrinsic fluorescence and Raman spectroscopy).

Chapter 6: In this chapter, we give a detailed description of the MMS clinical instrument and the probe, as well as explain changes in the modeling of the data.

Chapter 7: The results of an *ex vivo* clinical study performed using the MMS instrument are presented in this chapter. Prospective validation of a previously developed algorithm and the development of a new algorithm is also described.

Chapter 8: In this chapter we describe the results of a pilot feasibility study in which we use the diagnostic algorithm developed using the MMS instrument to assess malignancy grade. We also correlate the spectroscopic findings with the results of molecular biomarkers used to assess the disease status of the tissue.

Chapter 9: In this chapter, we begin by providing the motivation for switching from the front-viewing probe design to a side-viewing probe design, for clinical studies in which Raman spectroscopy is used to guide the acquisition of tissue samples during core needle biopsies. We then summarize several probe designs that are under consideration for this application. Finally we include the results of the proof-of-principle *ex vivo* study, during which we used the first prototype of Raman side-viewing probe in conjunction with a commercial vacuum- assisted biopsy device.

Chapter 10: In this final chapter we summarize the findings and conclusions of our investigations and discuss future directions for the project. We conclude with the summary of all accomplishments of this dissertation.

1.4 References

1.   Berry, D.A., et al., Modeling the impact of treatment and screening on U.S. breast cancer mortality: a Bayesian approach. *J Natl Cancer Inst Monogr*, 2006(36): p. 30-6.

2.   Dahnert, W., Radiology Review Manual. *4th Ed., Baltimore, Williams & Wilkins*, 1999: p. 449-474.

3.   Elmore, J.G., et al., Screening for breast cancer. *JAMA*, 2005. **293**(10): p. 1245-56.

4.   NCI, N.C.I.W.S. *Cancer Facts: Screening Mammorgamms: Qustions and Answers.* 2004 [cited Accessed November 20, 2004].

5.   Helbich, T.H., W. Matzek, and M.H. Fuchsjager, Stereotactic and ultrasound-guided breast biopsy. *Eur Radiol*, 2004. **14**(3): p. 383-93.

6.   Pfarl, G., et al., Stereotactic 11-gauge vacuum-assisted breast biopsy: a validation study. *AJR Am J Roentgenol*, 2002. **179**(6): p. 1503-7.

7.   Meric, F., et al., Positive surgical margins and ipsilateral breast tumor recurrence predict disease-specific survival after breast-conserving therapy. *Cancer*, 2003. **97**(4): p. 926-33.

8.   Balch, G.C., et al., Accuracy of intraoperative gross examination of surgical margin status in women undergoing partial mastectomy for breast malignancy. *Am Surg*, 2005. **71**(1): p. 22-7; discussion 27-8.

9.   Ferreiro, J.A., J.J. Gisvold, and D.G. Bostwick, Accuracy of frozen-section diagnosis of mammographically directed breast biopsies. Results of 1,490 consecutive cases. *Am J Surg Pathol*, 1995. **19**(11): p. 1267-71.

10.   Johnson, A.T., R. Henry-Tillman, and V.S. Klimberg, Breast conserving surgery: optimizing local control in the breast with the assessment of margins. *Breast Dis*, 2001. **12**: p. 35-41.

11.   Klimberg, V.S., K.C. Westbrook, and S. Korourian, Use of touch preps for diagnosis and evaluation of surgical margins in breast cancer. *Ann Surg Oncol*, 1998. **5**(3): p. 220-6.

12.   Anscher, M.S., et al., Local failure and margin status in early-stage breast carcinoma treated with conservation surgery and radiation therapy. *Ann Surg*, 1993. **218**(1): p. 22-8.

13.   Borger, J., et al., Risk factors in breast-conservation therapy. *J Clin Oncol*, 1994. **12**(4): p. 653-60.

14.   Gage, I., et al., Pathologic margin involvement and the risk of recurrence in patients treated with breast-conserving therapy. *Cancer*, 1996. **78**(9): p. 1921-8.

15. Park, C.C., et al., Outcome at 8 years after breast-conserving surgery and radiation therapy for invasive breast cancer: influence of margin status and systemic therapy on local recurrence. *J Clin Oncol*, 2000. **18**(8): p. 1668-75.

16. Smitt, M.C., et al., The importance of the lumpectomy surgical margin status in long-term results of breast conservation. *Cancer*, 1995. **76**(2): p. 259-67.

17. Freedman, G., et al., Patients with early stage invasive cancer with close or positive margins treated with conservative surgery and radiation have an increased risk of breast recurrence that is delayed by adjuvant systemic therapy. *Int J Radiat Oncol Biol Phys*, 1999. **44**(5): p. 1005-15.

18. Walls, J., et al., Can preoperative factors predict for residual malignancy after breast biopsy for invasive cancer? *Ann R Coll Surg Engl*, 1995. **77**(4): p. 248-51.

CHAPTER 2

Breast and breast pathology

The development of new methodologies to diagnose breast lesions must be based on a clear understanding of both the disease and the current medical procedures. This insures that the achieved results will provide relevant information for patients and clinicians and can be easily integrated into the clinical setting as a new standard. This chapter contains an overview of the macroscopic and microscopic structure of the breast. Both breast anatomy and pathology are described, including details on breast cancer staging and prognosis. Finally, a description of the current screening and treatment for breast cancer is provided, including the strengths and limitations of each method. This chapter provides the necessary foundation for interpreting the spectroscopic data described in the later chapters. Knowledge of the current biopsy and surgery procedures – areas that will benefit from the spectroscopic approach – is essential for designing studies in which spectroscopic approaches will be applied.

2.1 Breast anatomy

Development of the human breast is a process that starts in the embryo. Full breast differentiation is achieved with pregnancy and lactation. Breast development from puberty to adulthood can be defined by volume, number of structures present in the mammary gland, and the degree of differentiation of the individual structures. The female breast lies on top of the major pectoralis muscles between the second and sixth rib of the chest. Chest muscles located under the breast include the major and minor pectoralis, the serratus magnus, and the rectus abdominus. The main functional purpose of the adult female breast is milk production and secretion [1]. The female breast is composed of six to ten major duct systems, each of which is subdivided into lobules. Successive branching of the large ducts leads to the terminal ducts. The lobules are arranged around ducts that direct milk to the nipples. Each breast contains 15 to 20 lobes arranged in a circular fashion. The nipple and areola are covered by squamous epithelium and are located in the center of the breast. The stroma, which accounts for the majority of the breast volume in the non-lactating state, is composed of adipose (fat) and fibrous connective tissue. Figure 2.1 (modified from http://commons.wikimedia.org/wiki/File:Breast_anatomy_normal_scheme.png) shows a schematic of the female breast.
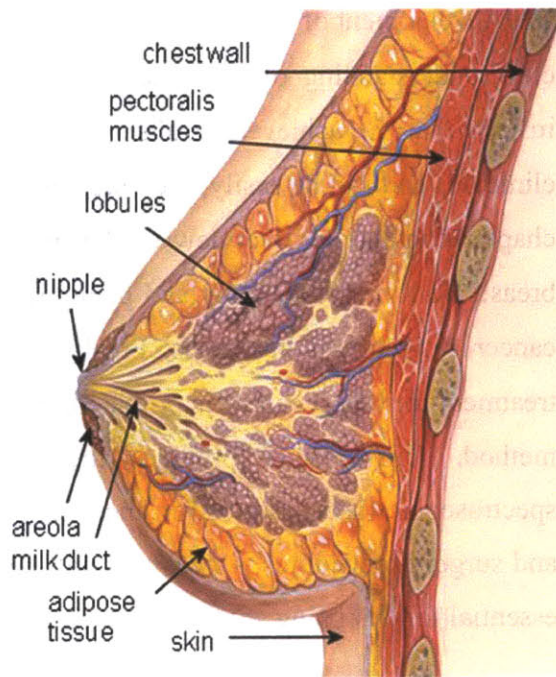
Figure 2.1. Diagram of anatomic sites of breast

The breast's blood supply is derived from the internal mammary artery. Breast tissue is drained by lymphatic vessels that lead to axillary nodes and internal

mammary nodes. Most lymphatic vessels in the breast drain into a network of lymph nodes located around the breast's edges, in the underarm, and near the collarbone. Axillary lymph nodes are often the first site of breast cancer metastasis. Because the long thoracic nerve innervates the muscles that helps move the upper arm, surgeons must be careful not to injure this nerve when operating near the axillary lymph nodes.

2.1.1 Normal breast

As previously mentioned, breast tissue is composed of adipose tissue, fibrous tissue and glands. A microscopic image of a thin (5 um) section of normal breast tissue stained with hematoxylin and eosin (H&E) is depicted in Fig. 2.2. The basic dye hematoxylin, stains basophilic structures (ribosomes, cell nucleus) with a blue-purple hue, while the alcohol-based acidic eosin Y, colors acidophilic structures (cytoplasm, fibrous tissue) bright pink. Fig. 2.2 clearly shows ducts and lobules that are lined with glandular epithelium. Adipose tissue can be seen as clear spaces, as fat is washed away during the tissue processing. The fatty tissue contains cells, adipocytes, which harbor
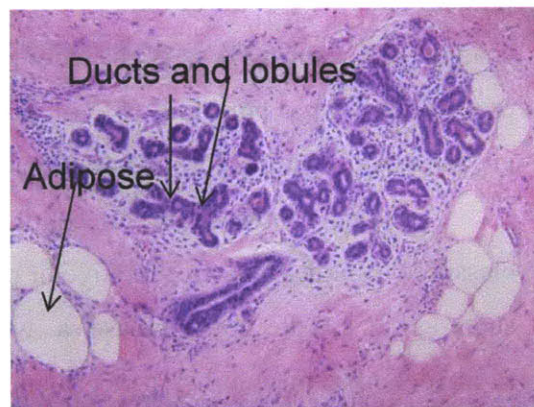
Figure 2.2. H&E slide of normal breast

copious amounts of cytoplasmic fat. The fibrous tissue is mainly composed of collagen and a small amount of glycosaminoglycans. The stroma also contains fibroblasts, cells that synthesize the extracellular matrix and collagen, and blood vessels [2]. The glandular tissue is comprised of lobes connected to ducts that carry milk to the nipple. The lobular units and the ducts are separated from the stroma by a basement membrane, which is composed of collagen, predominantly type IV. The basement membrane, which follows the contour of skin, ducts, and ductules, serves as a scaffold for regeneration of the epithelium and influences cell proliferation and growth. Fibrous connective tissue lies between the breast tissue and the skin and separates breast tissue from the chest muscles [3].

2.1.2 Benign lesions

Figure 2.3 shows the typical distribution of findings in women seeking evaluation of breast lumps (modified from [1]). Most of the suspected breast lesions are found to be benign upon biopsy. About 66% of all breast lesions are diagnosed as benign lesions, predominately fibrocystic
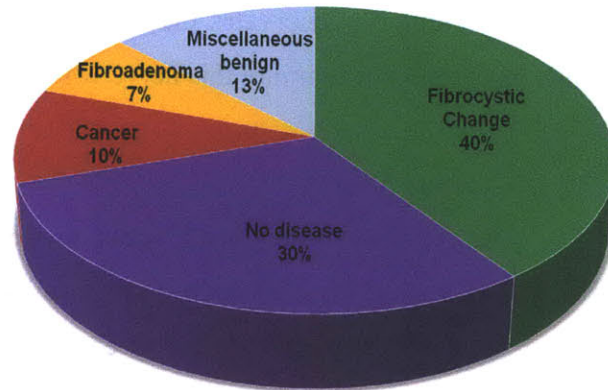
Figure 2.3. Distribution of findings in women seeking evaluation of breast lumps.

change (FCC) and 12% as fibroadenoma. It is important to note that during screening procedures a large portion (30%) of women are noted as having irregularities which are actually due to the normal variations in breast tissue.

Based on the degree of cellular proliferation, benign breast lesions can be classified as either non-proliferative or proliferative lesions. Non-proliferative lesions, such as FCC, do not increase a woman's risk for developing breast cancer. Fibroadenoma, on another hand, modestly increases the risk of developing breast cancer. Because of the differences in the risk for breast cancer, it is necessary to distinguish among different types of benign lesions as the treatment for them is different.

FCC is common in adolescents as well as 50% of women of reproductive age. Patients with FCC can palpate lumps, which are
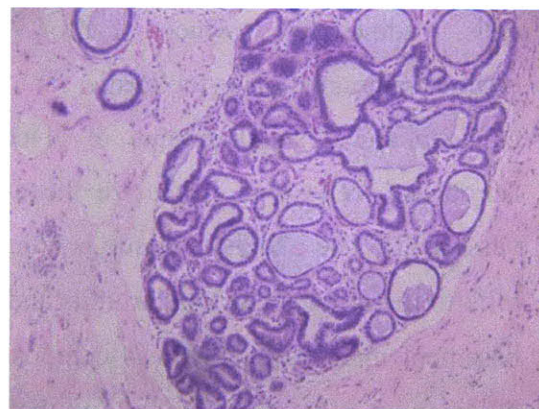
Figure 2.4. H&E stain of fibrocystic change.

generally found in the upper outer quadrants of the breast. FCC can manifest as: fibrosis, formation of fibrous tissue; adenosis, increase in the numbers of ductules; or cyst formation, dilation of ducts and lobules by semi-transparent fluid. There is

considerable variation in the degree to which each of these changes occur and the precise change or combination of changes that can manifest. Cysts are more frequent in women between the ages of 30 and 40. An H&E stained tissue specimen with FCC is shown in Fig. 2.4.

Fibroadenomas, the second most common benign breast lesions, are characterized by the presence of glandular tissue in addition to fibrous tissue as depicted on Fig. 2.5. It can occur at any age, but is most common in women under 30 years of age. The lesion is well-defined and mobile. Most
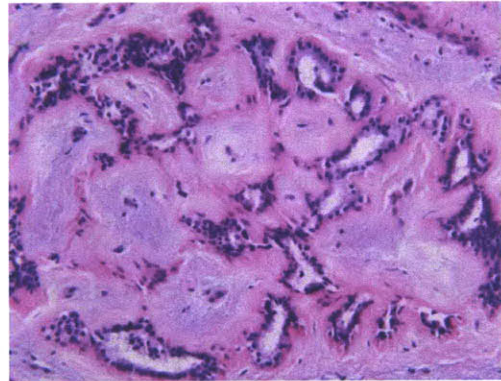
Figure 2.5. H&E stain of fibroadenoma

fibroadenomas are 2-3cm in size. Fibroadenomas show an accumulation of collagen due to fibroblast proliferation, which results in expansion of the stroma. Therefore, fibroadenomas often grow rapidly resulting in significant morbidity unless excised [4]. For this reason, it is important to evaluate the tissue surrounding fibroadenomas to determine the extent of disease and determine the appropriate treatment.

There are other benign conditions, such as fat necrosis, and intraductal papilloma, which are less common. Our spectroscopic work will focus on identifying the most common benign and malignant lesions, thus descriptions of such lesions are beyond the scope of this dissertation.

2.1.3 *Malignant lesions*

The incidence of breast carcinoma increases with age, with 85% of cases arising in women older than 30 years. Cancer is characterized by abnormal cell proliferation as well as abnormal maturation of cells. Genetic mutations often override the normal cell signaling system allowing cellular proliferation and growth to occur in the absence of any external stimulus. Thus, unlike normal cells, malignant cells do not stop proliferating after they have doubled 50 or 60 times. They may also become more resistant to the maturation of cells into a form adapted to a specific function. A fully mature cell of any particular cell line is described as highly

differentiated, whereas stem cells are relatively undifferentiated. Cancerous cells exhibit variable states of differentiation and often fail to achieve a highly differentiated state. Poorly differentiated cancers typically confer a worse prognosis.

Most malignant lesions (50%) occur in the upper outer quadrant of the breast. Breast cancers commonly develop in glandular tissue, and thus are classified as adenocarcinomas. The two major types of breast cancers, *in situ* and invasive carcinoma, arise in ducts or lobules. *In situ* carcinoma is defined by the absence of invasion of surrounding tissues (i.e. malignant cells are confined by the basement membrane). Approximately 80% of all non-invasive cancers are classified as ductal carcinoma *in situ* (DCIS), while 80% of all invasive cancers represent invasive ductal carcinoma (IDC). It is now believed that many cases of low-grade DCIS and most of the cases of high-grade DCIS progress to invasive carcinoma [5]. IDC by definition spreads through the duct walls, and invades the surrounding breast tissue. These findings once again emphasize the importance of accurate early diagnosis to ensure successful treatment.

A gross and microscopic view of an IDC tissue specimen are shown in Fig 2.6.
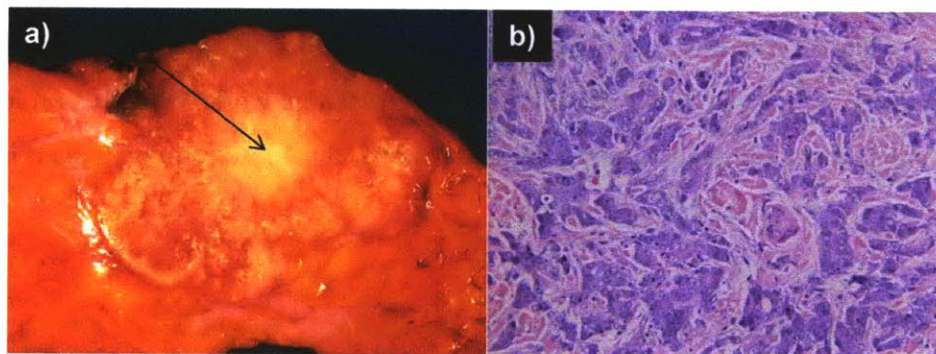
Figure 2.6. Invasive ductal carcinoma. a) Gross and b) Histopathology slide

The central white area (Fig. 2.6A) of the tumor (arrow) shown in the gross photograph is very hard and gritty because the neoplasm is producing a desmoplastic (formation of fibrosis) reaction with significant collagen deposition. This is often referred to as a "scirrhous" appearance. There is also focal dystrophic calcification leading to the gritty areas. Lesions diagnosed as IDC exhibit significant hyperplasia and often increased collagen content due to fibroblast proliferation in response to stromal invasion by the malignant epithelial cells.

Lobular carcinoma *in situ* (LCIS) consists of hyperplasia in the terminal breast ducts and acini. The cells are small and round. Invasive lobular carcinoma (ILC) accounts for 5-15 percent of invasive breast cancers. ILCs often have a diffusely invasive pattern making tumors difficult to detect by either physical examination or mammography.

2.1.4 Stages and grades of malignancy

Breast cancer has been divided into smaller groups in order to standardize comparisons of results of various therapeutic modalities among clinics and guide treatment. The American Joint Committee on Cancer Staging divides the clinical stages as shown in Table 2.1 [5]:

Stage	Description	5-yr survival
Stage 0	Cancerous lesions diagnosed as DCIS or LCIS	92%
Stage I	Invasive carcinoma with a size of 2 cm or less without nodal involvement and without any distant metastases	87%
Stage II	Invasive cancer that is less than 5 cm in size; involvement of movable axillary nodes; no metastases	75%
Stage III	A lesion is greater than 5 cm in size; breast cancer with fixed axillary nodes or that involves ipsilateral mammary lymph nodes; any breast cancer with skin involvement, pectoral and chest wall fixation, edema, or clinical inflammatory carcinoma.	46%
Stage IV	Breast cancer with distant metastases	13%

Table 2.1. Stages of breast cancer with the corresponding 5-year survival rate.

For a single breast lesion, older patients are more likely to have malignant lesions. Tumor size is another important prognostic factor used in staging a lesion, as a larger tumor increases the risk of axillary and systemic metastasis [6]. Although rare, very small tumors are capable of distant metastasis. The course of treatment depends on both the stage of the disease and the patient's preference. Treatment options include surgery, radiation therapy, chemotherapy, hormone therapy, and immunotherapy. If no axillary metastases are present, some patients may not receive systemic therapy, depending on the characteristics of the tumor. Almost all women with one to three positive axillary nodes receive some form of standard systemic treatment, either hormonal therapy or chemotherapy. Women with four to nine

positive axillary nodes are eligible for high-dose chemotherapy. If ten or more nodes are positive, patients are eligible for other experimental treatments [1].

The cell types themselves, along with the invasiveness of the cancer, help to predict the natural history of the cancer. As a general rule, all histologic types of invasive breast cancer (lobular, tubular, etc.) except ductal carcinoma tend to have a favorable prognosis, with the exception of the so-called "inflammatory" variant of invasive breast cancer, which has a worse prognosis [7]. Pathologists often assign a histologic grade to a patient's cancerous breast tumor to help determine the patient's prognosis. A completely uniform system of grading for breast cancers is not possible because of the wide variety of histologic cell types. The Scarff-Bloom-Richardson system [8, 9] is the most common type of cancer grading system used today and is presented in Table 2.2.

Tubule Formation (% of carcinoma composed of tubular structures)	Score
>75%	1
10-75%	2
less than 10%	3
Nuclear Pleomorphism	**Score**
Small, uniform cells	1
Moderate increase in size and variation	2
Marked variation	3
Mitotic Count (per 10 high power fields)	**Score**
Up to 7	1
8 to 14	2
15 or more	3

Table 2.2. The Scarff-Bloom-Richardson system

Histologic grading of all types of invasive breast cancer takes into account growth pattern (tubule formation), nuclear pleomorphism and mitotic rate and is usually expressed as grade I (well differentiated), grade II (moderately differentiated) or grade III (poorly differentiated). The grade is calculated by adding the above scores. Histologic grade has been shown to be a significant predictor of both survival and likelihood of local recurrence and/or metastasis in breast cancers. It has also been shown to correlate with prognosis [9].

The grade correlates with survival as shown in Table 2.3 [1] :

Grade	Description	Score	5 yr. survival	7 yr. survival
Grade I (lowest)	Well-differentiated breast cells; cells generally appear normal and are not growing rapidly	3,4,5	95%	90%
Grade II	Moderately-differentiated breast cells; have characteristics between Grade I and Grade II tumors	6,7	75%	63%
Grade III (highest)	Poorly differentiated breast cells; cells do not appear normal and tend to grow and spread more aggressively	8,9	50%	45%

Table 2.3. Correlation of grade and survival

2.2   Diagnostic Procedures: biopsy

Biopsy

Biopsy is the standard procedure for removing tissue from a potentially abnormal site previously found by mammography, ultrasound, or by a physician for further investigation and diagnosis. Traditionally, open excisional biopsies are performed under general anesthesia in the operating room. A surgeon removes the entire lesion, which can vary in size from a few centimeters to the entire breast (mastectomy). After removal, the tissue is sectioned, stained, and examined by a pathologist. Currently, a diagnosis by pathology is considered the gold standard for diagnosing breast lesions.

Needle Biopsy

In recent years, less invasive techniques than excisional biopsies for extracting tissue specimens have been developed, such as needle biopsy. Needle biopsies are less intrusive than excisional biopsies yet they provide the same diagnostic accuracy. In the case of stereotactic core needle biopsy a woman lies face down on a special table, as shown in Fig. 2.7.

stereotactic table
http://www.breastbiopsy.com/mammotome_theprocedure.jsp
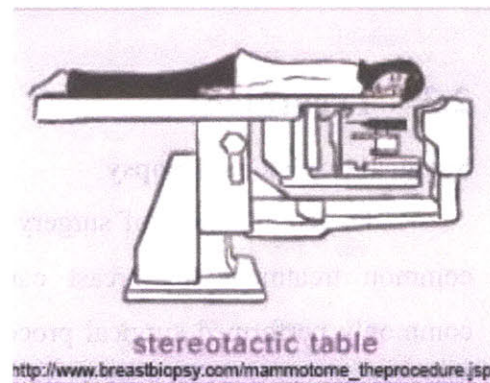
Figure 2.7. Instrumentation used in stereotactic biopsy procedures

Breast lumps are localized with the aid of mammography and ultrasound. Needle biopsies are performed in a radiologist's office on an outpatient basis under local anesthesia. The entire procedure can be performed in just a few minutes.

Fine Needle Aspiration (FNA)

Needles of various sizes are used to perform fine needle aspiration. In cases where the doctor wants to extract fluid from a cyst or cells from a solid lesion, they utilize very small 20-25 gauge (0.89-0.51 mm) needles. The procedure is performed under local anesthesia and requires a small incision. The procedure takes a few minutes and typically leaves no scarring and does not require stitches. FNA is the easiest method to provide pathologists with a breast biopsy. Due to the small size of the needle used for FNA, the healing process will be quick, but as a result, the cell sample is small and so evaluation of the suspicious lesion can be incomplete. A study of fine needle aspiration found that 34 percent of patients were insufficiently sampled and required repeat procedures.

Core Needle Biopsy

Core needle biopsies are similar to fine needle aspiration with the exception of the larger size of the needle (14-18 gauge, 2.11-1.25 mm). Increasing the size of the needle enables the doctor to obtain a larger sample that can lead to a better diagnostic accuracy and decrease the need for repeat procedures. During the core biopsy breast tissue is removed while under FNA only cells and fluids are removed.

2.3   Treatment

Surgical (excisional) biopsy

The combination of surgery with radiation and/or chemotherapy is the most common treatment for breast cancer. Lumpectomy and mastectomy are both commonly performed surgical procedures for removing (excision) breast tumors. A lumpectomy is a partial mastectomy, in that only part of the breast is removed. Depending on the case, lymph nodes may also be removed during this procedure. To

make sure that all of the cancerous cells are excised from the patient, a small amount of normal tissue surrounding the lesion (1-4mm, depending on policy of a particular hospital) is also excised (margins). The removed tissue is inked with different colors on all faces. Margins and the excised tissue samples are examined by a pathologist. If cancer cells are found touching or near the inked regions, margins are called positive, and it is assumed that malignant cells are likely still present in the patient. The color of the ink identifies the region of the surgical cavity which still has malignant cells. In cases where cancer cells are found at margins, the doctor recommends the patient undergo a re-excision. Generally, lumpectomy procedures take 60 to 90 minutes. Even in the case of negative margins (no cancerous cells have been found at margins) women receive 6 to 7 weeks of radiation therapy in order to eliminate any potentially remaining cancer cells.

There are three types of mastectomies: simple, modified radical and radical mastectomies. A simple mastectomy is the procedure, during which the entire breast tissue is removed, but axillary contents are undisturbed. The most common form of mastectomy is a modified radical mastectomy, under which the entire breast is removed along with the axillary contents, which is one reason for the limited range of motion in the arm and shoulder on the operative side after the surgery. The radical mastectomy procedure involves removing the entire breast, the axillary lymph nodes, and the pectoralis major and minor muscles behind the breast. This type of mastectomy is more disfiguring than a modified radical mastectomy. It is done in the case of tumors involving the pectoralis major muscle. Mastectomies require general anesthesia and must be done in the hospital. Patients have a choice of getting breast reconstruction immediately following the mastectomy as a part of the same surgery, or receiving it afterwards.

Radiation Therapy

Radiation therapy uses high-energy x-rays to destroy cancer cells. It is performed externally or by radioactive "seeds" that are placed directly into the tumor (brachytherapy). The patient may be asked to undergo radiation therapy in order to

shrink the tumor before surgery (neoadjuvant therapy) or after surgery to destroy all the cancerous cells remaining in the breast, underarm, or chest wall (adjuvant therapy). Radiation therapy is performed in a hospital or outpatient center. Radiation treatment lasts for 6 to 7 weeks, and each treatment session takes a few minutes.

Chemotherapy

Chemotherapy is a systemic treatment in which the patient takes a combination of drugs that circulates through the entire body via the bloodstream. The goal of this treatment is to slow tumor growth and destroy cancer cells. Drugs may be given to a patient orally or injected into the venous system. Chemotherapy can be used before and after the surgery similar to radiation therapy.

Hormone Therapy

The most effective and least toxic therapy currently available is endocrine manipulations. Estrogen, a hormone produced by the ovaries, promotes the growth of some breast cancers, particularly those with detectable amounts of estrogen receptor protein. The goal of hormone therapy is to block the effect of estrogen or lower estrogen levels. Tamoxifen is a SERM (selective estrogen receptor modulator). It is the most prescribed SERM. It works by competing with estrogen to bind to estrogen receptors in breast cancer cells. By blocking estrogen in the breast it helps slow the growth and reproduction of breast cancer cells. Tamoxifen is used for the treatment of ER (estrogen receptor) positive breast cancer in pre- and post-menopausal women. It can be prescribed to a patient before and/or after biopsy, as well as to treat cancer that has spread or regenerated after a previous treatment. It is also approved by the FDA for the prevention of breast cancer in women at high risk of developing breast cancer.

2.4 Summary

Breast cancer is the most common female cancer. The survival rate depends on early diagnosis and effective treatment. Pathology is the gold standard for diagnosis, but it is subject to human error, inconsistency, need of different stains and time consuming. Owing to the heterogeneity and complexity of the breast, a good understanding of breast pathology is necessary for the correct development of a diagnostic algorithm.

2.5 References

1.   Cotran, R., V. Kumar, and T. Collins, *Robbins Pathologic Basis of Disease.* W. B. Saunders Company, ed. 6th. 1999, Philadelphia.

2.   Farahmand, S. and D.F. Cowan, Elastosis in the normal aging breast. A histopathologic study of 140 cases. *Arch Pathol Lab Med,* 1991. **115**(12): p. 1241-6.

3.   Rosen, P., *Breast Pathology.* 1997, Philadelphia, PA: Lippincott-Raven.

4.   Dupont, W.D., et al., Long-term risk of breast cancer in women with fibroadenoma. *N Engl J Med,* 1994. **331**(1): p. 10-5.

5.   Rubin, E. and J. Farber, *Pathology.* 2nd ed. 1996: J. B. Lippincott company. 1578.

6.   Simpson, J.F. and D.L. Page, Prognostic value of histopathology in the breast. *Semin Oncol,* 1992. **19**(3): p. 254-62.

7.   Elston, C.W. and I.O. Ellis, Pathological prognostic factors in breast cancer. I. The value of histological grade in breast cancer: experience from a large study with long-term follow-up. *Histopathology,* 1991. **19**(5): p. 403-10.

8.   Elston, E.W. and I.O. Ellis, Method for grading breast cancer. *J Clin Pathol,* 1993. **46**(2): p. 189-90.

9.   Genestie, C., et al., Comparison of the prognostic value of Scarff-Bloom-Richardson and Nottingham histological grades in a series of 825 cases of breast cancer: major importance of the mitotic count as a component of both grading systems. *Anticancer Res,* 1998. **18**(1B): p. 571-6.

CHAPTER 3

Current technologies:

Imaging and spectroscopy

This chapter describes different imaging and spectroscopic technologies used in clinical and research practice for identification of breast lesions. The first part of the chapter is devoted to the imaging technologies, such as MRI, PET, DOT and OCT. This part of the chapter is focused on the strengths and weaknesses of these techniques. In the second part of the chapter, different spectroscopic modalities are depicted. The main focus of this topic is Raman, diffuse reflectance and intrinsic fluorescence spectroscopy. The theory behind these phenomena is introduced. Previously developed instruments to obtain spectroscopic signal as well as calibration and fitting data are provided in great details.

3.1 Introduction

The history of light application for diagnosing breast lesions can be traced to 1929, when Cutler applied light for monitoring status of breast lesions [1].

3.2 Strengths and weaknesses

3.2.1 MRI

Magnetic resonance imaging (MRI) is an imaging technique that uses radio waves to induce spin flips of protons, which are part of water molecules, while a person is placed inside a high magnetic field. By applying a spatial field gradient, MRI provides information about tissue density.

Unlike the other techniques, magnetic resonance (MR) imaging can non-invasively analyze molecular structure and composition in addition to anatomy. In forming images, however, conventional proton MR imaging techniques largely ignore and often suppress chemical shift information. As a result, as currently used clinically, they also mainly provide anatomic images. New high-resolution MR techniques may be able to identify breast lesions smaller than those currently detected with mammography [2], but will still require biopsy for diagnosis [3]. The most useful MRI technique for breast imaging uses a contrast agent, Gadolinium DTPA, which is injected into a vein in the arm prior or during the exam to improve the quality of the images. This contrast agent helps produce stronger and clearer images in order to highlight any abnormalities. However, one of the weaknesses of MRI is that it has been unable to effectively image microcalcifications, small calcium deposits that can be associated with breast cancer, as it will be discussed later, see Chapter 9 [4].

3.2.2 PET

Positron emission tomography (PET) detects pairs of gamma rays emitted indirectly by a positron-emitting radionuclide, which is introduced in to the body on a biologically active molecule. The vast majority of the work in breast tissue using PET has utilized a fluorodeoxyglucose labeled with Fluorine-18 (^{18}FDG). This technique

produces a three-dimensional image with a resolution of 5-8mm range in all three planes [5-8].

3.2.3 DOT

Diffuse optical tomography (DOT), an optical imaging technique to identify suspect lesions, is currently under study [9]. Similar to current screening techniques, it is noninvasive and can detect lesions deep within the breast. It employs light of a number of near-IR wavelengths. Contrast, provided by scattering and absorption, measures relative concentrations of oxy- and deoxyhemoglobin, as well as the presence of lipids and water content [10]. However, this technique has a low resolution [11, 12], due to which lesions of small size go undetected; a resolution of 4 to 13 mm has been reported, and the sources of contrast are limited [9, 10, 13]. Despite these challenges, DOT has been utilized in several reported breast cancer studies [14, 15].

3.2.4 OCT

Optical coherence tomography (OCT) is another promising imaging technique that is rapidly developing. OCT is based on low-coherence interferometry to produce a 2-dimentional cross-sectional image of tissue microstructure. OCT can provide a micrometer resolution [16, 17]. The imaging depth of OCT is about 2-3 mm and it can be incorporated into a endoscopic imaging devices [18]. Hsiung *et al* had studied OCT for evaluation of breast lesions during an *ex vivo* study [19]. Scientists observed structural changes associated with different histopathology diagnoses on the limited set of specimens. However, even though OCT images can be acquired rapidly, visualization and interpretation of the image takes a long time. The disadvantage of OCT is the fact that it can provide only structural information, and it does not provide biochemical information about tissue composition. In addition, the information is not quantitative and it is subject to interpretation.

3.3 Spectroscopy

3.3.1 Raman spectroscopy

Raman spectroscopy detects molecules by exciting vibrations amongst bonds which uniquely correspond to each molecule, and thus has been extensively studied in biomedical research [20-23]. Raman spectroscopy is a tool that can be used for studying the structure and biochemical changes in biological tissue; it has been used extensively for monitoring and diagnosis of disease *in vivo* and *in vitro*, for example in atherosclerosis, malignant lesions, and bone and teeth [24-26].

3.3.1.1 Theory

The Raman effect was discovered by C.V. Raman in 1928 [27]. It is an inelastic scattering process, during which photon of incident transfers energy to (Stokes) and from (anti-Stokes) the sample's vibrational or rotational modes. The frequency shift is equal to the molecular vibration frequency, and usually measured in wave numbers (cm^{-1}). The Stokes scattering is more intense than the anti-Stokes, because the Raman scattering is proportional to the population of the initial state. Individual bands in the Raman spectrum are characteristic of specific molecular motions. By measuring the energy of the emitted photon after the scattering event, and knowing the energy of the incident photon, the structure of the interrogated molecule can be analyzed.

Biological tissue, such as breast tissue, has a number of molecules that have vibrations, characterized by wavelength (frequency) and Raman scattering cross section; and the Raman spectrum of a particular molecule has a distinct pattern, which can be easily recognized. However, the Raman effect is a weak effect (as only 1 in 10^7 of incident photons cause Raman effect [28]), thus the intense Rayleigh light must be removed so it does not overwhelm the Raman scattering. In addition, it is important to remember, that the Raman frequency shifts are independent of the wavelength of the incident light. Thus, the frequency of the excitation light can be chosen for a specific application. In the case of biological samples, near infrared

(NIR) light is optimal because of a reduction of background fluorescence and deeper sampling depth.

Alfano *et al* acquired the first Raman spectra from breast tissue [20]. Since then, several other groups have investigated usage of Raman spectroscopy to diagnose breast cancer [23, 29-32]. Our laboratory has been involved in the research of applying Raman spectroscopy for diagnosing breast lesions [21, 23, 33-37]. We found out that usage of the 830 nm excitation wavelength is appropriate for biological tissue. Due to heterogeneity and complexity of breast disease (as described in Chapter 2), it is important to accurately detect a number of different molecules. Previously, our laboratory identified and collected eight Raman active morphological components of the breast tissue using 830 nm excitation light: calcium oxalate dehydrate, calcium hydroxyapatite, β-carotene, fat, collagen, cell nucleus, and cell cytoplasm [38]. Spectra are depicted in the Figure 3.1. In addition to these 8 Raman components, we
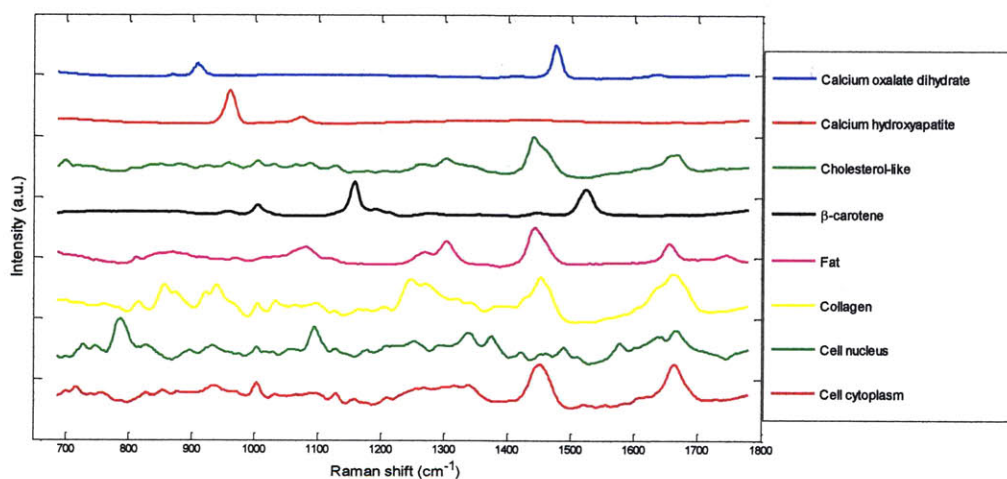
Figure 3.1. Raman spectra of morphological Raman active molecules found in the breast.

collected Raman spectra from water, as well as sapphire and epoxy – components that were used in the manufacturing of the probe (spectra not shown).

3.3.1.2 Clinical Raman system

The original spectra depicted on Figure 3.1. were collected using a laboratory based Raman microscope system [37]. In order to apply Raman spectroscopy technique as a valuable medical tool, the clinical Raman system was constructed.

Note, throughout the thesis we will refer to "system" as a combination of a clinical instrument and an appropriate probe that delivers light from the instrument to the tissue site that is under investigation.

3.3.1.2.1 Clinical Raman instrument

The clinical Raman instrument, developed in the Spectroscopy laboratory, is illustrated in Figure 3.2a [39]. Light from an 830-nm InGaAs diode (Process Instruments, Salt Lake City, UT) is collimated by two cylindrical lenses and passed through a bandpass filter centered at 830 nm (Kaiser Optical Systems, Inc., Ann Arbor, MI). Then, the light is focused into the 200μm core diameter excitation fiber of the Raman probe using a 10x microscope objective. Illumination of the sample is gated by a high-speed computer-controlled external shutter (LS6ZM2, Vincent Associates, Rochester, NY) redirected by a gold-coated mirror and focused onto the Raman probe excitation fiber by a 10×microscope objective. The Raman probe is terminated with an FC connector in order to provide day-to-day reproducibility of alignment. This vertical array serves as an entrance slit to the spectrograph (Holospec f/1.8i, Kaiser Optical Systems) attached via modified BNC connector. The collection light passes through a notch-filter and then it is dispersed onto a back-illuminated, deep-depletion CCD detector with a 1340x400 array of pixels (Spec-10:256 BR, Princeton Instruments, Trenton, NJ). The CCD detector has a 16 bit dynamic range and is liquid nitrogen cooled to -110°C. Instrument is controlled by a laptop computer. The Raman probe, depicted in Figure 3.2.b has a total diameter of 2mm a length of about 4m.

3.3.1.2.2 Front-viewing Raman probe

Clinical application of Raman spectroscopy requires an optical fiber probe for minimally invasive acquisition of Raman signal. The important aspect of the probe is the ability to collect Raman light in a clinically relevant time frame with a safe level of light exposure. Our Raman optical fiber probe provides an optimal collection efficiency probe that is capable of collecting high-quality data in seconds [40].

In order to efficiently transmit NIR light, fused silica optical fibers were employed [41]. However, even with a low laser excitation power the fused silica fiber background is intense and saturates the detector. The fiber background consists of Raman light from the fused silica core, fluorescence from impurities and dopants used to produce fibers of a particular numerical aperture (NA), and signal from jacket materials. This fiber background would overwhelm and mask the tissue Raman signal, thus it has to be removed. In addition, backscattering laser light generated in the tissue needs to be separated and removed from Raman signal generated in the tissue.

Our lab designed a set of dielectric filters at the distal end of the probe. The delivery fiber is terminated with a short-pass filter that is centered at 830nm wavelength. It transmits the laser excitation light while blocking the background generated in the delivery fiber. The distal end of the collection fibers are terminated with a long-pass filter, which transmits the tissue Raman signal to the spectrograph, while blocking Rayleigh-scattered light.
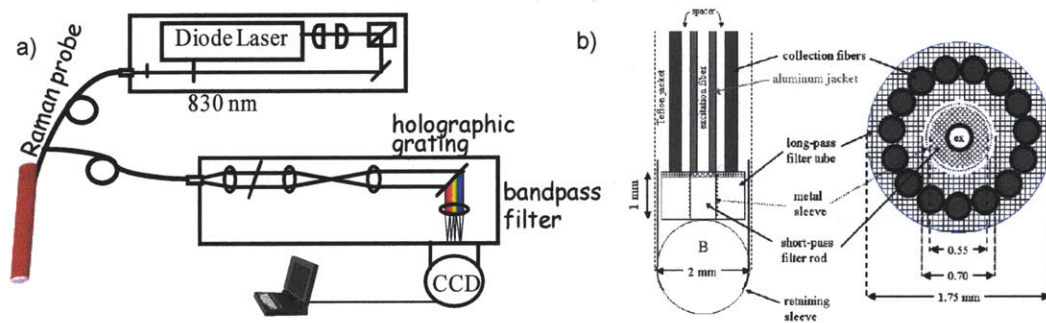
Figure 3.2. a) Schematic of Raman instrument; b) Schematic of Raman front-viewing probe

In addition, in order to efficiently collect Raman signal, the probe design contains 1 delivery fiber surrounded by 15 collection fibers. The central excitation fiber has a 200mm core diameter and 0.22 NA. The collection fibers have 200 mm core diameter and 0.27 NA, which is matched to the NA of the spectrograph. Also, the distal tip of the probe contains an anti-reflection coated sapphire ball lens (MKPhotonics, Albuquerque, NM) secured to the fiber bundle and filter unit in a stainless steel tube. All components of the probe are constructed using medical grade

materials that can withstand standard cold gas ethylene oxide sterilization for surgical procedures.

3.3.1.3 Calibration and data modeling

The Raman acquired spectra have to be post processed to configure them into the form that will be diagnostically useful. The calibration process ensures a day-to-day, system-to-system, and user-to-user reproducibility of the data.

A wavenumber calibration needs to be performed for determination of Raman band frequencies. Given small changes in the instrumentation alignment, changes may occur in the pixel position of a particular Raman band. Tylenol 4-acetaminophenol is used as a standard for wavenumber calibration. In order to correct Raman spectra for the system wavelength response, collection of the light from a wavelength-calibrated tungsten halogen lamp (LS-1, Ocean Optics, FL) diffusely scattered from a reflectance standard, BaSO$_4$, that has a flat response, is performed. The remaining probe background generated in the optical fibers is characterized by collecting the excitation light scattered from a roughened aluminum surface.

All of the data modeling is based on the assumption that the Raman spectrum of a mixture can be viewed as a linear combination of the spectra of its constituents (basis spectra), P_i, a d that the signal intensity, S, at a specific wavenumber (w) and chemico-morphological concentration, C_i, are related as follows:

$$S(w) = \sum C_i \cdot P_i(w)$$

Eq 3.1

Non-negativity constrained ordinary least squares minimization is used for model fitting, yielding the relative contribution of the basis spectrum of each component, given in Fig 3.1, to the observed spectrum of the mixture. The accuracy of a given model can be qualitatively determined by observing the residual of the model that was calculated by subtracting model fit from the observed tissue spectrum. The smaller the structureless residual, the more completely the model has accounted for the observed spectral features, and thus the better the model. One of the biggest advantages of our modeling procedure over that of other groups' one is that the basis spectra can be correlated with the presence or absence of a specific chemical or a

morphological feature providing both quantitative and qualitative information about tissue composition. All constructed algorithms that are based on fit coefficients – relative concentrations of different chemico-morphological constitute – that are physically meaningful, and thus will be easier to explain and can lead to deeper knowledge of cancer development. In addition, this type of algorithm is believed to be more robust provided that it is constructed on an adequate set of data.

Logistic regression is used to generate decision algorithms. Logistic regression is a method that classifies points in a space that we used throughout the dissertation. Logistic regression is a method for classifying a sample according to discrete categories. Specifically in our study, lesions are characterized by vectors, whose elements are spectral parameters – fit coefficients, and the labels indicate disease classification provided by a pathologist, for example IDC – infiltrating ductal carcinoma. Pathological diagnoses are used as a gold standard in all of our diagnostic algorithms. Thus, it used to correlate fit coefficients, obtained by modeling Raman spectra, with disease diagnoses. Logistic regression is a linear technique, which assumes that a discriminant score, $R_{m\delta}$, for the mth sample to be in class δ, can be determined from the relative fit contributions (C_{mj}) of the j basis spectra, such that

$$R_{m\delta} = \alpha_\delta + \sum_j C_{mj} \beta_{j\delta} \qquad\qquad 3.2$$

where α is a constant offset and β is an adjustable coefficient for each morphological structure in each diagnostic class [42]. This method is preferred over traditional discriminant analysis because logistic regression does not make any assumptions about the fit-coefficients being normally distributed, and it allows discrete variables as inputs. A maximum likelihood estimation is the core manipulation involved in logistic regression [43].

An analytical error formula that estimates the uncertainty in spectral contributions predicted by linear multivariate calibration has been also derived [44, 45]. The formula provides the standard deviation of the predicted contribution of a tissue component for a given signal to noise ratio and spectral model overlap. The overlap factor accounts for the similarity between the Raman spectrum of the tissue

component of interest and the spectra of all the other tissue components. This standard deviation, termed Δc, for the kth model component of interest can be expressed as:

$$\Delta c_k = \frac{\sigma}{s_k} * olf_k \qquad\qquad 3.3$$

In the above equation, σ is the standard deviation of the noise in the system, s_k is the signal strength of the kth model component, and the olf_k is the spectral overlap factor between the kth model component and the rest of the model spectra.

Thus, prior to developing or prospectively applying diagnostic Raman algorithms, the fluorescence background from each spectrum was removed by means of a sixth-order polynomial. Following spectral correction, the basis spectra of the Raman spectral model were fit to the spectrum obtained from the breast tissue via non-negatively constrained least-squares minimization. In addition, Raman spectra of epoxy and sapphire – two probe components – were added to the model, to correctly model the data. Following the procedure used in the calibration study, the fit coefficients for each Raman spectrum of the data set were normalized to sum to unity. An example of a raw and processed Raman spectrum is illustrated in Fig 3.3.
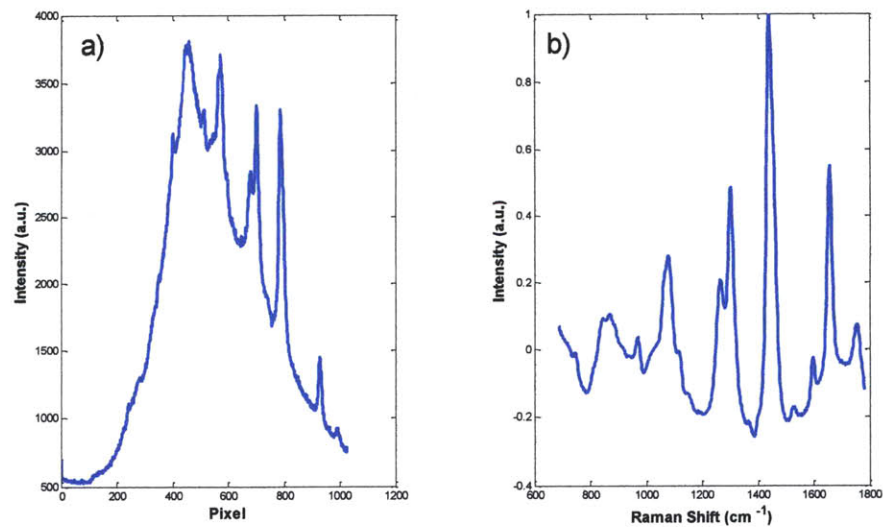
Figure 3.3. Example of Raman a) raw and b) processed data.

3.3.2 DRS/IFS spectroscopy

3.3.2.1 Theory

Diffuse reflectance spectroscopy (DRS)

Diffuse reflectance spectroscopy (DRS), an elastic scattering spectroscopy, is a non-invasive technique that uses the interaction of light with a sample through absorption and scattering phenomena to produce a characteristic reflectance spectrum that provides information about the structure and composition of the medium. Diffusion theory is appropriate in a medium dominated by scattering rather than absorption so that each photon undergoes many scattering events before being terminated by an absorption event.

Elastic scattering is the most prominent optical property of tissue. The scattering coefficient, μ_s, which represents an average number of scattering events per unit length, is in the range of μ_s=10-100mm^{-1} for soft tissue. Scattering arises from the microscopic variations and inhomogeneities of the refractive index that correspond to various scattering centers [46]. The angular distribution of the scattering is described by the scattering phase function, $p(\theta)$, which provides the probability of a photon to be scattered at an angle, θ, with respect to the initial direction. The scattering coefficient is essentially the cross-sectional area per unit volume of tissue. The reduced scattering coefficient is a lumped property incorporating the scattering coefficient μ_s and the anisotropy parameter g:

$$\mu_s' = \mu_s(1 - g), \text{ where } g = 2\pi \int p(\theta) \cos \theta \sin \theta d\theta \qquad 3.4$$

Anisotropy, g, is used to indicate how strongly forward-directed the scattering is. Typical values for tissue are g = 0.8 − 0.95, which corresponds to average scattering angles between 45 and 20 degrees, respectively.

Mie theory provides an exact solution for scattering of light with wavelength λ by a spherical object with diameter d and refractive index n that is located in a surrounding medium with refractive index n_0. In this study μ_s' was modeled using a power law in the following way:

$$\mu_s' = A\lambda^{-B}, \qquad 3.5$$

where A can be interpreted as the amount (or concentration) of Mie scatterers, B is related to the sizes of the scatterers.

Absorption is measured by means of the absorption coefficient, μ_a, which is defined as the amount of absorption present in units of inverse length. Water, being the major component of soft tissue has negligible absorption in the visible range ($<10^{-4}$ mm^{-1}). Tissue absorption, which depends on wavelength, is due to a number of characteristic biochemical molecules.

Hemoglobin is a major absorber in the blue region of the visible spectrum. Other biochemical compounds with characteristic light absorption in the visible range include β-carotene, bilirubin, and in the skin, melanin. Many other absorbers are present in the tissue at much smaller concentrations and can be ignored. Several other research groups have applied DRS for separating malignant breast lesions from non-malignant lesions [47-49]. In this study, oxyhemoglobin, deoxyhemoglobin and β-carotene will be treated as the major absorbers of light in breast tissue. Their absorption spectra are illustrated in Figure 3.4. The total absorption coefficient, μ_a, can be expressed as a linear combination of the extinction spectra of the two absorbers as follows:

$$\mu_a = c_{HbO_2} \cdot \varepsilon_{HbO_2}(\lambda) + c_\beta \cdot \varepsilon_\beta(\lambda)), \qquad\qquad 3.6$$

where c_β is the concentration of β-carotene and c_{HbO_2} is the concentration of oxyhemoglobin. Note, if the excised tissue is under study, i.e. *ex vivo* study, the tissue is exposed to air, thus deoxyhemoglobin is not used as one of the absorbers.
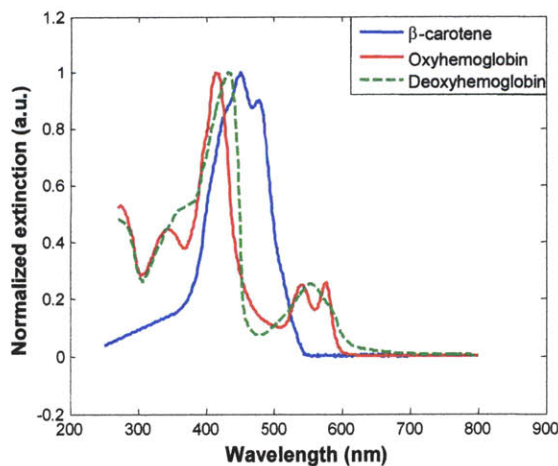
Figure 3.4. Absorption spectra of oxyhemoglobin deoxyhemoglobin, and β-carotene.

Intrinsic fluorescence spectroscopy (IFS)

Fluorescence is one of the categories of luminescence and occurs from electronically excited states. Fluorescence is more dominant in the UV than in the IR range. Autofluorescence from tissue can be observed from reduced nicotinamide adenine dinucleotide (NADH), collagen, oxidized flavins (FAD, the adenine dinucleotide, and FMN, the mononucleotide), elastin and pyridoxal phosphate. Fluorescence excitation and emission spectra in tissue can be used to identify fluorophores and monitor their concentrations. In biological tissue, with the progression of a disease the relative concentration of fluorophores can change, thus leading to changes in the observed fluorescence intensity and its lineshape. Autofluorescence spectroscopy has been used to explore diagnosing different diseases, such as atherosclerosis, oral cancer, cervical dysplasia, and breast cancer. Alfano *et al.* were the first to measure the fluorescence spectra of malignant and nonmalignant breast tissue [50]. Several groups [51-53] showed promising results in separation malignant lesions from non-malignant using empirical algorithms. Such empirical algorithms do not emphaze the importance of biochemical and morphological information contained in the spectra.

However, fluorescence spectra acquired from a bulk tissue are distorted by absorption and scattering, thereby limiting the accuracy of the extracted information. To overcome this problem, DRS can be used in conjunction with the measured fluorescence spectrum to extract the intrinsic (undistorted) fluorescence [46, 54]. This process is called intrinsic fluorescence spectroscopy (IFS).

3.3.2.2 DRS/IFS system

DRS and IFS spectra can be collected by means of a FastEEM system previously developed by our laboratory [55].

3.3.2.2.1 DRS/IFS instrument

The FastEEM instrument collects white light reflectance and fluorescence excitation-emission matrices (EEM's) within a fraction of a second in order to collect diffuse reflectance and intrinsic fluorescence spectra [56]. A schematic of the

FastEEM instrument, that is capable of collection of white light reflectance and fluorescence spectra in fraction of seconds, is presented in Fig. 3.5. It delivers a sequence of ten laser pulses (308 - 480 nm) and two white light pulses to the tissue via an optical fiber probe (see below for details of the probe design). The XeCl laser (Lambda Physik Optex, Ft. Lauderdale, FL, 308 nm, 8 mJ per pulse, FWHM 8 ns) excited fluorescence at 308nm wavelengths as well as pumped 10 dyes circularly arranged on the dye-wheel providing an additional 10 excitation wavelengths in the 308-480nm range. When the wheel spins, the individual dye cells are consecutively pumped by the XeCl excimer laser. The Xe arc flashlamp (Hamamatsu L7684, Bridgewater, NJ, 1 J per pulse, FWHM 2 µs) was used to excite tissue reflectance. The same probe collects the white light reflectance and fluorescence and delivers it to the entrance slit of a diffraction grating spectrometer where it is dispersed onto an intensified CCD detector. All ten laser-induced emission spectra and the two white light reflectance spectra can be collected in approximately 0.3 s. Several of these acquisitions can be averaged together to increase the signal-to-noise ratio (SNR).
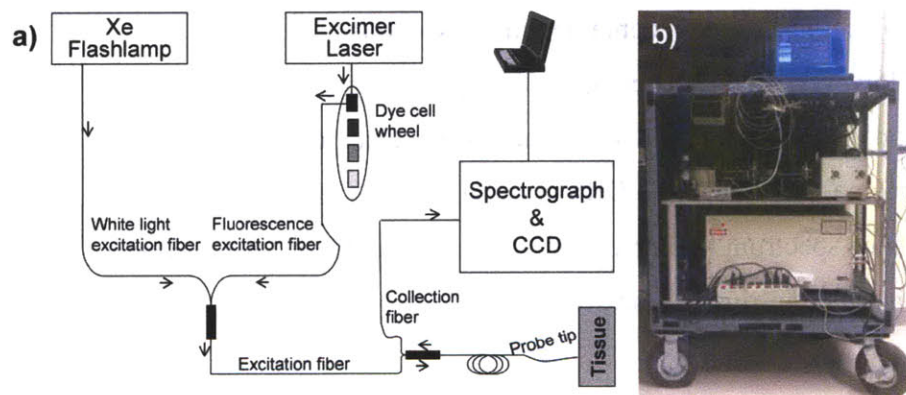
Figure 3.5. a) Simplified schematic of the FastEEM instrumentation; b) a photograph of developed FastEEM instrument

Previously, we found that the acquisition of five measurements provides sufficient SNR in most tissues, making a typical acquisition time on the order of 1.5 s. Reflectance and fluorescence light was coupled into the optical probe, which is used for light delivery and collection (illustrated in Figure 3.6). It is in the form of a flexible catheter, with an overall length of over 3 m and a diameter of approximately 1.2 mm.

3.3.2.2.2 Front-viewing probe
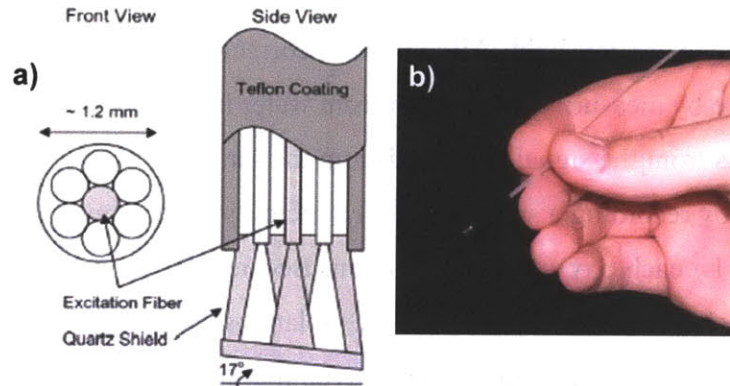
Figure 3.6. a) A diagram of the DRS/IFS optical fiber probe showing front and side view; b) A photograph of the probe.

An optical fiber probe is used to deliver the excitation light from the two sources (from the flash lamp for DRS and from excimer laser for fluorescence spectroscopy), as well as to convey light emitted from the tissue to the detection components [56]. The probe consists of a single central delivery fiber surrounded by 6 collection fibers in a closest-packed configuration. The fiber core is composed of fused silica and has a diameter of 200 μm (Numerical Aperture (NA) = 0.22). With the cladding, the diameter of each fiber is 220 μm. The entire 3 m length of the probe is enclosed in Teflon tubing for protection. At the probe tip, the fibers are exposed from the cladding, fused, embedded in a protective silver epoxy, and surrounded by a protective sheath. A 1.5 mm long quartz shield is placed at the very tip to create a reproducible geometry when in contact with the tissue. With the cladding and protective sheath, the probe tip has a diameter of approximately 1.2 mm. The tip of the probe is polished to an angle of approximately 17° to prevent specular reflections from entering the probe and producing artifacts in the measured signal. At the distal end of the probe, the 6 collection fibers are separated from the source fiber and coupled to the detection portion of the instrument via a set of 6 SMA connectors. Similarly, the distal end of the delivery fiber is coupled to the excitation sources via another SMA connector.

3.3.2.3 Calibration and modeling DRS and IFS

Prior of collecting spectroscopic data from tissue specimens, calibration of the system was performed. Background calibration is used to remove effects of CCD dark currents and stray light. All data were corrected for background reflectance and fluorescence by measuring a spectrum from water in a black container and subtracting these counts from the signal measured from the sample. The wavelength calibration is performed by recording a spectrum from a mercury argon lamp (HG-1, Ocean Optics, Dunedin, FL) each day of data collection. Because the wavelengths of the mercury peaks are known, we determine the relationship between pixel number and wavelength by fitting a second-order polynomial to a plot of the wavelength of each peak versus the pixel number of the peak. White light reflectance calibration is achieved by dividing the background corrected tissue spectrum by that of a reflectance standard (20 % reflectance standard, Labsphere Inc., North Sutton, NH). Calibration of the measured reflectance corrects for the spectral profile of the flashlamp and the wavelength-dependence of the detector response. Each EEM is corrected for excitation intensity of the dye lasers by measurement of a standard Rhodamine B dye mixture (5 g/L in ethylene-glycol). The known quantum yields of Rhodamine B are then used to correct the intensity of each emission spectrum.

The calibrated diffuse reflectance spectrum were fit over the range of 350 − 750 nm using a constrained nonlinear least-squares fitting algorithm. First, calibrated diffuse reflectance spectrum, DRS, is calculated by the following formula:

$$DRS(\lambda) = \frac{Spectrum - Background}{Spectralon - Background} \cdot SpecCal \qquad 3.7$$

All data were corrected to take into account background reflectance and fluorescence via measuring a spectrum from water in an opaque container, as well as spectralon spectrum acquired from Spectralon (LabSphere, Inc., North Sutton, NH) 20% reflectance standard; SpecCal is an intrinsic property of the material and its value were provided by the manufacturer, and represents a fraction of the light reflected by the spectralon reflectance standard.

A non-linear least-squares fitting algorithm was used to fit the calibrated reflectance data, *DRS*, to the Zonios model [46]. The best fit is found by minimization of X^2:

$$X^2 = \sum_\lambda \left(\frac{DRS(\lambda) - Fit(\lambda)}{\delta(\lambda)} \right)^2 \qquad 3.8$$

, where $\delta(\lambda)$ is the error in DRS and calculated using the following formula:

$$\delta(\lambda) = \sqrt{\sum_i \left(\frac{\delta DRS(\lambda)}{\delta x_i} \sigma_i(\lambda) \right)^2} \qquad 3.9$$

We obtain several parameters from modeling tissue reflectance: A [mm^{-1}],B, Hb [mg/ml], β-carotene [mg/ml]. Note, in the case of *ex vivo* studies, where tissue is exposed to air, we assume that tissue is oxidized, and Hb presents only oxidized hemoglobin.

Based on photon migration theory, light propagation in a turbid medium is described by photons traveling in paths with discrete nodes, at which absorption,
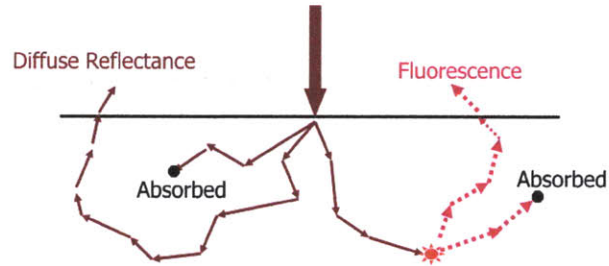
Figure 3.7. Photon migration theory

scattering, and fluorescence events occur, Fig. 3.7. Reflectance is related to the product of albedo, *a*, which represents the fraction of unabsorbed photons at each interaction event, and the escape probability of a photon that enters the medium, undergoes *n* scattering events, and is collected after exciting, ρ_n. The reflectance, *R*, can de described by a following expression:

$$R(\lambda) = \sum_{n=1}^{\infty} a^n \rho_n , \qquad \text{where} \quad a = \frac{\mu_s}{\mu_s + \mu_a}, \qquad 3.10$$

and μ_s is a scattering coefficient and μ_a is a absorption coefficient.

An analytical expression for ρ_n, was derived based on Monte Carlo simulations by Wu *et al* [57]., modified by Zhang *et al.* *[46]*, and given as follows:

$$\rho_n = \alpha \cdot \exp(-\beta n), \text{ where } \beta = S(1-g), \quad \alpha = R_0 \cdot \varepsilon, \quad \text{and } \varepsilon = \exp(\beta) - 1 \qquad 3.11$$

Note, parameter S is a constant related to the probe geometry, g is the anisotropy parameter of the medium, and R_0 is the reflectance in the absence of the absorption. We assume that g is constant over all wavelengths of the fluorescence spectrum.

In the case when excitation light is absorbed after an initial i scattering events at the excitation wavelength, the fluorescence occurs at the $(i+1)^{\text{th}}$ node, and the fluorescence photon undergoes n-i-1 scattering events at the emission wavelength, where n is the total number of scattering events. The measured fluorescence can be found using the following equation:

$$F_{xm} = \sum_{n=1}^{\infty} \sum_{i=0}^{n-1} a_x^{i+1} \cdot \frac{f_{xm}}{\mu_{sx} \cdot l} \cdot a_m^{n-i-1} \rho_{ni} \qquad 3.12$$

The fluorescence escape probability is derived based on Monte Carlo simulations by Wu *et al.* [57]., modified by Zhang *et al.*, and given as follows:

$$\rho_{ni} = (\alpha_x \alpha_m)^{1/2} \exp[-\beta(i+1)] \exp[-\beta_m(n-i-1)]. \qquad 3.13$$

The quantity f_{xm} is intrinsic fluorescence and is given by:

$$f_{xm} = \left(\frac{I_x}{h\nu_x}\right) \mu_{fx} l \phi_{xm} h \nu_m. \qquad 3.14$$

The subscripts x and m provide dependency of each variable on the excitation and emission wavelengths, respectively. The intensity of the incident light is denoted by I, h is Planck's constant, and ν is frequency of light. The absorption coefficient of the fluorophore and its quantum yield are denoted by μ_f and Φ, respectively. The constant l has dimension of length and characterizes a given light delivery-collection geometry; it is, therefore, probe-specific. Combination of above equations lead to the formula for the intrinsic fluorescence as follows:

$$f_{xm} = \frac{F_{xm}}{\frac{1}{\mu_{sx}l} \cdot \left(\frac{R_{0x}R_{0m}}{\varepsilon_x \varepsilon_m}\right)^{1/2} \cdot \frac{R_x}{R_{0x}} \cdot \left(\frac{R_m}{R_{0m}} + \varepsilon_m\right)} \qquad 3.15$$

Using this expression we can extract the intrinsic fluorescence spectrum from the measured fluorescence by use of the diffuse reflectance collected from the same tissue site with the same probe.

Once intrinsic fluorescence is derived it can be linearly decomposed into its constituents. The spectrum of tissue intrinsic fluorescence is modeled as a linear combination of tissue fluorophore basis spectra. The basis spectra were extracted from the intrinsic fluorescence spectra using multivariate curve resolution (MCR). In order to reduce patient-to-patient variation in fluorescence spectra, the areas under the IFS spectra, as well as basis spectra, were normalized to a value of one.

3.4 Summary

In this chapter the theories behind the spectroscopic techniques employed in the thesis, DRS, IFS and Raman, as well as other optical techniques were explained. Each modality provides additional information about biochemical composition of tissue, thus the combination of all three modalities might lead to a superior technique. A brief overview of the instrumental design and collected data was also presented. Evaluation of spectroscopic modalities as a tool to diagnose breast lesions is present in the next chapters.

3.5 References

1.   Cutler, M., Transillumination as an aid in the diagnosis of breast lesions. *Surg. Gynecol. Obstet*, 1929. **48**: p. 721.

2.   Morris, E.A., Screening for breast cancer with MRI. *Semin Ultrasound CT MR*, 2003. **24**(1): p. 45-54.

3.   Pettit, K., et al., The impact of breast MRI on surgical decision-making: Are patients at risk for mastectomy? *J Surg Oncol*, 2009.

4.   Valenzuela, M. and T.B. Julian, Ductal carcinoma in situ: biology, diagnosis, and new therapies. *Clin Breast Cancer*, 2007. **7**(9): p. 676-81.

5.   Powe, J.E., Positron emission tomography (PET) scanning in breast cancer. *Br J Radiol*, 1997. **70**(835): p. 668-70.

6.   Raylman, R.R., et al., The positron emission mammography/tomography breast imaging and biopsy system (PEM/PET): design, construction and phantom-based measurements. *Phys Med Biol*, 2008. **53**(3): p. 637-53.

7.   Hoh, C.K., et al., Cancer detection with whole-body PET using 2-[18F]fluoro-2-deoxy-D-glucose. *J Comput Assist Tomogr*, 1993. **17**(4): p. 582-9.

8.   Wahl, R.L., et al., Primary and metastatic breast carcinoma: initial clinical evaluation with PET with the radiolabeled glucose analogue 2-[F-18]-fluoro-2-deoxy-D-glucose. *Radiology*, 1991. **179**(3): p. 765-70.

9.   Hebden, J.C., et al., Three-dimensional time-resolved optical tomography of a conical breast phantom. *Appl Opt*, 2001. **40**(19): p. 3278-87.

10. Guven, M., et al., Diffuse optical tomography with a priori anatomical information. *Phys Med Biol*, 2005. **50**(12): p. 2837-58.

11. Culver, J., et al., Optimization of Optode Arrangement for Diffuse Optical Tomography: A Singular-Value Analysis. *Opt Lett*, 2001. **26**: p. 701-703.

12. Pogue, B.W., et al., Spatially variant regularization improves diffuse optical tomography. *Appl Opt*, 1999. **38**(13): p. 2950-2961.

13. Quaresima, V., S.J. Matcher, and M. Ferrari, Identification and quantification of intrinsic optical contrast for near-infrared mammography. *Photochem Photobiol*, 1998. **67**(1): p. 4-14.

14. Cheng, X., et al., Breast cancer detection by mapping hemoglobin concentration and oxygen saturation. *Appl Opt*, 2003. **42**(31): p. 6412-21.

15. Boverman, G., et al., Quantitative spectroscopic diffuse optical tomography of the breast guided by imperfect a priori structural information. *Phys Med Biol*, 2005. **50**(17): p. 3941-56.

16. Huang, D., et al., Optical coherence tomography. *Science*, 1991. **254**(5035): p. 1178-81.

17. Fujimoto, J.G., et al., Optical biopsy and imaging using optical coherence tomography. *Nat Med*, 1995. **1**(9): p. 970-2.

18. Tearney, G.J., et al., In vivo endoscopic optical biopsy with optical coherence tomography. *Science*, 1997. **276**(5321): p. 2037-9.

19. Hsiung, P.L., et al., Benign and malignant lesions in the human breast depicted with ultrahigh resolution and three-dimensional optical coherence tomography. *Radiology*, 2007. **244**(3): p. 865-74.

20. Alfano, R.R., et al., Human breast tissues studied by IR Fourier transform Raman spectroscopy. *Lasers in the Life Sciences*, 1991. **4**(1): p. 23-28.

21. Haka, A.S., et al., Diagnosing breast cancer by using Raman spectroscopy. *Proc Natl Acad Sci U S A*, 2005. **102**(35): p. 12371-6.

22. Hanlon, E.B., et al., Prospects for in vivo Raman spectroscopy. *Phys Med Biol*, 2000. **45**(2): p. R1-59.

23. Manoharan, R., et al., Raman spectroscopy and fluorescence photon migration for breast cancer diagnosis and imaging. *Photochem Photobiol*, 1998. **67**(1): p. 15-22.

24. Ozaki, Y., Medical application of Raman spectroscopy. *Appl. Spectroscopy Reviews*, 1988. **24**: p. 259-312.

25. Scepanovic, O.R., et al., A multimodal spectroscopy system for real-time disease diagnosis. *Review of Scientific Instruments*, 2009. **80**: p. 043103.

26. Mahadevan-Jansen, A., Raman spectroscopy for detection of cancers and precancers. *J Biomed Opt*, 1996. **1**: p. 31-70.

27. Raman, C.V. and K.S. Krishnan, A new type of secondary rdiation. *Nature*, 1928. **121**: p. 501-502.

28. Ferraro, J.R. and K. Nakamoto, *Introductory Raman Spectroscopy*. 1st edition ed. 1994: Academic Press. 370.

29. Frank, C.J., et al., Characterization of human breast biopsy specimens with near-IR Raman spectroscopy. *Anal Chem*, 1994. **66**(3): p. 319-26.

30. Frank, C.J., R.L. McCreery, and D.C. Redd, Raman spectroscopy of normal and diseased human breast tissues. *Anal Chem*, 1995. **67**(5): p. 777-83.

31. Henry, C.M., Raman spectra of breast tissue. *Anal Chem*, 1996. **68**(23): p. 718A-719A.

32. Redd, D., et al., Raman spectroscopic characterization of human breast tissues: implications for breast cancer diagnosis. *Appl Spectrosc*, 1993. **47**: p. 787-791.

33. Haka, A., *Development of in Vivo Raman Spectroscopy for the Diagnosis of Breast Cancer and Intra-Operative Margin Assessment*, in *HST*. 2005, MIT: Cambridge. p. 314.

34. Haka, A.S., et al., Identifying Microcalcifications in Benign and Malignant Breast Lesions by Probing Differences in their Chemical Composition Using Raman Spectroscopy. *Cancer Res*, 2002. **62**: p. 5375-5380.

35. Haka, A.S., et al., In vivo margin assessment during partial mastectomy breast surgery using raman spectroscopy. *Cancer Res*, 2006. **66**(6): p. 3317-22.

36. Shafer-Peltier, K.E., et al., Raman microspectroscopic model of human breast tissue: implications for breast cancer diagnosis in vivo. *J Raman Spec*, 2002. **33**(7): p. 552-563.

37. Shafer-Peltier, K.E., et al., Model-based biological Raman spectral imaging. *J Cell Biochem Suppl*, 2002. **39**: p. 125-37.

38. Shafer-Peltier, K., *Chemical Basis for Breast Cancer Diagnosis Using Raman Spectroscopy*, in *Chemistry*. 2001, MIT: Cambridge. p. 145.

39. Motz, J.T., et al., Real-time Raman system for in vivo disease diagnosis. *J Biomed Opt*, 2005. **10**(3): p. 031113.

40. Motz, J.T., et al., Optical fiber probe for biomedical Raman spectroscopy. *Appl Opt*, 2004. **43**(3): p. 542-54.

41. Shim, M. and B. Wilson, Development of an in vivo Raman spectroscopic system for diagnostic applications. *J Raman Spec*, 1997. **28**: p. 131-142.

42. Sharma, S., *Applied Multivariate Techniques*. 1996, New York: Wiley.

43. Duda, R.O., P.E. Hart, and D.G. Stork, *Pattern classification*, ed. Willey. 2001, New York.

44. Koo, T., *Measurement of blood analytes in turbid biological tissue using near-infrared Raman spectroscopy*, in *Mechanical Engineering*. 2001, MIT: Cambridge.

45. Scepanovic, O.R., et al., Determination of uncertainty in parameters extracted from single spectroscopic measurements. *J Biomed Opt*, 2007. **12**(6): p. 064012.

46. Zonios, G., et al., Diffuse Reflectance Spectroscopy of Human Adenomatous Colon Polyps In Vivo. *Appl. Opt.*, 1999. **38**: p. 6628-6637.

47. Bigio, I.J., et al., Diagnosis of breast cancer using elastic-scattering spectroscopy: preliminary clinical results. *J Biomed Opt*, 2000. **5**(2): p. 221-8.

48. Breslin, T.M., et al., Autofluorescence and diffuse reflectance properties of malignant and benign breast tissues. *Ann Surg Oncol*, 2004. **11**(1): p. 65-70.

49. Zhu, C., et al., Diagnosis of breast cancer using diffuse reflectance spectroscopy: Comparison of a Monte Carlo versus partial least squares analysis based feature extraction technique. *Lasers Surg Med*, 2006. **38**(7): p. 714-24.

50. Alfano, R.R., et al., Fluorescence spectra from cancerous and normal human breast and lung tissues. *IEEE Journal of Quantum Electronics*, 1987. **23**(1806-1811).

51. Palmer, G.M., et al., Comparison of multiexcitation fluorescence and diffuse reflectance spectroscopy for the diagnosis of breast cancer (March 2003). *IEEE Trans Biomed Eng*, 2003. **50**(11): p. 1233-42.

52. Gupta, P.K., S.K. Majumder, and A. Uppal, Breast cancer diagnosis using N2 laser excited autofluorescence spectroscopy. *Lasers Surg Med*, 1997. **21**(5): p. 417-22.

53. Majumder, S., et al., UV excited autofluorescence spectroscopy of human breast tissues for discriminating cancerous tissue from benign tumor and normal tissue. *Lasers Life Sci*, 1998. **00**: p. 1-16.

54. Georgakoudi, I., et al., NAD(P)H and collagen as in vivo quantitative fluorescent biomarkers of epithelial precancerous changes. *Cancer Res*, 2002. **62**(3): p. 682-7.

55. Mueller, M.G., et al., A reflectance spectrofluorimeter for real-time spectral diagnosis of disease. *Review of Scientific Instruments*, 2002. **73**: p. 3933-3937.

56. Tunnell, J.W., et al., Instrumentation for multi-modal spectroscopic diagnosis of epithelial dysplasia. *Technol Cancer Res Treat*, 2003. **2**(6): p. 505-14.

57. Wu, J., M.S. Feld, and R.P. Rava, Analytical Model for Extracting Intrinsic Fluorescence in Turbid Media. *Applied Optics*, 1993. **32**(19): p. 3585-3595.

CHAPTER 4

Clinical Raman studies: *ex vivo* and *in vivo*

In this chapter we describe the clinical application of Raman spectroscopy for the discrimination of breast lesions. We begin by presenting a description of an *in vitro* tissue study (study on tissue that was frozen-thawed for days-weeks) in which we develop a Raman diagnostic algorithm based on parameters extracted from the Raman spectra. Raman spectra were collected from freshly excised breast specimens from patients undergoing excisional biopsy: lumpectomy or mastectomy. After developing the diagnostic algorithm, we then test it prospectively. First, we applied the algorithm to assess a new set of tissue samples collected during an *ex vivo* study (study on a freshly excised tissue). Lastly, we used the algorithm to prospectively evaluate the status of margins in an *in vivo* study. For the *in vivo* study we implemented Raman spectroscopy in the operating room setting, which has never been performed in previous studies in the literature. The success of the study shows that if the Raman technology can be implemented in real-time to provide the surgeon the information about the disease status of the margins around a lesion; it could prevent patients from undergoing a second surgery.

4.1 Introduction

Our laboratory has studied Raman spectroscopy for a number of years. Raman spectroscopy is very sensitive to the presence of proteins, fats, etc, which are Raman active, in the medium. Thus Raman spectroscopy has been extensively studied for diagnosing breast lesions.

4.2 Development of Raman diagnostic algorithm

The development of the Raman diagnostic algorithm was based on data acquired from frozen-thawed *in vitro* specimens collected from 58 patients, who were undergoing surgical (excisional) breast biopsy, reduction mammoplasties and prophylactic mastectomies. Additional information can be found in [2, 3]. A total of 130 spectra were collected using the Raman system [4, 5] using an integration time that varied between 10 and 30 seconds based on the signal intensity. The average laser excitation power delivered to the tissue was between 100 and 150 mW. Sites of data acquisition were marked with India ink for future correlation with pathology. All specimens were then fixed in formalin and routinely processed. The histopathology examination was performed by an experienced pathologist blinded to the results of the spectroscopy. The histopathology results for the study samples were as follows: 49 normal tissues, 50 benign lesions (16 fibrocystic change (FCC) lesions and 31 fibroadenoma lesions) and 31 infiltrating ductal carcinoma (IDC) lesions.

Spectroscopic data was processed as described in the Chapter 3.3.2. Model fitting was performed using a linear combination of basis spectra of biochemical/tissue components present in the breast tissue with a nonnegativity constraint. The contribution of each basis spectrum, extracted from the modeled fit to the tissue spectrum was normalized so the sum of all fit coefficients would sum to one (Chapter 3). Fit coefficients are a function of both the concentration of the each basis spectrum and its Raman scattering cross section, which represents the strength of the signal at a unit concentration. The fit coefficients represent the amount that each model basis spectrum must be weighted to recreate the tissue spectrum, thereby providing insight into the chemical/morphologic makeup of the tissue. The Raman diagnostic algorithm is based on physically-meaningful fit

coefficients. Out of eight fit coefficients there were found two, fat and collagen, fit coefficients that had the most diagnostic capabilities.

A large fit coefficient for fat for normal breast tissue correctly suggests that normal breast tissue is primarily composed of fat (adipose tissue). Based on the anatomy of the breast it is known that breast tissue consists of both glandular and adipose tissue [7]. Glandular tissue consists of ducts and a supportive collagenous extracellular matrix, while ducts represent only a small volume of the tissue. The Raman model correctly characterizes normal breast tissue as a tissue that mostly consists of fat and a small contribution of collagen. Another important observation was that the amount of collagen increases in all abnormal tissues. This is also consistent with breast pathology, as the formation of lesions is associated with fibrosis– a scarring process characterized by increased accumulation of collagen in the stroma.. FCC lesions demonstrated the largest collagen composition. Lesions diagnosed as fibroadenoma were also marked by an increased contribution of collagen. This is consistent with the fact that these lesions are characterized by the proliferation of fibroblasts, the cells which produce collagen, and as a result, accumulation of collagen in the stroma [8]. IDC is associated with a fibroblast proliferation as a response to stromal invasion by the malignant epithelial cells. These lesions also showed an increased contribution of collagen. The fit coefficients for collagen varied for different histopathology diagnoses [3].

Logistic regression, a discriminate analysis technique, was used to correlate the normalized fit coefficients with the histopathology diagnoses for all of the eight components in the model. A likelihood ratio test was used to determine the importance of each of the
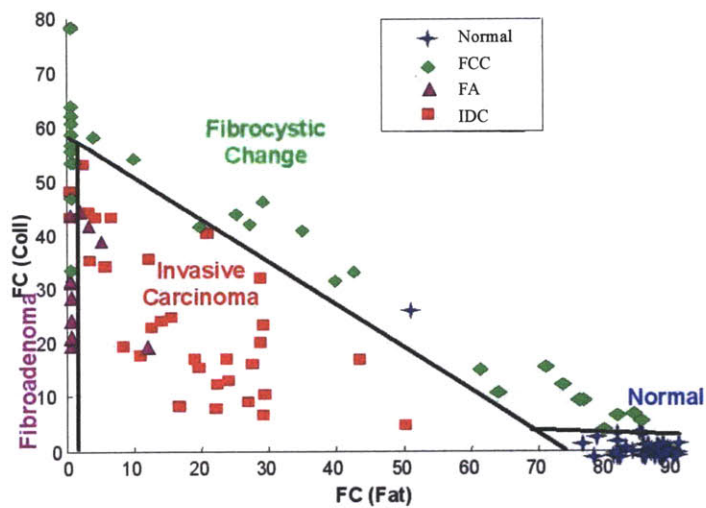
Figure 4.1. Raman diagnostic algorithm. This figure is modified from [3] and reprinted with the permission of the publisher.

model components to the correct classification of the lesions at each step in the algorithm. Leave-one-out cross-validation analysis was used to obtain the most robust diagnostic algorithm.

Note, the diagnostic algorithm is evaluated based on its performance on the testing data set. The best way, is to test robustness of the diagnostic algorithm is on an independent data set, which does not include the data points used for calibration and development of the algorithm. However, not always it is possible to acquire an independent data set for validation purposes, as large number of specimens and patients might be difficult to acquire. In the case of small number of samples, one can perform a cross-validation. Is allows an efficient use of a data set because only a small number of samples are reserved, and the spectra of the remaining samples are used for calibration. The leave-one-out method is one of the cross validation techniques, in which only one spectrum at a time is left out of the calibration. The diagnostic algorithm is calibrated using logistic regression excluding that one data point (spectrum). The excluded data point is used for validation and the prediction made on it, is compared to the diagnosis provided by a pathologist. The same procedure is repeated sequentially, excluding each spectrum from calibration set.

The fit coefficients for fat and collagen proved to be most diagnostically relevant for discrimination among the four pathology categories. Therefore, a diagnostic algorithm was developed based on the normalized fit coefficients of fat and collagen. A scatter plot of the fit coefficient (FC) of collagen versus FC of fat for the four histopathology categories, and the diagnostic decision lines that separate samples are shown in Figure 4.1. Using maximum likelihood estimation, we determined the probability that a breast sample is normal, FCC, fibroadenoma, or IDC. Receiver operating characteristic (ROC) curves were generated by changing the probability threshold for assigning a classification in order to separate malignant lesions (IDC) from non-malignant (normal, FCC and fibroadenoma) lesions. (Fig 4.2).

Note, a receiver operating characteristic (ROC) curve is a plot of the sensitivity vs. specificity for a binary classifier (two-class prediction) system as its discrimination threshold is varied. A decision boundary can be associated with any particular threshold probability from the logistic function (not necessarily a 50% probability). As the decision boundaries are moved depending on the probability threshold, so is a tradeoff

Figure 4.2. ROC curve demonstrates ability of Raman spectroscopy to diagnose breast lesions. This figure is taken from [3] and reprinted with the permission of the publisher.

between sensitivity and specificity. Thus, ROC curve represents the tradeoff between sensitivity and specificity. Often, the ROC is used to generate a summary statistic. The area under the ROC curve, or "AUC", is equal to the probability that a classifier will rank a randomly chosen positive instance higher than a randomly chosen negative one.

The performance of the algorithm was very promising, yielding a sensitivity, specificity, positive predictive value (PPV), negative predictive value (NPV) and overall accuracy of 94%, 96%, 88%, 98%, and 86% respectively. Sensitivity is defined as probability of correctly diagnosed malignant (IDC) specimens, while specificity is defined as probability of correctly diagnosed non-malignant specimens. The overall accuracy is the percentage of correctly classified samples for all pathological categories (see appendix for more explanations on the sensitivity, specificity, PPV, NPV, and overall accuracy).

Any newly developed algorithm needs to be tested prospectively on a new set of data, in order to make sure that the algorithm is robust and also to make sure that the data that was used for development of the algorithm is representative of the disease spread and disease prevalence. The next section of this chapter will describe the first study where the spectroscopic algorithm was applied in a prospective fashion.

4.3 Prospective application of Raman diagnostic algorithm

4.3.1 *Clinical data collection protocol*

In order to validate the Raman diagnostic algorithm, a new clinical *ex vivo* study [6] was designed and carried out in the Mather Surgical Pavilion at University Hospitals-Case Medical Center. The study was approved by the University Hospitals-Case Medical Center Institutional Review Board and the Massachusetts Institute of Technology Committee On the Use of Humans as Experimental Subjects. Informed consent was obtained from all subjects prior to their surgical procedures. Over the span of two months data was collected from 28 consecutive patients undergoing excisional breast biopsy (n=20), partial mastectomy (lumpectomy; n=7) or simple mastectomy (n=1).

Data were collected from freshly excised surgical specimens in the pathology suite adjacent to the operating rooms, typically within 30 minutes of tissue excision. Upon removal, the surgical specimens were inked and sectioned following standard pathology protocol, and Raman spectra were acquired from breast tissue sites (regions of interest) chosen by the pathologist. Depending on the region of interest identified by pathologist, the number of spectra taken per patient varied. The data were taken in the frozen section room (adjacent to the operating rooms), where several pathologists and residents work simultaneously, thus it was not possible to turn the lights off during data acquisition. In order to reduce the ambient light, all breast specimens were placed in a box that was impermeable to light during acquisition of the Raman data. Following spectral acquisition, the breast specimens were marked with multicolored colloidal inks to uniquely identify each site sampled and fixed in 10% neutral buffered formalin. The fixed tissue samples were routinely processed, paraffin embedded, sectioned in 5 μm thick sections, and stained with H&E. The histology slides were evaluated by an experienced breast pathologist who was blinded to the outcome of the Raman spectroscopy analysis.

4.3.2 Pathology

The pathology results were used as the gold standard against which the Raman spectral diagnoses were compared. Overall, a total of 220 Raman spectra from the 28 patients were collected. Of these, 129 Raman spectra from 21 patients were analyzed in the prospective analysis: 41 spectra from normal breast tissue, 82 from benign lesions (73 FCC lesions and 9 fibroadenomas), and 6 from malignant lesions (IDC). Ten spectra were excluded from the analysis due to contamination from ambient light (6 normal, 1 FCC, 3 IDC). As the purpose of this study was the prospective validation of the diagnostic algorithm, histopathological categories that were not present in the calibration data set were excluded from this study. Therefore, twenty spectra acquired from specimens diagnosed as ductal carcinoma *in situ* (DCIS) were also excluded. Sixty-one spectra acquired from two patients with breast cancer who had undergone pre-operative chemotherapy (16 normal, 9 FCC, 3 IDC) and five patients undergoing re-excision surgery to ensure negative margins (14 normal, 17 FCC, 2 IDC) were also excluded from the prospective analysis. Note the original algorithm was constructed on the excised specimens from patients who were not treated with chemotherapy and did not undergo a re-excisional biopsy. Thus, the data set for a prospective validation was constructed to simulate the same conditions, i.e. patients who underwent pre-operative chemotherapy or re-excisional surgery were excluded from the prospective validation of the algorithm.

4.3.3 Data acquisition and data analysis

Data were collected using the clinical Raman instrument and Raman optical fiber probe described in Chapter 3. On average, the excitation laser power was 100 mW. Before data collection, calibration spectra were acquired (Chapter 3).

In the next step of the procedure, the fit coefficients for the 8 components (calcium oxalate dehydrate, calcium hydroxyapatite, b-carotene, fat, collagen, cell nucleus, and cell cytoplasm) used to fit the Raman spectra were normalized to sum to unity. The contributions of calcium I and calcium II spectra were excluded from this normalization, as these species were not present in the tissue samples used for diagnostic algorithm development. Increased contributions from cholesterol-like lipid deposits was observed in this data set, possibly due to differences in the Raman scattering cross-

section of this component in frozen-thawed and fresh tissue. Thus, the cholesterol-like component was excluded from normalization.

4.3.4 Results

Each of the 129 Raman spectra from the 21 patients in the prospective data set was analyzed as described above to obtain the normalized fit coefficients of collagen and fat. The Raman diagnostic algorithm developed previously was then applied prospectively to obtain the Raman spectral diagnoses, and subsequently compared to the histopathology diagnoses. The results of the prospective classification of lesions using the diagnostic algorithm are shown in Fig 4.3. Prospective application of this algorithm to excisional biopsy specimens resulted in the correct diagnosis of 5 of 6 cancerous sites (IDCs) and 114 of 123 non-cancerous sites (normal breast tissues and benign lesions). Based on these results, a sensitivity of 83% and a specificity of 93% were obtained. The overall accuracy of correctly classifying each of the four tissue types individually was 78% (101/129). The positive predictive value (PPV) and negative predictive value (NPV) for this study were 36% and 99%, respectively. A comparison of the Raman spectral diagnoses and the histopathology is shown in Table 4.1.
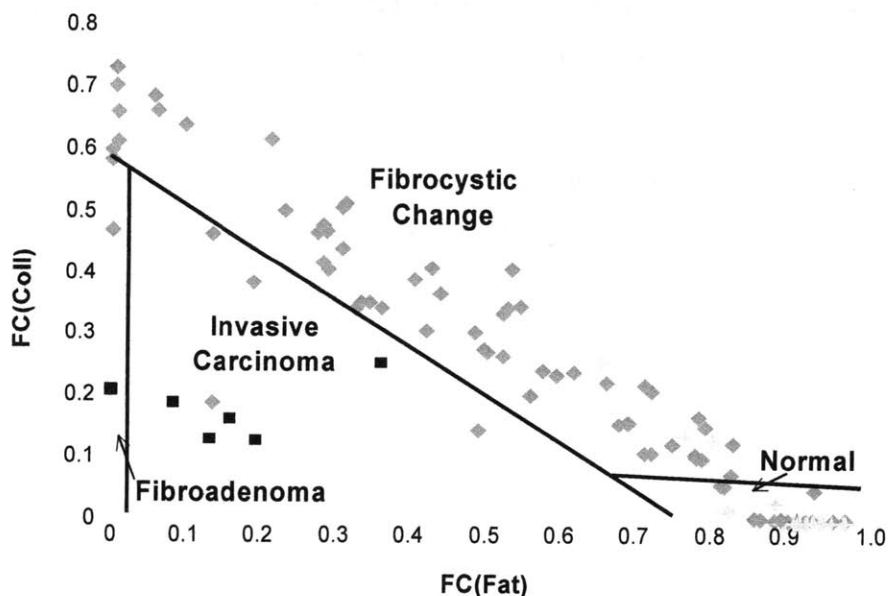
Figure 4.3. Prospective application of the Raman diagnostic algorithm. This figure is taken from [6] and reprinted with the permission of the publisher.

Raman \ Pathology	Normal (41 samples)	Fibrocystic Change (73 samples)	Fibroadenoma (9 samples)	Infiltrating Ductal Carcinoma (6 samples)
Normal	38	13	0	0
Fibrocystic Change	3	54	0	0
Fibroadenoma	0	2	4	1
Infiltrating Ductal Carcinoma	0	4	5	5

Table 4.1. Comparison of histopathology diagnoses and Raman spectroscopic classification of breast disease.

The Raman diagnostic algorithm proved to be successful on the new set of data. Four factors influenced the performance of the diagnostic algorithm in this prospective study as compared to the performance in the original study (*in vitro study*). First, the internally-validated original data is always expected to give more apparently efficacious results than those of a prospective study since the cross-validation employed to develop the algorithm in the original study was optimized only for the calibration data set. It should be noted that some research groups regard such internal-validation techniques to be prospective [9, 10]. However, their techniques are not equivalent to a prospective test, in which an algorithm developed based on one data set is applied to new data set. A prospective test is the best method for evaluating the efficacy of the diagnostic algorithm in clinical setting, as was performed in this study. Second, differences in the patient populations studied affect the findings[11]. As discussed below, potential sources of bias in the patient populations must be properly taken into account to interpret the efficacy of the diagnostic algorithm in the prospective study. Third, the use of freshly-excised surgical samples in the prospective study, as opposed to fresh-frozen samples in the original data set, which was used for calibration, may produce differences in the spectral properties of the tissue. Past studies have shown that the Raman spectral lineshape is equivalent in the two types of samples with regard to the eight components that comprise our diagnostic algorithm, since they are structural rather than metabolic in nature [12]. However, there were a few differences in the contribution of particular model components (cholesterol-like component) between the calibration and prospective studies. This may be due to changes in disease spectrum, as discussed below, or alternatively to changes in the Raman scattering cross-section as a result of freezing and thawing the tissue. Finally, factors related to the instrumentation, particularly SNR, may contribute to the differences in the findings [13].

CHAPTER 4: Clinical Raman studies: ex vivo and in vivo

4.3.5 Significance of prevalence

Unlike the sensitivity and specificity, the PPV and NPV depend heavily on the prevalence of the various lesions in the data set. Disease prevalence (or prior probability) refers to the proportion of individuals with an attribute or disease in a given population. PPV gives the probability of disease if a test result is positive, while NPV gives the probability of no disease if a test result is negative. PPV and NPV can be calculated as follows:

$$PPV = \frac{TP}{TP + FP} = \frac{p \cdot se}{\left(p \cdot se + (1-p)\right) \cdot (1-sp)} \qquad 4.1$$

$$NPV = \frac{TN}{TN + FN} = \frac{(1-p) \cdot sp}{(1-p) \cdot sp + p \cdot (1-se)} \qquad 4.2$$

where TP/N is true positive/negative and FP/N is false positive/negative. As the disease prevalence in a particular data set decreases, PPV decreases and NPV increases. Thus, the lower the disease prevalence the lower the probability that a positive result will be "correct", regardless of sensitivity and specificity. Therefore, the prevalence of lesions in each of the studies needs to be taken into account when comparing the predictive values. Also, according to Bayes' Theorem, the prospective value can be expressed in terms of prior probability, p (disease prevalence), sensitivity, and specificity see the second part of Eq. 4.1 and Eq. 4.2. [14].

Tissue samples were obtained by different methods in the calibration and prospective studies. Our initial calibration study was a case-control study, in which tissues were procured from 58 patients with grossly visible/palpable lesions and paired with normal control tissues whenever possible. Thus, the prevalence of cancer was artificially increased (31/126; 25%) in the calibration data set. In the current prospective study, 28 consecutive patients were examined. Only 6 of these patients had grossly visible/palpable lesions; the remainder had mammographically suspect/non-palpable lesions, the majority of which were non-cancers. This significantly reduced the prevalence of cancer (IDC) in the prospective study. It should be noted that the decreased

cancer prevalence (6/129; 5%) in the *ex vivo* prospective data set better represents the disease prevalence in the general patient population [15]. An excellent NPV (99%) was obtained in the prospective test for distinguishing cancerous from non-cancerous tissues. In the clinical setting, NPV is the most important parameter for making clinical decisions. In contrast, the NPV remained very high, the PPV was greatly reduced. The decreased disease prevalence in the *ex vivo* prospective data set adversely affected the PPV of the diagnostic algorithm, as discussed below.

The predictive values of our Raman diagnostic algorithm calculated for the calibration and prospective data sets were based on the disease prevalence in the two data sets, which differed. The cancer prevalence in the calibration study was 25%, while in the prospective study it fell to 5%. As a result, PPV decreased and NPV increased in the prospective study.

By evaluating these equations it was possible to compare effectiveness of the Raman diagnostic algorithm for both of the data sets as a function of the prevalence. As shown in Figure 4.4, with a drop in the prevalence of invasive cancer from 25% to 5%, the PPV is expected to decrease from 88% to 53% while the NPV is expected to increase from 98% to 99%. This indicates that the decrease in PPV seen in the prospective study (from 88% to 36%) is due, in large part, to the decrease in cancer prevalence in the patient cohort, rather than poor performance of the diagnostic algorithm.
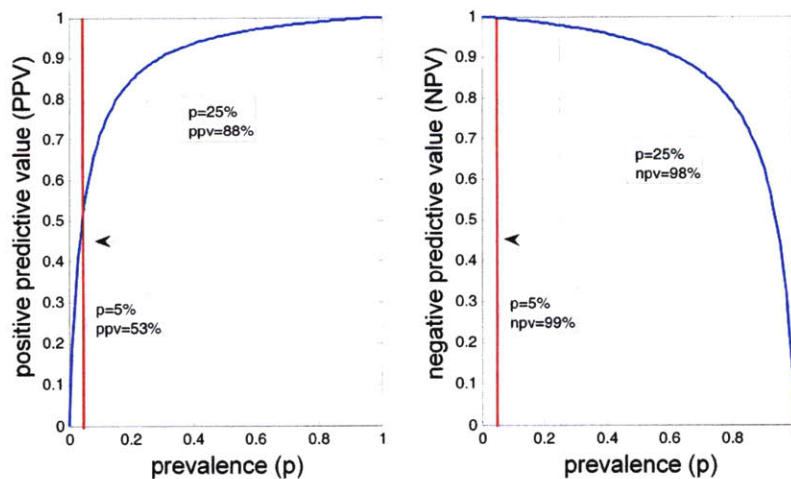
Figure 4.4. Predictive values as a function of prevalence of the disease

4.3.6 Significance of spectrum of the disease

The sensitivity and specificity of the algorithm, applied prospectively, were lower than for the original data set. The sensitivity, which is the probability of a positive test result among patients with the disease, depends only on the distribution of positives (lesions), while the specificity – the probability of the negative result among patients without the disease – depends only on the distribution of negatives. At the same time, both of these probabilistic variables are independent of the relative number of all positives and negatives in the given data set. For that reason, some investigators suggest that sensitivity and specificity are the best measures with which to compare diagnostic algorithm performance from study to study [13]. However, sensitivity and specificity are affected by the disease spectrum, the variability in severity of disease in the study population [16]. When the target group – cancer – is distinctly different from the control group – non-cancer, then the sensitivity and specificity will be high. When the difference between the two groups is less prominent, the sensitivity and specificity will decrease, (i.e. the spectrum of disease in the control group lessens the difference between non-disease group and diseased one) [16].

In the prospective data set, we observed that the FCC specimens demonstrated a broader diversity in their histological appearance compared to the original calibration data set. In the original study, the predominant feature observed for FCC lesions was stromal fibrosis, a pathology characterized by collagen accumulation. In the prospective study, three different manifestations of FCC were observed: stromal fibrosis, cyst formation, and adenosis (gland proliferation). In addition to the presence of ductal cysts and adenosis, there was a marked increase in the amount of fat relative to stromal fibrosis. This change in the disease spectrum of FCC between the two studies was reflected in the Raman spectra as well as the fit coefficients for fat and collagen. The mean fit coefficient of fat increased from 0.32 in the original study to 0.50 in the prospective study and the mean fit coefficient of collagen decreased from 0.38 in the original study to 0.29 in the prospective study. These differences likely contribute to the increased in the rate of misdiagnosis between FCC and IDC in the prospective data set, which in turn contributes to the observed decrease in both sensitivity and specificity in the prospective study.

4.3.7 Instrumental factors

Although we have minimized the effects of SNR through our spectral error analysis, we may not have completely nullified all SNR effects. Any remaining SNR effects would likely have the greatest effect on the diagnosis of fibroadenoma, as this diagnostic category occupies the smallest area in our diagnostic plane.

Although it is difficult to quantify the effects of changes in disease spectrum on algorithm performance due in part to the small size of the relevant subgroups of fibrocystic change, it is clear that the decrease in sensitivity and specificity in the prospective study results at least in part from changes in disease spectrum. The changes in disease spectrum also effect PPV and NPV, which depend not only on disease prevalence but additionally on sensitivity and specificity. Thus, the change in performance of the Raman diagnostic algorithm can be largely explained by differences in the two patient populations in the calibration and prospective studies with respect to disease spectrum and cancer prevalence.

4.3.8 Significance of the study

The current study has validated a Raman spectroscopic algorithm for the diagnosis of breast cancer that was developed *in vitro* on a large prospective *ex vivo* data set that closely mimics the target patient population in our *in vivo* clinical studies, described below.. It is the first prospective application of Raman spectroscopy in diagnosing normal, benign and malignant human breast tissue in freshly excised surgical specimens. The NPV of our diagnostic algorithm in this prospective study was excellent, indicating that the algorithm that was devised in laboratory calibration studies can be applied successfully in clinical studies. Changes in disease prevalence and disease spectrum in the prospective data set were found to significantly affect the PPV, sensitivity and specificity of the diagnostic algorithm.

4.4 *In vivo* study of margin assessment

The excellent results of the Raman spectroscopy in diagnosing breast cancer on excised tissue led to the first ever *in vivo* study to use Raman for the assessment of the status of margins during mastectomy and lumpectomy surgeries. The study was performed at the operating room of the Cleveland Clinic Foundation. The clinical protocol was approved by both the Massachusetts Institute of Technology Committee on the Use of Humans as Experimental Subjects and the Institutional Review Board of the Cleveland Clinic Foundation, in accordance with an assurance filed with and approved by the Department of Health and Human Services. Informed consent was obtained from all subjects before the surgical procedures [1].

4.4.1 Motivation

As described in Chapter 1, a surgeon removes not only the entire malignant tumor, but a small margin (1-2 mm) of normal breast tissue surrounding the lesion during mastectomy and lumpectomy. To verify that the surgeon has removed the entire malignant lesion, a pathologist performs an assessment of the tissue margins to confirm that no malignant cells are present within 1 to 2 mm of the border of the excised lesion. If the margin is found to be positive (malignant cells are identified) during the pathology review, then the patient has to undergo a second surgery (re-excisional surgery) in which additional tissue is excised. A technique that can perform accurate, real-time *in vivo* margin assessment would reduce the number of re-excisional procedures required to achieve negative margins. In addition, it may also extend partial mastectomy to those women who do not have a sufficiently small or localized breast cancer to qualify for partial mastectomy by current standards.

4.4.2 Study protocol

The *in vivo* study was conducted in the operating room during partial mastectomy surgery [1]. A total of 30 Raman spectra were collected from nine patients, 29 from margins subsequently found to be negative on pathology examination and 1 spectrum from a margin subsequently found to be positive on pathology examination. Of the 29 negative margins, 21 were composed of normal breast tissue and 8 were FCC. The one

positive margin was diagnosed as high-grade DCIS. Two spectra were excluded from the present analysis. The first, a benign papilloma, is a pathology not encountered in our previous studies and thus our diagnostic algorithm does not encompass this type of lesion. The second was a margin noted by the pathologist to demonstrate significant cautery artifacts a result of the surgical procedure. This was the only specimen where cautery artifacts of this degree were observed. We were able to accurately fit all 30 spectra with our previously developed spectral model of breast (Chapter 4.1) [17].

The experimental system was aligned and the probe was submitted for cold-gas ethylene oxide sterilization prior to data acquisition. Just before surgery, the proximal ends of the sterilized Raman probe were coupled to the experimental system. The distal end of the probe was kept sterile and placed in gentle contact with the margin tissue while spectra were acquired. All room and surgical lights were turned off during the measurements. Raman spectra were collected from several of these margins before excision and, thus, only tissue that would normally be excised during the procedure was removed. Each spectrum was collected for a total of 1 second. A range of powers (82 to 125 mW) were used depending on the throughput of the probe used. The standard practice of the surgeon in this study was to excise six samples from the margins of the surgical cavity following removal of the main tumor specimen. Following data acquisition, a volume of tissue corresponding roughly to that probed by the spectroscopic measurement was excised by the surgeon. The margin specimens were then fixed in formalin, routinely processed, and the histologic slides were examined by an experienced breast pathologist who was blinded to the outcome of the Raman spectroscopy analysis.
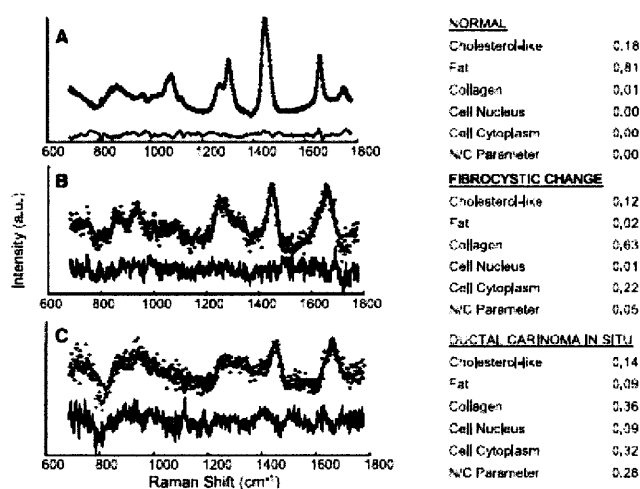
Figure 4.5. Model fits and fit coefficients to Raman spectra acquired from normal, fibrocystic change and DCIS lesions.

The data was analyzed in real-time as detailed in Chapter 4.2 and the spectral-based diagnosis was displayed within 1 sec [18].

4.4.3 Results

Model fits to *in vivo* Raman spectra acquired from normal, benign, and malignant breast tissue are shown in Fig 4.5. The difference between the measured spectrum and the model fit, the residual, is shown below each spectrum. The lack of significant structure in the residuals indicates that the model accounts for the majority of the spectroscopic features observed and describes the data well.

As in the previous study, the fit coefficients of normal breast tissue exhibit a large contribution from fat. There is more noise evident in spectra acquired from diseased tissue; however, they still yielded excellent model fits. Differences in the SNR in the spectra between normal breast tissue and malignant tissue may be explained by the presence of a large amount of cytoplasmic fat (which also has a large Raman scattering cross section compared to other model components) in a normal tissue. The margin site characterized as FCC showed an increase in the fit coefficient for collagen, due to fibrosis, and epithelial cell cytoplasm, as a consequence of adenosis. The positive margin diagnosed as high-grade DCIS, also displayed an increase in the amount of epithelial cell cytoplasm. In our studies, the spectroscopic variable characterizing the nucleus-to-cytoplasm ratio was obtained by dividing the fit coefficient of the cell nucleus basis spectrum by the fit coefficient of the epithelial cell cytoplasm basis spectrum. The nucleus-to-cytoplasm ratio was much larger for the cancerous specimen than for any of the FCC lesions encountered in this study, as shown in Fig. 4.5C, a histologic signature of cancer is enlargement of cell nuclei, and thus a higher nucleus-to-cytoplasm ratio than seen in benign conditions. In fact, the nucleus-to-cytoplasm ratio is a criterion routinely used by pathologists in the diagnosis of breast cancer [19, 20].

Fig 4.6.displays a scatter plot of the fit coefficients for collagen and fat, FC (Coll) and FC (Fat), respectively, for all data acquired in this study. The diagnostic algorithm developed earlier (Chapter 4.2) was applied in prospective manner. Table 4.2. provides a comparison between pathology diagnoses with those of the spectroscopic diagnoses for
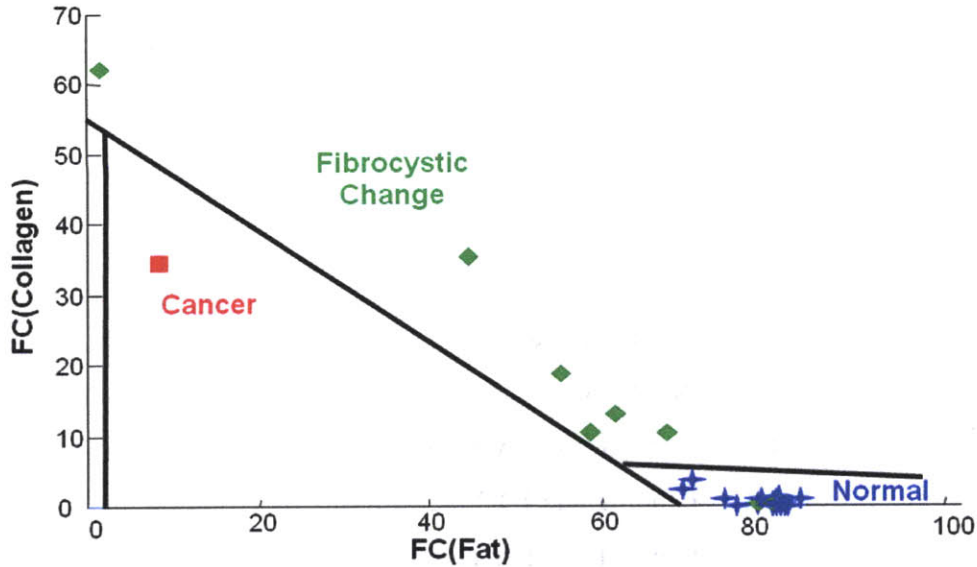
Figure 4.6. Performance of Raman diagnostic algorithm for the *in vivo* study. This figure is taken from [1] and reprinted with the permission of the publisher.

our data set. The algorithm demonstrated a sensitivity for detecting carcinoma of 100%, a specificity of 100%, and an overall accuracy of 93.3% (28 of 30). Note, although there is only one malignant sample in the present data set, this algorithm has been previously validated on 31 cancer specimens. The high-grade DCIS correctly identified by Raman spectroscopy was grossly invisible. Upon pathologic review, the finding that this margin was positive necessitated that the patient undergo a second surgery to excise the remaining cancerous tissue. Had Raman spectroscopy been used in a real-time fashion to guide excision during the initial surgery, the additional procedure could have been avoided.

Pathology / Raman	Normal (21 samples)	Fibrocystic change (8 samples)	Cancer (1 sample)
Normal	21	2	0
Fibrocystic change	0	6	0
Cancer	0	0	1

Table 4.2. Comparison between histopathology diagnoses and spectroscopic diagnoses of breast lesions obtained during *in vivo* clinical study.

4.4.4 Significance of the study

This pilot study was the first use of Raman spectroscopy to examine breast cancer *in vivo*. It clearly showed the feasibility of Raman spectroscopy as a clinical technique for

real-time margin assessment during partial mastectomy surgery. The data provided a good agreement with the previously developed spectral model and diagnostic algorithm.

4.5 Summary

The main goal of this work was to show that the Raman spectroscopy can be successfully used in the clinical setting for diagnosing breast lesions. Through the years of extensive research, Raman spectroscopy has moved from the laboratory setting into the clinic. A Raman diagnostic algorithm was developed in an *in vitro* study for classifying normal, FCC, fibroadenoma and IDC breast tissue based on fat and collagen composition. We then prospectively applied this algorithm to another set of *ex vivo* data. The sensitivity and specificity of the prospective study decreased slightly, reduced mostly due to differences in the prevalence of the disease between two studies as well as differences in the spread of disease spectrum. Most clinically important is that NPV of the prospective study, described in Section 4.3, was 98%, which means that a surgeon can be 98% confident that he/she is not leaving behind in the breast cancerous cells.

Real time application of the technology was proven in the first ever *in vivo* clinical study for the assessment of the status of margins. Once again the performance findings were in good agreement with the previously developed spectral model and diagnostic algorithm. Using Raman spectroscopy, a grossly invisible cancer was correctly identified via Raman spectroscopy and later diagnosed as DCIS by pathologist. Thus, it was shown that the additional procedure could have been avoided if Raman spectroscopy had been applied in the operating room to provide a real time feedback to surgeons.

Future Raman spectroscopy studies should be focused on the development of additional algorithms to add other pathology diagnoses, such as ductal carcinoma in situ (DCIS) and benign lesions other than FCC and fibroadenomas. Also, since the original algorithm was developed using *in vitro* specimens it did not contain any calcified lesions. Thus, a new diagnostic algorithm needs to be developed in order to classify these types of lesions.

4.8 References

1. Haka, A.S., et al., In vivo margin assessment during partial mastectomy breast surgery using raman spectroscopy. *Cancer Res*, 2006. **66**(6): p. 3317-22.

2. Haka, A., *Development of in Vivo Raman Spectroscopy for the Diagnosis of Breast Cancer and Intra-Operative Margin Assessment*, in *HST*. 2005, MIT: Cambridge. p. 314.

3. Haka, A.S., et al., Diagnosing breast cancer by using Raman spectroscopy. *Proc Natl Acad Sci U S A*, 2005. **102**(35): p. 12371-6.

4. Shafer-Peltier, K.E., et al., Model-based biological Raman spectral imaging. *J Cell Biochem Suppl*, 2002. **39**: p. 125-37.

5. Brennan, J., et al., Near Infrared Raman Spectrometer Systems For Human Tissue Studies. *Appl Spectrosc*, 1997. **51**: p. 201-208.

6. Haka, A.S., et al., Diagnosing breast cancer using Raman spectroscopy: prospective analysis. *J Biomed Opt*, 2009. **14**(5): p. 054023.

7. Rosen, P., *Breast Pathology*. 1997, Philadelphia, PA: Lippincott-Raven.

8. Cotran, R., V. Kumar, and T. Collins, *Robbins Pathologic Basis of Disease*. W. B. Saunders Company, ed. 6th. 1999, Philadelphia.

9. Ramanujam, N., et al., Development of a multivariate statistical algorithm to analyze human cervical tissue fluorescence spectra acquired in vivo. *Lasers Surg Med*, 1996. **19**(1): p. 46-62.

10. Ramanujam, N., et al., Spectroscopic diagnosis of cervical intraepithelial neoplasia (CIN) in vivo using laser-induced fluorescence spectra at multiple excitation wavelengths. *Lasers Surg Med*, 1996. **19**(1): p. 63-74.

11. Galen, R.S. and S.R. Gambino, eds. *Beyond Normality: The Predictive Value and Efficiency of Medical Diagnoses*. ed. W.a. Sons. 1975 New York.

12. Brennan, J.F., *Near Infrared Raman Spectroscopy for Human Artery Histochemistry and Histopathology*, in *EE*. 1995, MIT: Cambridge.

13. Utzinger, U., et al., Performance Estimation of Diagnostic Tests for Cervical Precancer based on Fluorescence Spectroscopy: Effects of Tissue Type, Sample Size, Population, and Signal-to-Noise Ratio. *IEEE Trans. Biomed. Engineer*, 1999. **46**: p. 1293-1303.

14. Harris, E.K. and A. Albert, eds. *Multivariate Interpretation of Clinical Laboratory Data*. ed. Decker. 1987: New York.

15. Jobsen, J.J., et al., Differences in outcome for positive margins in a large cohort of breast cancer patients treated with breast-conserving therapy. *Acta Oncol*, 2007. **46**(2): p. 172-80.

16. Mulherin, S.A. and W.C. Miller, Spectrum bias or spectrum effect? Subgroup variation in diagnostic test evaluation. *Ann Intern Med*, 2002. **137**(7): p. 598-602.

17.   Shafer-Peltier, K.E., et al., Raman microspectroscopic model of human breast tissue: implications for breast cancer diagnosis in vivo. *J Raman Spec*, 2002. **33**(7): p. 552-563.

18.   Motz, J.T., et al., Real-time Raman system for in vivo disease diagnosis. *J Biomed Opt*, 2005. **10**(3): p. 031113.

CHAPTER 5

Clinical DRS/IFS *ex vivo* study

Previous diffuse reflectance (DRS) and intrinsic fluorescence (IFS) spectroscopy studies by our laboratory have shown promising results for the detection of cervical dysplasia and oral cancer [1, 2]. The combination of DRS and IFS provides a more complete biochemical and morphological profile than any of these modalities individually. In this chapter we describe an *ex vivo* clinical study we performed to test the potential of a combined DRS/IFS approach for the detection of breast cancer. We used the clinical FastEEM instrument (Chapter 3) to collect data from the same freshly excised breast tissue sites evaluated in the previous chapter using the Raman clinical instrument. Using the physically meaningful parameters extracted from the data, we developed a DRS/IFS diagnostic algorithm. A multimodal spectroscopic algorithm, which included diagnostic parameters from DRS, IFS, and Raman spectroscopy, was also constructed to determine whether this would lead to further improvement in the overall diagnostic accuracy.

5.1 Introduction

The *ex vivo* clinical study was conducted at the University Hospitals-Case Medical Center (UHC) after being approved by the UHC Institutional Review Board and the MIT Committee on the Use of Humans as Experimental Subjects. Data were acquired using the FastEEM system over a period of 2 months from 17 consecutive patients undergoing surgical biopsies. Data were acquired from the same tissue sites and samples as were evaluated by the clinical Raman system in Chapter 4.

5.2 Data acquisition

Prior to data collection, calibration spectra were acquired as described in Chapter 3. Spectra were collected in the frozen section room of the hospital from freshly excised breast surgical specimens within 30 minutes of excisional biopsy (n=16) and partial mastectomy (lumpectomy; n=1) procedures. Most of the 30 minute delay was due to the gross examination, inking and sectioning of the specimen performed as part of the routine pathology intraoperative consultation. Each surgical specimen was interrogated at multiple sites of interest as indicated by the pathologist. In addition, spectra were also acquired from the colloidal inks used to mark the surgical margins of each specimen, after confirming that no artifacts were introduced in the data as a result of this processing step. Two sets of DRS and IFS spectra were taken at each site of interest to ensure that the spectra were free from artifacts. Overall, 202 sets of DRS and IFS spectra from 104 sites were obtained from 17 patients, providing approximately 2 spectra per site.

Spectra that were unreliable or of poor quality were excluded from the analysis according to a defined set of criteria. Specifically, DRS data in which the overall reflectance was less than 1 percent were excluded. The low signal prevents the reliable processing of the reflectance spectra, and thus extraction of information needed to obtain the intrinsic fluorescence. Spectra from 11 sites failed to meet these criteria as a result of contamination of the tissue surface by blood, which strongly absorbs the reflected light. Additionally, specimens from patients with pre-operative chemotherapy or who underwent re-excisional biopsy were excluded from analysis. Sites classified into histological categories other than normal, fibrocystic change

(FCC), fibroadenoma, and infiltrating ductal carcinoma (IDC) were also excluded because their limited numbers precluded development of a robust diagnostic algorithm. These included 2 sites diagnosed as ductal epithelial hyperplasia, 1 site diagnosed as fat necrosis and 6 sites diagnosed as ductal carcinoma *in situ* (DCIS) Following these exclusions, 202 IFS and DRS spectra acquired from a total of 104 breast tissue sites (1 and often 2 spectra per site) in specimens from 17 consecutive patients remained and were used for spectroscopic analysis.

5.3 Pathology

After acquisition of the spectra, the exact site of probe placement was marked with colloidal ink for correlation with histopathology. The breast specimens were then fixed in formalin and submitted for routine pathology evaluation, performed by an experienced breast pathologist blinded to the spectroscopy results. The histopathology diagnoses for the 104 breast tissue sites were as follows: 31 normal, 55 fibrocystic change, 9 fibroadenomas and 9 invasive carcinomas (all infiltrating ductal carcinoma) [5, 6]. The relative number of samples in each diagnostic category in this data set closely resembles the typical prevalence for diseases of breast tissue [7].

5.4 Development of a DRS/IFS diagnostic algorithm

We analyzed the DRS spectrum from each breast tissue site using a mathematical model based on the diffusion approximation of light propagation in tissue to determine the values of absorption coefficient, $\mu_a(\lambda)$ and reduced scattering coefficient, $\mu_s'(\lambda)$ (Chapter 3) [8]. In order to extract the absorption coefficient, μ_a, two major absorbers, oxyhemoglobin and β-carotene, were used to model the absorption of the tissue [9]. Because this study was performed *ex vivo*, the tissue was exposed to room air and hemoglobin was fully oxygenated; therefore, deoxyhemoglobin was not included. The wavelength-dependence of the reduced

scattering coefficient, $\mu_s'(\lambda)$, was modeled according to the following equation: $A\lambda^{-B}$ [10].

IFS spectra were extracted from the measured fluorescence spectra as previously described in the Chapter 3 [11]. In a turbid medium such as tissue, differences in the local chemical environment, may alter the shape of the measured fluorescence from that of the pure components [12]. In contrast, the IFS spectrum is composed of a linear combination of the spectra of the individual fluorophores present in the tissue. Therefore, pure component spectra were fit to the intrinsic fluorescence spectra. The fit coefficients for the individual fluorophores were extracted using multivariate curve resolution (MCR), a standard chemometric method [13].

5.4.1 *Multivariate curve resolution (MCR)*

MCR calculates basis spectra—MCR components— by minimizing the fitting error of a given spectrum using an initial set of guess spectra as the input. For the analysis, we extracted MCR basis spectra using spectra extracted from tissue measurements as an initial guess [12]. Despite the original spectra being noisy, good fits were obtained using MCR. Although, different initial guess basis spectra were used for the MCR analysis, we confirmed that the MCR components extracted using the various initial guess basis spectra overlapped. This suggests that minimization of the fitting error does not rely heavily on the initial guess spectra. This is very beneficial, as it is difficult to know the exact spectral shape of the various fluorophores present in tissue due to variations in the tissue microenvironment.
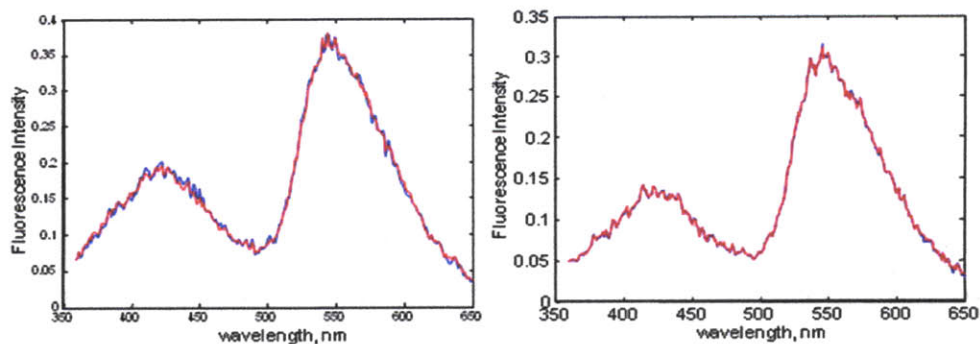
Figure 5.1. MCR from basis spectra for fitting mixture data: FAD, elastin: a) 1:2 concentrations; b) 1:3 concentrations, respectively. Data (blue), fit (red)

In order to investigate the physical meaning and the reliability of the parameters (e.g. fit coefficients) extracted from the intrinsic fluorescence, a chemical study was performed in the Spectroscopy Laboratory using the FastEEM instrument. Additional information can be found in [5]. The purpose of the study was to ensure that the fit coefficients extracted using MCR have a physical basis. To test this assumption, fluorescence spectra obtained from pure components (elastin and flavin adenine dinucleotide (FAD)) were used to fit experimental data obtained from mixtures of these pure components and linearity was confirmed using ordinary least squares (OLS) fitting. After verifying that the system response was linearly dependent on the concentration of the components, parameters obtained from MCR were used to fit the experimental data collected from mixtures of pure components and the resulting fit coefficients compared to expected values. Mixtures of FAD and elastin were created in concentration ratios of 1:2 and 1:3 as is shown in Fig 5.1. As expected, a linear combination of the spectra from the pure components fit the data well, confirming system linearity.

The fit coefficients for a 1:2 ratio of FAD:elastin were 0.356 and 0.644, respectively. The fit coefficients for a 1:3 ratio of FAD:elastin were 0.255 and 0.745, respectively. In this case the error was no more than 7 percent. From this analysis we concluded that in a simple system MCR provides reliable fit coefficients with a physical meaning from spectra obtained from mixtures.

5.4.2 Choosing diagnostically-relevant wavelength

Based on the results of this study, we analyzed the IFS spectra from the *ex vivo* tissue using two MCR components. The initial input spectra used for the MCR analysis were the pure component spectra of fluorophores known to be present in breast tissue, as described in Table 5.1 [12]. The maximum number of the initial input spectra was not constrained; however, after analyzing the data, we found that only two spectra were required to produce good fits to the data. The resulting MCR-generated spectral components at 340 nm are shown in Figures 5.2a and 5.2b. The combined basis spectra and fit to a representative IFS spectrum are shown in Figure

5.2c. The MCR-generated spectral components are similar to the spectra of pure NADH and collagen, respectively, but are broader and red-shifted, likely as a result of the local properties of the tissue microenvironment [14].
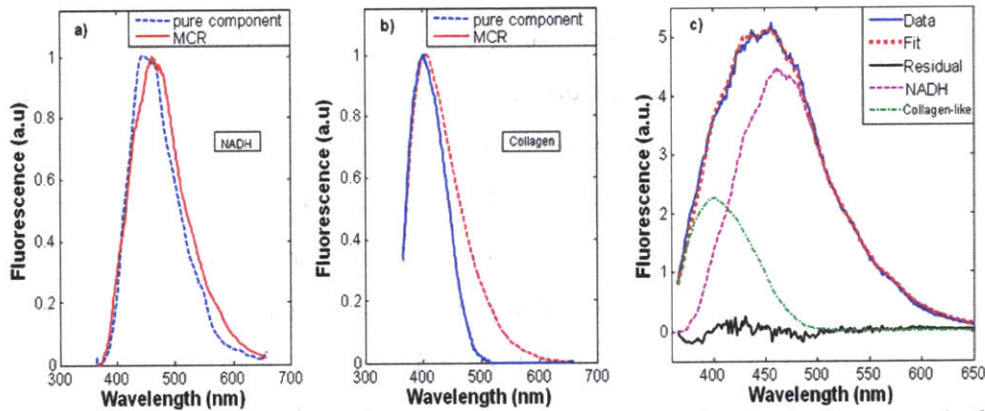
Figure 5.2. Comparison of pure component spectra(blue) and MCR basis spectra (red) excited at 340 nm for a) NADH, and b) collagen; c)representative spectrum fit with a linear combination of NADH (magenta) and collagen-like (green) basis spectra; data (blue), fit (red), residual (black).

As was described previously in Chapter 3, the FastEEM instrument provides emission spectra at 10 different excitation wavelengths. Collagen, NADH, elastin, tryptophan, FAD, and porphyrins, the native fluorophores of breast tissue, have their maximum emission at 308, 340, 360, and 425nm excitation wavelengths (Table 5.1) [14]. Thus, these four fluorescence excitation wavelengths were employed in the initial analysis.

	Excitation Wavelength			
	308nm	340nm	360nm	425nm
Fluorophores	NADH	NADH	NADH	Collagen
	Collagen	Collagen	Collagen	Elastin
	Tryptophan	Elastin	FAD	FAD
			Porphyrins	

Table 5.1. Expected fluorophores for different excitation wavelengths.

However, it was found that not all of these fluorophores could be detected, presumably because they were not present in our specimens at high enough quantities. Undetected fluorophores included elastin (340 nm excitation) and FAD and porphyrins (both excited at 360 nm). The absence of these fluorophores was

confirmed by attempting to extract additional basis spectra using MCR and finding that the contributions were negligible.

Of the measured fluorophores, only NADH and the collagen-like component excited at 340 and 360 nm were required to obtain good fits to the IFS spectra. The contributions of these two fluorophores at 340 and 360 nm, respectively, were very similar, which is not surprising given the closeness of these two excitation wavelengths. These excitation wavelengths associate with different penetration depth of the light. However, this difference was estimated to be less than $5\mu m$ and was not sufficient enough to provide different parameters that could be diagnostically
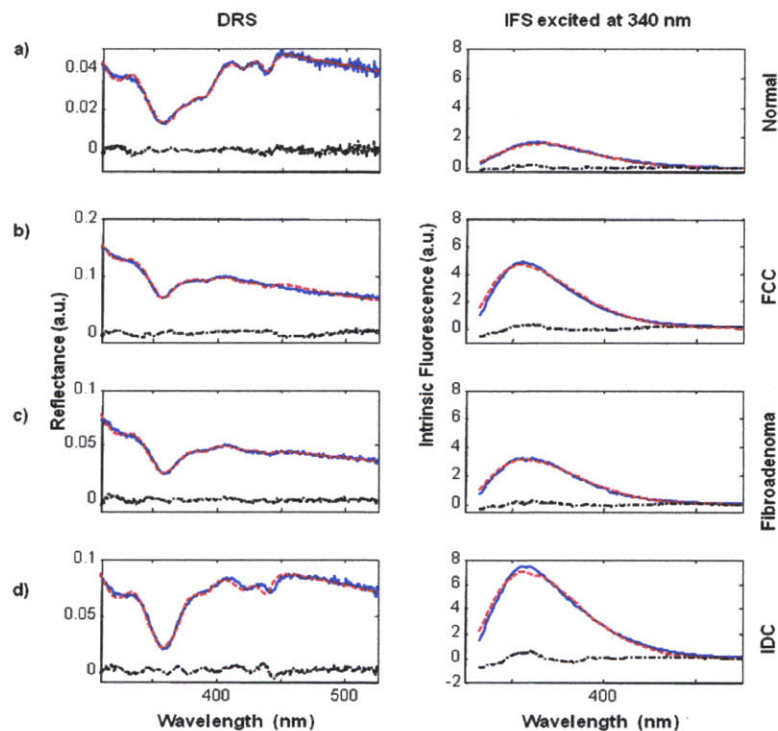
Figure 5.3. Representative DRS and IFS spectra excited at 340 nm for a) normal tissue, b) a lesion with fibrocystic changes, c) a fibroadenoma and d) infiltrating ductal carcinoma. Data (blue), fit (red), residual (black). This figure is taken from [3] and reprinted with the permission of the publisher.

significant. Averaging the information at these two wavelengths did not improve the fits. Therefore, we opted to evaluate the contributions of NADH and the collagen-like component excited at 340 nm for each tissue site, as this is the excitation wavelength at which NADH emission is maximal. By analyzing a single wavelength we reduced the complexity of the subsequent analyses. The additional benefit of this approach is

that only a single UV source is required for future clinical instruments. Thus, the next generation of the DRS/IFS instrument can be more compact, which is a significant advantage in the clinical setting. Representative DRS and IFS spectra collected at 340 nm excitation are shown in Fig 5.3.

A total of six spectroscopy parameters were extracted from the spectra and used to characterize the tissue—four DRS parameters (A, B, oxy-hemoglobin and,β-carotene) and two IFS parameters (a collagen-like component and NADH).

5.4.3   Step-wise algorithm

All of the fit parameters except B were found to be diagnostically significant. Boxplots of the diagnostic parameters as a function of lesion type are shown in Fig 5.4. (A boxplot is a graphical representation of the spread in a set of data, in which the second and third quartiles are bounded by the box and the median for the data set is indicated by the red center line. The inter-quartile range is defined as the distance between the first and third quartiles. The extreme values are defined as 1.5 times the inter-quartile range, measured from the median. Data points outside of this range are defined as outliers and indicated by crosses. Depicting data using boxplots is useful for visually examining the diagnostic capability of each parameter. For example, the boxplot for the collagen-like component indicates that normal breast sites may be
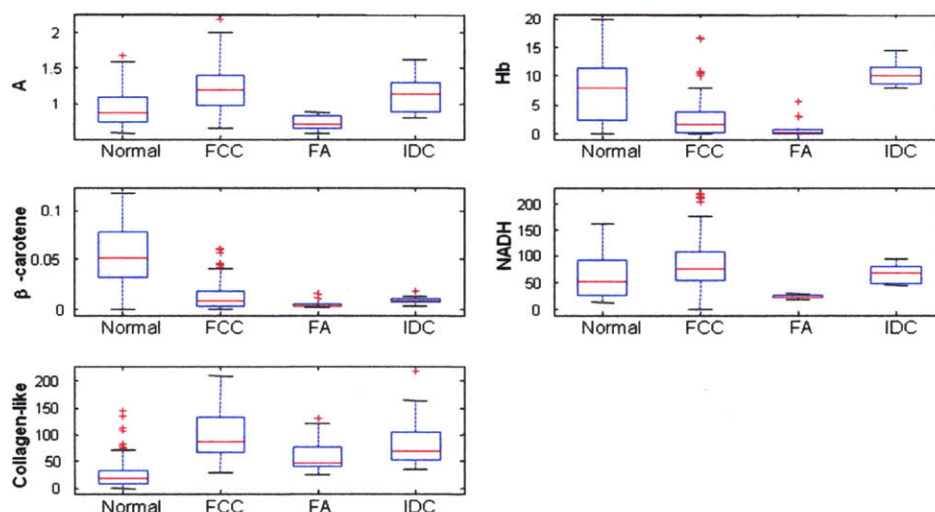
Figure 5.4. Boxplots of normal (Normal), fibrocystic change (FCC), fibroadenoma (FA), and infiltrating ductal carcinoma (IDC) for diagnostically relevant parameters. This figure is modified from [3] and reprinted with the permission of the publisher.

distinguished from other lesions using this parameter because they demonstrate lower contributions of this component. It is important to note that diagnostic parameters in a particular tissue type may be correlated. Hence, one parameter may provide only partial separation, but combining it with additional parameters may lead to an even greater separation. The benefit of combining multiple parameters cannot be visualized using boxplots.

In order to be clinically relevant, a spectroscopic diagnostic algorithm must be able to classify tissue sites according to the following 4 histopathology diagnoses: invasive breast cancer (in our case infiltrating ductal carcinoma (IDC)), benign breast lesions (fibroadenoma and fibrocystic change (FCC)), and normal breast tissue. In addition, it is important to distinguish different types of benign lesions from normal tissue.

Because tissue from different pathology categories are likely to be characterized by different diagnostic parameters, we performed the analysis in a step-wise fashion, as illustrated in Fig 5.5. In the first step, normal specimens are separated from the rest of the specimens. Following this step, fibroadenomas are
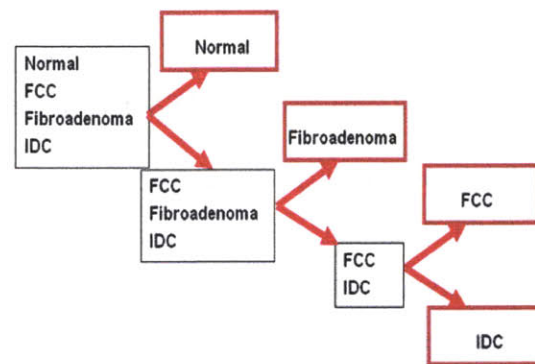
Figure 5.5. Step-wise diagnostic algorithm. This figure is taken from [3] and reprinted with the permission of the publisher.

separated from FCC and IDC, and in the third and final step, IDC is separated from FCC. The diagnostic algorithm was developed using logistic regression and leave-one-out cross validation. Histopathology diagnoses were used as the "gold" standard against which the spectroscopic diagnoses were compared. Identification of the most diagnostically important parameters was performed by optimizing the sensitivity at each step in the algorithm. The diagnostic step-wise algorithm is presented in Fig 5.6. In step 1, normal sites are classified using the collagen-like component and β-carotene fit coefficients extracted from IFS and DRS, respectively (Fig 5.6a). In step 2, fibroadenoma sites are discriminated from FCC and IDC using the DRS scattering

parameter A and the NADH fit coefficient extracted from IFS (Figure 5.6b). Finally, in the third step, IDC sites are distinguished from FCC primarily based on oxyhemoglobin, and to a lesser extent, the collagen-like component (Figure 5.6c).

5.4.4   Results

Table 5.2 compares the DRS/IFS spectral diagnoses and the histopathology diagnoses. The diagnostic algorithm was successful in distinguishing normal, FCC, fibroadenoma and IDC using physically-meaningful parameters extracted from combination of DRS and IFS. All of the invasive carcinomas are correctly classified

Pathology / DRS/IFS	Normal (31 samples)	Fibrocystic Change (55 samples)	Fibroadenoma (9 samples)	Infiltrating Ductal Carcinoma (9 samples)
Normal	26	3	0	0
Fibrocystic Change	2	51	0	0
Fibroadenoma	0	0	9	0
Infiltrating Ductal Carcinoma	3	1	0	9

Table 5.2. Comparison of DRS/IFS classifications and histopathology diagnoses

and only 3 normal specimens and 1 fibrocystic change lesion were misclassified (both as IDC). The total efficiency (overall accuracy) is 91% (95/104). The sensitivity and specificity are 100% and 96%, respectively, with sensitivity defined as the fraction of cancers correctly identified by the algorithm, and specificity defined as the fraction of non-cancerous lesions correctly identified. The positive and negative predictive values are 69% and 100%, respectively. PPV is the probability that a positive result is accurate (i.e. that the patient actually has the specified disease). NPV is the probability that a negative result is accurate [15]. NPV is the most important value for our clinical work because it is more tolerable to excise normal or benign lesions (as might occur when a technique has a low PPV) than to miss treating a cancerous lesion (owing to a low NPV). Therefore, it is important that our technique have a high NPV in order to be effective in clinical practice. As described in Chapter 4, predictive values depend on the prevalence of disease. The prevalence for the lesions in our data set is similar to the known prevalence encountered for clinical practice and therefore the predictive values achieved by our technique are representative of what would be observed if applied to the general population.

In contrast to studies reported by other groups [16-18], we find that the DRS parameters contribute the most to the distinction of benign from malignant lesions. For example, using only the DRS parameters (A and the relative contributions of β-carotene and oxyhemoglobin), we obtain a sensitivity, specificity, PPV, NPV, and total efficiency of 100, 100, 100, 100, and 81 percent (85/104), respectively. All malignant sites were correctly diagnosed, however some benign sites were misclassified. A total of 6 normal and 1 fibroadenoma were misclassified as FCC, 8 FCC lesions were misclassified as normal and 4 FCC lesions were misclassified as fibroadenomas. None of these are clinically significant misclassifications.

An accurate classification scheme could not be generated from IFS parameters alone (relative contributions of NADH and the collagen-like component). Results for the sensitivity, specificity, PPV, NPV and total efficiency were 89, 66, 20, 98, and 80 percent, respectively. It is important to note that although the inclusion of IFS parameters into the combined algorithm does not improve the distinction of benign from malignant lesions, IFS significantly improves the total efficiency (increase of 12 percent from the DRS algorithm alone). The total efficiency is the only metric that considers the accuracy of the technique in subclassifying the benign lesions, specifically normal, FCC and fibroadenoma.
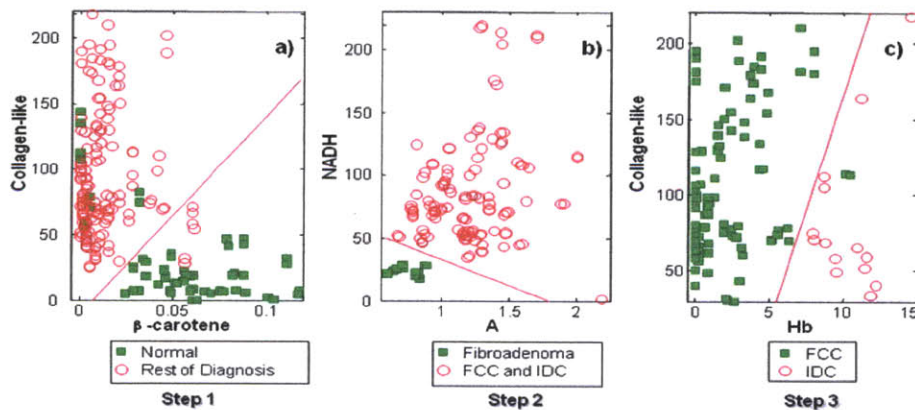
Figure 5.6. Step-wise DRS/IFS diagnostic algorithm. a) Step 1 – identification of normal tissue from rest of diagnoses; b) Step 2 – identification of fibroadenoma; c) Step 3 – identification of FCC and IDC. This figure is taken from [4] and reprinted with the permission of the publisher.

5.4.5 Correlation with pathology

The DRS/IFS analysis accounts for physical changes in tissue composition that contribute to changes in histopathology. Normal breast tissue consists mostly of adipose tissue (fat). In contrast most breast lesions are characterized by an increase in fibrous stroma, and thus an increase in the amount of collagen [7]. Therefore, in the first stage of our diagnostic algorithm, we would expect normal tissue to be distinguished from the three other types of breast lesions by the relative contributions of the collagen-like component and β-carotene, a lipid-soluble marker of adipose tissue. In the second stage of the algorithm, fibroadenomas are separated from FCC and IDC based on NADH and A. By histopathology, FCC and IDC are both cellular proliferative lesions, accounting for their relatively large contributions of NADH, a product of cellular metabolism. The A parameter is representative of the density of scatterers in the tissue [8]. We expect IDC to have a relatively high value of the A parameter as a result of fragmentation and disorganization of the collagen fibers in the stroma of invasive cancers due to the action of matrix metalloproteinases [19]. Finally, in the third stage of the algorithm, IDC is separated from FCC on the basis of collagen-like component and oxyhemoglobin fit coefficients. As with most malignant tumors, IDC is characterized by angiogenesis (increased vasculature) [7], therefore it is not surprising that oxyhemoglobin is useful for separating IDC from FCC. Interestingly, oxyhemoglobin is also a diagnostic parameter in diffuse optical tomography imaging of breast cancer. It is not as clear why the collagen-like component is useful in distinguishing IDC from FCC, as both demonstrate stromal fibrosis. However, since there are differences in the types of collagen present in the stroma of these two lesions [20], it is possible that the MCR collagen-like component basis spectrum better reflects the type of collagen present in FCC. The number of DCIS specimens was too small to develop a diagnostic algorithm. A larger clinical study is needed to identify DCIS using our technique, as will be discussed in the subsequent chapter.

5.4.6 Significance of the study

The DRS/IFS spectroscopy study showed promising results in discriminating breast lesions. This study is the first to show the benefit of combining diffuse reflectance and fluorescence modalities. The step-wise diagnostic algorithm is based on physically-meaningful parameters extracted from tissue spectra using a mathematical model based on the diffusion approximation and multivariate curve resolution. A diagnostic algorithm was developed based on A, β-carotene, oxyhemoglobin, NADH and the collagen-like component using logistic regression and a leave-one-out cross validation scheme. The diagnostic algorithm resulted in 100% sensitivity, 96% specificity, 69% positive predictive value, 100% negative predictive value and 91% total efficiency. As our diagnostic algorithm was constructed using an *ex vivo* data set and the prevalence of lesions in our study closely reflect those observed in the general population, we expect the performance of the algorithm to remain high in a larger study. As an important next step, our diagnostic algorithm should be prospectively tested in an independent clinical study with a larger number of patients. In Chapter 7 we present the results of a prospective clinical trial we performed based on the successful findings of this *ex vivo* study.

5.5 Development of MMS diagnostic algorithm

So far we have presented the results of two individual studies to develop diagnostic algorithms for breast cancer: Raman Spectroscopy (Chapter 4) and the combination of DRS and IFS spectroscopy (Chapter 5.4). In these studies, the same tissue sites were interrogated with DRS, IFS and Raman [21] spectroscopy. Therefore, we investigated the possibility of further improving our diagnostic capabilities by combining the respective information into one diagnostic algorithm. Specifically, we would use diagnostic parameters from all three modalities to construct a multimodal spectroscopic (MMS) diagnostic algorithm. In developing the MMS algorithm, only parameters that were diagnostic in each of the individual modalities were used: A, oxyhemoglobin, and β-carotene from DRS, NADH and collagen from IFS, and the fit coefficients for fat and collagen from Raman spectroscopy. Both IFS and Raman are sensitive to collagen. However, because each

uses a different wavelength of light (830 nm for Raman and 340 nm for IFS), the sampling depths are different. This fact explains why collagen fit coefficients extracted via Raman spectroscopy do not strongly correlate with collagen fit coefficients extracted using IFS.

5.5.1 Result and Significance of the study

In order to distinguish among each of the histopathology categories, leave-one-out cross validation and logistic regression were performed after classifying the tissue sites with the MMS diagnostic algorithm. As in the case of DRS/IFS diagnostic algorithm, the MMS diagnostic algorithm was constructed in a sequential fashion. Fig 5.7 illustrates the MMS step-wise diagnostic algorithm. In the DRS/IFS diagnostic
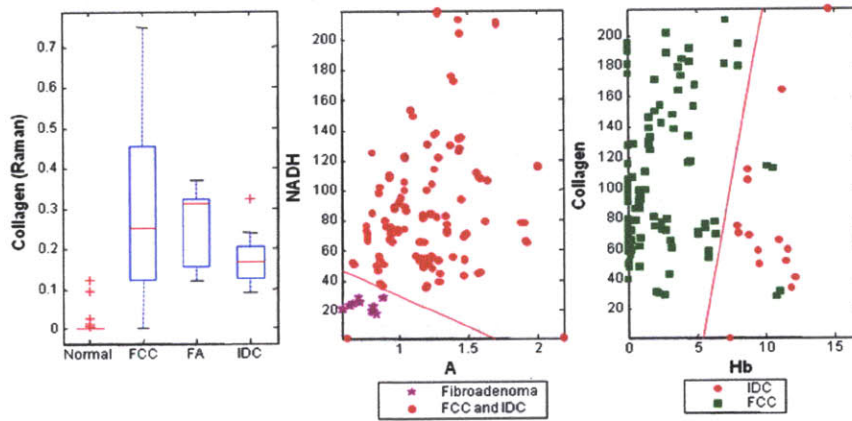
Figure 5.7. MMS step-wise algorithm

Pathology / MMS	Normal	Fibrocystic Change	Fibroadenoma	Invasive Carcinoma
	(32 samples)	(55 samples)	(9 samples)	(9 samples)
Normal	30	4	0	0
Fibrocystic Change	2	49	0	0
Fibroadenoma	0	0	9	0
Invasive Carcinoma	0	2	0	9

Table 5.3. Comparison of MMS discrimination and histopathology classification

algorithm developed in the previous section, 2 normal tissue sites were misdiagnosed as FCC and 3 normal tissue sites were misdiagnosed as IDC. By introducing the fit coefficient of collagen obtained from the analysis of the Raman spectra to the first step of the analysis (distinction of normal sites from lesions) we achieve a better separation. Rather than 5 misclassifications, only two normal tissue sites were misclassified (both as FCC, a benign condition). The results for the two subsequent diagnosis steps were identical to those obtained in DRS/IFS diagnostic algorithm. In the second step, all 9 fibroadenoma lesions were correctly diagnosed, while in the third step both DRS/IFS and Raman misclassified the same two samples. The fact that both modalities misclassified the same limited number of samples suggests a possible registration error. Table 5.3 provides an overview of the MMS algorithm performance. The MMS algorithm improved the number of sites correctly diagnosed as normal and FCC over that from algorithms based on either DRS/IFS or Raman. Additionally, fewer histopathology categories were misclassified as cancerous, which is a major benefit in that it increases the sensitivity and overall accuracy of this technique. The MMS algorithm resulted in sensitivity, specificity and overall accuracy of 100%, 98%, 92%, respectively.

5.6   Summary

In the clinical *ex vivo* study presented in this Chapter, we first described the development of a diagnostic algorithm based on physically-meaningful parameters extracted from DRS and IFS. The DRS/IFS diagnostic algorithm was developed using logistic regression and leave-one-out cross-validation. Using these two modalities to classify the data we obtained a sensitivity, specificity and overall accuracy of 100%, 96% and 91% respectively. For comparison, we then constructed a MMS diagnostic algorithm that combined spectroscopic data obtained from DRS, IFS and Raman spectroscopy. All data were collected on the exact same tissue specimens. The MMS algorithm showed a slight improvement over individual modalities and the DRS/IFS algorithm, resulting in a sensitivity, specificity, and overall accuracy of 100%, 98%, and 92%, respectively.

This study showed the potential to improve the accuracy of spectroscopic diagnostic algorithms by combining DRS, IFS and Raman spectroscopy as compared to when any one technique is used. For this study it is important to note that two different instruments and two different probes were used, thus there is some uncertainty in whether the exact same tissue site was evaluated by each probe. Therefore, to rigorously test the robustness of the MMS diagnostic algorithm a multimodal spectroscopy instrument needs be constructed which can be tested in the clinic. The development of such an instrument is described in Chapter 6.

5.7 References

1. Georgakoudi, I., et al., NAD(P)H and collagen as in vivo quantitative fluorescent biomarkers of epithelial precancerous changes. *Cancer Res*, 2002. **62**(3): p. 682-7.

2. Georgakoudi, I., et al., Fluorescence, reflectance, and light-scattering spectroscopy for evaluating dysplasia in patients with Barrett's esophagus. *Gastroenterology*, 2001. **120**(7): p. 1620-9.

3. Volynskaya, Z., et al., Diagnosing breast cancer using diffuse reflectance spectroscopy and intrinsic fluorescence spectroscopy. *J Biomed Opt*, 2008. **13**(2): p. 024012.

4. Haka, A.S., et al., Diagnosing breast cancer by using Raman spectroscopy. *Proc Natl Acad Sci U S A*, 2005. **102**(35): p. 12371-6.

5. Volynskaya, Z., *Multi-modal spectroscopy of breast tissue*, in *Electrical Engineering and Computer Science*. 2005, MIT: Cambridge. p. 67.

6. Volynskaya, Z., et al., Diagnosis of Breast Cancer Using Diffuse Reflectance Spectroscopy and Intrinsic Fluorescence Spectroscopy. *J Biomed Opt*, 2008. **13**(2): p. 024012.

7. Cotran, R., V. Kumar, and T. Collins, *Robbins Pathologic Basis of Disease*. W. B. Saunders Company, ed. 6th. 1999, Philadelphia.

8. Zonios, G., et al., Diffuse Reflectance Spectroscopy of Human Adenomatous Colon Polyps In Vivo. *Appl. Opt.*, 1999. **38**: p. 6628-6637.

9. Yang, Y., et al., DNA and protein changes caused by disease in human breast tissues probed by the Kubelka-Munk spectral functional. *Photochem Photobiol*, 2002. **75**(6): p. 627-32.

10. van Staveren, H.J., et al., Light scattering in intralipid-10% in the wavelength range of 400-1100 nm. *Appl Opt*, 1991. **30**(31): p. 4507-4514.

11. Mueller, M., et al., Intrinsic fluorescence spectroscopy in turbid media: disentangling effects of scattering and absorption. *Appl Opt*, 2001. **40**(25): p. 4633-4646.

12. Shafer-Peltier, K., *Chemical Basis for Breast Cancer Diagnosis Using Raman Spectroscopy*, in *Chemistry*. 2001, MIT: Cambridge. p. 145.

13. Navea, S., A. de Juan, and R. Tauler, Detection and resolution of intermediate species in protein folding processes using fluorescence and circular dichroism spectroscopies and multivariate curve resolution. *Analytical Chemistry*, 2002. **74**(23): p. 6031-6039.

14. Richards-Kortum, R. and E. Sevick-Muraca, Quantitative optical spectroscopy for tissue diagnosis. *Annu Rev Phys Chem*, 1996. **47**: p. 555-606.

15. Fitzmaurice, M., Principles and pitfalls of diagnostic test development: implications for spectroscopic tissue diagnosis. *J Biomed Opt*, 2000. **5**(2): p. 119-30.

16. Gupta, P.K., S.K. Majumder, and A. Uppal, Breast cancer diagnosis using N2 laser excited autofluorescence spectroscopy. *Lasers Surg Med*, 1997. **21**(5): p. 417-22.

17. Palmer, G.M., et al., Comparison of multiexcitation fluorescence and diffuse reflectance spectroscopy for the diagnosis of breast cancer (March 2003). *IEEE Trans Biomed Eng*, 2003. **50**(11): p. 1233-42.

18. Breslin, T.M., et al., Autofluorescence and diffuse reflectance properties of malignant and benign breast tissues. *Ann Surg Oncol*, 2004. **11**(1): p. 65-70.

19. Kauppila, S., et al., Aberrant type I and type III collagen gene expression in human breast cancer in vivo. *J Pathol*, 1998. **186**(3): p. 262-8.

20. Barsky, S.H., et al., Increased content of Type V Collagen in desmoplasia of human breast carcinoma. *Am J Pathol*, 1982. **108**(3): p. 276-83.

21. Haka, A.S., et al., Diagnosing breast cancer using Raman spectroscopy: prospective analysis. *J Biomed Opt*, 2009. **14**(5): p. 054023.

CHAPTER 6

Multimodal system: instrument and probe

This chapter describes the multimodal spectroscopy (MMS) instrument, which combines Raman, diffuse reflectance and fluorescence modalities. The (MMS) instrument is based on our previously described Raman and DRS/IFS instruments; several key parts of the instrumentation, including hardware and software, are presented in Chapter 3. One of the most challenging parts of the MMS system development was the design and construction of the new MMS front-viewing probe. This probe is capable of delivering and collecting both visible and near infrared light. Differences in fitting data obtained with the MMS and FastEEM probes are due to difference in probe geometry and are explained further. Additional information on the MMS instrument can be found in [1, 2].

6.1 Motivation

In previous chapters (Chapters 4 and 6) it was shown that breast lesions were successfully studied using two different instruments. Each of these instruments has its own probe and software. The clinical Raman instrument [3] and probe [4] have been developed for real-time clinical study of disease status of tissue, such as breast lesions and atherosclerosis. The FastEEM instrument [5] has been used to extract DRS and IFS spectra excited at several wavelengths within the range of 308 nm to 500 nm; and it was used to study breast lesions, atherosclerosis, cervical dysplasia and oral cavity. In the case of breast tissue, each of these techniques, Raman and the combination of DRS and IFS, were able to correctly distinguish among four different pathology diagnoses: normal tissue, two benign lesions – fibrocystic change (FCC) and fibroadenoma, and a malignant lesion – infiltrating ductal carcinoma (IDC). However, in order to apply spectroscopic techniques in a clinical setting to assess status of margins during surgical excisions such as mastectomy and lumpectomy, the spectroscopic technique would have to be able to diagnose ductal carcinoma *in situ* (DCIS) as well. If the margin status is positive according to histopathology diagnosis, most often it is due to the presence of DCIS. In our studies, Raman and DRS/IFS individually are unable to distinguish DCIS from the other pathologies. Thus, the combination of all three modalities – multimodal spectroscopy – has been explored.

6.1.1 Complementarity

Each of the spectroscopic modalities provides complementary information about the biochemical state of biological tissue. As discussed in Chapter 3, diffuse reflectance spectroscopy provides information about absorbers and scatterers such as β-hemoglobin, oxy and deoxy-hemoglobin; fluorescence spectroscopy provides information about autofluorophores such as collagen and NADH; and Raman spectroscopy provides information about Raman active molecules found in the tissue such as fat, collagen, calcium, and others.

6.1.2 Elimination of the probe placement error

Development of a combined instrument should be done in parallel with development of an efficient unitary probe that is able to simultaneously collect spectra from all three modalities. Previously, when data was collected with two different instruments, and thus two different probes, error between sampling sites of each probe could have been introduced. Although great care was taken to place the FastEEM probe in the same location as the Raman probe, the absolute precision and accuracy of probe placement could not be guaranteed. The design and development of the multimodal (MMS) probe will eliminate this sampling error.

6.1.3 Compact clinical system

Simultaneous usage of two clinical instruments is possible; however, clinical settings are usually limited in space and already crowded with medical instruments. Thus, it is desirable to have a single portable instrument that can be easily rolled in and out of the operating room or radiology room. The system should be able to provide diagnostically relevant information in real time and should be easy to operate. This system will be used not only for research purposes, but if the MMS instrument shows promising results, it will be given to the hospitals and will be operated by nurses or technicians.

6.2 MMS instrument design

6.2.1 Instrument development

The clinical portable MMS instrument [1] (Figure 6.1) merges optimized designs of the clinical Raman and FastEEM instruments. The MMS instrument contains three excitation sources: an 830 nm diode laser (Process Instruments, Salt Lake City, UT) used to excite Raman spectra; a Xe flash lamp (L7684, Hamamatsu Corp., Bridgewater, NJ) used to obtain diffuse reflectance spectra (DRS); and a 337 nm N_2 laser (NL100, Stanford Research Systems, Sunnyvale, CA) used to excite
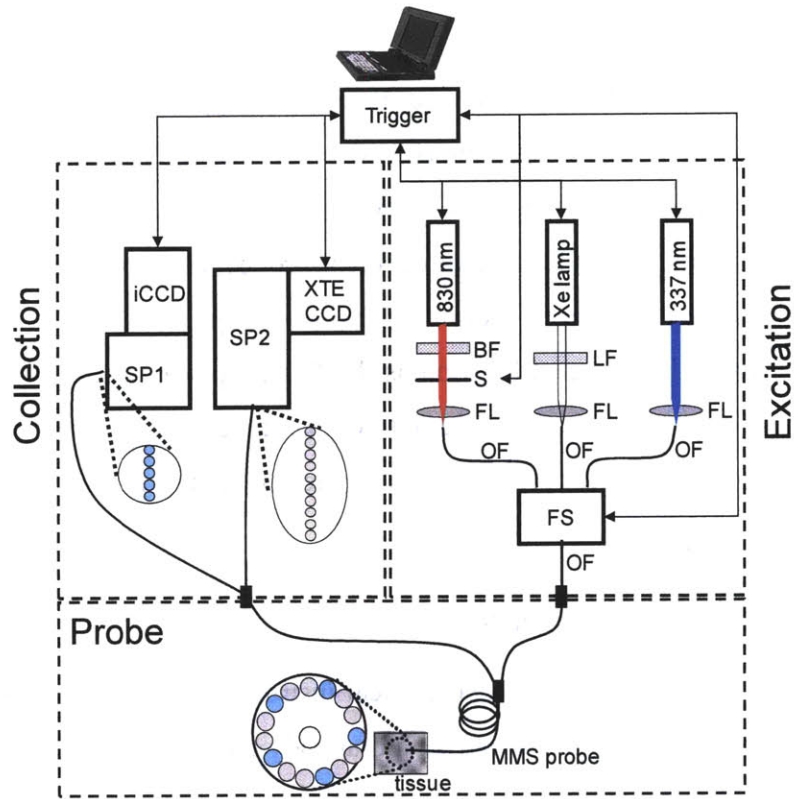
Figure 6.1. Diagram of the MMS instrument. LF – long pass filter, BF – bandpass filter, FL – focusing lens, S – shutter, OF – optical fiber, FS – fiber switch, SP_1 and SP_2 – visible and NIR spectrograph, respectively, iCCD and XTE CCD – intensified and thermoelectrically cooled charge-coupled devices, respectively. This figure is taken from [1] and reprinted with the permission of the publisher.

fluorescence. All of these sources are externally triggered via automated software. The diode laser is capable of providing up to 500 mW of continuous-wave 830 nm light, driven by a user-specified analog signal. The 830 nm laser light is filtered by an 830 nm bandpass filter (LL01-830-12.5, Semrock, Rochester, NY) and gated by a mechanical shutter (LS6ZM2, Vincent Associates, Rochester, NY) before being focused into an optical fiber. The Xe lamp provides a 2.9 µs FWHM white light pulse, 1 J/pulse max. The light from the Xe lamp passes through a 370 nm long pass filter (LP02-364RS-25, Semrock, Rochester, NY) and is then focused into a fiber. This long pass filter guarantees that the reflectance, collected over the range 370-740 nm is free of second order diffraction from the spectrograph grating. The N_2 laser provides externally triggered 3.5 ns FWHM pulses of 337 nm light, 170 µJ per pulse, with a 10 Hz repetition rate. This light passes through a UV-coated lens and is focused into an optical fiber.

An optical fiber switch (FSM14, Piezo Jena, Germany) is used to sequentially couple all three excitation sources into the MMS probe. An optical fiber switch is a MEMS device that provides superior coupling of the individual sources and is controlled by user-configurable binary code. This switch contains four optical fiber inputs and a single optical fiber output with each fiber terminated by an SMA connector. Thus it is possible to couple up to four sources into the output fiber. The outputs of the Xe lamp, N_2 laser, and diode laser are directly channeled into three input fibers of the switch. The remaining input channel is left vacant for a possible future light source. The output fiber of the switch is connected to the MMS probe by means of an SMA-to-SMA connector that produces a reproducible and efficient connection. The overall transmission efficiency of the switch is ~60%, resulting from an 80% switching efficiency and an 80% SMA-to-SMA coupling efficiency.

Detection of the collected light is performed with two spectrograph/CCD modules, one optimized for NIR detection (Raman) and the other for visible wavelengths (reflectance and fluorescence). The operation of both cameras is controlled by modular LabVIEW drivers (R^3 Software, Princeton, NJ).

The distal ends of the 10 collection fibers carrying the Raman light are aligned in a linear array, serving as the entrance slit to the spectrograph (Holospec f/1.8i, Kaiser Optical Systems), resulting in a ~9 cm^{-1} spectral resolution. The fibers are encased in a modified male FC connector to ensure highly reproducible alignment with the connector plate of the spectrograph. Any spectral changes incurred by disconnecting and reconnecting the linear array are found to be below the system's spectral resolution. The numerical aperture of the collection fibers (NA=0.26) is matched to the spectrograph (f/# = 1.8) to conserve throughput. The spectrograph contains an 830 nm notch filter to further suppresses the elastically scattered Rayleigh light, and a holographic grating to disperse the Raman scattered light onto a back-illuminated, deep-depletion CCD detector with a 1024x256 array of pixels (Spec10 XTE, Princeton Instruments/Acton, Acton, MA). The CCD detector has a 16 bit dynamic range and can be thermoelectrically cooled within minutes to -90°C, a significant practical improvement over the older Raman system, which had a liquid nitrogen cooled CCD that needed about 1.5 hours to be cooled to -120°C.

The five remaining collection fibers that are used for reflectance and fluorescence light are arranged vertically and coupled into a diffraction grating spectrometer (Spectra Pro 150, Princeton Instruments/Acton, Acton, MA), resulting in a ~6 nm spectral resolution. The collection fibers have individual male SMA adapters that connect to corresponding female SMA adapters mounted to a plate adjacent to the spectrograph; this ensures easy reproducibility when the MMS probe is disconnected from and reconnected to the system. The collected light is then dispersed onto an intensified CCD detector (PIMAX, Princeton Instruments/Acton, Acton, MA). The PIMAX CCD has a 16 bit dynamic range and is thermoelectrically cooled to -20°C. The CCD is operated in a gated mode, where the intensifier is biased on for only the short period of time (~30 μs) extending from immediately prior to immediately after each laser/white light pulse. All spectra must be collected with room lights off because the Raman signal is weak compared to ambient background light.
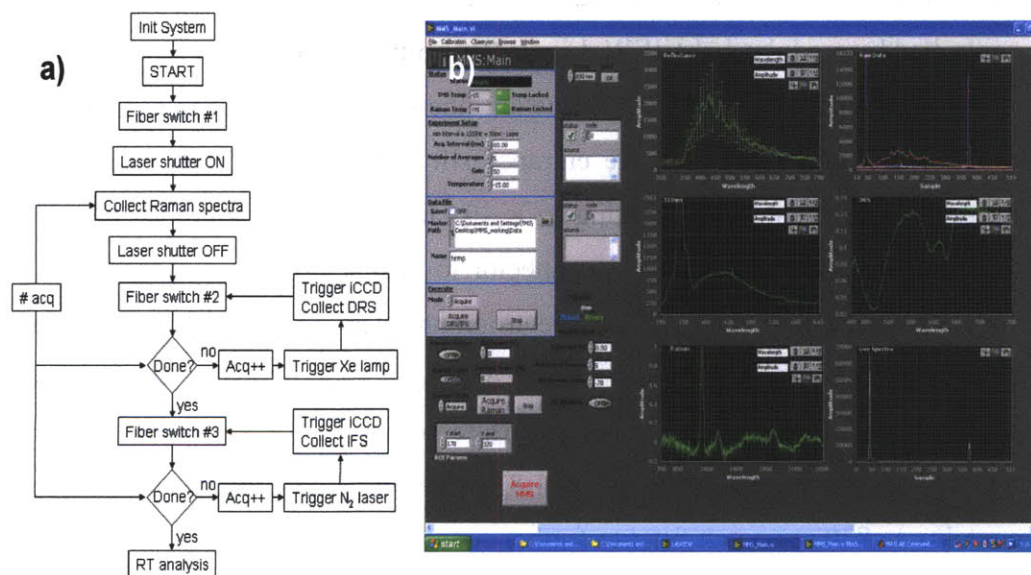
Figure 6.2. a) Flow-chart of the MMS software **b)** Front panel of the MMS instrument. This figure is modified from [1] and reprinted with the permission of the publisher.

The MMS instrument is controlled by software developed in LabVIEW (National Instruments, Austin, TX) and Matlab R2008b. The flow-chart of the software of a single MMS acquisition is depicted in Fig. 6.2a, indicating periods of

time required by each source and detector for data collection. Two data acquisition cards (DAQ) (6062 and 6035E, National Instruments, Austin, TX) are used to trigger sources and cameras. Figure 6.2b shows the front panel of the MMS software. User-friendly software allows one to choose to acquire MMS data (all three modalities) or separately Raman and the combination of DRS and IFS spectra. Exposure time and number of spectra can be easily changed depending on the needs of the user and the quality of the signal. All data is displayed in real time.

6.2.2   Instrument calibration and stability

Real-time data analysis and diagnosis depends on acquiring spectra for calibration and background subtraction prior to data collection. The software allows acquisition and storing of calibration spectra, which provides easy operation of experimental and clinical data collection and instant feedback about the collected spectra quality, fits, and diagnostic parameters.

The Raman-shift axis is calibrated using spectra acquired from 4-acetamidophenol (Tylenol), with known peak positions. The fused silica Raman background arising from the optical fiber probe is taken into account by acquisition of a spectrum from roughened aluminum. The roughened aluminum provides enough reflected light to record the Raman signal from the probe alone, which is later used in fitting to experimental data. Finally, the spectral response of the Raman spectrograph is obtained by collecting a spectrum of calibrated tungsten white-light source diffusely scattered by a reflectance standard ($BaSO_4$).

The wavelength of the reflectance and fluorescence spectra is calibrated by obtaining a spectrum of a mercury lamp. In order to remove effects of CCD dark current and stray light, a spectrum is acquired of deionized water contained in an opaque cup. The amplitude of the reflectance signal is calibrated by collecting a spectrum from a reflectance standard (20% reflectance standard, Labsphere Inc., North Sutton, NH). Finally, to normalize the fluorescence spectra, the output power from the N_2 laser is recorded on a daily bases via an energy meter.

It is important to note that the MMS instrument must be stable for day-to-day operation. Based on the design of the probe coupling, disconnecting and reconnecting the MMS probe to the instrument does not change the calibration parameters and intensity of the light delivered to the tissue.

6.2.3 Instrument layout

The MMS instrument has been designed to be used in a clinical setting in which floor space is at a premium and ease of portability is essential. SolidWorks software was used for designing the instrument cart and for optimal positioning of the various components. The metal cart has dimensions 27"x27"x58" and can be wheeled in and out of the operating or frozen section room for clinical data collection. The final layout of the system and a photograph of the developed instrument are shown in Fig 6.3.
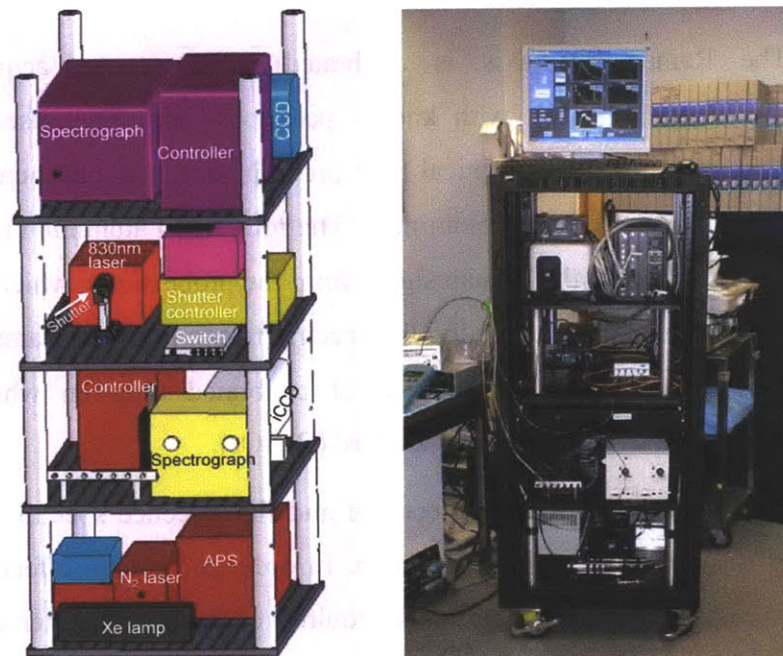
Figure 6.3. The design layout of the MMS instrument and photo of the final MMS instrument. This figure is modified from [1] and reprinted with the permission of the publisher.

6.2.4 Safety

The clinical MMS system must adhere to strict safety guidelines in the clinical environment. The excitation laser energies cannot exceed predetermined maximum values that are safeguarded prior to entering the operating room. The Xe flash lamp and the N_2 laser are pulsed sources, which are internally shuttered and controlled by LabVIEW. The 830 nm diode laser delivers a continuous-wave laser beam that is gated by an external high-speed shutter, which is also controlled by LabVIEW. The shutters open immediately before data acquisition begins and closes immediately after completion of data acquisition. The shutters remain closed until the system receives a signal through LabVIEW for another data acquisition.

Importantly, all parts of the system that enter the sterile environment (directly or indirectly comes in contact with a patient) must be kept sterile. In the case of the MMS system, only the probe is near the patient. Sterilization of the MMS probe is performed using cold-gas ethylene oxide.

6.3 MMS front-viewing probe design

The MMS instrument delivers light to and from the tissue via an optical fiber probe. The MMS probe is based on the previously designed Raman probe. The MMS probe design is modified to allow an efficient collection of DRS and IFS in the UV/visible wavelength range and Raman in the NIR wavelength range.

6.3.1 Probe development

The schematic of the MMS front-viewing probe is provided in Fig 6.4. There are several distinct differences between the MMS probe and the Raman probe: the optical fibers that are used for delivery and collection; the filter characteristics of the excitation rods and collection tubes; and the type of adhesives used to glue the components in the probe tip.

The MMS probe's fibers must be optimized for the particular wavelength range set by the spectroscopic modality it serves. The central excitation fiber, which
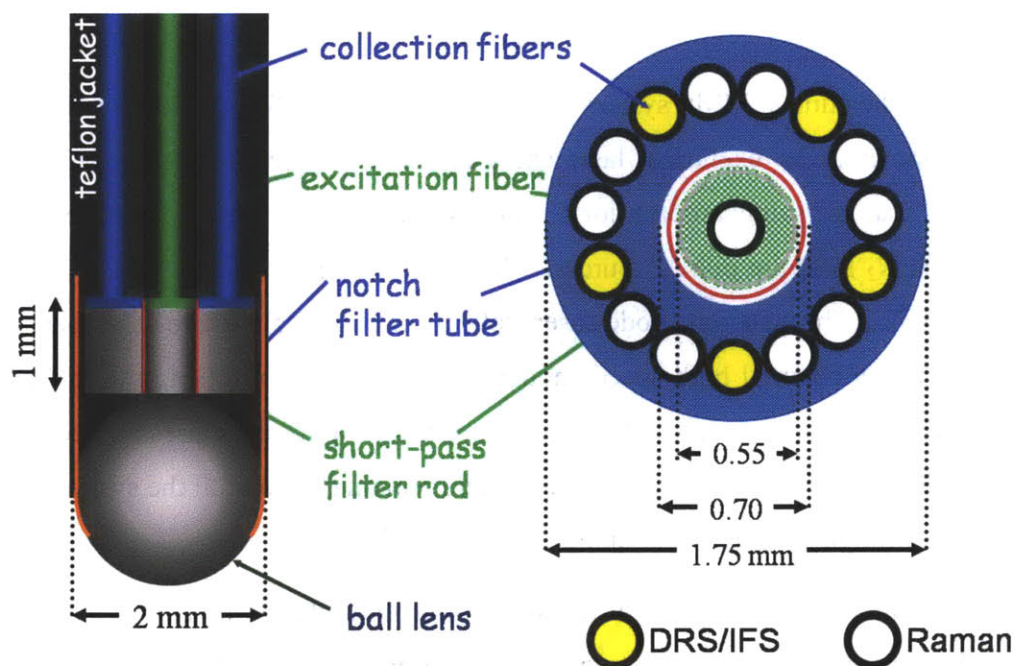
Figure 6.4. Schematic of the MMS front-viewing probe.

delivers light for all modalities, must efficiently transmit excitation light in the range from 340 nm to 830 nm. The collection fibers must be divided to optimize transmission of visible light and NIR light, respectively. Therefore, the material of the collection fibers can be optimized based on the wavelength range of light they will be transporting.

There are two primary materials used for the wavelength ranges of interest: low-OH fused silica (trade name Anhydroguide) and high-OH fused silica (trade name Superguide). Anhydroguide is best suited for long-wavelength light whereas Superguide is best for short-wavelength light. Thus, Anhydroguide fibers (diameter of 200μm, NA = 0.26, Fiberguide Industries, Stirling, NJ) are used for NIR (Raman), while Superguide fibers are used for the visible (DRS and IFS). The excitation fiber is selected to be Superguide (diameter of 200 μm, NA = 0.22, Fiberguide Industries, Stirling, NJ) as it is the best compromise for both wavelength ranges.

The Raman signal is weaker than that of DRS or IFS and thus more fibers need to be allocated for collection of NIR light. As a result, out of the 15 collection fibers, 10 fibers are dedicated for Raman, while the remaining 5 fibers are dedicated for DRS and IFS. This design allows a near equivalent signal collection with the MMS probe as compared with the FastEEM and Raman probes used individually.

Another very important change in the MMS probe from the Raman or FastEEM probes are the filters. For the purposes of acquiring all three modalities, the excitation and collection filters need to transmit visible light in the range of 300-800 nm. The excitation fiber rod contains a shortpass filter that transmits 300-830 nm light and cuts off light with wavelength longer than 850 nm to limit fused silica Raman signal. This shortpass filter is deposited onto a cylindrical rod with diameter of 0.5 mm and 1mm in length. In order to collect 300 – 800 nm light and 850 – 1000 nm light while blocking light around the Raman excitation wavelength (800 – 850 nm), the collection fiber filter is a notch filter. The collection fiber filter tube is donut-shaped with inner diameter 0.7 mm, outer diameter 1.8 mm, and length 1 mm. The filter characteristics are depicted in Fig 6.5. These filters are custom manufactured (Barr Associates, Westford, MA) and deposited onto polished fused silica pieces.

Components of the fiber tip (rods and tubes) need to be glued to the fibers. Ordinary epoxy is not optically clear in the UV wavelength range, thus a special epoxy (Epo-tek 305, Epoxy Technology, Billerica, MA) is used for the MMS probe. The sapphire ball lens that is used in the Raman probe is also appropriate for the MMS probe as sapphire is optically clear in the range of 300-1000nm. The sapphire
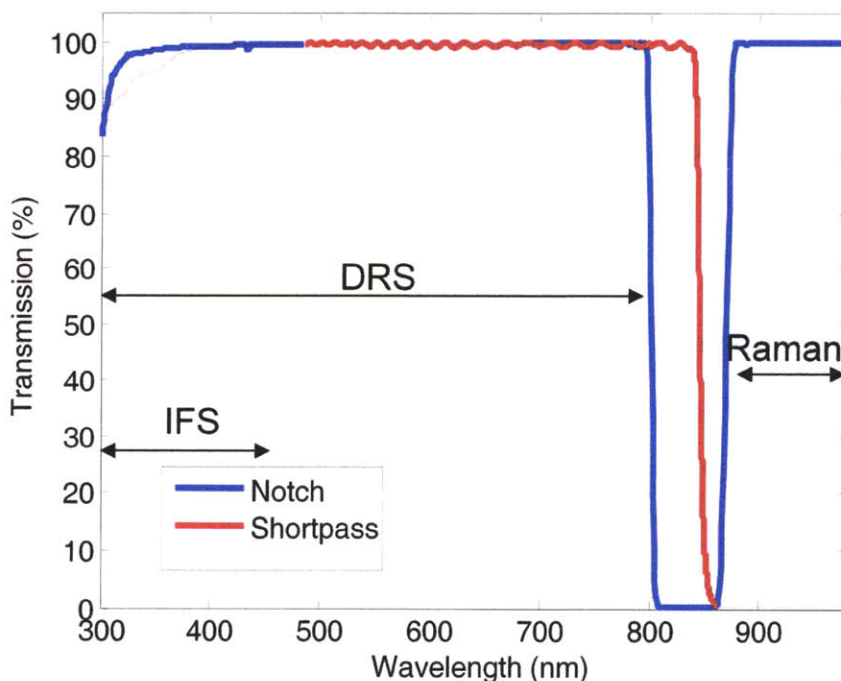
Figure 6.5. The filter characteristics of the MMS probe. This figure is modified from [1] and reprinted with the permission of the publisher.

ball lens is held in place by a stainless steel retaining sleeve rather than epoxy in order to minimize optical losses. In addition, the ball lens has an anti-reflection coating at 830 nm to substantially reduce reflection losses at the boundary between the fused silica fiber and the ball lens. This is to increase the amount of Raman excitation light on the tissue. Reflection losses at 337nm (~6%) are acceptable as fluorescence has much higher signal strength than Raman.

6.3.2   Data modeling

The MMS probe has a similar geometry as the previously designed Raman probe; however the inclusion of the sapphire ball lens and filter unit makes it substantially different from the FastEEM probe. Previously, the geometry was such that the excitation and collection spots on the sample were in the form of partially overlapping circles. The diffuse reflectance spectral model developed by Zonios *et al* [6] is dependent on this probe geometry. Now, in the MMS probe, the excitation/collection geometry has changed by increasing the spatial overlap between the excitation and collection regions and the angles collected as compare to the FastEEM probe. The IFS modeling can be still done in the manner described by Zhang et al [7] with modification of probe-specific parameters. Thus, modeling for both DRS and IFS needs to be modified to account for the geometrical changes of the MMS probe. In addition, each MMS probe must be calibrated individually to ensure correct extraction of optical tissue parameters.

6.3.2.1 Raman modeling

Modeling of the Raman spectra remains the same for the MMS probe as its geometry did not change for this modality. Modeling of Raman spectra is described in Chapter 3.

6.3.2.2 DRS modeling

Farrell *et al.* [8] calculated the diffuse reflectance from a narrow beam of light incident on the surface of a semi-infinite turbid medium in the diffusion approximation. The Green's function for reflectance density, $R(\lambda, r)$, in units mm^{-2}, at a distance r from the point of incidence, depends on tissue parameters: the absorption coefficient $\mu_a(\lambda)$, the reduced scattering coefficient $\mu_s'(\lambda)$, and A, a diffusion model parameter that depends on the refractive index of the tissue, which is assumed to be A≡3.2 [6]. In order to calculate the calibrated reflectance collected by a probe, $R_p(\lambda)$, the Green's function must be integrated over the delivery and collection areas, characterized by the radius of delivery, r_d, and radius of collection, r_c, and normalized by the delivery area, πr_d^2, to obtain the unitless quantity:

$$R_p(\lambda) = \frac{1}{\pi r_d^2} \int_0^{2\pi} d\phi_c \int_0^{r_c} r\, dr \int_0^{2\pi} d\phi_d \int_0^{r_d} R(\lambda, |r - r'|) r'\, dr', \qquad 6.1$$

where $|r - r'|$ specifies the distance between a point on the delivery area and a point on the collection area. Eq. 6.1. can be evaluated numerically, but it can be further simplified by making the approximation of point source delivery ($r_d \ll 1$). With this approximation, Zonios *et al.* obtained a closed form solution [6] for the reflectance collected by a FastEEM probe, which is used for DRS modeling of the FastEEM probe. As discussed below, this approach does not hold for the MMS probe.

The objective is to accurately extract $\mu_s'(\lambda)$ and $\mu_a(\lambda)$ from the acquired reflectance spectrum of tissue. To do this, r_d and r_c must be evaluated for a given probe, which can be accomplished by the following calibration technique. First, a calibration set of physical tissue models ("phantoms") is used to determine r_d and r_c; then, these probe-specific parameters are used prospectively on tissue spectra for accurate extraction of $\mu_s'(\lambda)$ and $\mu_a(\lambda)$. Five physical tissue models ("phantoms") were prepared to mimic breast tissue reflectance properties, as shown in Table 6.1. Polystyrene beads with 1 μm diameter and 1% solids by volume (64030 Polysciences, Warrington, PA) were used to simulate scattering. Absorption was simulated by using

a solution of hemoglobin (16 mg/ml) created by dissolving 12 mg of dry hemoglobin (H0267, Sigma-Aldrich, St. Louis, MO) with 1.5 ml of deionized H_2O. The five phantoms included variations of scattering amplitude and hemoglobin concentration similar to that found in normal breast tissue.

Phantom	Beads (ml)	Hb (ml)	H_2O (ml)
1	1.4	0.0	1.4
2	2.6	0.1	0.1
3	2.6	0.2	0.0
4	2.6	0.1	1.3
5	1.4	0.2	1.2

Table 6.1. Five phantoms used to calibrate DRS probe-specific parameters. Mixture of beads, hemoglobin and deionized water mimics optical properties of breast tissue.
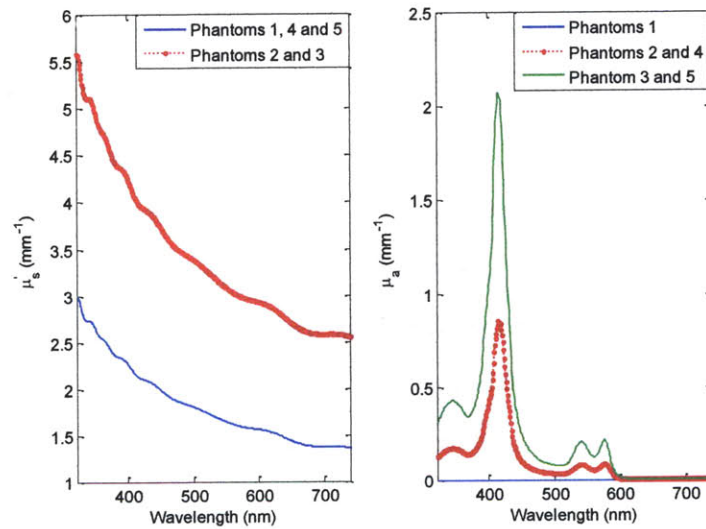
Figure 6.6. The $\mu_s'(\lambda)$ and $\mu_a(\lambda)$ values for the five phantoms used for calibration probe-specific parameters.

The $\mu_s'(\lambda)$ values were calculated using a standard Mie code that evaluates the total scattering cross section, $\sigma_s(\lambda)$, as presented in Eq. 6.2. For biological tissue in the visible region, $\mu_a(\lambda)$ is dominated by hemoglobin absorption and can be calculated using Eq 6.3.

$$\mu_s'(\lambda) = \mu_s(\lambda)(1-g) = \rho_s\sigma_s(\lambda)(1-g) \qquad 6.2$$

$$\mu_a(\lambda) = (log_e 10)C_{Hb}\left(\alpha\epsilon_{Hb}(\lambda) + (1-\alpha)\epsilon_{Hb}(\lambda)\right) \qquad 6.3$$

The $\mu_a(\lambda)$ parameter depends on the known extinction spectrum of hemoglobin, ϵ_{Hb}, the concentration of hemoglobin c_{Hb}, and the oxygen saturation of hemoglobin, α, which was taken to be 100% for the phantoms as the hemoglobin is completely oxygenated. The resulting $\mu_s^{'}(\lambda)$ and $\mu_a(\lambda)$ are shown in Fig 6.6.

The phantoms were mixed in small glass vials and thoroughly agitated to prevent clumping of the beads. Diffuse reflectance spectra were then collected using the MMS probe and instrument. The DRS spectra were obtained using the following expression:

$$R_{p,observed}(\lambda) = \frac{Reflectanc\ e\ (\lambda) - Background\ (\lambda)}{(Spectralon\ (\lambda) - Background\ (\lambda))\ /\ calibStd\ (\lambda)} \qquad 6.4$$

where *Reflectanc e*(λ) is the recorded reflectance spectrum from the phantom, *Background* (λ) is the background spectrum collected deionized water contained in an opaque cup, *Spectralon* (λ) is the reflectance spectrum recorded from a calibrated standard (20% reflectance standard, Labsphere Inc., North Sutton, NH), and *calibStd* (λ) is the manufacturer-specified response of the standard. In this way, the $R_{p,observed}(\lambda)$ is expressed in calibrated reflectance units.

The probe-specific r_d and r_c values were calculated through an optimization that minimized the residual $(R_{p,observed}(\lambda) - R_p(\lambda))^2$, where $R_{p,observed}(\lambda)$ was obtained from Eq. 6.4 and $R_p(\lambda)$ was calculated by numerically evaluating Eq. 6.1 with the known and specified values of $\mu_s^{'}(\lambda)$ and $\mu_a(\lambda)$ for each phantom. Then the measured DRS spectrum was compared to the spectra in the lookup table. The spectrum from the lookup table that fitted the best also associated with the particular set of r_d and r_c. The best fit spectra are shown in Fig 6.7. in red. This figure also depicts the best fits (shown in black) obtained using the Zonios formulation. It is clear from Fig 6.7 that fits obtained by the Zonios formulation do not accurately model the experimental data, $R_{p,observed}(\lambda)$. Therefore, Eq. 6.1 should be used to model
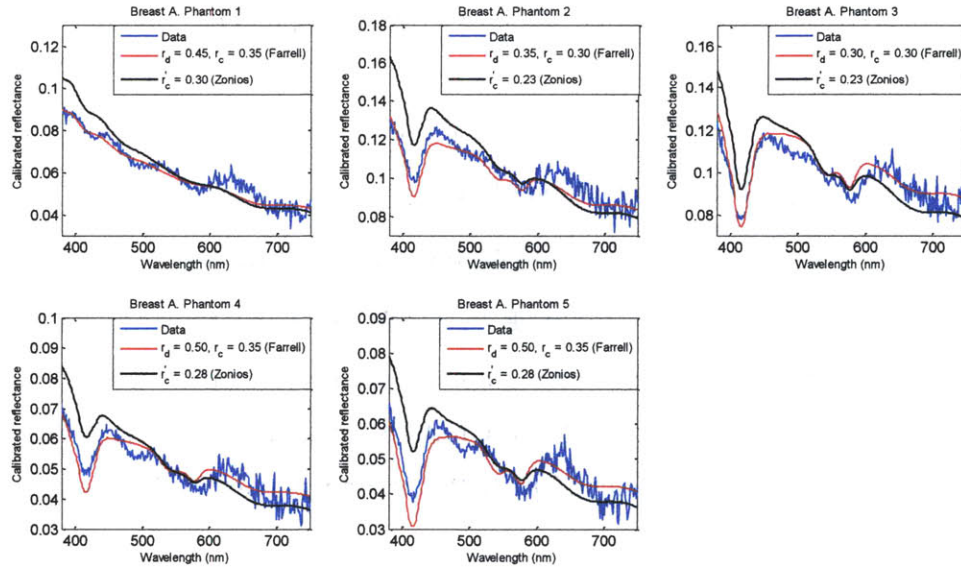
Figure 6.7. Experimental DRS spectra for five phantoms (blue), the best fits using a lookup table with Eq. 6.1. (red), and best fits using Zonios approximation (black).

DRS data collected via the MMS probe. Although the optimal values of r_d and r_c varied slightly across the five phantoms, we found for the particular probe used that the intermediate values ($r_d = 0.45$ mm and $r_c = 0.35$ mm) can model well all five phantoms. These average parameters also make physical sense, given the MMS probe ball lens that specifies both delivery spot and also a range of reflected angles that can couple into the collection.

The same operation was performed for all newly developed MMS probes. It is noted that the values obtained were slightly different for different probes. Probe-specific parameters were recorded for each MMS probe.

Once the calibrated values of r_d and r_c were obtained, we are able to prospectively extract accurate values of the optical parameters of tissue, $\mu_s'(\lambda)$ and $\mu_a(\lambda)$, from an unknown tissue sample. In order to do so, a prospective lookup table was used, in which DRS spectra are generated by numerically integrating Eq. 6.1 over a range of values of $\mu_s'(\lambda)$ and $\mu_a(\lambda)$ with fixed values of the calibrated probe-specific parameters r_d and r_c. In this case, $\mu_s'(\lambda)$ was calculated by a power law,

$A\lambda^{-B}$, with two free parameters A and B. As discussed above, $\mu_a(\lambda)$ depends on the concentrations of the particular absorbers present in the tissue (in this cause hemoglobin) and their extinction coefficients.

An unknown tissue spectrum is then compared to the entries in the lookup table to obtain the optimal values of A, B, c_{Hb}, and α, that in turn specify $\mu_s'(\lambda)$ and $\mu_a(\lambda)$. To check the accuracy of the predictive lookup table, it was used to fit spectra obtained from unknown phantoms, and the extracted spectral quantities $\mu_s'(\lambda)$ and $\mu_a(\lambda)$ were compared to the known (measured) quantities. The difference between the extracted and measured values was on average only a few percent, which demonstrates the accuracy of the predictive fitting. In addition, computation using the lookup table is fast and can be accomplished in real time.

6.3.2.3 IFS modeling

As discussed in Chapter 5, the raw tissue fluorescence spectrum contains information about tissue autofluorophores, but the spectrum is distorted by the presence of absorbers and scatterers found in tissue. Intrinsic fluorescence (IFS) is defined as the spectrum free of these interferences and can thus be modeled as a linear combination of fluorophores [9]. Zhang *et al* [7] presented a method based on photon migration for extracting IFS spectra from turbid media, which built on the previously developed model of Wu *et al* [10]. The IFS spectrum, $f_{xm}(\lambda)$, is related to the experimentally measured fluorescence spectrum, $F_{xm}(\lambda)$, and the DRS spectrum, $R_m(\lambda)$, by means of Eq 6.5 [7]:

$$f_{xm}(\lambda) = \frac{F_{xm}(\lambda)}{\dfrac{1}{\mu_{sx}l}\left(\dfrac{R_{0x}R_{0m}(\lambda)}{\varepsilon_x\varepsilon_m(\lambda)}\right)^{1/2}\dfrac{R_x}{R_{0x}}\left(\dfrac{R_m(\lambda)}{R_{0m}(\lambda)}+\varepsilon_m(\lambda)\right)}, \qquad 6.5$$

where R_x is a constant obtained from $R_{p,observed}(\lambda)$ at the fluorescence excitation wavelength, R_{0x} is a constant similar to R_x but computed using Eq.6.1 by setting

$\mu_a = 0$, $R_{0m}(\lambda)$ is a spectrum evaluated from $R_{p,observed}(\lambda)$ for all fluorescence emission wavelengths, and μ_{sx} is evaluated at the fluorescence excitation wavelength and is extracted from μ_s' using the known value of anisotropy, g. Finally, ε_x and $\varepsilon_m(\lambda)$ are evaluated at the excitation and all emission wavelengths, respectively, using $\varepsilon = e^{\beta} - 1$, with $\beta = S \cdot (1 - g)$, for a fixed parameter S and anisotropy g, and l is related to the optical thickness of the sample.

The parameters S and l are probe-specific and need to be calibrated for each of the probes. This is done in a similar fashion as the DRS calibration to establish r_d and r_c. First, a set of known phantoms using polystyrene beads, hemoglobin, and furan for fluorescence, were used to calibrate the values of S and l. In this step, it was determined that the optimal values of these parameters for one particular MMS probe were $S = 0.7$ and $l = 40$ µm. These probe-specific parameters were then held fixed for the particular probe and plugged into Eq.6.5 to extract $f_{xm}(\lambda)$ prospectively from unknown samples. Once the correct IFS spectrum is extracted, it can be fit using least squares to a specific linear model of constituent spectra.

6.4 Summary

We have described the design and calibration of the MMS instrument and MMS probes. This instrument is the first system that is capable of simultaneously collecting reflectance, fluorescence, and Raman spectra from the same tissue site in less than 5 seconds. The outer diameter of the probe is approximately 2 mm and contains one central delivery fiber surrounded by 15 collection fibers. Of the collection fibers, 5 fibers are designated for visible light collection and the remaining 10 fibers are designated for NIR Raman light collection. All probe components are optimized for their particular spectroscopic modality. Each of the 6 probes that were manufactured for the clinical study in the following chapter were carefully calibrated to ensure an accurate extraction of spectral and diagnostic parameters.

6.5 References

1.   Scepanovic, O.R., et al., A multimodal spectroscopy system for real-time disease diagnosis. *Review of Scientific Instruments*, 2009. **80**: p. 043103.

2.   Scepanovic, O.R., *Development of Multimodal Spectroscopy for the Detection of Vulnerable Atherosclerotic Plaques*, in *EECS*. 2008, MIT: Cambridge. p. 228.

3.   Motz, J.T., et al., Real-time Raman system for in vivo disease diagnosis. *J Biomed Opt*, 2005. **10**(3): p. 031113.

4.   Motz, J.T., et al., Optical fiber probe for biomedical Raman spectroscopy. *Appl Opt*, 2004. **43**(3): p. 542-54.

5.   Tunnell, J.W., et al., Instrumentation for multi-modal spectroscopic diagnosis of epithelial dysplasia. *Technol Cancer Res Treat*, 2003. **2**(6): p. 505-14.

6.   Zonios, G., et al., Diffuse Reflectance Spectroscopy of Human Adenomatous Colon Polyps In Vivo. *Appl. Opt.*, 1999. **38**: p. 6628-6637.

7.   Zhang, Q.G., et al., Turbidity-free fluorescence spectroscopy of biological tissue. *Optics Letters*, 2000. **25**(19): p. 1451-1453.

8.   Farrell, T.J., M.S. Patterson, and B. Wilson, A diffusion theory model of spatially resolved, steady-state diffuse reflectance for the noninvasive determination of tissue optical properties in vivo. *Med Phys*, 1992. **19**(4): p. 879-88.

9.   Volynskaya, Z., *Multi-modal spectroscopy of breast tissue*, in *Electrical Engineering and Computer Science*. 2005, MIT: Cambridge. p. 67.

10.   Wu, J., M.S. Feld, and R.P. Rava, Analytical Model for Extracting Intrinsic Fluorescence in Turbid Media. *Applied Optics*, 1993. **32**(19): p. 3585-3595.

CHAPTER 7

Ex vivo clinical application of the MMS system

This chapter describes the data analysis of the first clinical study in which the MMS system is used to diagnose breast lesions. Prospective validation of the previously developed Raman and DRS/IFS diagnostic algorithms was performed on 99 consecutive patients during two *ex vivo* studies of tissue acquired from excisional biopsy and needle biopsy procedures. Raman diagnostic algorithm was successfully validated on the data set from the excisional biopsy, while its performance on the needle biopsy was not as good. DRS/IFS algorithm had to be changed to distinguish among different lesions. The last part of the chapter presents a new diagnostic algorithm that was developed to enable the discrimination of two additional pathology categories: ductal carcinoma *in situ* (DCIS) and infiltrating lobular carcinoma (ILC).

7.1   Motivation

The clinical studies described in the previous chapters of this thesis were conducted using a separate Raman clinical system and DRS/IFS system demonstrated that we could accurately classify four different types of breast lesions. Successful development and testing of the MMS system provided a unique opportunity to sequentially collect data from all three modalities within seconds at the exact the same site on the lesion, thus eliminating registration errors caused by switching probes in between measurements. The two major aims of this study were as follows: 1) To apply the previously developed Raman and DRS/IFS diagnostic algorithms (Chapter 4 and 5, respectively) in a prospective manner to determine if the algorithms are sufficiently robust to be applied to any set of breast specimens; 2) to construct a new algorithm which is capable of distinguishing additional pathology categories, including DCIS and ILC. Another very important aim of this project was to be able to acquire data from calcified specimens along with non-calcified specimens. Measurements from calcified specimens can only be acquired in the clinic and not from *ex vivo* samples.

7.2   Study protocol

The clinical *ex vivo* study was carried out at the University Hospitals-Case Medical Center (UH-CMC). The study was approved by the UH-CMC Institutional Review Board and the Massachusetts Institute of Technology Committee On the Use of Humans as Experimental Subjects. Data were collected either in the frozen section room adjacent to the operating room where patients underwent surgical biopsy (mastectomy or lumpectomy), or in the Mather Surgical Pavilion on patients undergoing core needle biopsy (stereotactic and ultrasound). Measurements from both sets of patients would yield samples from pathology categories that were not included in the previously develop algorithms. In particular, DCIS is commonly associated with the microcalcifications that are targeted during core needle biopsy. Pathology categories which were most relevant for validating our diagnostic algorithms were primarily collected from surgical patients. Informed consent was obtained from all

subjects prior to their surgical and biopsy procedures. During a period of 9 weeks, data were acquired from 99 patients and consisted of patients undergoing ultrasound core needle biopsy (n=40), stereotactic core needle biopsy (n=19), excisional procedures (n=38), and re-excision procedures (n=10).

Data were collected from breast specimens typically within 30 minutes of excision. Before data acquisition, the surgical specimens were inked and sectioned according to the standard pathology protocol, while breast cores from needle biopsy procedures were simply placed in a petri dish. Depending on the region of interest identified by pathologist, the number of MMS spectra acquired from each patient varied. Several other pathologists and residents were working simultaneously on different specimens in the frozen section room and we could not interrupt their work by turning off the lights during our measurements. Therefore, each specimen was placed inside a newly designed light tight box to prevent ambient light from entering the probe and the spectrograph during data collection. During data acquisition in the radiology room in the Mather Surgical Pavilion, the probe was placed in contact with the region of interest and the room lights were turned off. Following data acquisition, the breast specimens were marked with various colors of colloidal ink to uniquely identify each site sampled, and then fixed in 10% neutral buffered formalin.

Pathology

The fixed tissue samples were routinely processed, paraffin embedded, sectioned at the marked locations (5 μm thick), and stained with H&E. The histology slides were evaluated by an experienced breast pathologist who was blinded to the outcome of the MMS spectroscopy analysis, and the results were used as the gold standard against which the MMS findings were compared. .A total of 865 sets of MMS spectra (each set of Raman, DRS and IFS spectra) were acquired from 99 patients: 476 spectra from core needle biopsy specimens and 389 from excisional biopsy specimens. As will be discussed in Chapter 9, 9 gauge ATEC biopsy needles were used during stereotactic while 12 gauge ATEC needles were used during

ultrasound core needle biopsy procedures. The histopathology diagnoses are shown in Table 7.1.

Histopathology Diagnosis	Surgical Biopsy Specimens	Needle Biopsy Specimens
	# spectra/patients	# spectra/patients
Normal	98/ 37	204/52
FCC	91/27	152/40
Fibroadenoma	1/1	21/7
Lipoma	6/1	--
Healing Bx Cavity	21/12	--
Hemorrhage	12/7	--
Fat necrosis	14/9	--
DCIS	8/4	12/3
LCIS	3/1	--
IDC	23/5	18/7
ILC	21/3	--

Table 7.1. Distribution of histopathology diagnoses for the surgical and core needle biopsy specimens, respectively.

As shown in Table 7.1, these data sets contained lesions with histopathology diagnoses that we did not have in our previous studies. Healing biopsy cavity (Healing Bx Cavity), hemorrhage and fat necrosis are all benign lesions, while lobular carcinoma *in situ* (LCIS), ductal carcinoma *in situ* (DCIS) and infiltrating lobular carcinoma (ILC) are malignant breast lesions.

Several spectra had to be excluded from the analysis due to poor signal quality of (n = 22), the presence of ambient light in the signal (Raman spectra; n = 15), and in the case of DRS and IFS spectra, an overall reflectance of <1 % (n = 28). The latter group of samples was excluded because when the reflectance values are low, we cannot accurately extract the parameters necessary for calculating the intrinsic fluorescence.

7.2.1 Surgical biopsy specimens
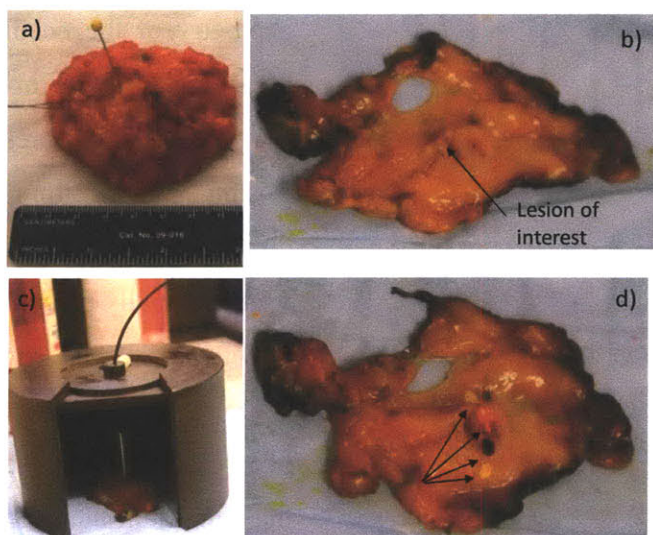
Figure 7.1. Surgical biopsy specimen. a) original specimen; b) one slice of specimen, 5mm thick; c) placing specimen and acquiring data inside the black box; d) inking exact sites with multicolor colloidal ink

Surgical specimens were obtained from excisional and re-excisional surgical biopsy procedures from 48 consecutive patients within 30 min from the procedure. The study protocol was similar to one described in Chapter 4. Analysis of the data set shows that the majority of all lesions are found to be normal or benign (FCC) upon pathology evaluation.

In order to collect more data from malignant lesions, one has to acquire data from more patients.

Surgical specimens, usually 5-7cm in diameter, were cut by a medical resident or pathologist in 5mm thick sections. The sites of interest were identified by a certified pathologist. However, it is impossible to turn lights of in the busy frozen section room. So, the specimens were placed inside the light tight black box in order to acquire MMS data. Once all of the spectra from one specimen were obtained, the exact sites locations were marked with multicolored colloidal ink (see Fig 7.1) for later identification/correlation of sites/MMS spectra. The power delivered to the breast tissue was approximately 100mW over $1mm^2$ spot. The acquisition time for all three modalities was approximately 5 seconds, providing 10 spectra for each of the modalities (for example, 10 Raman spectra of 0.5s acquisition time each) for averaging and increasing signal-to-noise. In the few cases, for which the data was too noisy, the acquisition time was increased to 1s per spectrum.

7.2.2 Core needle biopsy specimen
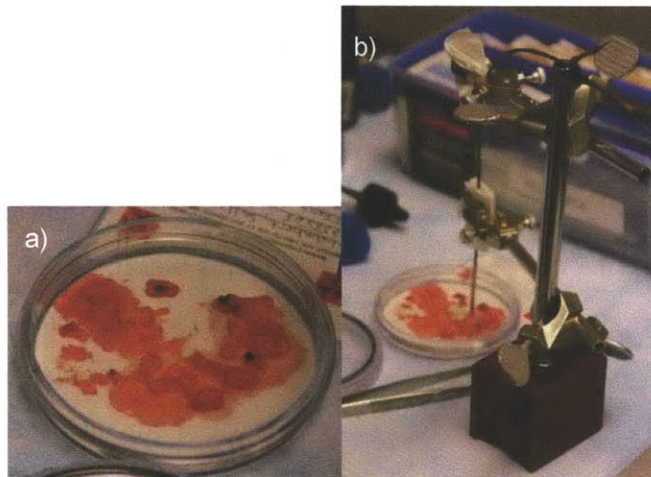
Figure 7.2. Core needle biopsy specimen. a) biopsy cores; b) Data acquisition setup

Because of the geometry of the needle, the breast biopsy cores obtained during such procedures are ~ 1.7mm x 20mm in dimension. All of the cores were originally placed inside a petri dish, but once the pathologist identified a core of interest, it was placed on the aluminum block for data collection. However, number of spectra were acquired from biopsy cores while they were still placed inside a petri dish, see Fig 7.2. The power and acquisition time were similar to the power and time during data collection from surgical biopsy specimens.

7.2.3 Data Analysis

All of the data were collected using the clinical MMS instrument and the MMS optical fiber probe described in Chapter 6. On average, the excitation laser power was 100 mW. Calibration spectra were obtained prior to data collection as previously described (Chapter 3).

In addition, an increased contribution from cholesterol-like lipid deposits was observed in this data set, possibly due to changes in the Raman scattering cross-section of this component upon tissue freeze thaw in the *in vitro* study (Chapter 4.2), and thus the cholesterol-like fit contribution was not included in the normalization.

The previously developed diagnostic algorithm (Chapter 4 and 5) discriminated among four pathology categories: normal, fibroadenoma, FCC, and IDC tissue. In the present study, we prospectively tested the algorithm only on data measured from samples assigned to these same four categories.

# 7.3 Results: Application of the DRS/IFS diagnostic algorithm

7.3.1 *Prospective application of DRS/IFS diagnostic algorithm*

The previously developed DRS/IFS diagnostic algorithm (Chapter 5) was applied to specimens classified as normal, FCC, fibroadenoma and IDC in the current data set. Data collection was performed using 4 different MMS probes that were previously tested as described in Chapter 6. For each probe we had generated a different lookup table for fitting procedures of DRS, as r_d and r_c were slightly different for each MMS probe. Fig. 7.3 shows a boxplot of values of A, concentration of β-carotene and oxyhemoglobin, as well as relative concentration of collagen and NADH.
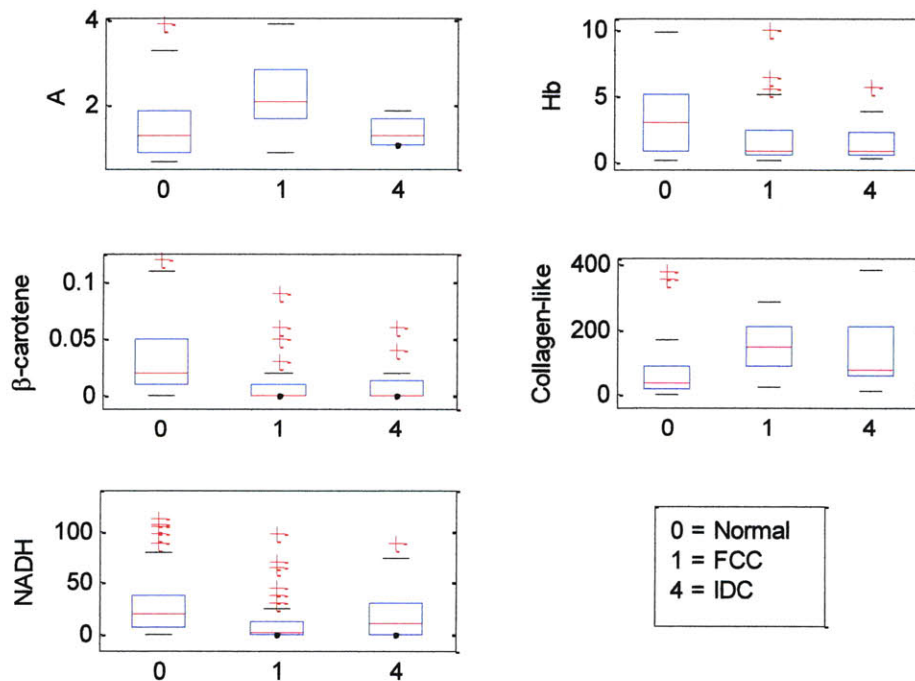
Figure 7.3. Boxplots of normal (Normal), fibrocystic change (FCC), fibroadenoma (FA), and infiltrating ductal carcinoma (IDC) for diagnostically relevant parameters of excisional biopsy specimens.

As in the previous study, the amount of β-carotene is much higher and the contribution of collagen-like is smaller in normal lesions as compared to other lesions. Thus the first step of the step-wise algorithm is based on the combination of β-carotene and collagen-like component (Fig 7.4a). Step II was not needed for this particular data set, as there was only one FA specimen. Step III, in which we separate FCC from IDC lesions was based on the contribution of hemoglobin and the collagen-like component (Fig.7.4.b). In the previous study we noted an increase in the value of oxyhemoglobin in malignant lesions compared to FCC samples. This is consistent with the fact that most malignant tumors are characterized by angiogenesis (increase in vasculature), which should result in a larger contribution of hemoglobin. However, in the data set on excisional biopsy specimens, the difference in the value of oxyhemoglobin between FCC and IDC samples is insignificant. The distinction between these two pathology groups based on concentration of oxyhemoglobin and collagen-like was not as good as in the previous study. Eight of the 23 IDC specimens were incorrectly classified as FCC, and the decision line had to be changed to minimize the number of misclassified IDC samples. The reason for the low
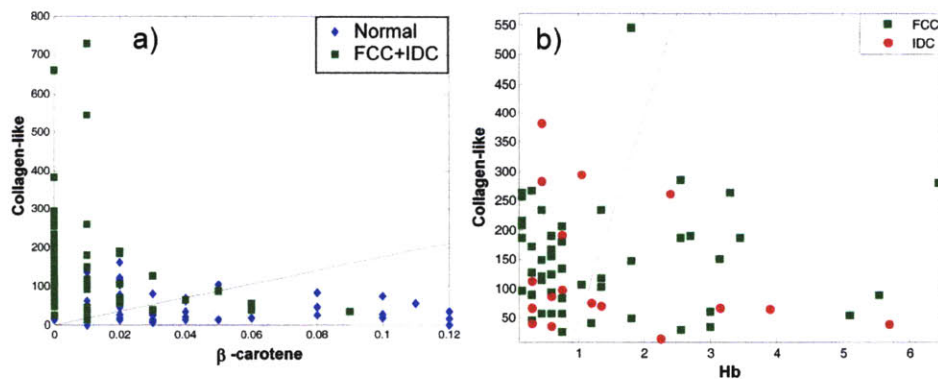
Figure 7.4. Prospective performance of DRS/IFS algorithm in excisional biopsy specimens. a) Step I; b) Step III.

contribution of hemoglobin in malignant specimens in this study is unclear. Thus, it resulted in a sensitivity, specificity, PPV, NPV, and overall accuracy of 43%, 91%, 37%, 93%, and 79%, respectively.

The performance of the DRS/IFS algorithm for the data set acquired from core needle biopsy specimens is shown in Fig. 7.5. The plot for Step I of the algorithm (Fig.7.5a) shows that the contribution of β-carotene is more significant in normal lesions than in abnormal lesions (both benign and malignant). The plot for Step II of the algorithm (Fig.7.5b) shows that the contribution of NADH is smaller in FA specimens than in FCC and IDC. However, as seen for excisional biopsy specimens, the contribution of oxyhemoglobin does not provide a good separation between IDC and FCC, as 8 IDC specimens are incorrectly classified as FCC. Thus, it resulted in a sensitivity, specificity, PPV, NPV, and overall accuracy of 44%, 98%, 57%, 97%, and 87%, respectively.
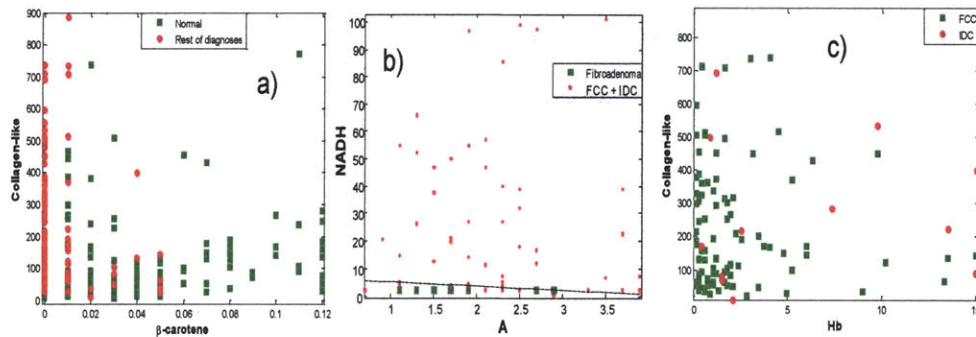
Figure 7.5. DRS/IFS step-wise algorithm applied prospectively on core needle biopsy specimens. a) step I; b) step II; c) step III.
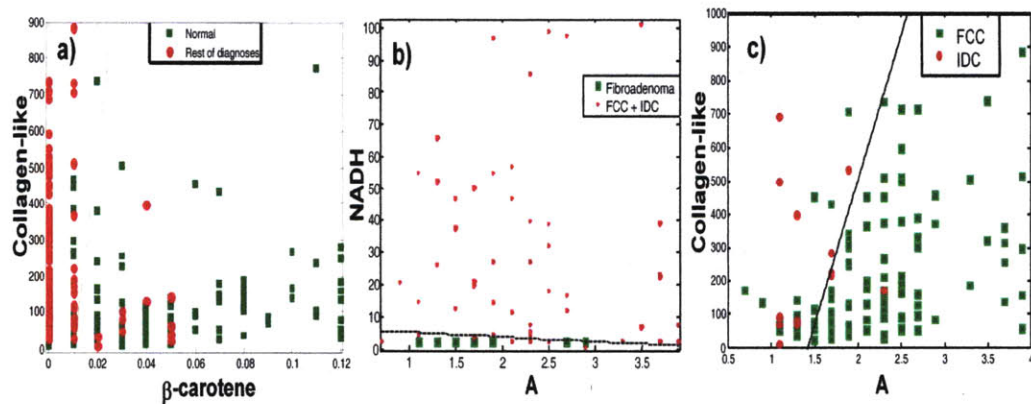
7.3.2 *A new DRS/IFS diagnostic algorithm*

Careful examination of physical parameters obtained from DRS and IFS (see Fig. 7.5) showed, that A parameter can be used to separate IDC specimens from FCC both in excisional biopsy and core needle biopsy data sets. Thus, a new DRS/IFS algorithm was constructed for these data sets. The new algorithms are depicted in Fig. 7.6 and Fig. 7.7 respectively.
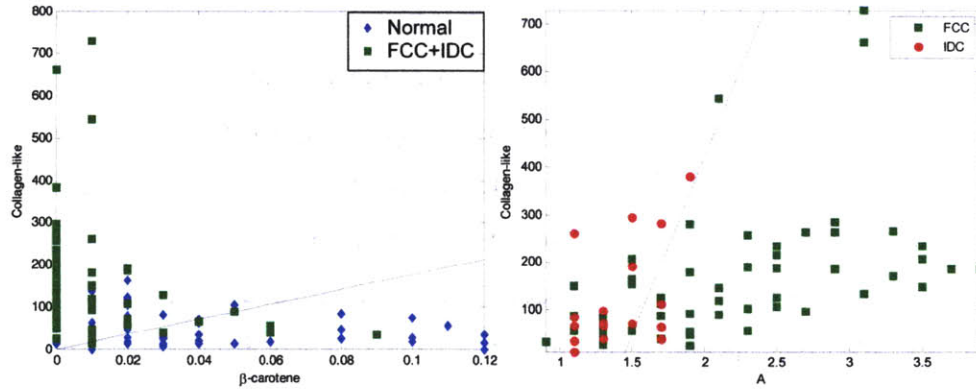
Figure 7.6. New DRS/IFS diagnostic algorithm for excisional biopsy specimens

The new algorithm is also a step-wise algorithm. We can separate Normal from the rest of the diagnoses using the concentration of β-carotene and collagen-like (the same two parameters as before). In order to separate IDC from FCC lesions, we use A parameter and relative concentration of collagen-like. The change in the last step increases the diagnostic performance of DRS/IFS technique, as only 3 IDC are

Figure 7.7. New DRS/IFS diagnostic algorithm for core needle biopsy specimens

classified as FCC. A sensitivity, specificity, PPV, NPV, and overall accuracy of 78%, 91%, 60%, 97%, and 85%, respectively were obtained.

The same parameters were used to classify specimens from the core needle biopsy data set. The first two steps remained the same as in the original DRS/IFS algorithm. In the last step, the use of A parameter instead of concentration of oxyhemoglobin, resulted in misclassification of only 3 IDC as FCC. A sensitivity,

specificity, PPV, NPV, and overall accuracy of 78%, 97%, 54%, 99%, and 87% respectively was obtained.

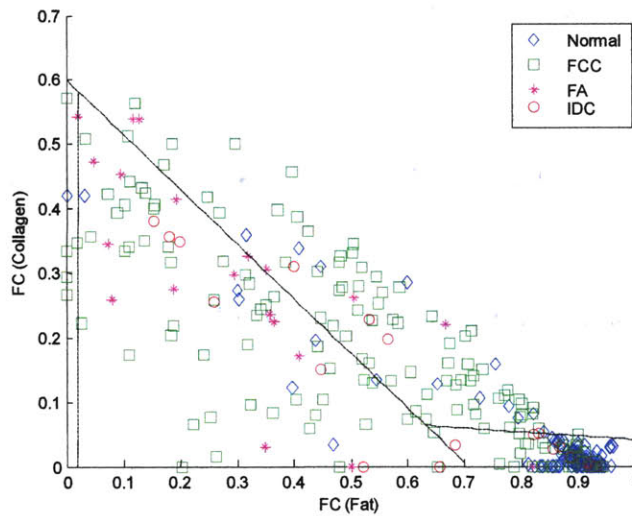## 7.4 Results: Application of the Raman diagnostic algorithm

7.4.1 *Prospective application of Raman diagnostic algorithm*
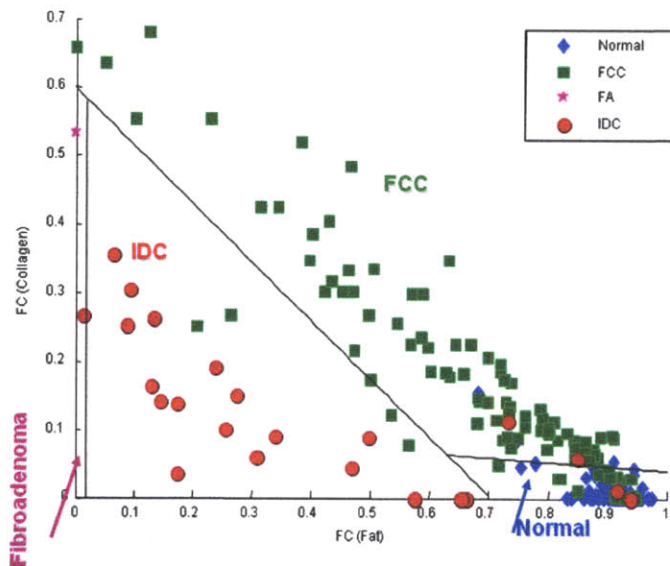
Figure 7.8. Prospective application of Raman diagnostic algorithm on excisional biopsy specimens

For the excisional biopsy data set, as shown in Fig. 7.8., we have successfully prospectively validated the Raman diagnostic algorithm on 48 new patients, which resulted in a sensitivity, specificity, PPV , NPV and overall accuracy of 78%, 98%, 82%, 98%, and 86%, respectively. Two IDC specimens were incorrectly diagnosed as FCC, and two were incorrectly classified as normal. In the case of the samples classified as normal, we found that only a few malignant cells were present and the sample consisted almost entirely of adipose tissue. The presence of even a few malignant cells would classify this specimen to be malignant by pathology; however, Raman spectroscopy was not sensitive enough to detect such a small number of malignant cells. Thus, there are some limitations in the use of spectroscopy to diagnose lesions.

Figure 7.9. Prospective application of Raman diagnostic algorithm on core needle biopsy specimens

The performance of Raman diagnostic algorithm on core needle biopsy specimens is depicted in Fig. 7.4. This is the first time we have acquired data from core needle biopsy specimens. These samples are much smaller in size than specimens from excisional biopsies. Application of the Raman diagnostic algorithm yielded a 50% sensitivity, 83% specificity, and 68% overall efficiency. The PPV was 13%, and the NPV was 97%. These values are almost equivalent to those observed in the *in vitro* study.

It is clearly seen that the contribution of fat and collagen is reduced in a large number of FCC specimens, and that this resulted in FCCs samples being misclassified as IDC and normal. There are several reasons why this may occur. First, the impact of the specimen size needs to be studied further. Second, the spread in the samples diagnosed as FCC diagnosis could contribute to number of misclassified lesions. As discussed in Chapter 2, specimens classified as FCC may be predominately characterized by fibrosis, adenosis, ducts or any combination of these features. We further analyzed FCC specimens to determine whether there was any correlation between the predominant feature and Raman findings. It was found that 38 of the 44 misclassified specimens had adenosis (19), microcalcifications (11) or duct cysts (8). These are all space occupying lesions, where the proliferating ducts (adenosis), microcalcifications or duct cysts occupy space that would otherwise be occupied by collagen-rich stroma. As a result of this, they have less collagen (and lower collagen fit contributions) than FCCs that lack adenosis, microcalcifications and duct cysts.

Thus, the increase number of FCC lesions with features of adenosis, microcalcifications and duct cysts accounts for most of the misclassified FCC lesions.

Pathology / Raman	Normal	Fibrocystic Change	Fibroadenoma	Infiltrating Ductal Carcinoma
	(204 samples)	(152 samples)	(21 samples)	(18 samples)
Normal	185	29	2	5
Fibrocystic Change	12	72	6	4
Fibroadenoma	1	6	1	0
Infiltrating Ductal Carcinoma	6	45	12	9

Table. 7.2. Comparison of histopathology diagnoses and Raman spectroscopic classification of breast disease for core biopsy specimens

7.4.2 *A new 3D Raman diagnostic algorithm*

As previously mentioned, the current data set from the excisional biopsy contains malignant lesions that were not seen before in previous data sets (*in vitro* and *ex vivo* previous study), such as DCIS and ILC. The previously developed Raman diagnostic algorithm did not perform well on needle biopsy specimens. Thus, there was a need to develop a new diagnostic algorithm that can be used for needle biopsy procedures, and it should be able to correctly classify DCIS and ILC.

Careful analysis of the parameters from all three spectroscopic modalities (Raman, DRS, and IFS), lead to development of the new diagnostic algorithm. As it is shown in Fig. 7.10 and Fig. 7.11, the new algorithm employs three fit coefficients obtained from Raman spectroscopy: fat, collagen and a sum of cell nucleus and cell cytoplasm.
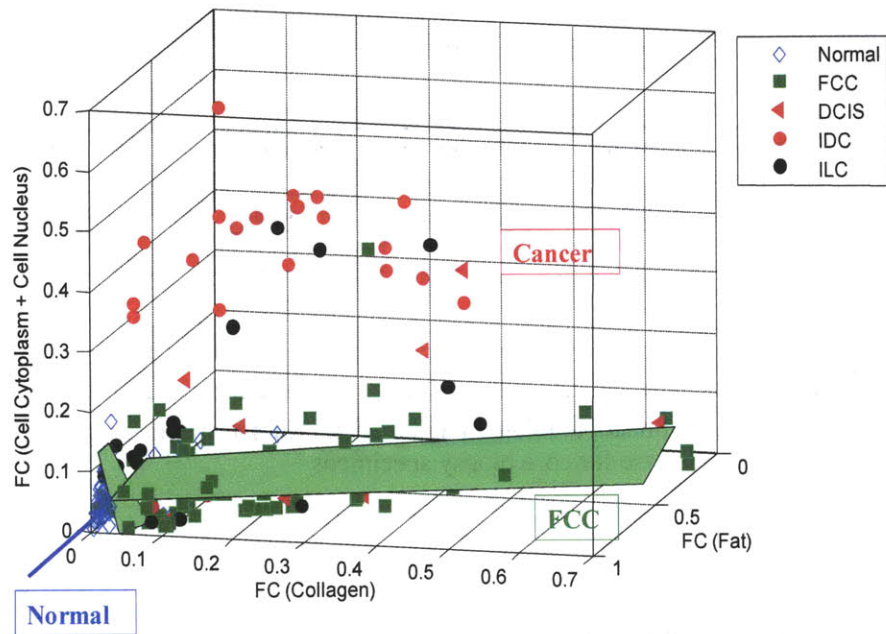
Figure 7.10. 3D Raman diagnostic algorithm applied on excisional biopsy specimens.
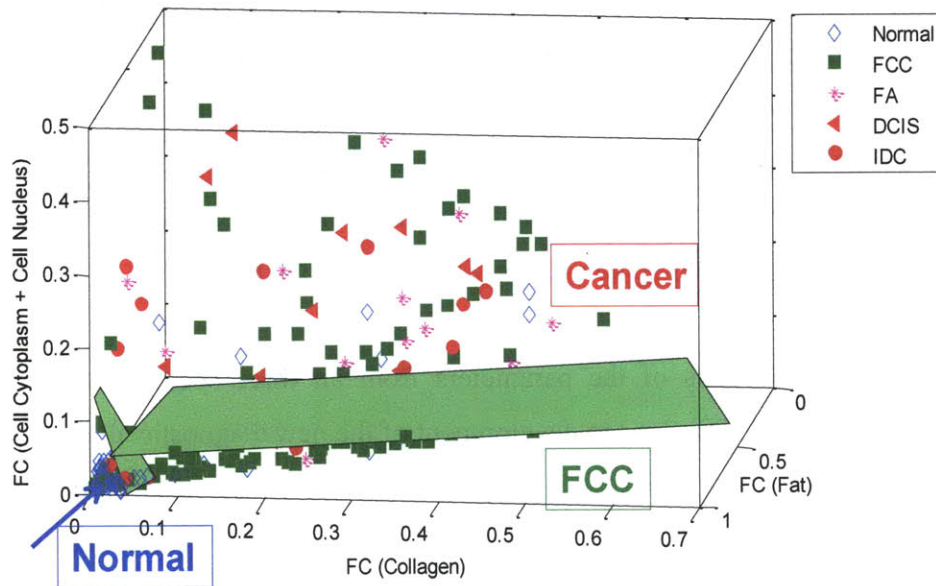

Figure 7.11. 3D Raman diagnostic algorithm applied on needle biopsy specimens.

Table 7.3 and Table 7.4 provide information on the performance of the 3D (three dimensional) Raman algorithm applied on the excisional and needle biopsy specimens, respectively. The sensitivity (malignant lesions vs. non-malignant

lesions), specificity, PPV and NPV were 88%, 92%, 75%, and 97% for excisional biopsy specimens; and 82%, 91%, 41%, and 98% for needle biopsy specimens.

Pathology / Raman	Normal (98 samples)	Fibrocystic Change (91 samples)	Cancer		
			Ductal Carcinoma *In Situ* (8 samples)	Infiltrating Ductal Carcinoma (23 samples)	Infiltrating Lobular carcinoma (21 samples)
Normal	96	0	0	0	0
Fibrocystic Change	0	78	2	1	3
Cancer — Ductal Carcinoma *In Situ*	0	0	6		
Cancer — Infiltrating Ductal Carcinoma	2	13		22	
Cancer — Infiltrating Lobular Carcinoma	0	0			18

Table 7.3. Performance of the 3D Raman diagnostic algorithm on excisional biopsy specimens

Pathology / Raman	Normal (204 samples)	Fibrocystic Change (152 samples)	Cancer	
			Ductal Carcinoma *In Situ* (12 samples)	Infiltrating Ductal Carcinoma (18 samples)
Normal	199	5	0	2
Fibrocystic Change		119	2	3
Cancer — Ductal Carcinoma *In Situ*			10	
Cancer — Infiltrating Ductal Carcinoma	5	28		13

Table 7.4. Performance of the 3D Raman diagnostic algorithm on needle biopsy specimens.

7.5   Discussion

The previously developed Raman diagnostic algorithm were successfully tested on data from excisional biopsy resulting in sensitivity, specificity, overall accuracy, PPV, and NPV of 78%, 98%, 86%, 82%, and 98%, respectively. Note, that the original study on *in vitro* specimens has resulted in sensitivity, specificity, overall accuracy, PPV and NPV of 94%, 96%, 86%, 88%, 98%, respectively. The difference in the performance of the algorithm is a result of the difference in prevalence of malignancy (IDC). In the original study the prevalence was 25% (31/126), while for this study the prevalence was 10% (23/236). Also, as stated above, Raman spectroscopy resulted in the incorrect diagnosis of two IDC sites as normal tissue,

because only a few malignant cells were present in those specimens. The performance of the Raman algorithm on core needle biopsy specimens was not as good, yielding a sensitivity, specificity, overall accuracy, PPV and NPV of 50%, 83%, 68%, 13%, 97%, respectively. The most clinically significant value, NPV, remained virtually unchanged from that obtained in the original study (~97-98%). The difference in performance between the two types of specimens may be related to the fact that the algorithm was developed using excisional biopsy specimens. We first determined whether this difference resulted from the type of material on which the sample was placed (paper in the Petri dish versus aluminum). However, we found that the contribution of the Raman signal arising from the paper was insignificant, and that accounting for this signal did not improve the classification of core biopsy specimens. In addition, we compared the performance of the algorithm on specimens from ultrasound guided biopsy versus stereotactic core needle biopsy. The specimens from stereotactic core needle biopsies were usually bloodier and larger in size because a 9G biopsy needle, rather than the 12G needle used for ultrasound guided biopsy. The performance of the algorithm was approximately the same for both types of core needle biopsy, as 21 FCC sites out of total 90 FCC were incorrectly diagnosed as IDC in the case of stereotactic core needle biopsy, while 24 FCC specimens out of 62 FCC were incorrectly classified as IDC in case of ultrasound core needle biopsy. The DRS/IFS diagnostic algorithm was tested on the same data set.

The need to diagnose additional types of malignant lesions led to the development of a new 3D Raman diagnostic algorithm based on the fit coefficients of fat, collagen and sum of cell cytoplasm and cell nucleus. Note, that the fit coefficients of fat and collagen were used in the original Raman diagnostic algorithm. The diagnostic components makes sense from the anatomy, that cancer cells have larger cell cytoplasm and cell nucleus compare to normal cells. The new algorithm is more powerful due its ability to diagnose two cancerous lesions (DCIS and ILC), in addition to IDC lesions.

7.6   Microcalcification study

7.6.1 *Results of the study*

During data collection from stereotactic core needle biopsy specimens, additional study was performed to investigate the feasibility of Raman spectroscopy to detect microcalcifications. The data set contained 31 calcified sites and 97 non-calcified.

In this study the approximate location of the microcalcifications within the tissue core was determined via comparison with the corresponding radiograph of the specimen. Raman spectra were obtained in several locations of the core: in the approximate location of the targeted microcalcifications, as well as in adjacent non-calcified areas of the same tissue core. The Raman spectra were then analyzed in real time (Chapter 3).
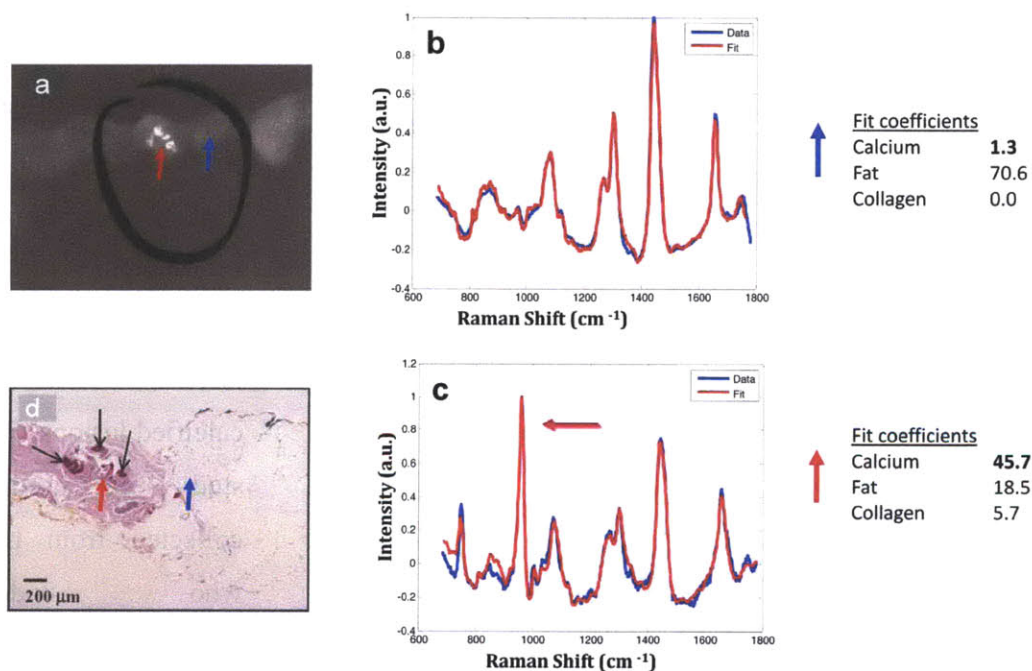
Figure 7.12. a) Specimen radiograph of strereotactic needle biopsy of the breast with microcalcifications (circled); b) Raman spectrum from normal region of the core indicated in blue arrow; c) Raman spectrum from calcified region of the core indicated in red arrow; d) histopathology slide indicating microcalcifications (red arrow) in the area corresponding to the Raman spectrum in Fig. 7.12.c, and fatty tissue in the area corresponding to the spectrum in Fig. 7.12.b.

Real time analysis of Raman spectra allowed to locate the exact position of the microcalcifications within the tissue cores, as illustrated in Fig. 7.12. Figure 7.12a presents a specimen radiograph of a biopsy tissue core that contained microcalcifications (circled). By translating the probe along the biopsy specimen and examining the values of fit coefficients of calcium oxalate dehydrate and calcium hydroxyapatite at various locations, we were able to identify the exact location of the microcalcifications. The difference between Raman spectra acquired from calcified and non-calcified sites can be clearly seen in Fig. 7.12b (non-calcified site) and Fig 7.12c (calcified site). The large contribution of calcium salts (the sum of calcium hydroxyapatite and calcium oxalate) of 45.7% indicates the presence of microcalcifications, which was later confirmed by histopathology, shown in Fig. 7.12d. When the probe was placed on the site indicated with the blue arrow of the core (Fig. 7.12b), the contribution of calcium salts was 1.3%, indicating that it was a non-calcified lesions, later confirmed by histopathology (Fig. 7.12d blue arrow). Similar results were found in [1].
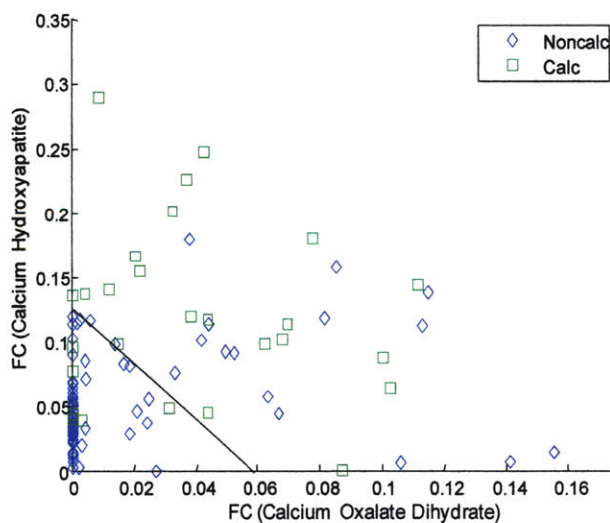
Figure 7.13. Classification of calcified vs. non-calcified lesions. Data from stereotactic core needle biopsy.

Great success with this small study, lead us to another proof-of-principle study: separation calcified lesions from non-calcified lesions. For this study we used data collected from patients who underwent stereotactic core needle biopsy procedure. Overall we acquired data from 97 non-calcified lesions, including 58 normal and 39 FCC lesions; also we collected data from 31 calcified lesions: 29 FCC and 2 fibroadenoma. Fig. 7.13 shows that we are able to distinguish between calcified and

non-calcified lesions using Raman fit coefficients of Calcium oxalate dihydrate and calcium hydroxyapatite. We were able to correctly identify 81% (25/31) calcified lesions 82% (80/97) non-calcified lesions. This is a preliminary result as more data has to be collected in order to see the feasibility of this algorithm. Also, it might be important to create a separate diagnostic algorithm for calcified lesions. However, at the present state it is impossible, as the data set does not have enough data (only 31 calcified lesions) to construct a robust diagnostic algorithm.

7.6.2 *Significance of the microcalcification study*

The ex vivo studies using front-viewing optical fiber probes demonstrate the potential of Raman spectroscopy to detect and precisely localize microcalcifications in breast needle biopsies using real-time spectroscopic feedback. The capability of our spectroscopic system to provide a real time feedback allowed us to perform this study.

7.7 Summary

This study showed the first application of MMS system during *ex vivo* study. The previously developed algorithms were tested during two types of biopsy procedures: excisional biopsy and core needle biopsy. The Raman diagnostic algorithm was successfully tested in a prospective manner for excisional biopsy specimens. However, we observed a smaller contribution of collagen and fat in FCC lesions of the needle biopsy specimens, which resulted in a poorer sensitivity and specificity in this lesions. The DRS/IFS algorithm was also applied to the same two data sets, and we observed a smaller contribution of oxyhemoglobin in malignant cells, thus the algorithm had to be revised to include A parameter in addition to relative concentration of collagen-like. Based on these two parameters all IDC specimens could be correctly classified.

Finally, we developed an algorithm to classify additional types of lesions. A new 3D Raman diagnostic algorithm was constructed. Two fit coefficients, fat and

collagen, were the same as in the original Raman diagnostic algorithm. With the addition of the third component, sum of cell cytoplasm and cell nucleus, we were able to correctly diagnose DCIS and ILC specimens.

Additionally, we studied the feasibility of Raman spectroscopy to indicate location of microcalcifications in the core biopsy specimens. We correlated the presence of microcalcifications with contribution of calcium hydroxyapatite and calcium oxalate dihydrate. This study showed that Raman spectroscopy could be used for guidance of core needle biopsy to correctly target microcalcifications, which will be described in Chapter 9.

7.8 References

1.   Haka, A.S., et al., Identifying Microcalcifications in Benign and Malignant Breast Lesions by Probing Differences in their Chemical Composition Using Raman Spectroscopy. *Cancer Res*, 2002. 62: p. 5375-5380.

CHAPTER 8

New prognostic algorithms

The objective of the study presented in this chapter was to establish the feasibility of using Raman spectroscopy to predict prognosis or outcomes for patients with breast cancer. Raman spectra were measured *ex vivo* from breast tissue specimens obtained from excisional biopsies. As in previous chapters, the extracted spectroscopic parameters were correlated with the histopathology results for the lesions. In addition, the spectroscopic parameters were correlated with conventional clinicopathologic indicators of prognosis and response to therapy, including malignancy grade, and the expression of the estrogen receptors (ER) and the progesterone receptors (PR). Diagnostic algorithms were developed to differentiate among malignancy tumor grade (grade I, II and III) and ER and PR status. The findings of this study are presented in this chapter.

8.1 Motivation

In order to determine the patient's prognosis, pathologists assign a histologic grade to the cancerous breast tumor. Chapter 2 described the Scarff-Bloom-Richardson system that is used to determine malignancy grade. Grade of the malignancy is a significant predictor of patients' survival, as well as the possibility of local recurrence and metastasis, as described in the Table 2.3.

Currently, the American Society of Clinical Oncology guidelines recommend routine testing of all invasive breast cancers for only three tumors markers with established-- albeit modest-- prognostic value, ER, PR and Her 2 neu. ER and PR are ligand-activated transcription factors belonging to the family of nuclear hormone receptors. ER protein is expressed by 50-70 % of invasive breast cancers; PR is less frequently expressed.

In 1975 Rosen et al. [1] first determined the existence of correlations between ER / PR expression and the histopathology of breast carcinoma. The expression of PR is estrogen regulated, thus most PR-positive carcinomas are ER-positive as well. Less than 10% of carcinomas are ER-negative and PR-positive [2]. Patients with ER-positive and PR-positive carcinomas have a longer disease–free survival than women with ER/PR-negative tumors [3]. Estrogen stimulates cell proliferation. In order to block estrogen from binding to estrogen receptors, "antiestrogen" drugs were developed that allow antiestrogens to bind to estrogen receptors. As seen in Chapter 2, Tamoxifen is commonly used to bind to estrogen receptors of breast cells. By interfering with estrogen receptors, tamoxifen blocks the ability of estrogen to stimulate the proliferation of breast cells. The status of the ER is an important predictor of patient's response to hormone therapy in patients with recurrent carcinoma [4, 5]. Patients with ER-positive tumors tend to have a lower recurrence and significantly improved survival rate. Positive expression of estrogen and progesterone receptors indicate and increased likelihood that hormonal therapy will be effective in treating the cancerous tumor.

The motivation of the present study is to explore the potential of Raman spectroscopy to not only diagnose lesions, but also to predict of prognosis and response to therapy. This study

may reveal spectroscopic signatures predictive of clinical outcome that can be used for *in vivo* prediction of clinical outcome, independently of current clinic-pathologic indicators, which are subjective.

8.2   Protocol of the study

A subset of the data acquired during the prior *ex vivo* clinical study of excisional breast biopsies (Chapter 7.1) was used in the present analysis. The details of the data collection protocol are also described in Chapter 7.1. Spectroscopic data acquired from malignant lesions were used to create diagnostic algorithms for distinguishing lesions by tumor grades and the absence or present of estrogen and progesterone receptor expression. Overall 40 malignant lesions were evaluated in the study, including 23 IDC and 17 ILC. A summary of the data set is presented in Table 8.1.

	I	10
Grade	II	20
	III	10
ER	Negative	14
	Positive	26
PR	Negative	26
	Positive	14

Table 8.1. Data set for Raman analysis

In order to distinguish among tumor grades, specific features that are characteristic for each grade must be identified. Grade I represents an early stage of cancer, which is not always caught on time, and stage III tumor represents the latest and most aggressive malignancy. Most women receive treatment before the tumor has progressed to grade III.
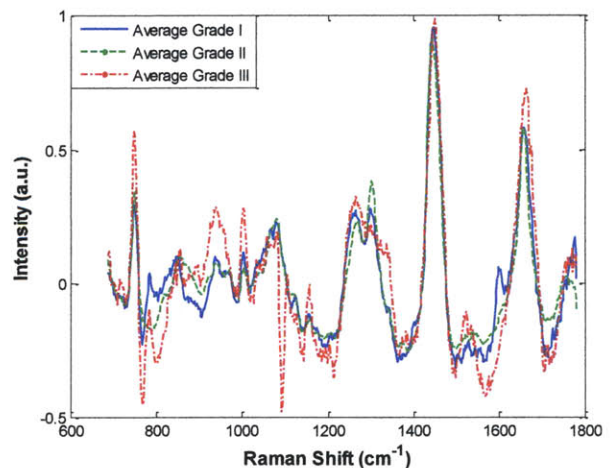

Figure 8.1. Average spectra of tumors with grade I (blue solid), grade II (green, dashed), grade III (red, dashed-point)

8.3   Data analysis

8.3.1   *Tumor grades*

The average spectra for lesions from each tumor grade are depicted in Fig 8.1. The most prominent differences among the average spectra for the various grades were observed in the regions of $750 - 100cm^{-1}$ and $1500 - 1600cm^{-1}$. Spectra from all 40 malignant sites were analyzed using a linear combination of the Raman components previously described in Chapter 3. Spectral differences among comparison groups become more apparent using difference spectra, such as the plots of the residuals we use to assess spectral model fits.

The Raman spectra of all cancers with the same grade were averaged, and difference spectra calculated by subtracting the average spectrum of one group from that of another. The results are shown in Fig. 8.2. There are significant spectral differences at ~750, ~950 and ~1550cm^{-1}.
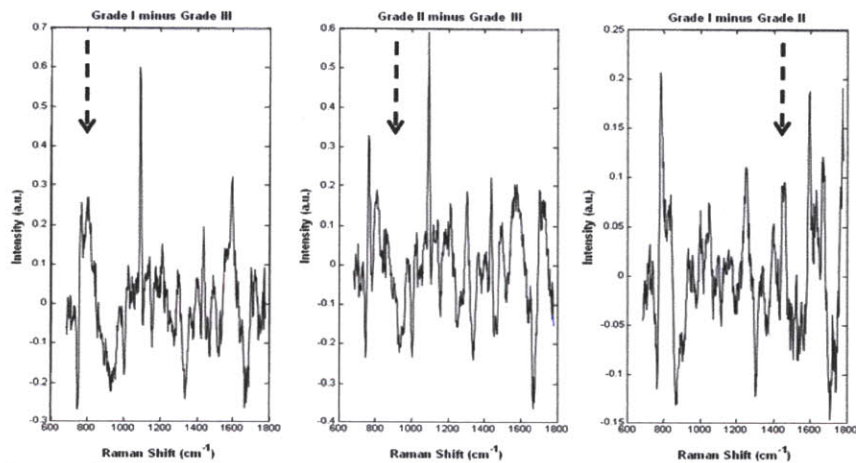

Figure 8.2. Differences between the average spectra of different tumor grades.

Comparison of the differences spectra with our existing chemical and morphologic basis spectra shows that only the basis spectra of epithelial cell nuclei and purified DNA (Fig 8.3.) have prominent bands at ~750 cm^{-1}, suggesting that the spectral differences noted between grade I and grade III cancers in the region may be due to difference in the DNA of the malignant epithelial cells. The origin of the spectral differences noted at ~950 and ~1550 cm^{-1} is less clear, as the basis spectra of several of our Raman components have bands in these regions.

Figure 8.4. shows plots comparing the fit coefficients of all eight basis spectra for each tumor grade. Trends in the fit coefficients for several components are clearly visible among different tumor grades, including for calcium oxalate dehydrate, cholesterol-like, cell cytoplasm, and cell nucleus. Using logistic regression and cross-validation, we found that for this particular data set, fit coefficients of calcium oxalate dehydrate and the

Figure 8.3. Spectra of cellular components. a) DNA, b) cell nucleus, c) actin and d) epithelial cell cytoplasm.

cholesterol-like component are the most diagnostically significant spectroscopic parameters.
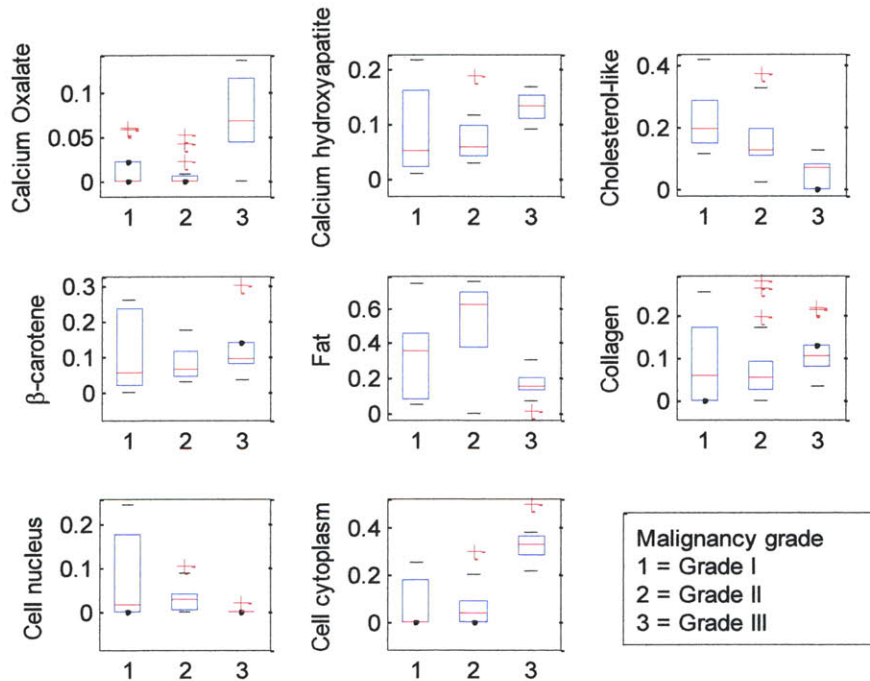
**Figure 8.4.** Boxplot of all fit coefficients for different tumor grades
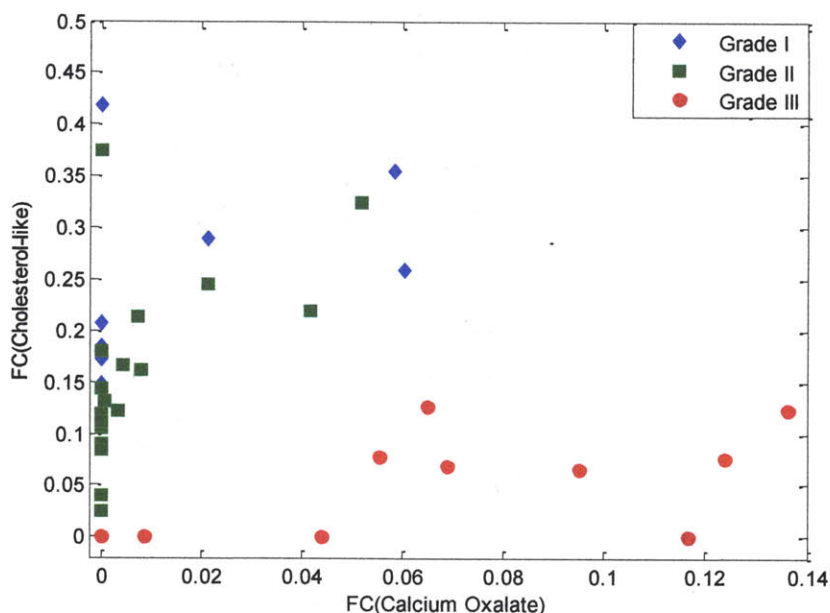
Figure 8.5. Diagnostic Raman algorithm for discriminating among tumor grades

Fig. 8.5. shows the decision plot that separates all grades using these two fit coefficients. All grade III specimens are characterized by a small contribution of the cholesterol-like component and a large contribution of calcium oxalate dehydrate. Grade II specimens tend to have a smaller contribution of cholesterol-like component compared to the grade I. The spectroscopic diagnostic algorithm correctly predicts the tumor grade for 9 out of 10 grade I specimens, 13 out of 20 specimens with grade II, and all 10 grade III specimens.

8.3.2 Biomarker

An analysis procedure similar to that used to distinguish among tumor grades was used to evaluate negative (absence) or positive (presence) ER and PR expression. The most significant differences between positive and negative ER expression were found in the fit coefficients for β-carotene and cell nucleus (Fig. 8.6).
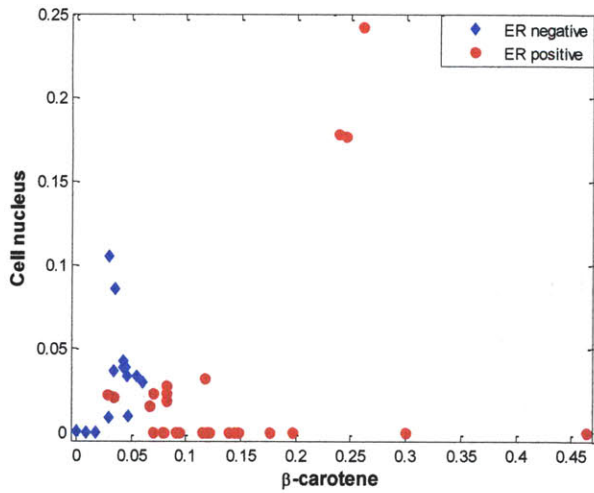
**Figure 8.6.** Decision plot for distinguishing between positive and negative ER statuses
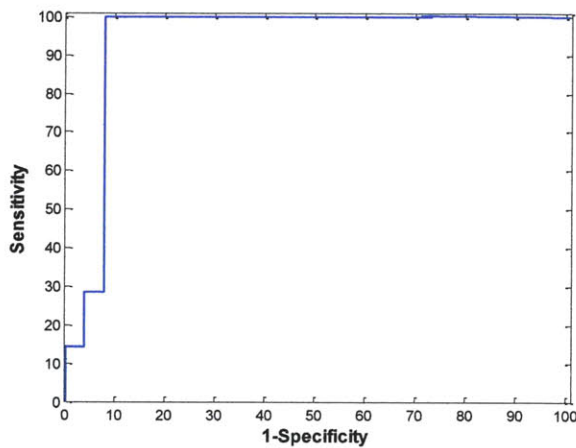
Figure 8.7. ROC curve for ER status

A decision line (y=1.34x-0.0615) based on these two components, correctly separated 38 of the 40 specimens based on their ER status. The ROC curve for this separation is shown in Figure 8.7. A sensitivity of 100% and specificity of 92.3% was achieved in discriminating between ER-positive and ER-negative specimens.

A similar analysis was performed to distinguish between positive and negative PR status.

However, in case of PR the trends among the fit coefficients were not as pronounced as for ER status. The most diagnostically relevant fit components were β-carotene and calcium oxalate dehydrate. The decision line y=4.06x+0.05 separates two clusters, as is shown in Fig. 8.8a. Figure 8.8b depicts the ROC curve for the Raman algorithm
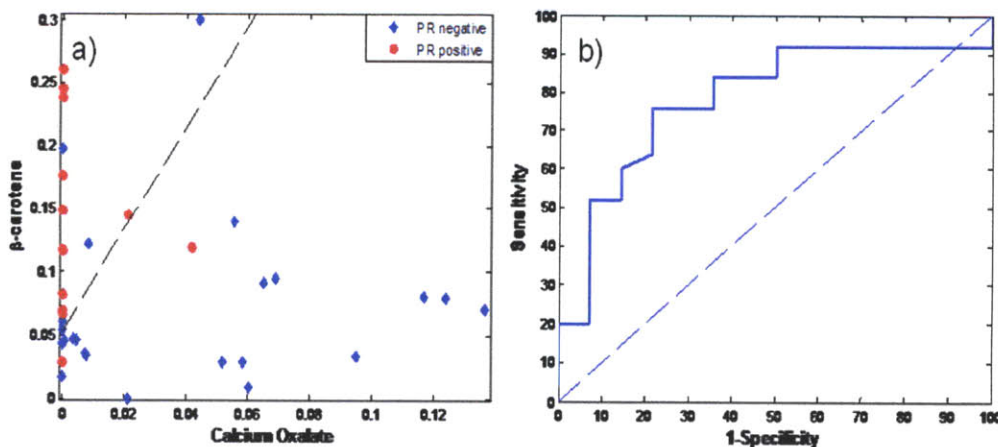
Figure 8.8. a) Diagnostic algorithm for determining PR status; b) ROC curve for PR status

to distinguish between PR positive and negative specimens. A sensitivity of 76% and specificity of 78.6%, was obtained for this separation.

8.4   Significance of the study

This is the first study, to our knowledge, that utilizes Raman spectroscopy to predict tumor grade and status of ER and PR receptors. The results clearly indicate that Raman spectroscopy can potentially contribute to the evaluation of the prognosis and outcome of breast lesions. Additional larger scale studies need to be performed to fully assess use of Raman spectroscopy for this application.

8.5 References

1. Rosen, P.P., et al., Pathological review of breast lesions analyzed for estrogen receptor protein. *Cancer Res*, 1975. **35**(11 Pt 1): p. 3187-94.

2. Lesser, M.L., et al., Estrogen and progesterone receptors in breast carcinoma: correlations with epidemiology and pathology. *Cancer*, 1981. **48**(2): p. 299-309.

3. Clark, G.M. and W.L. McGuire, Steroid receptors and other prognostic factors in primary breast cancer. *Semin Oncol*, 1988. **15**(2 Suppl 1): p. 20-5.

4. Kinne, D.W., et al., Estrogen receptor protein in breast cancer as a predictor of recurrence. *Cancer*, 1981. **47**(10): p. 2364-7.

5. Bezwoda, W.R., et al., The value of estrogen and progesterone receptor determinations in advanced breast cancer. Estrogen receptor level but not progesterone receptor level correlates with response to tamoxifen. *Cancer*, 1991. **68**(4): p. 867-72.

.

CHAPTER 9

Apparatus for guiding core needle biopsy

This chapter describes the design of a side-viewing Raman probe that will be used in the future study of targeting microcalcifications during core needle biopsy. The goal of this project is to design a probe that can be easily incorporated into an ATEC 9 gauge needle device, provided by Hologic company, which is used during stereotactic breast biopsy procedures at the University Hospitals Case Medical Center. In order to design an optimal fiber optic probe, a design strategy was implemented to fully utilize system throughput by characterizing the distribution of Raman signal from tissue. Monte Carlo simulations were used to estimate the interaction of light with tissue. Zemax simulations were carried out to develop the optimal probe geometry to maximize the Raman signal intensity.

9.1 Motivation

It is estimated that more than 1.5 million breast needle biopsies are performed in the U.S. annually [Preventive Services Task Force 2002]. Vacuum-assisted needle biopsy is a safe, reliable alternative for patients who wish to avoid surgical biopsy of suspicious microcalcifications discovered at mammography. Vacuum-assisted breast biopsies for non-palpable lesions, including microcalcifications, are typically done under stereotactic mammographic guidance.

The complete diagnostic work up of mammographically suspect microcalcifications may take days to weeks and include multiple biopsies and extensive pathology evaluation. For the patient, the biopsy and wait for a diagnosis is a traumatic experience both physically and mentally. In a small but significant number of cases the resulting biopsy will be either non-diagnostic or yield false negative results despite all precautions. There is a clinical need for a technology that can provide real-time feedback to the radiologist during stereotactic biopsy and detect microcalcifications in the tissue. Such a clinical tool would have a number of benefits. First, it would enable the radiologist to be better informed when deciding whether the needle should be re-positioned, without the need to wait for a specimen radiograph. Second, it could also minimize the procedure time, and thus the radiation exposure, risk of intra-procedural hemorrhage and patient anxiety/distress. Third, by significantly improving retrieval of microcalcifications, both the number of non-diagnostic/false-negative breast needle biopsies for microcalcifications and the need for follow up surgical biopsy should be reduced. Finally, the number of tissue cores removed would also be reduced because only targeted biopsies would be taken. The tool should be able to interrogate a large volume of breast tissue in a short period of time.

9.1.1 Stereotactic core needle biopsy

In current medical practice, a core needle biopsy is performed under stereotactic mammographic guidance in order to diagnose a non-palpable lesion. During the

stereotactic breast needle biopsy for microcalcifications, small cores of tissue are removed from the breast using a hollow needle, which is precisely guided to the correct location using x-ray mammography and computer-automated stereotaxis. In a vacuum-assisted needle biopsy, the patient lies in the prone position on the biopsy table, with the breast protruding through an opening in the table. The patient and table are elevated and the radiologist positioned underneath the table (Fig 9.1.a) (this figure obtained from Hologic website: www.hologic.com/womens-health/lbs). The skin of the breast is manually incised under local anesthesia and a 9 or 11G needle containing a circular blade (or cutting canula) is advanced to the lesion position as identified by digital spot view mammography.

Accurate 3-D localization of the microcalcifications and placement of the needle requires at least two planar digital spot x-ray views. The Hologic console (also shown in Fig 9.1.a) is necessary to operate biopsy needle device. When suction is applied, the breast tissue is drawn into a side-viewing port in the needle and the blade incises the trapped tissue (Fig 9.1.b). The suction also draws out the incised breast tissue cores, which are passed through the hollow lumen of the needle and into a collection basket. Successive biopsies can be


Figure 9.1. a) Stereotactic Biopsy Procedure using Hologic equipment; b) ATEC 9G needle with biopsy aperture; c) ATEC vacuum-assisted needle biopsy device.

performed over 360° around the axis of the needle without any need to withdraw the needle between biopsies. In the majority of cases, twelve cores of tissue are removed and in some cases, the entire lesion may be excised. However, recent studies have documented the failure of this technique to retrieve microcalcifications in up to 15% of needle biopsies [1]. In these cases, a larger number of digital spot views (sometimes more

than 20) must be taken. This was the case for one of the 19 patients undergoing vacuum-assisted needle biopsy for microcalcifications in our most recent pre-clinical study (Chapter 7 and 8). Upon removal, tissue cores are radiographed to confirm that microcalcifications are present in the tissue to be submitted for microscopic examination by a pathologist. While the radiograph of the specimen is being processed, the needle remains in position in the patient's breast and the patient must remain still in order to keep the needle in place. Additional tissue cores may be removed if microcalcifications are seen in the radiograph of the specimen. This significantly increases procedure time and the risk of biopsy site hemorrhage, which in turn decreases the likelihood of microcalcification retrieval [2]. Failure to retrieve microcalcifications is most common in patients with dense breasts [1]. Therefore, optical techniques such as Raman spectroscopy may have an advantage over conventional x-ray imaging techniques like mammography. A follow-up surgical biopsy is indicated if no microcalcifications are retrieved. If microcalcifications are seen on the radiograph, great care is taken on pathology examination of the needle biopsy to ensure that the breast lesion associated with the microcalcifications is found. Overall, the biopsy procedure takes at least an hour and often lasts much longer. In patients with multiple foci of suspicious microcalcifications, it must be repeated for each focus. At the completion of the procedure, a small metallic clip may be deployed through the needle to mark the biopsy site in case surgery and/or radiation therapy needs to be performed later for invasive cancer.

9.1.2 Microcalcifications

Mammography is currently the standard method for detecting small, non-palpable, highly curable breast cancers [3]. X-ray mammography is a non-invasive procedure that uses x-rays to create images of breast
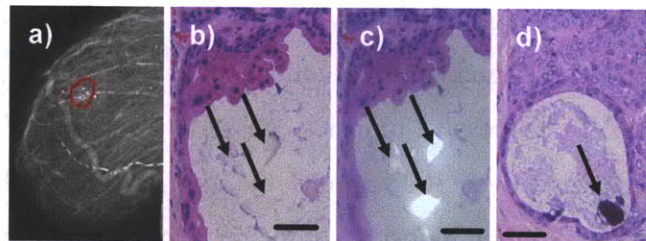
Figure 9.2. Breast microcalcifications. A) In clinical mammogram (circled); b) Type I in duct cyst (arrows; clear crystals; H&E; 40X; 50 micron bar); c) Type I in duct cyst (arrows; birefringence under polarized light; H&E; 40 X; 50 micron bar); d) Type II in DCIS (arrow; basophilic concretion; H&E; 40X; 50 micron bar).

tissue. Microcalcifications are deposits of calcium mineral salts [4]. They strongly absorb x-rays and, thus, have a distinctive (white) appearance on mammography. Microcalcifications geographically target the location of the most clinically significant abnormality within the breast and are a key feature that radiologists look for during mammography [5]. Over 350,000 screening mammograms are performed in the U.S. annually [Breast Cancer Surveillance Consortium], 10% of which are interpreted as abnormal using the Breast Imaging and Reporting and Data (Bi-Rad) System [6] and referred for diagnostic mammography and potentially biopsy [7]. Roughly 10% of all abnormal mammograms are interpreted as such because of the presence of suspicious microcalcifications [8].

Microcalcifications are classified into two types based on their chemical composition and histologic appearance. Type I microcalcifications are composed of calcium oxalate, while type II microcalcifications are composed of calcium phosphates, mainly calcium hydroxyapatite. Type I microcalcifications appear as colorless crystals on light microscopic examination of hematoxylin and eosin (H&E) stained tissue sections and are birefringent under polarized light (see Fig 9.2.b and c) whereas type II microcalcifications appear as basophilic concretions on H&E stained tissue sections and are non-birefringent as shown in Fig 9.2.d.

Microcalcification type appears to correlate with disease state [9]. Type I microcalcifications are seen almost exclusively in benign duct cysts and are rarely found in foci of breast cancer, while type II microcalcifications are most often seen in proliferative lesions, including invasive and *in situ* cancer. This is consistent with the hypothesis that type I microcalcifications (calcium oxalate) are a product of degradation of secretions in the breast ducts, whereas type II microcalcifications (calcium hydroxyapatite) result from cellular degradation or necrosis. Type II microcalcifications occur 2-3 times more frequently than type I [10], and therefore account for the majority of microcalcifications seen on mammography. There is no reliable way to distinguish between type I and type II microcalcifications in a clinical mammogram [11-14]. Therefore, patients with suspicious microcalcifications on mammography must undergo breast biopsy for diagnosis.

9.2 Side-viewing probe design

9.2.1 Why Raman?

Raman spectroscopy is an ideal candidate technology to improve stereotactic core needle biopsy by precisely targeting microcalcifications and providing diagnostically valuable information in real-time. Raman spectroscopy can be obtained in a non-destructive manner via an optical fiber probe that is compatible with needle biopsy devices, such as the ATEC needle. Raman spectroscopy is extremely sensitive to the presence of calcium mineral salts and can thus be used to detect and localize microcalcifications and provide real-time feedback to the radiologist to improve retrieval of microcalcifications during vacuum-assisted stereotactic needle biopsy. Because Raman spectroscopy can be performed in real-time, a large number of tissue sites can be interrogated in a short time span, potentially minimizing the amount of excised tissue.

Calcium salts like calcium oxalate, calcium hydroxyapatite and calcium carbonate, undergo symmetric molecular stretching and thus have large Raman cross sections-- several orders of magnitude larger than those of other breast tissue constituents. They are therefore easily detected and differentiated in breast tissue using Raman spectroscopy. Figure 5.3 shows the distinctive Raman spectra of a type I breast microcalcification (in red), with a prominent C-O symmetric stretching band at 1477cm^{-1} due to calcium oxalate. Type II breast microcalcifications have a prominent phosphate symmetric stretching band at 960cm^{-1} due to calcium hydroxyapatite. The ability to detect calcium mineral salts, and therefore microcalcifications, is a distinct advantage of Raman spectroscopy over other optical spectroscopy
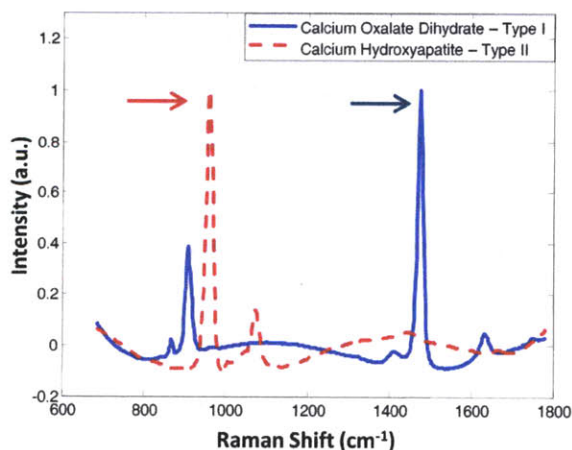
Figure 9.3. Raman spectra of a type I microcalcification (blue), with a prominent band at 1477 cm^{-1} due to calcium oxalate (arrow), and a type II microcalcification (red) with a prominent band at 960 cm^{-1} (arrow) due to calcium hydroxyapatite.

techniques that have been explored in breast, such as diffuse reflectance and fluorescence spectroscopy.

9.2.2 Probe constraints

In order to develop a spectroscopic system that will be used in a clinical setting, the Raman instrument and probe should be optimized to work in conjunction with the Automated Tissue Excision and Collection (ATEC) System (Suros Surgical Systems, Inc., Indianapolis, IN), which is the commercial vacuum-assisted stereotactic needle biopsy system used in the UHC-CMC Breast Center. Because ATEC needle devise has only a side-viewing port in which tissue is pulled by vacuum and subsequently excised, the fiber optic probe has to be able to acquire spectroscopic data from the side of the probe and not from the front of it. That is why, the new probe has to have a side-viewing geometry and still be able to collect good quality of data that will be useful for diagnosis.

In order to develop a system with high sensitivity the following steps were undertaken: 1) the efficiency of each component of the system was determined to maximize Raman collection; 2) the delivery geometry of the excitation beam was chosen to confine the radiance distribution of the Raman signal to a small area at the tissue surface; and 3) the sample damage threshold was considered owing to the focused excitation beam and potential for tissue damage. The optimal collection spot size and collection angle were considered in determining the collection geometry based on conservation of radiance.

9.2.3 Throughput estimation

The conservation of radiance is the optical principle used in designing new optical systems. The conservation of radiance theorem is based on Abbe's sine condition in optical systems and states that the radiance of a source cannot be increased by instrumentation. Therefore the radiance of an image cannot exceed that of the object. Thus, for an optical system the radiance at the output is at most equal to the input radiance

$$n_1 \sin \vartheta_1 h_1 = n_2 \sin \vartheta_2 h_2 \qquad\qquad 9.1$$

where n is the index of refraction, θ is the ray angle with respect to the optical axis, and h is the height of the source, as shown in Figure 9.4.
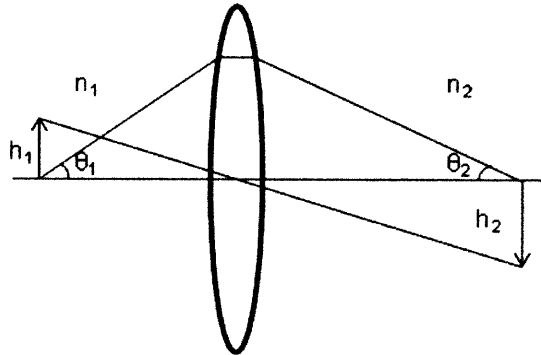

Figure 9.4. Diagram of Abbe's sine condition

From the conservation of radiance theorem we can derive the throughput theorem that states that throughput at the source plane is equal to the throughput at the image plane. The throughput (Θ, *or etendue*) of an optical system is given by the product of its collection area (A) and its solid angle (Ω).

$$\Theta = A_c(r_c)\Omega_c(\theta_c) \qquad\qquad 9.2$$

where r_c is the collection radius, and θ_c is collection angle. The conservation of throughput implies that these two parameters cannot be independently selected, as there is a trade-off between collection area, $A_c(r_c)$, and collection solid angle, $\Omega_c(\theta_c)$.

Diffuse scattering in tissue results in emission of Raman light over an area and solid angle of a particular distribution. Optimization of signal collection requires consideration of two parameters. First, the distribution of the Raman light emerging from the turbid medium (tissue) must be estimated. This distribution defines the potential light-collection efficiency for a given Raman source as the area or angle of collection is varied for particular throughput constraints. Second, the overall throughput of an optical system is determined by the optical element with the lowest throughput. In spectroscopic systems, the spectrograph is often the element of the lowest throughput; therefore we want to use the spectrograph with the highest possible throughput.

The current clinical Raman system has a Holospec f/1.8i, Kaiser Optical Systems spectrograph. Our f/1.8i spectrograph provides a numerical aperture (NA) =0.278 (f/# = 1/2NA). The spectrograph contains an 830 nm notch filter that suppresses the elastically

scattered Rayleigh light and a holographic grating to disperse the Raman scattered light onto a back-illuminated, deep-depletion CCD detector with a 1024x256 array of pixels (PIXIS: 256, Princeton Instruments/Acton, Acton, MA). The pixel size is 26x26 μm, giving a CCD height of 6.7 mm. The height of the array of collection fibers cannot be larger than the height of the CCD, otherwise substantial light loss will occur. Collection fibers that are under consideration are low-OH fibers (AFSH200-2407) with a core diameter 200μm, cladding diameter of 220μm surrounded by the jacket with diameter of 250μm. The product of the number of fibers and their maximum diameter should be less than or equal to 6.7mm. Thus, the maximum number of fibers with core diameter 200μm is 26. Stripping off the jacket would permit a greater number of fibers in the probe, however, the probe would be too fragile for practical use.

The optics in the distal end of the optical fiber probe must also be designed to transform the Raman light for efficient coupling into the collection fibers. The collection fibers must have the same NA as the spectrograph, assuming a 1:1 imaging system. In addition, to optimize signal collection it is necessary to maximize the cross-sectional area of the collection fibers in the distal probe tip. This can be achieved by using a single excitation fiber surrounded by closely-packed rings of collection fibers. As determined above, the maximum number of fibers that can be accommodated by the spectrograph-CCD unit is 26. Moreover, the probe that is under construction will be incorporated into a 9 gauge ATEC needle device, which has an inner diameter of 2.7mm. Thus, at the distal end of the probe, the outer diameter of the optical fiber probe should be less than 2.7mm, thereby limiting the number of fibers.

$$\Theta = A_c(r_c)\Omega_c(\theta_c) = \left(\#_{fibers} \cdot d_{core}^{\ 2} \cdot \frac{\pi}{4} \right) \cdot \left(\pi \cdot NA^2 \right) = \#_{fibers} \cdot \left(\frac{\pi \cdot d_{core}}{2} \cdot NA \right)^2 \qquad 9.3$$

Eq. 9.3 describes the relationship between the number of collection fibers and the throughput of the system. The throughput linearly increases with increasing number of fibers up to 26 fibers. The throughput of the system that uses 26 fibers is 0.187mm^{2}sr. However, according to a Zemax simulation the maximum number of fibers that can be packed in the optical probe with an outer diameter of less than 2.7mm is 15. The

throughput of the system that uses 15 fibers is $0.1079 \text{mm}^2\text{sr}$, thus utilizing 58% of the maximum throughput of the system.

To maximize throughput it is also crucial to select the proper excitation optics. While it is important to match the NA of the collection fibers to that of the spectrograph, it is desirable to choose an excitation fiber of low NA. This is because the intensity of the unwanted Raman background generated in the fibers is proportional to the square of the NA and relatively independent of the core diameter. A smaller NA results in smaller beam divergence at the distal end, which improves the performance of the short-pass filter. Previous studies in our laboratory have shown that fibers of very low NA (<0.12) exhibit substantially increased fiber background associated with the doping material used in the cladding. Thus, an excitation fiber NA of 0.22 is optimal.

Finally, the excitation diameter must be chosen to ensure safe illumination fluence at the tissue while confining the spot size to provide efficient collection of Raman signal. While a tighter focus spot enhances Raman signal collection, it also increases the deposited thermal energy leading to sample damage.

9.3   Optimization with Zemax

We estimated the distribution of Raman light from the tissue in order to determine the optimal collection geometry. The total power of Raman scattered light that can be collected from the tissue can be calculated using the following equation

$$P_{Raman} = \iint_{A,\Omega_s} B(r,\theta) dA d\Omega \approx \int_{A_s=0}^{\infty} B_1(r) dA \int_{\Omega_s=0}^{\pi/2} B_2(r) d\Omega = P_r P_\theta \qquad 9.4$$

where $dA = (2\pi r)dr$, $d\Omega = 2\pi \sin(\theta)d\Omega$, and P_r and P_θ are the integral radial and angular distributions, respectively. It is also assumed that $B(r, \theta)$ is separable.

The excitation radiant power is independent of the collection geometry and is derived as follows:

$$\eta(r_c,\theta_c) \approx \eta_1(r_c) \cdot \eta_2(\theta_c) = \frac{\int\limits_{r=0}^{r_c} rB_1(r)dr}{\int\limits_{r=0}^{\infty} rB_2(r)dr} \cdot \frac{\int\limits_{\theta=0}^{\theta_c} \sin(\theta)B_2(\theta)d\theta}{\int\limits_{\theta=0}^{\pi/2} \sin(\theta)B_2(\theta)d\theta} \qquad 9.5$$

where η_1 and η_2 are radial and angular efficiency, respectively. By using throughput conservation theory we established the relationship between collection angle and radius of the collection spot.
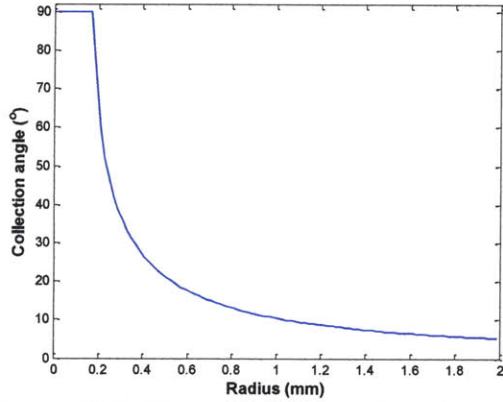
Figure 9.5. The collection angle, Ω, as a function of the radius of the collection spot, r, in an optical system with a throughput of 0.3248mm^{2}sr limited by the throughput of spectrograph-CCD.

Angular efficiency, $\eta_2(\theta)$, can be calculated as a function of radius, Eq 5.6. Thus, a linear array of collection fibers with core diameter 200µm is used as the input slit to the spectrograph. However, if we use the entire slit height that is available, the limiting collection area would be 1.34mm^2, and the limiting collection solid angle for the f/1.8 spectrograph would be 0.2424.

$$\Theta = A_c(r_c)\Omega_c(\theta_c) = \left(\#_{fibers} \cdot d_{core}^2 \cdot \frac{\pi}{4}\right) \cdot \left(\pi \cdot NA^2\right) = \#_{fibers} \cdot \left(\frac{\pi \cdot d_{core}}{2} \cdot NA\right)^2 \qquad 9.6$$

Thus, the throughput of this system is

$$\Theta = A\Omega = 1.34mm^2 \cdot 0.2424\,sr = 0.3248\,mm^2 sr \qquad 9.7$$

As seen from Eq 9.7, the maximum signal intensity can be obtained represents a trade-off between the collection area and the collection angle. Thus, the collection angle within the system throughput can be calculated: $\Omega = 0.3248/A$. The collection angle cannot be greater than $90°$, therefore the throughput is not conserved when a collection spot radius is less than 0.17mm due to the geometric constraint as shown in Fig. 9.5. The data is then integrated and normalized to determine angular collection efficiency, η_2, depicted in Fig. 9.6.
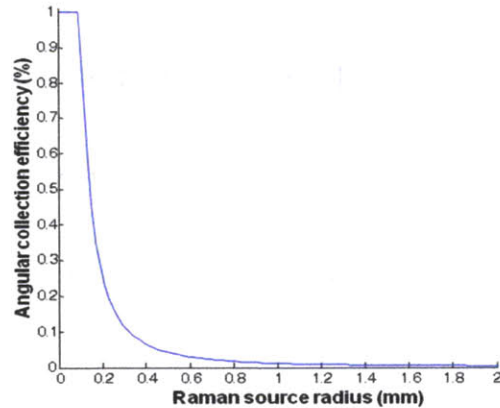
Figure 9.6. The angular collection efficiency
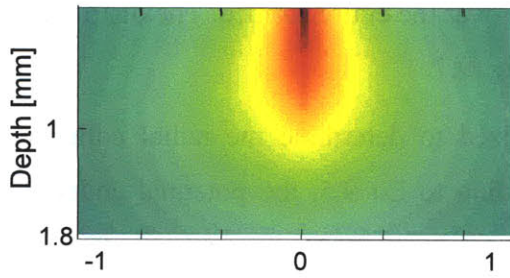
9.3.1 Monte Carlo simulations
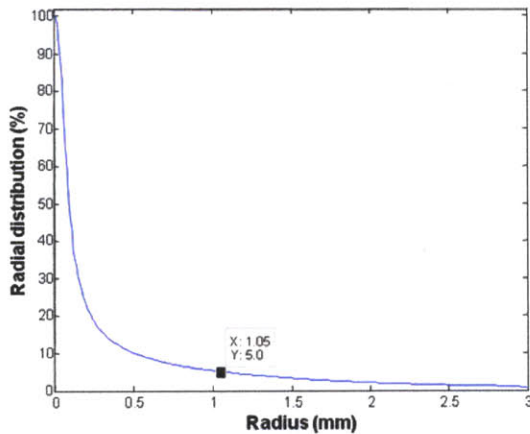
Figure 9.7. Radial distribution of Raman signal from tissue

It is crucial to understand the effect of scattering and absorption in breast tissue in order to study the generation of the Raman signal inside the sample and its distribution and intensity at the surface. Monte Carlo simulations were used to model Raman scattering light in turbid media.

As discussed in Chapter 3, light propagation in tissue is subject to elastic scattering and absorption of photons in the tissue. Tissue is characterized by several optical properties, including absorption coefficient, μ_a, scattering coefficient, μ_s, and the anisotropy factor, g. The Monte Carlo simulation method is a probabilistic model for photon propagation. The accuracy of a simulation result from Monte Carlo depends on the probability density function. A large number of photons are necessary to correctly simulate the distribution of light.

Figure 9.8. Monte Carlo simulation of side-viewing Raman probe sampling volume

The sampling volume is difficult to measure experimentally, thus Monte Carlo modeling was implemented to obtain a good approximation of depth of penetration. The Monte Carlo simulation depicted in Fig. 9.8 provides an estimate of the depth penetration profile of 830 nm light in breast tissue. The sampling depth, δ_s, can be defined as:
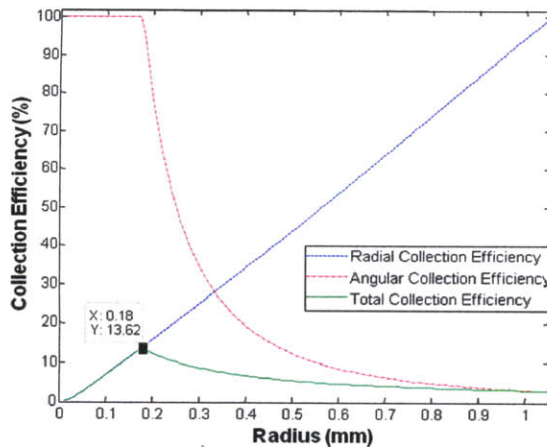
$$\frac{1}{\delta_s} = \frac{1}{\delta_{ex}} + \frac{1}{\delta_{em}}, \text{ and } \delta = \frac{1}{\sqrt{3\mu_a(\mu_a + \mu_{s'})}}$$

9.8

where δ_{ex} and δ_{em} are the penetration depth of the excitation and emission light, respectively. Using this equation, it was estimated that the sampling depth for our current prototype Raman probe is 1.27mm.
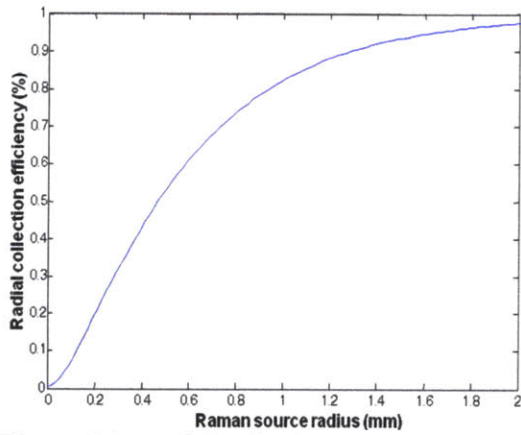
Figure 9.9. Radial collection efficiency of Raman signal

The Monte Carlo simulation was performed with the following parameters: 1) the geometry of the sample was a semi-infinite medium; 2) the excitation beam was a 200µm collimated beam with Gaussian profile; 3) parameters of normal breast tissue were used: $\mu_a = 0.05\text{cm}^{-1}$, $\mu_s = 90\text{cm}^{-1}$, and g=0.9 [15]; and 4) one million photons were used for the simulation.

Light emitted from tissue has a Lambertion distribution. The geometry was assumed to be independent of the azimuthal angle, thus measuring the spatial distribution from a single scan

Figure 9.10. Potential probe collection efficiency

was sufficient enough to describe the distribution over the entire surface. The distribution of the Raman signal on the surface is plotted in Fig. 9.7.

The data is then integrated and normalized to determine the radial collection efficiency $\eta_1(r)$ depicted in the Fig. 9.9. According to Eq 9.5, the potential collection efficiency, η, was determined by the product of $\eta_1(r)$ and $\eta_2(r(\theta))$. The optimal efficiency of 13.6% occurs at a collection radius of 1.05mm and a corresponding 90° angle. According to Fig. 9.10, it is desirable to collect the full angular range of Raman light from the most intense area of illumination, rather than collecting a smaller range of angles while radially expanding to the weaker tails in the edge of the distribution

The throughput of the system is subsequently reduced from 0.3248mm^{2}sr to 0.1079mm^{2}sr due to the restriction of the number of fibers to fit within the allotted diameter and the dead space between the fibers caused by the cladding and jackets. The reduced throughput results in a potential collection efficiency of 7.82% as shown in Figure 9.11.
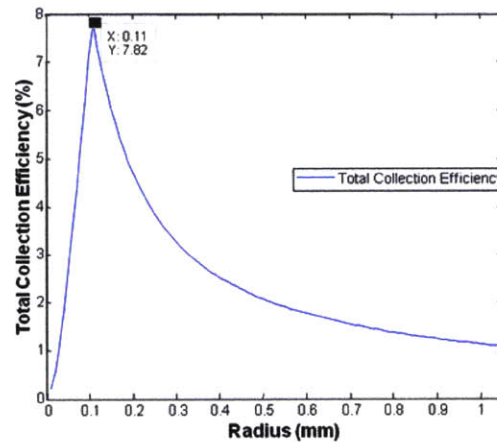

**Figure 9.11.** Potential total collection efficiency of the probe.

9.3.2 Half ball lens design

In order to apply our Raman spectroscopic technique in real time in the clinical setting during stereotactic core needle biopsy, we have designed and fabricated a prototype side-viewing probe that is capable of delivering and collecting light from the tissue in a lateral geometry as required by the commercial vacuum-assisted needle biopsy systems. A photograph of the side-viewing probe inserted into the biopsy aperture of a 9G ATEC vacuum-assisted biopsy needle is shown in Fig. 9.12. As shown in the figure, we can place our probe inside the needle and align the side-viewing window of the probe with the side-viewing biopsy aperture of the needle. A schematic diagram of the probe is depicted in Fig. 9.13.

Our designed side-viewing probe has an outer diameter of 2.4 mm, with one central delivery fiber and 9 surrounding collection fibers [16]. The distal tip of the probe is terminated by a half-ball lens mounted on a 45° mirror, to direct the excitation light (shown in orange) laterally through a sapphire window. The half-ball lens also greatly improves collection efficiency, which is critically important for Raman spectroscopy where the signals of interest are weak. The side-viewing probe has the same set of filters as the front-viewing probe.
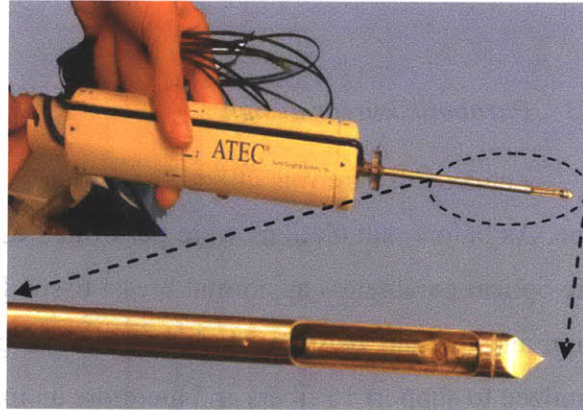
Figure 9.12. Side-viewing Raman probe inside biopsy aperture of 9G ATEC biopsy needle. Half ball lens design
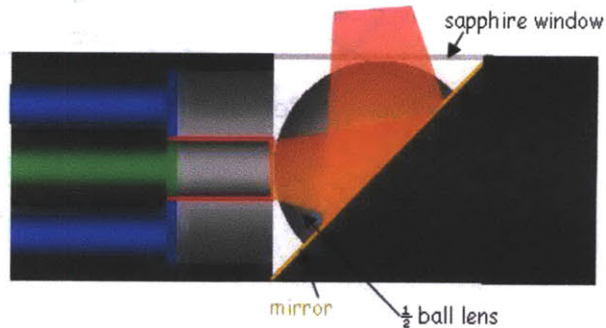
Figure 9.13. Schematic of the side-viewing Raman probe with a half ball lens design

9.3.2.1 Collection efficiency and probe manufacturing

The prototype was recently been successfully tested in surgically excised breast tissue, see Chapter 5.5, but has not yet been implemented in a clinical setting. This probe has identical collection capabilities to a similarly designed front-viewing probe, with collection efficiencies of 3.5% and 1.7% for air and tissue interfaces, respectively. Even though this probe was not optimized to work with the ATEC 9 gauge needle, it can easily fit inside it as demonstrated in Fig. 9.12. However, it is unknown if this probe design will support a stainless sheath of 55cm that is necessary to add to the probe to ensure proper alignment of the probe with respect to the needle and good connection between the probe and breast tissue in anticipated *in vivo* clinical studies. This probe design can be manufactured in-house at the G.R. Harrison Spectroscopy Laboratory, while all other designs given in this chapter must be manufactured elsewhere, providing additional complexity to the process of moving this project to the clinic.

9.3.3 Parabolic mirror design

Zemax software was utilized to further improve the efficiency of the side-viewing probe. As before, simulations were performed using a semi-infinite medium that has the same optical parameters as normal breast tissue [15]. The largest difference between this design and the half ball lens design is that the geometry of the side-viewing piece was optimized to support 15 fibers and therefore an increase in Raman signal.

15 collection around 1 excitation
fiber core diameter: 0.2 mm
filter size: 0.5 mm, 1.9 mm
parabolic mirror: r=2mm
f-silica block: d=2mm, l=2.5mm
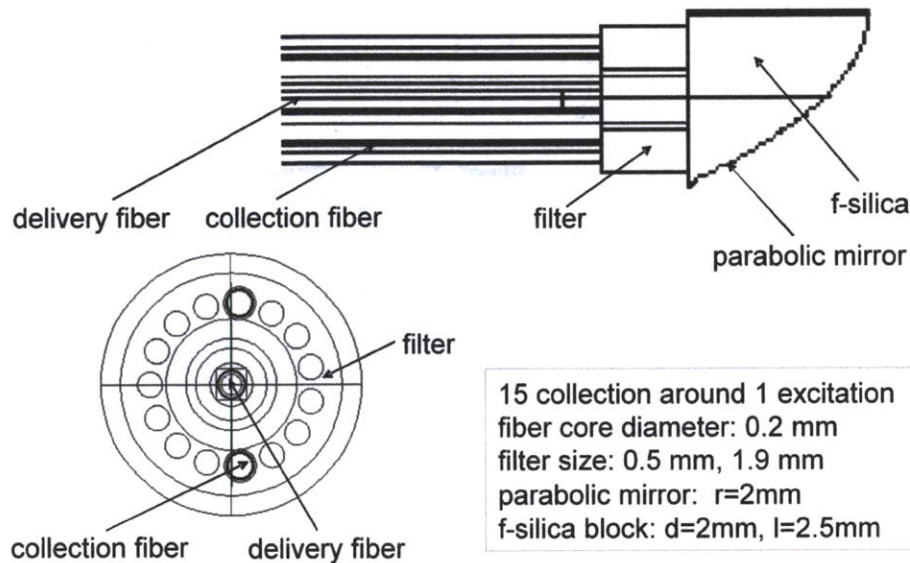
Figure 9.14. Side-viewing Raman probe design with solid-state, gold-coated parabolic mirror.

This new probe design has solid state imaging optics and has several advantages over the current prototype design which improve collection efficiency. The new design (Fig. 9.14) has an outer diameter of 2.4 mm, which is the maximum allowed by the inner diameter of the ATEC needle. The distal tip now terminates in a gold-coated parabolic mirror etched on a sapphire or fused silica block, which Zemax ray tracing (Fig. 9.15) revealed to be the geometry with maximal collection efficiency. This has several advantages. First, it makes use of imaging optics, which has inherently higher collection efficiency than the non-imaging optics used in the prototype probe. Second, it has a solid state design. This eliminates air space between the optical components and thus the need for the sapphire window, which (due to fabrication constraints) extended laterally beyond the fiber bundle. This unwanted feature added 200-300 um to the probe outer diameter

and thus limited the number of fibers that could be accommodated within the allowable probe outer diameter. Zemax simulations
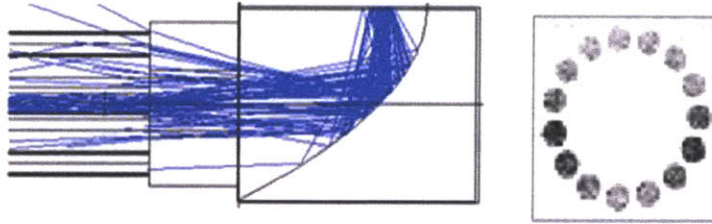
Figure 9.15. Zemax simulation of light collection of Raman probe with gold-coated parabolic mirror.

show that, using solid state optics, we can now accommodate 15 (rather than 9) collection fibers surrounding the excitation fiber, which further improves collection efficiency. Overall, the collection efficiency of this second probe design utilizing the parabolic mirror etched into a solid sapphire or fused silica block is 4.7% for the Raman distribution source discussed above, a factor of 3 improvement over that of the current prototype Raman probe.

This second probe design is more efficient than the probe with the half ball lens design and will be optimal for usage in clinical studies. However, due to its small size, the gold-coated parabolic mirror will be challenging to manufacture. In fact, a number of manufacturing companies have been contacted and none of them can manufacture the small parabolic piece. Therefore, we have worked on another design that should be easier to implement than the parabolic mirror design while still remaining more efficient than the half ball lens design.

9.3.4 Three-cut design

In the three-cut design, the distal tip of the probe terminates in a half ball lens similar to that in the first prototype, but the lens is now mounted on a sapphire or fused silica block, the distal surface of which is cut at several angles optimized using Zemax simulations, see Fig. 9.16.

This design will result in a collection
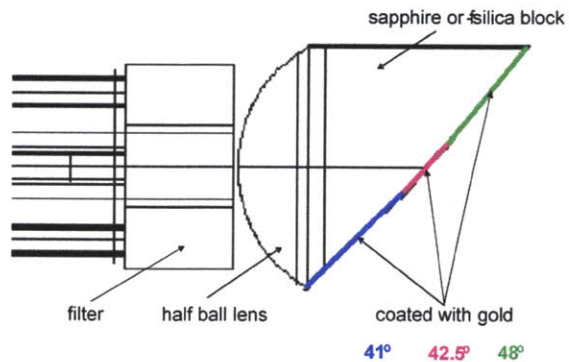
Figure 9.16. Schematic of Side-viewing Raman probe design with the three-cut design.

efficiency of 2.2%, a 30% improvement over that of the half ball lens Raman probe.

9.4   Side-viewing probe and ATEC needle

As was discussed in the beginning of the chapter, the final goal of this part of the project is to be able to provide diagnostic information about tissue composition in real-time during core needle biopsy by acquiring Raman data. In order to do so, one has to adopt Raman side-viewing probe to the currently used vacuum-assisted biopsy needle. ATEC biopsy devices manufactured by Hologic company were used in this study, because these devices are exclusively used at University Hospitals of Cleveland (our clinical collaborators) on a daily basis.

9.4.1   *Adaptor*
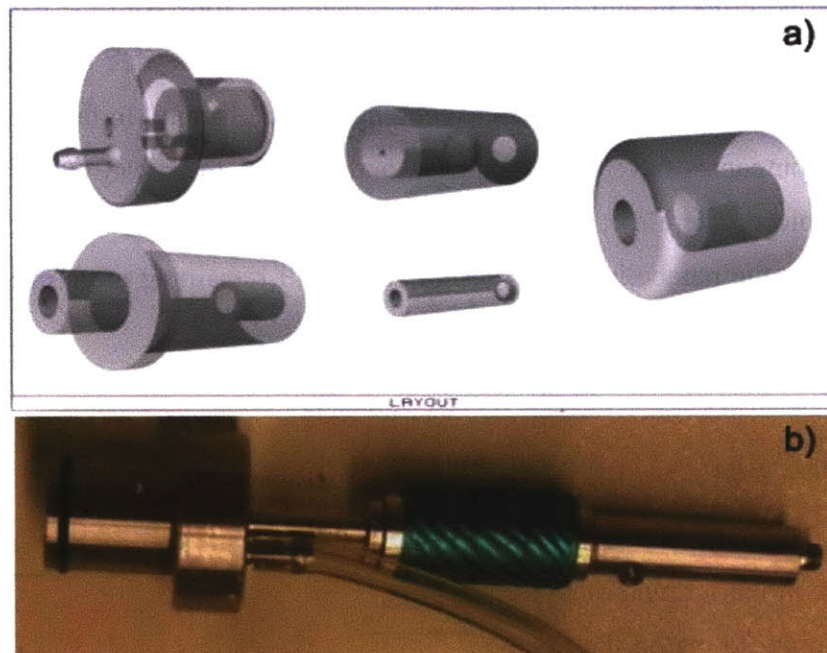
Figure 9.17. Adapter for the ATEC biopsy needle. a) Layout; b) Photo of the final version of the adapter.

The primary need for an adaptor is threefold. We need to be able to: 1) secure the Raman probe to the ATEC needle; 2) withdraw the probe throughout the side-viewing port of the needle in a very controlled manner; 3) provide vacuum and saline flush with the probe in place within the needle.

A standard ATEC 9-gauge needle has a side-viewing port of 20mm, while a side-viewing probe can acquire Raman spectrum from a 1mm^2 area. Thus, the Raman probe has to be withdrawn from the needle in 1mm increments along the length of the 20mm port in order to cover the entire area (and volume) of the biopsy cores. Figure 9.17a depicts a schematic of parts of the adapter, while Figure 9.17b shows the final version of the adapter. All parts of the adapter are made of stainless steel (#316), which is necessary for medical devices. The adapter was designed using emachineshop software.

Figure 9.18a-b shows the configuration of ATEC needle, the tissue collector and adapter that connects the needle and the tissue collector. Fig. 9.18c shows two ports of the adapter, where one is used to place a probe and another one is used to apply a vacuum, which is necessary for biopsy. Fig 9.18d-e shows the Raman side-viewing probe inside the ATEC needle. The adapter allows the user to withdraw the probe in 1mm increments without rotating the probe. When the needle is rotated during the biopsy procedure, the probe will rotate simultaneously with the needle, as it is secured by the adapter.
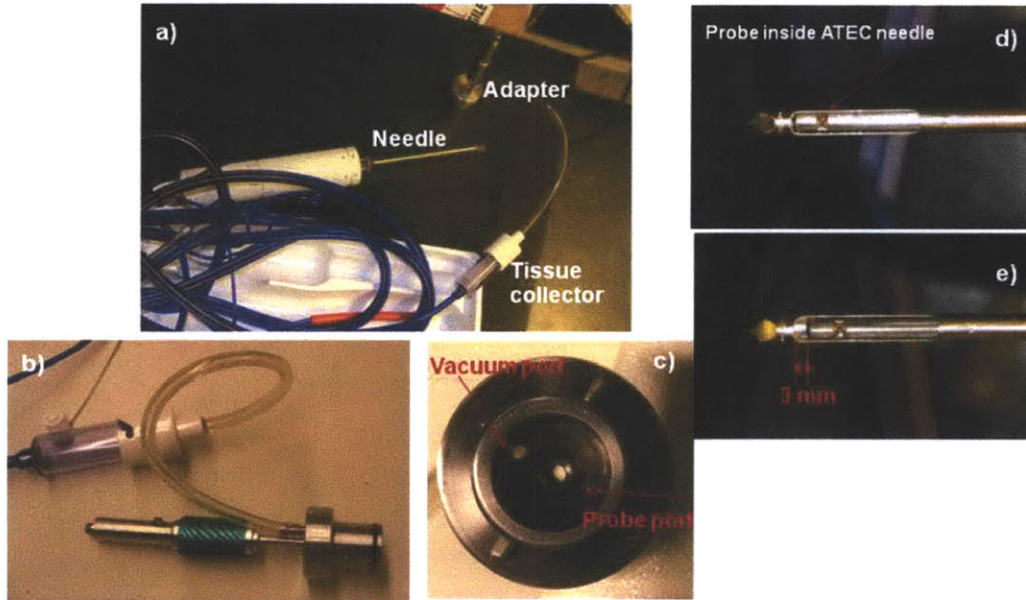

Figure 9.18. a) Combining ATEC needle, adapter and a tissue collector; b) Detailed view of adapter connected to tissue collector; c) end-view of the adapter; d) side-viewing probe at the tip of the needle; e) side-viewing probe is moved by 3mm inside the aperture.

Using Suros console we were able to apply a vacuum while the probe was placed inside the ATEC needle and secured using the adapter. This is a necessity to make sure the proper prober/tissue contact. Due to the fact that central port of the adapter is used for probe placement, the vacuum port is off centered. The tissue collector is connected to the vacuum port (Fig 9.18b). The adapter and the probe have to be removed from the needle prior of removing biopsy cores. The adapter has to be further modified to allow collection of cores without detaching the adapter.

9.4.2   Side-viewing probe

Due to the difficulties of manufacturing the parabolic mirror, the half ball lens design (Section 9.3.2) was chosen for the second-generation version of the Raman side-viewing probe. The second-generation probe has approximately 50cm of rigid stainless steel tubing that is 20µm smaller than the inner diameter of the cutting tube of the ATEC needle. That allows enough space to apply a vacuum.
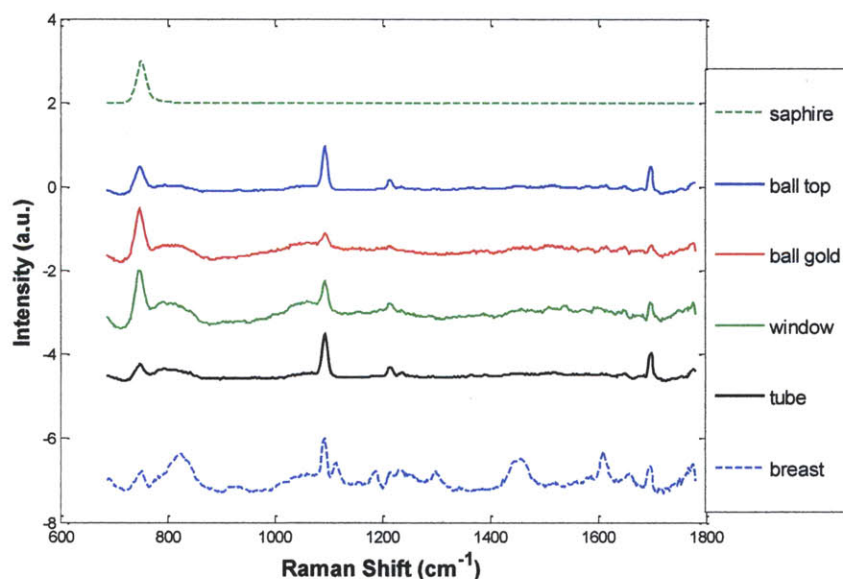
Figure 9.19. Raman spectra of sapphire components of the side-viewing probe

The probe has a sapphire half ball lens, a sapphire tube that is used to facilitate the probe's manufacturing, and a sapphire side-viewing window that is used for index matching that preventing contact between optical parts of the probe and blood or tissue. Figure 9.19 illustrates Raman spectra of all sapphire parts used in the probe. The top
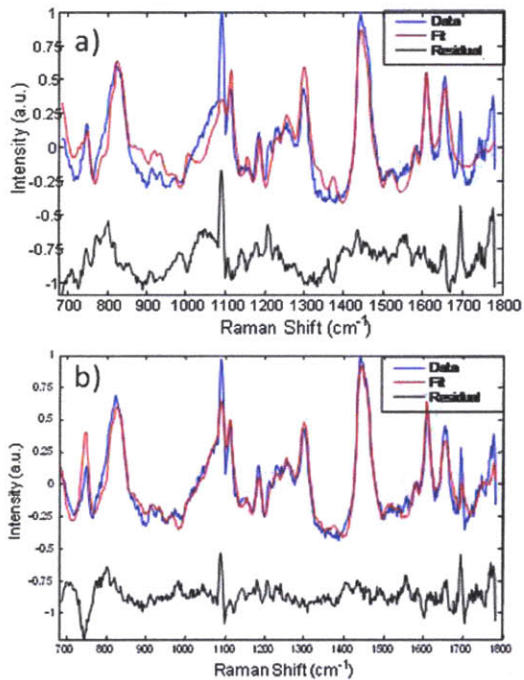


Figure 9.20. Raman spectra and fit using a) pure sapphire spectrum; b) spectrum of sapphire side-viewing window

spectrum is that of the pure sapphire that was used in the model for fitting data collected from breast specimens, see Chapter 3. The next four plots are the Raman spectra of actual components used in the probe. The flat side of the half ball lens has a gold coating. Data was acquired from the sapphire side of the ball lens ("ball top") and from the gold side of the ball lens ("ball gold"). These spectra have additional Raman features that are not seen in the pure sapphire spectrum. In order to fit data acquired by the side-viewing probe ("breast" spectrum), we have to include the spectrum of the side-viewing window

into the model, as this spectrum has the most Raman features out of all sapphire components in the probe. Figure 9.20 shows a side-by-side comparison of fits to the data using: a) pure sapphire; and b) sapphire used in the side-viewing window; for fitting Raman data. Fitting the data with the sapphire spectrum of the side-viewing window results in the least amount of structure in the residual spectrum .The difference between these two sapphire spectra is still under study. Impurities in the material used in the side-viewing window could be the source of the additional Raman peaks.

9.5 *Ex vivo* study with side-viewing probe

An *in vitro* proof-of-principle study has been conducted, in which spectra were collected for the first time through a biopsy needle, using our second generation side-viewing Raman probe, from frozen-thawed normal breast tissues obtained from a breast reduction specimen (Fig. 9.21). A 9-gauge ATEC vacuum-assisted biopsy needle was inserted into the breast tissue, and then the side-viewing Raman probe was inserted into
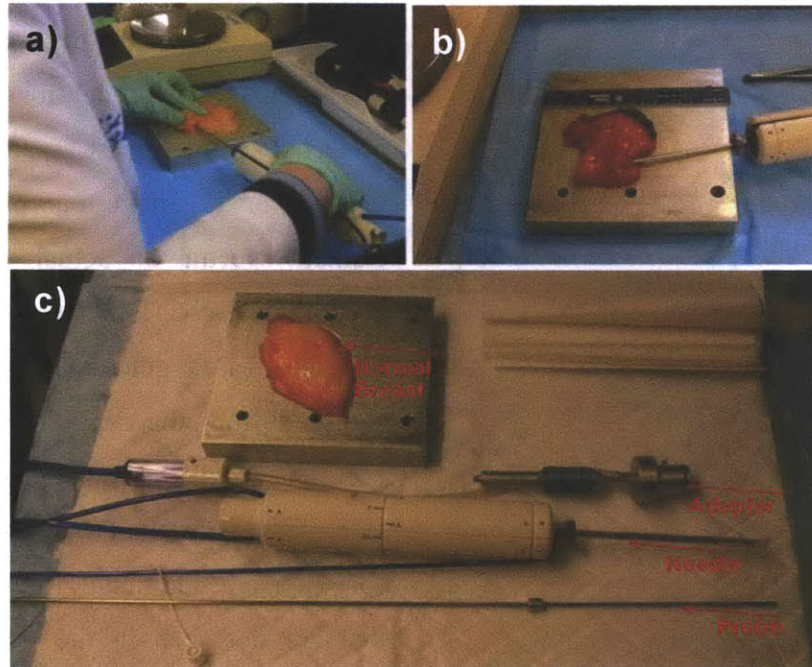
Figure 9.21. *Ex vivo* study. a) ATEC needle is inserted into a breast specimen; b) The probe is inserted into ATEC needle, and needle is placed inside breast tissue in order to acquire Raman spectra; c) adapter, side-viewing probe and needle used in the study

the needle until it made contact with the breast tissue in the biopsy aperture. Raman spectra with excellent SNR were obtained from the breast tissue in 0.5s without application of a vacuum (Fig. 9.21b). The probe was moved throughout the length of the needle's aperture in 1mm increments in order to collect Raman spectra over the entire length of the tissue core. Finally, the Raman diagnostic algorithm developed using the front-viewing probe was applied to these data, Fig. 9.22. All of the breast samples were
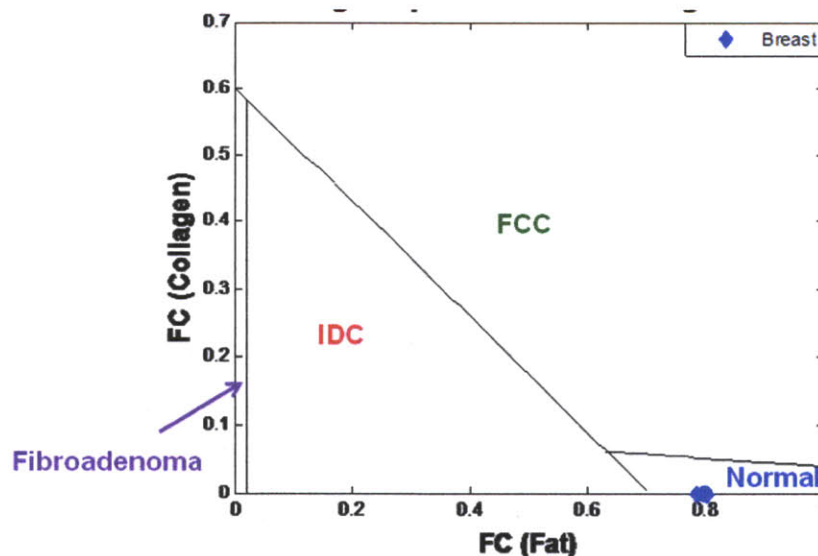
Figure 9.22. Side-viewing probe experiment: breast lesion diagnosis using Raman algorithm.

correctly diagnosed as normal tissue. This indicates that the fitting procedure and the diagnostic algorithm designed for data collected via the front-viewing probe may be able to be used in future studies with the side-viewing probe.

9.6 Summary

Two potential Raman side-viewing probe designs have been developed based on Zemax and Monte Carlo simulations. We have developed both instrumentation and data analysis techniques for the clinical application of Raman spectroscopy for the diagnosis of breast disease. The *ex vivo* study using one of the side-viewing optical fiber probes (first design) demonstrated that it is feasible to collect Raman spectra of high S/N in a clinically-relevant time frame through the biopsy aperture of a commercial vacuum-assisted needle biopsy device. A previously developed Raman diagnostic algorithm for a front-viewing Raman probe was successfully applied to data acquired using the side-viewing probe. These are important capabilities in developing Raman spectroscopy as a clinical tool to provide real-time feedback to the radiologist to improve retrieval of microcalcifications during stereotactic biopsy procedures. The ability to identify and localize microcalcifications as the optical fiber probe is scanned (pulled back) along the biopsy aperture in the stereotactic biopsy needle, and obtain information on the type of microcalcification and breast lesion associated with the microcalcification, will allow the radiologist to make better informed decisions as to whether to biopsy and how many biopsy tissue cores to remove at a particular needle location. This should result in improved retrieval of microcalcifications during stereotactic needle biopsies.

9.7   References

1.   Jackman, R.J. and J. Rodriguez-Soto, Breast microcalcifications: retrieval failure at prone stereotactic core and vacuum breast biopsy--frequency, causes, and outcome. *Radiology*, 2006. **239**(1): p. 61-70.

2.   Burbank, F., Stereotactic breast biopsy: comparison of 14- and 11-gauge Mammotome probe performance and complication rates. *Am Surg*, 1997. **63**(11): p. 988-95.

3.   Rim, A. and M. Chellman-Jeffers, Trends in breast cancer screening and diagnosis. *Cleve Clin J Med*, 2008. **75 Suppl 1**: p. S2-9.

4.   Guinebretiere, J.M., et al., Use of radiology for the pathologist in the management of breast lesions. *Eur J Radiol*, 2005. **54**(1): p. 15-25.

5.   Johnson, J.M., et al., Histological correlation of microcalcifications in breast biopsy specimens. *Arch Surg*, 1999. **134**(7): p. 712-5; discussion 715-6.

6.   Burnside, E.S., et al., Use of microcalcification descriptors in BI-RADS 4th edition to stratify risk of malignancy. *Radiology*, 2007. **242**(2): p. 388-95.

7.   Sohlich, R.E., et al., Interpreting data from audits when screening and diagnostic mammography outcomes are combined. *AJR Am J Roentgenol*, 2002. **178**(3): p. 681-6.

8.   Freer, T.W. and M.J. Ulissey, Screening mammography with computer-aided detection: prospective study of 12,860 patients in a community breast center. *Radiology*, 2001. **220**(3): p. 781-6.

9.   Radi, M.J., Calcium oxalate crystals in breast biopsies. An overlooked form of microcalcification associated with benign breast disease. *Arch Pathol Lab Med*, 1989. **113**(12): p. 1367-9.

10.   Rosen, P., *Breast Pathology*. 1997, Philadelphia, PA: Lippincott-Raven.

11.   Sato, M., et al., Accuracy in estimating tumor extension according to mammographic subtypes in patients with ductal carcinoma in situ. *Jpn J Clin Oncol*, 2002. **32**(5): p. 157-61.

12.   Hermann, G., et al., Mammographic pattern of microcalcifications in the preoperative diagnosis of comedo ductal carcinoma in situ: histopathologic correlation. *Can Assoc Radiol J*, 1999. **50**(4): p. 235-40.

13.   Dinkel, H.P., A.M. Gassel, and A. Tschammler, Is the appearance of microcalcifications on mammography useful in predicting histological grade of malignancy in ductal cancer in situ? *Br J Radiol*, 2000. **73**(873): p. 938-44.

14.   Lee, C.H., et al., Follow-up of breast lesions diagnosed as benign with stereotactic core-needle biopsy: frequency of mammographic change and false-negative rate. *Radiology*, 1999. **212**(1): p. 189-94.

15.   Tromberg, B.J., et al., Non-invasive in vivo characterization of breast tumors using photon migration spectroscopy. *Neoplasia*, 2000. **2**(1-2): p. 26-40.

16.   Motz, J.T., *Development of in vivo Raman spectroscopy of atherosclerosis*, in *HST*. 2003, MIT: Cambridge.

CHAPTER 10

Accomplishments and future directions

The first part of this chapter, we summarize the accomplishments of the work presented in this thesis and critically discuss the strengths and weaknesses of the spectroscopic techniques. In the second part of the chapter, we discuss potential future directions for the breast project.

10.1 Accomplishments of the thesis

10.1.1 Development of a DRS/IFS diagnostic algorithm

The diagnostic potential of a combined approach utilizing DRS and IFS was shown via a pilot *ex vivo* study. Physical parameters extracted from these spectroscopic modalities were used to develop a step-wise algorithm for distinguishing among breast tissue diagnosed as either normal, fibroadenoma, FCC, or IDC by histopathology. Raman spectra were collected from the same location on the tissue using a second instrument; therefore, we were able to assess the diagnostic potential of MMS – a combination of all three modalities. The diagnostic algorithm based on DRS/IFS successfully distinguished malignant from non-malignant lesions, as well as benign lesions (FCC and fibroadenoma) from normal tissue. The results of the study demonstrated a sensitivity, specificity, PPV, NPV, and total efficiency of 100%, 96%, 69%, 100% and 91%, respectively. By combining Raman with DRS/IFS, we were able to correctly diagnose 4 normal sites previously misdiagnosed by the algorithm based on DRS/IFS, and improve the overall accuracy to 92%. The promising results from this study supported the further development of an integrated MMS probe and instrument to rigorously evaluate the MMS approach.

10.1.2 Prospective application of the Raman and DRS/IFS diagnostic algorithms

A Raman diagnostic algorithm which was previously developed was prospectively validated on a large data set from two subsequent *ex vivo* studies. The NPV, the most clinically important value, remained ~98% in all studies. The sensitivity and specificity decreased slightly in the present study, which is likely due to differences in the disease prevalence and disease spectrum. To our knowledge this is the first spectroscopy study to date which evaluates a diagnostic algorithm for breast lesions in prospective manner. This is very significant step in bringing our technology to the clinic, where it can aid physicians with tissue diagnosis.

10.1.3 Development of the MMS clinical instrument

We designed and developed a compact, a novel portable clinical MMS system capable of acquiring and analyzing reflectance, fluorescence and Raman spectroscopic data and providing a diagnosis in ~2-3 seconds. The MMS instrument was tested in the clinic in an *ex vivo* study involving 99 patients. Future improvements of the instrument may include the use of a single spectrograph/CCD unit for both visible and near infrared light (once this technology becomes available) to further reduce the size of the system

10.1.4 Clinical implementation and evaluation of MMS

A clinical *ex vivo* study was performed at the UH-CMC using the MMS instrument. Spectroscopic data were collected from 99 patients undergoing both excisional and core needle biopsies. The system collected reproducible and reliable data. The difference in performance of DRS and IFS is still under investigation. One of the possible reasons is the difference in the sample volume associated with different spectroscopic modalities. The data set included several lesions that were not seen during previous investigations, including malignant (DCIS and ILC) lesions. We developed a new diagnostic algorithm which enabled the identification of these additional lesion types.

10.1.5 Development of new Raman algorithm to predict patients' outcome

In addition to relating the spectroscopic parameters to histopathology categories, we evaluated the potential of spectroscopy to predict the outcomes of patients with malignant lesions. We developed a Raman algorithm to distinguish among different tumor grades and the status of estrogen and progesterone receptors. We found that the Raman fit coefficients from calcium oxalate dehydrate and cholesterol-like can distinguish among tumor grades. The combination of the fit coefficients from β-carotene and cell nucleus distinguished between ER negative and ER positive statuses, misclassifying two ER positive sites. Fit coefficients of calcium

oxalate dehydrate and β-carotene were the most promising in identifying PR status. The findings from this study demonstrated that Raman spectroscopy may provide information which is relevant for determining the treatment course.

10.1.6 Development of a mini-Raman clinical system for guidance of core needle biopsy

Finally, we developed a mini-Raman clinical system to guide the clinician when performing stereotactic core needle biopsies by identifying microcalcifications. A side-viewing probe geometry was developed that enabled the probe to be inserted into a 9G ATEC biopsy needle device. Several different prospective side-viewing probes were designed to maximize collection of the Raman signal. However, due to the manufacturing constraints a sub-optimal design was used in the initial proof-of-principle study. The findings from this study revealed that the diagnostic algorithm developed for the front-viewing Raman probe could be successfully applied to data collected using the side-viewing probe. This study demonstrated that it is possible to collect high quality Raman signals in this geometry and has led to collaboration between the G.R. Harrison Spectroscopy laboratory and Hologic Inc., a commercial company that is a leading developer and manufacturer of diagnostic products related to the healthcare needs of women.

10.2 Future directions

The future of this project may involve following:

10.2.1 Improved instrumentation

The current design of the side-viewing optical fiber Raman can be further optimized for clinical use. Replacing the half-ball lens with a parabolic mirror (Chapter 9.3) would result in a more sensitive fiber probe that can collect good quality Raman spectra in less time than current probe. Decreasing the acquisition time required per site ultimately decreases the time data collection adds to the core needle

biopsy procedures. It would be extremely beneficial to redesign the current adapter used to incorporate the side-viewing Raman probe into the ATEC needle such that tissue cores can be extracted without completely removing the probe from the needle. This change would also minimize procedure time, thus making Raman spectroscopy more attractive to clinicians as a tool for identifying sites of microcalcifications that should be targeted for biopsy.

A future *in vivo* study is being planned to evaluate the use of the Raman system to guide core needle biopsy. The first pilot study will involve a small number of patients (~10). The aim of this study is to optimize the study protocol and answer the following questions: 1) How many Raman spectra should be taken from each core in order to provide clinically relevant information? 2) Is vacuum necessary for good probe-tissue contact? and 3) Where should the Raman instrument be located in the radiology room? The results of this pilot study will also address whether there is a need to change the adapter or to modify the instrument because of space constraints in the radiology room.

10.2.2 Development of new algorithms

As we described in Chapter 7, current data obtained from 48 patients undergoing excisional biopsy provided 36 number of calcified lesions. Based on this data set, we had found correlations between the Raman spectroscopy results and histopathology diagnoses. The algorithm for distinguishing calcified from non-calcified lesions should be prospectively validated on a larger data set and modified as necessary. We were unable to construct a diagnostic algorithm to distinguish between calcified lesions, because of the limited data set. Thus, the algorithm needs to be designed and tested on a larger data set to test its reliability for this distinction. In addition, a larger data set should provide us with enough data to distinguish between type I and type II microcalcifications. The data required to develop and assess algorithms for these applications will be acquired during the large *in vivo* study in which Raman spectroscopic is used to identify microcalcifications (10.2.1).

10.2.3 Raman basis spectra

The Raman basis spectra used in the studies described in this thesis were obtained several years ago and have not been updated. The fits to the measured Raman spectra are generated based on a linear combination of all Raman basis spectra– each of which is related to a chemical or morphological component within breast tissue (Chapter 3). Although the residuals from the fits to the Raman spectra are generally featureless, it would be important to collect the basis spectra once more for the following reason: as described in Chapter 7, IDC lesions have large contribution of the sum of cell cytoplasm and cell nucleus compared to other lesions. This finding is consistent with histopathology. These features are particularly important to note when the pathologist making a diagnosis. In order to provide better algorithm based on fit coefficient of cell cytoplasm and cell nucleus, we may need to add additional basis spectra to the breast model, such as Raman spectra of cytoplasm and nucleus from stroma (currently we have spectra of epithelial cells, only). This would require a Raman confocal microscope setup.

Appendix

Performance Matrix
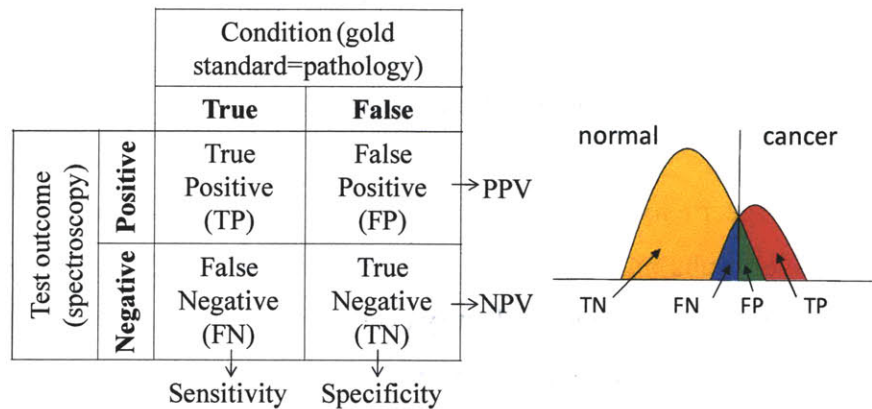
Figure A.1. Binary classifier plot. Visual definition of sensitivity, specificity, positive predictive value (PPV) and negative predictive value (NPV)

Sensitivity and specificity are two statistical measurements of diagnostic performance most often reported in the medical literature. The sensitivity of a test is a measure of how well the classification test identifies a condition, i.e. proportion of true positives of all malignant lesions in the data set. The specificity of a test is a measure of how well the classification test identifies the negative case or the absence of a condition, i.e. the proportion of true negatives of all the non-malignant lesions. The positive predictive value (PPV) is a posterior measure that shows the proportion of data points with a positive test outcome that are correctly classified. The negative predictive value (NPV) is a posterior measure that specified the proportion of data points with a negative test outcome that are correctly classified. These parameters can be calculated as follow (p is the prevalence of disease):

$$sensitivity = se \equiv \Pr\{test\ positive|condition\ true\} = \frac{TP}{TP + FN} \qquad A.1$$

$$specificity = sp \equiv \Pr\{test\ negative|condition\ false\} = \frac{TN}{TN + FP} \qquad A.2$$

$$PPV \equiv \Pr\{condition\ true|test\ positive\} = \frac{TP}{TP + FP} = \frac{p \cdot se}{p \cdot se + (1 - p) \cdot (1 - sp)} \qquad A.3$$

$$NPV \equiv \Pr\{condition\ false|test\ negative\} = \frac{TN}{TN + FN} = \frac{(1 - p) \cdot sp}{(1 - p) \cdot sp + p \cdot (1 - se)} \qquad A.4$$

High sensitivity is wanted in the case of serious and treatable disease, which should not be missed; and false positive results do not have serious adverse consequences for the patient. In this situation, one wants to identify every single patient with the disease for further clinical evaluation and treatment, even at the cost of misdiagnosing few healthy patients as diseased [1].

High specificity is wanted in the case of serious but not treatable disease; and false positive results may have serious adverse consequences for the patient. In this situation, one wants to correctly identify every single non-diseased or healthy patient, even at the cost of misclassifying some diseased patients as healthy.

High PPV is wanted in the case of a serious and treatable disease, which should not be missed; and false positive results may have serious adverse consequences for the patient. In this situation, one wants to be certain that every patient with positive test has the disease in question, even at the risk of missing some diseased patients.

High NPV is wanted in the case of serious but not treatable disease; and false negative results will not have serious adverse consequences for the patient.

Overall efficiency is defined as the ration of the total number of correct test results to the total number of tests performed. High overall efficiency is wanted when the disease is serious and treatable; and false positive and false negative results are equally serious or potentially injurious to the patient. In this situation, one wants to be certain that the test result is accurate whether it is positive or negative.

1. Fitzmaurice, M., Principles and pitfalls of diagnostic test development: implications for spectroscopic tissue diagnosis. *J Biomed Opt*, 2000. 5(2): p. 119-30.

Clinical Raman Instrumentation

Manual

RAMAN CLINICAL INSTRUMENT MANUAL

BY

Chae-Ryon Kong
Michael S. Feld

CONTRIBUTIONS FROM

Zoya Volynskaya
Luis Galindo

MIT Spectroscopy Laboratory

September 25, 2009

TABLE OF CONTENTS

1. OVERVIEW

Raman scattering provides chemical information from a sample based on the specific spectral shifts that result from molecular vibrations. Since Raman scattering can occur without damaging the sample, it can serve to be an effective tool for extracting chemical and morphological information in a non-invasive manner [1]. Early Raman spectroscopy studies have used excised and cadaver tissues, and whole blood samples for the examination of atherosclerosis, detection of cancer, and the measurement of blood analytes [2, 3, 4, 5]. With the development of flexible and high-throughput optical fiber probes [6], as well as compact and improved spectroscopic devices, it has become possible to apply Raman spectroscopic techniques in the clinic *in vivo* [7, 8].

The ability to rapidly collect Raman information, and provide immediate feedback to the physician during a clinical procedure has the potential to greatly improve patient care by facilitating real-time disease management, improving diagnostic accuracy, and allowing early disease diagnosis as well as long-term monitoring of therapy. The Raman clinical instrument described in this manual serves to be a necessary step towards achieving these goals. The manual will explain each portion of the Raman clinical instrument and describe the operating procedures. It will also provide some useful troubleshooting steps, as well as basic analytical techniques for Raman spectroscopy.

References:

1. E. B. Hanlon, R. Manoharan, T. W. Koo, K. E. Shafer, J. T. Motz, M. Fitzmaurice, J. R. Kramer, I. Itzkan, R. R. Dasari, and M. S. Feld, "Prospects for *in vivo* Raman spectroscopy," Phys. Med. Biol. 45(2), R1–R59 (2000).

2. H. P. Buschman, G. Deinum, J. T. Motz, M. Fitzmaurice, J. R. Kramer, A. van der Laarse, A. V. Bruschke, and M. S. Feld, "Raman microspectroscopy of human coronary atherosclerosis: biochemical assessment of cellular and extracellular morphologic structures in situ," Cardiovasc. Pathol. 10(2), 69–82 (2001).

3. A. S. Haka, K. E. Shafer-Peltier, M. Fitzmaurice, J. Crowe, R. R. Dasari, and M. S. Feld, "Identifying microcalcifications in benign and malignant breast lesions by probing differences in their chemical composition using Raman spectroscopy," Cancer Res. 62(18), 5375–5380 (2002).

4. A. M. K. Enejder, T. W. Koo, J. Oh, M. Hunter, S. Sasic, M. S. Feld, and G. L. Horowitz, "Blood analysis by Raman spectroscopy," Opt. Lett. 27(22), 2004–2006 (2002).

5. R. R. Alfano, A. Pradhan, G. C. Tang, S. J. Wahl, "Optical spectroscopic diagnosis of cancer and normal breast tissues ," J. Opt. Soc. Am. B. 6(5), 1015–1023 (1989).

6. J. T. Motz, M. Hunter, L. H. Galindo, J. A. Gardecki, J. R. Kramer, R. R. Dasari, and M. S. Feld, "Optical fiber probe for biomedical Raman spectroscopy," Applied Optics. 43(3), 542-554, (2004).

7. J. T. Motz, S. J. Gandhi, O. R. Scepanovic, A. S. Haka, J. R. Kramer, R. R. Dasari, and M. S. Feld, "Real-time Raman system for in vivo disease diagnosis," J. Biomed. Opt. 10(3). 031113, 1-7, (2005).

8. O. R. Scepanovic, Z. Volynskaya, C.-R. Kong, L. H. Galindo, R. R. Dasari, and M. S. Feld, "A multimodal spectroscopy system for real-time disease diagnosis," Rev. Sci. Instrum. 80(4). 043103, 1-9, (2009).
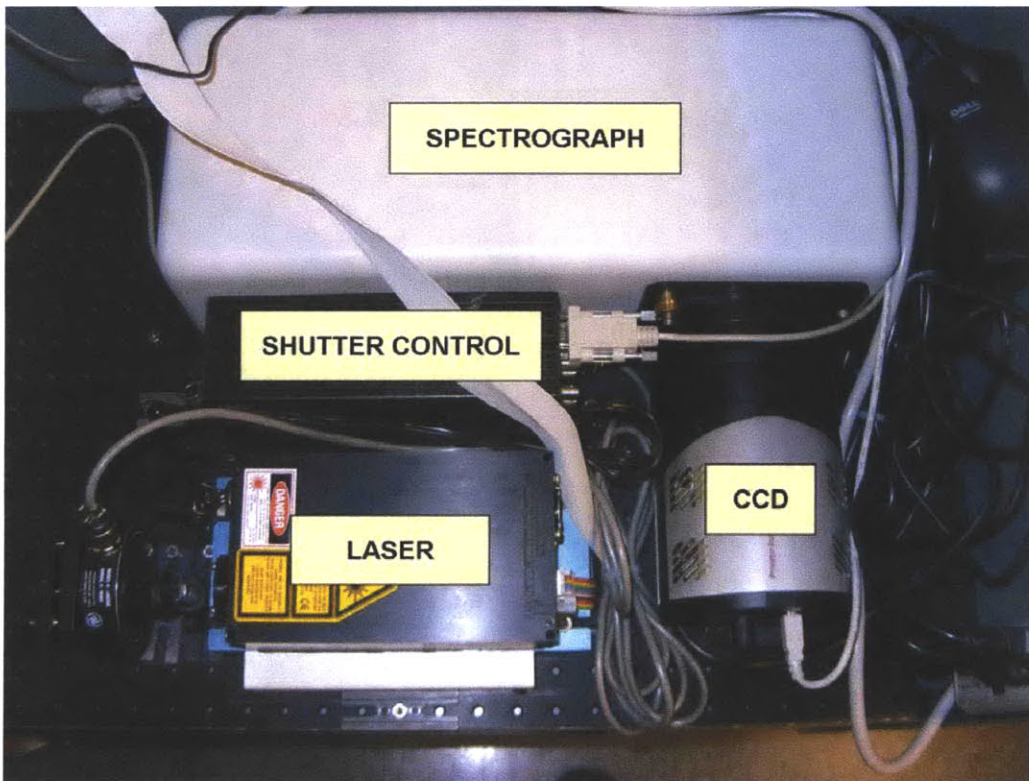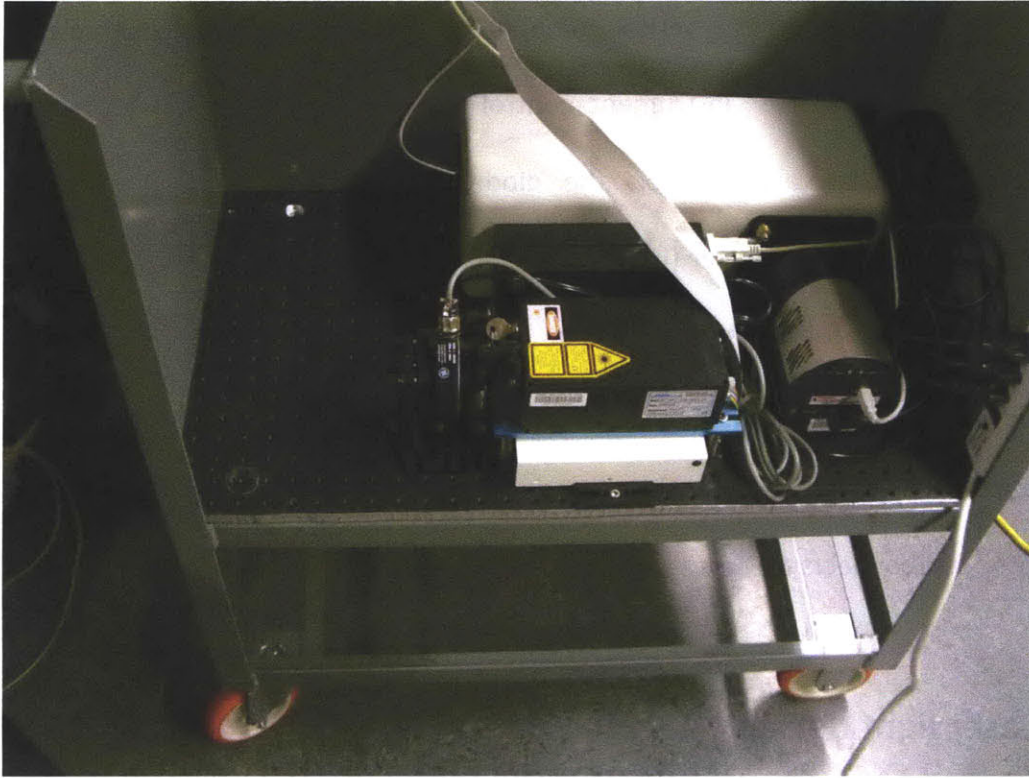
2. INSTRUMENTATION

A. Overall setup

A schematic of the Raman clinical instrument is shown in Figure 1. The Raman clinical instrument consists of the following optical components: an 830nm diode laser (500mW maximum power, Process Instruments, Salt Lake City, UT) for excitation light source, an optical fiber probe [1] for delivering excitation light and collecting Raman scattered light from the tissue, a spectrograph (Holospec f/1.8i, Kaiser Optical Systems), and a thermoelectrically cooled CCD camera (PIXIS 256, 26x26μm pixels, 1024x256 array, Princeton Instruments) for spectrum analysis and detection, and various optics.
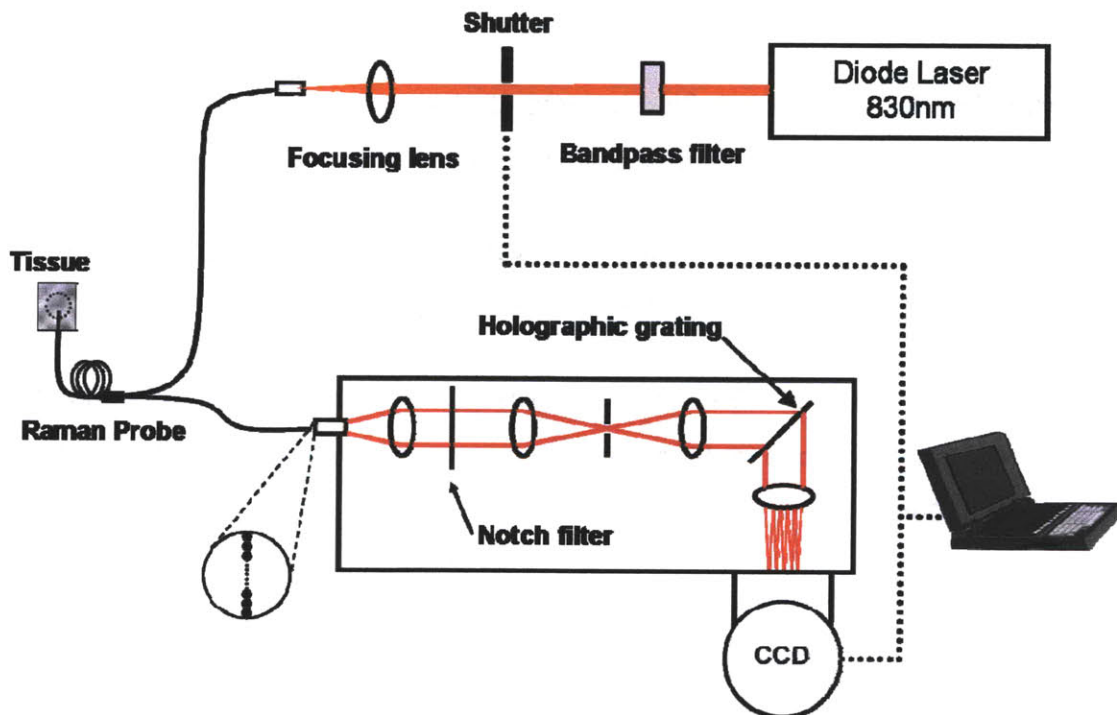
Figure 1 A schematic diagram of the portable Raman clinical instrument.

Figure 2 Major components and instruments fixed on the cart optical breadboard

In addition to these optical components, the Raman clinical instrument also includes a computer for instrument control and data collection. Specifically, the computer monitors and controls the diode laser power and CCD temperature, opens/closes the laser shutter (Uniblitz, Vincent Associates) and collects data from the CCD. Data transfer to and from the instrument is achieved by PCI (peripheral component interconnect) and USB (universal serial bus) connections located at the bottom of the computer. The white box under the laser shown in Figure 2 encloses the adapter that connects the laser and the control card in the computer.

B. Laser light delivery alignment
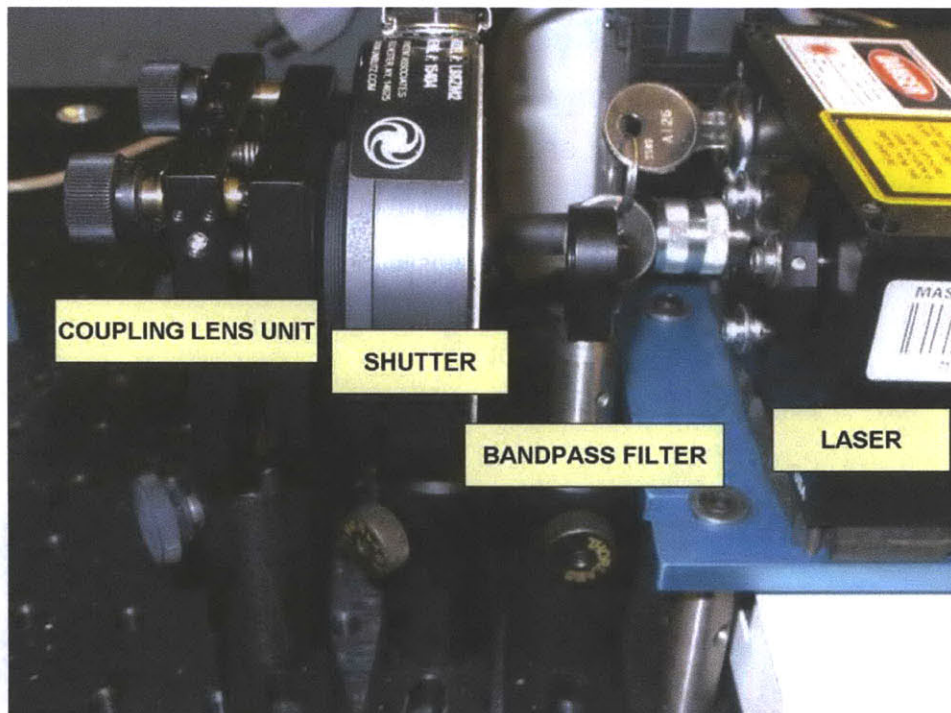
Figure 3 Laser light delivery components. The 830 nm beam from the laser is filtered through a bandpass filter and is gated by a computer-controlled shutter. The beam is then focused and collimated through a lens unit to be coupled to the optical fiber probe.

Figure 3 shows the components used for excitation light delivery. The beam from the 830 nm diode laser is filtered through a bandpass filter and it is gated by a computer-controlled shutter. The beam is then focused and collimated through a lens, and coupled to the excitation light delivery fiber of the optical fiber probe.

Figure 4 shows a close-up view of the coupling lens unit and the optical fiber probe. The laser, bandpass filter, shutter, coupling lens unit and the delivery fiber are carefully aligned to minimize losses in laser power. The power of the laser can be controlled by the Labview software, as described later in Figure 12. The "Set Power" setting should not exceed 1.26V, at which approximately 440mW is delivered from the laser output. With 440mW at the laser output, the power after passing through the bandpass filter, the shutter, and the coupling lens unit should be no less than 380mW. Usually, the most significant power loss occurs between the coupling lens unit and the optical fiber. If correctly aligned, the power of the excitation light measured at the distal tip of the optical fiber should be about 130mW with 440mW at the laser output. However, for typical spectroscopic measurements, the power measured at the tip of the optical fiber should be at 100mW. Before measurements, adjust the "Set Power" setting to reach this power level. Laser power greater than 100mW should not be used on human subjects, as it may induce tissue damage. The ANSI (American National Standards Institute) maximal permissible exposure to continuous wave near infrared laser light for 10 seconds is 0.36 W/cm^2, which is an extremely conservative standard [2]. An 830nm light excitation power of 100mW over a 200μm diameter spot corresponds to

irradiance of 318 W/cm^2, which is clearly above the ANSI standards, but comparable to what is currently being used safely by many research labs including our own [3-9].
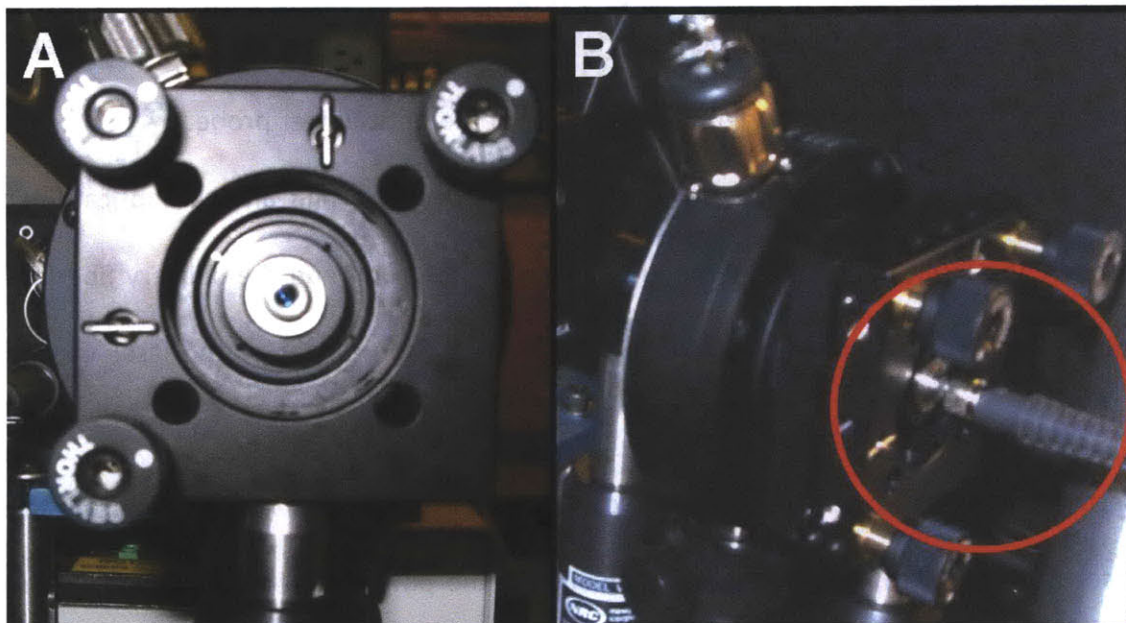

Figure 4 A : Front view of the coupling lens unit.
           B : Excitation light delivery fiber coupled to the lens unit.

C. Optical fiber probe, spectrograph, and CCD

The optical fiber probe serves dual functions of delivering excitation light to the target tissue as well as collecting Raman scattered light from the target tissue. The probe (Figure 5) has a central excitation fiber (multimode, 200μm core, 0.22 NA) with an aluminum jacket for optical isolation to prevent cross-talk with the 15 collection fibers (multimode, 200μm core, 0.27 NA). [1]
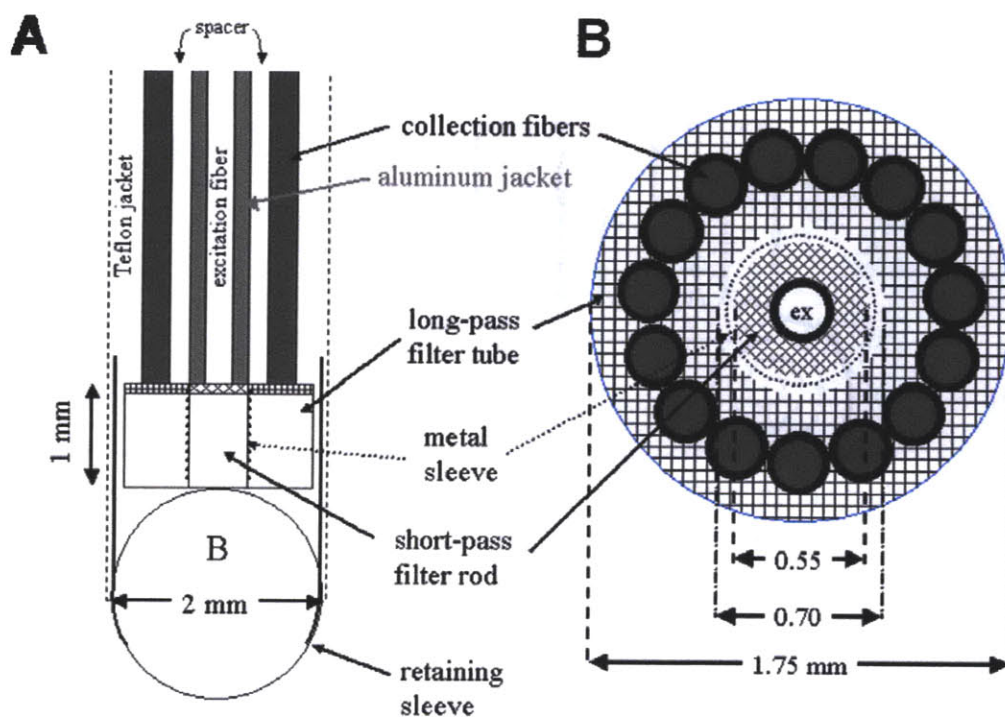
Figure 5 Schematic of the Raman probe tip. [1]
      A : Longitudinal view, **B :** Transverse cross section at the fiber-filter interface.

The distal tip of the probe has a ball lens mounted inside the metal sleeve to enhance light collection (Figures 5, 6). When collecting Raman spectra, the probe should be in gentle contact with the sample. At the proximal end, the collection fibers are aligned in a column to form the slit of the spectrograph (Figure 6A). When coupling to the spectrograph, the column of fibers must be in a vertical position so that the column of light spots can be evenly dispersed by the spectrograph. This alignment can be achieved by monitoring the optical fiber patterns through the CCD camera under WinSpec (section 3B(i)).
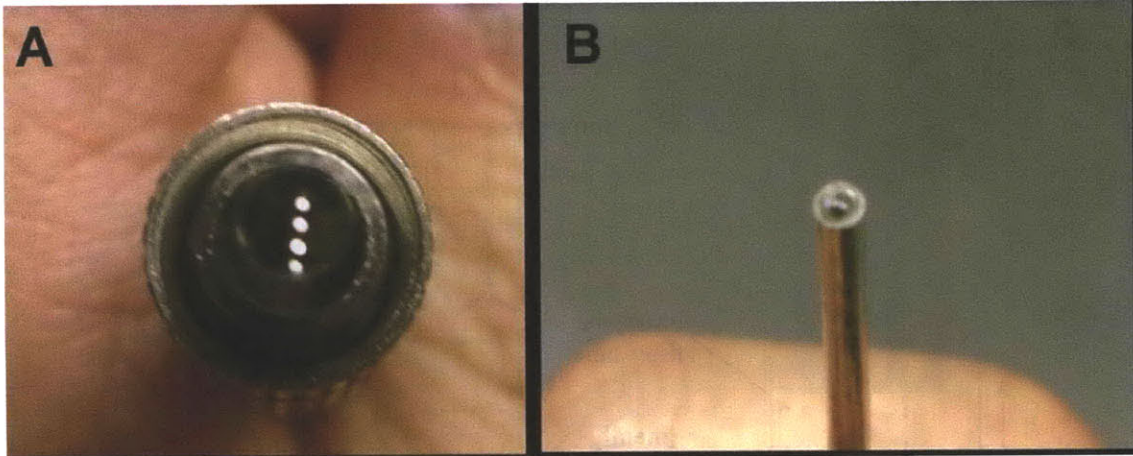
Figure 6 **A :** Column of collection fibers lighting up on the optical fiber probe connector
B : Distal tip of the optical fiber probe

References:

1. J. T. Motz, M. Hunter, L. H. Galindo, J. A. Gardecki, J. R. Kramer, R. R. Dasari, and M. S. Feld, "Optical fiber probe for biomedical Raman spectroscopy," Applied Optics. 43(3), 542-554, (2004).

2. ANSI.Z136-1 (2000). Safe Use of Lasers, American National Standards Institute.

3. M. G. Shim, B. C. Wilson, "Development of an *in vivo* Raman spectroscopic system for diagnostic applications," Journal of Raman Spectroscopy 28. 131–142, (1997).

4. P. J. Caspers, G. W. Lucassen, E. A. Carter, H. A. Bruining and G. J. Puppels, "*In vivo* confocal Raman microspectroscopy of the Skin: noninvasive determination of molecular concentration profiles," Journal of Investigative Dermatology 116. 434–442, (2001).

5. J. T. Motz, S. J. Gandhi, O. R. Scepanovic, A. S. Haka, J. R. Kramer, R. R. Dasari, and M. S. Feld, "Real-time Raman system for in vivo disease diagnosis," J. Biomed. Opt. 10(3). 031113, 1-7, (2005).

6. H. P. Buschman, E. T. Marple, M. L. Wach, B. Bennett, T. C. B. Schut, H. A. Bruining, A. V. Bruschke, A. van der Laarse and G. J. Puppels. "In vivo determination of the molecular composition of artery wall by intravascular Raman spectroscopy," Analytical Chemistry, 72(16):3771-3775, (2000).

7. O. R. Scepanovic, Z. Volynskaya, C.-R. Kong, L. H. Galindo, R. R. Dasari, and M. S. Feld, "A multimodal spectroscopy system for real-time disease diagnosis," Rev. Sci. Instrum. 80(4). 043103, 1-9, (2009).

8. A. S. Haka, Z. Volynskaya, J. A. Gardecki, J. Nazemi, J. Lyons, D. Hicks, M. Fitzmaurice, R. R. Dasari, J. P. Crowe, and M. S. Feld, "In vivo margin assessment during partial mastectomy breast surgery using Raman spectroscopy," Cancer Research, 66, 3317-3322, (2006).

9. I. V. Ermakov, R. W. McClane, W. Gellermann and P. S. Bernstein. "Resonant Raman detection of macular pigment levels in the living human retina," Optics Letters, 26(4): 202-204, (2001).

3. OPERATING INSTRUCTIONS

A. Hardware operations

The first step of initializing the Raman clinical instrument is to power up the hardware. The next step is to turn on the computer and the laser. The computer power switch is located on the lower back of the computer, and the laser is switched on by turning the key clockwise, as shown in Figure 7.
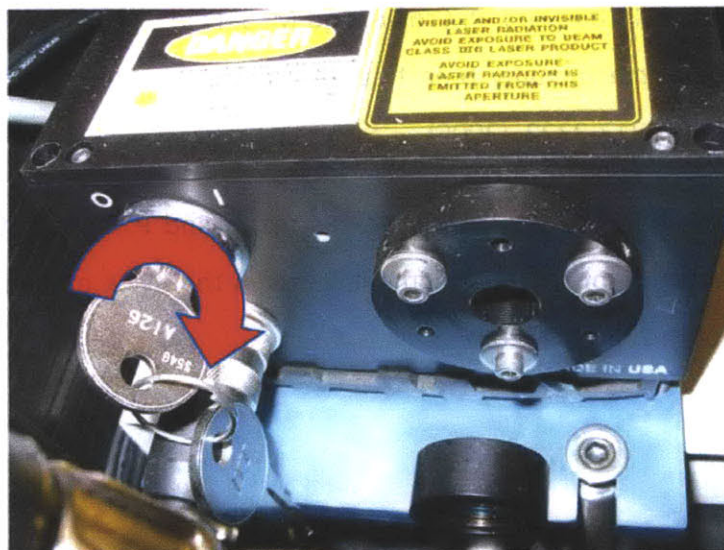
Figure 7 The 830 nm diode laser is switched on by turning the key.

Next, the shutter controller must be turned on to enable gating of the laser. The shutter controller power switch is located on the back of the controller. For proper operations, the shutter controller settings should be set as follows :

Mode turn key = "STD"; Normally closed ("N.C."); "REMOTE"

These controller settings are shown in Figure 8.

Figure 8 The shutter controller power switch and control settings

If the optical fiber probe is not attached already, attach the delivery fiber to the coupling lens unit and the modified SMA connector to the spectrograph. As described in the "Instrumentation" section, make sure that the bandpass filter, shutter, coupling lens unit and delivery fiber are properly aligned so that approximately 100mW is delivered at the distal tip of the probe. To enable laser light delivery, use the Labview software to open the laser shutter remotely from the computer, as described later (Figure 20). For troubleshooting, the shutter can also be opened without the computer by adjusting the shutter control setting to normally open "N.O.". However, leave the setting to "N.C." for normal operations (Figure 8). The laser power is controlled remotely from the computer software with maximum allowable setting at 1.26V (Figure 19). For

troubleshooting, the power can also be adjusted locally by removing the cable connection to the computer and turning the power adjust knob on the laser (Figure 9).
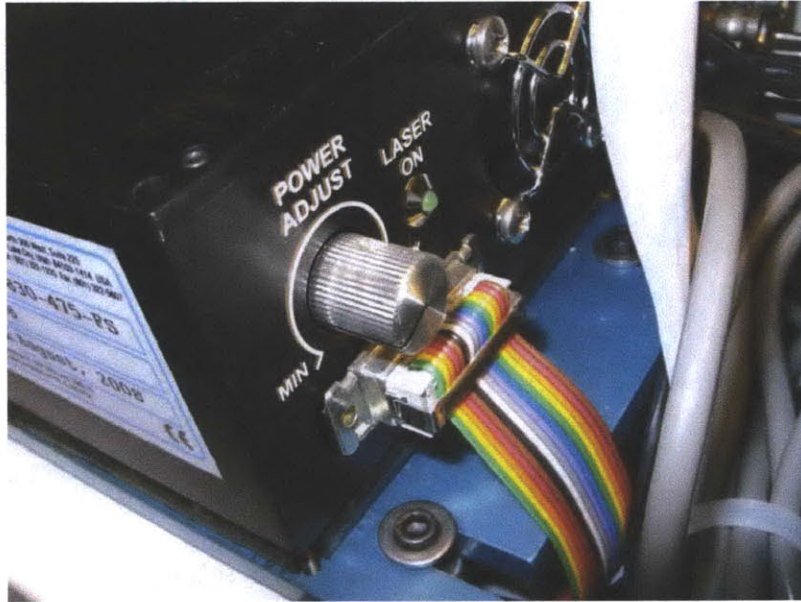
Figure 9 Power adjustment knob of the diode laser

B. Software operations

Three major software packages are used in the operation of the Raman clinical instrument. The first is WinSpec, which is used for troubleshooting steps and determining the region of interest of the CCD. The second is Labview virtual instrument (VI) software "Raman_main.vi", which is the main software used in the normal operation of instrument control and data acquisition. These two software packages should not be run simultaneously, as it would create conflicts in software and freeze the computer. If this happens by mistake, restart the computer. The third is Matlab, which is utilized by Labview during operation.
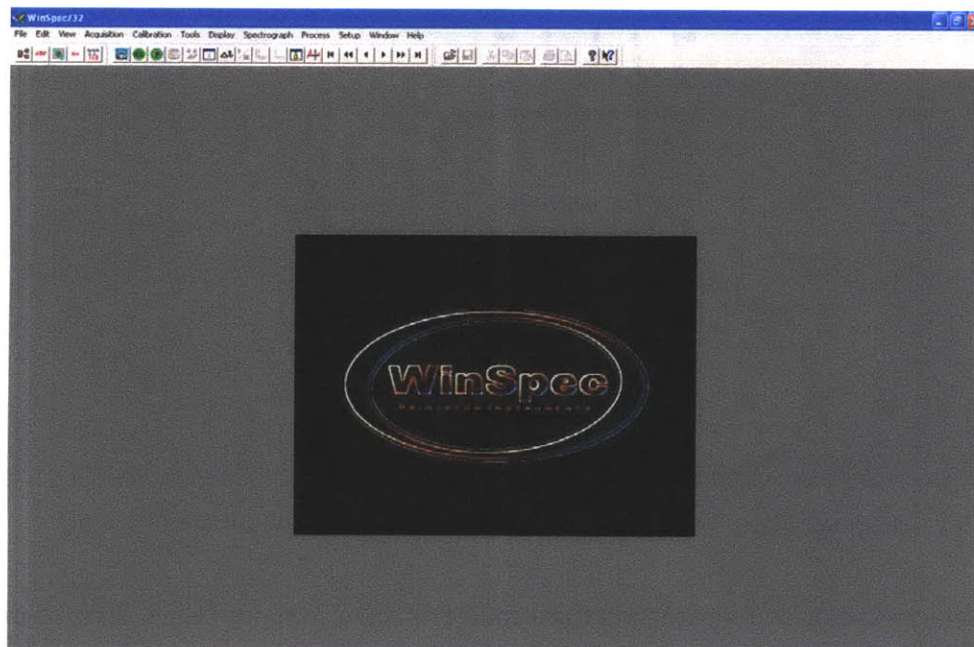
Figure 10 WinSpec initialization screen

(i) WinSpec Software

a. First, determine the region of interest of the CCD by using the WinSpec software. Locate the WinSpec icon from the Start menu and run it (Figure 10). If the software shows an error message about not being able to find the camera, check the USB and power connections. Next, open the "Setup" menu and click on "Detector Temperature". Set the target temperature to $-70°C$.

b. Before acquiring Raman spectra, turn off the room light. Go to the "Acquisition" menu and select "Experimental Setup" (Figure 11).
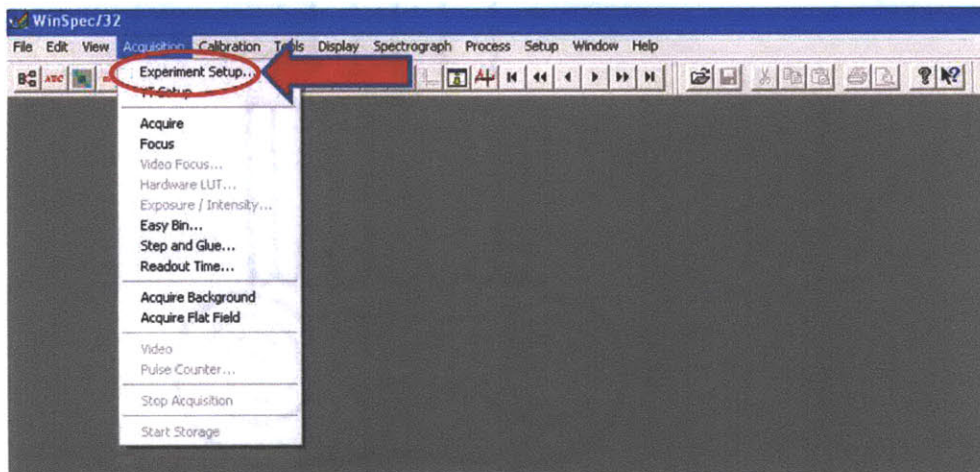
Figure 11 Locating "Experimental Setup" command under "Acquisition" menu.

c. Select exposure time, starting from shorter exposure times (e.g. 0.25 s) to prevent

CCD saturation (Figure 12).
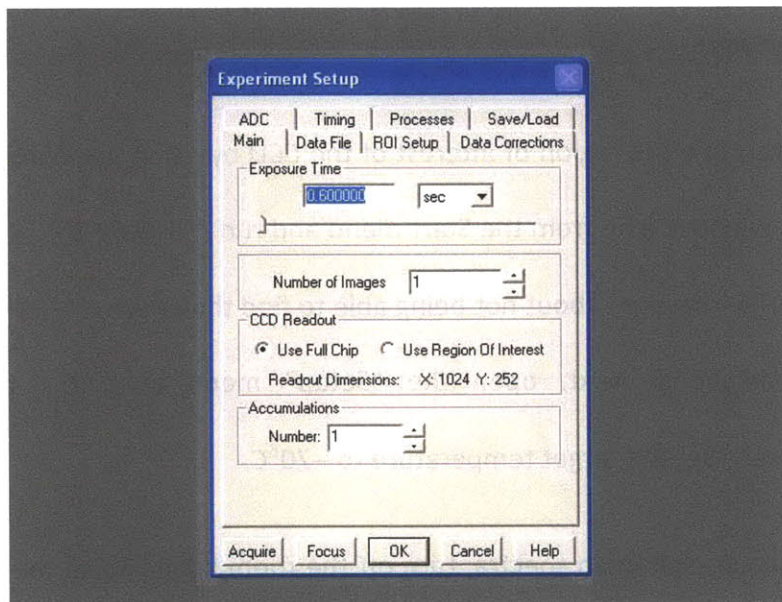

Figure 12 "Experimental Setup" setting window

d. Obtain a Tylenol (4-acetamidophenol) calibration sample, turn on the laser, turn

off the room light, and execute "Easy Bin" under the "Acquisition" menu (Figure 13).
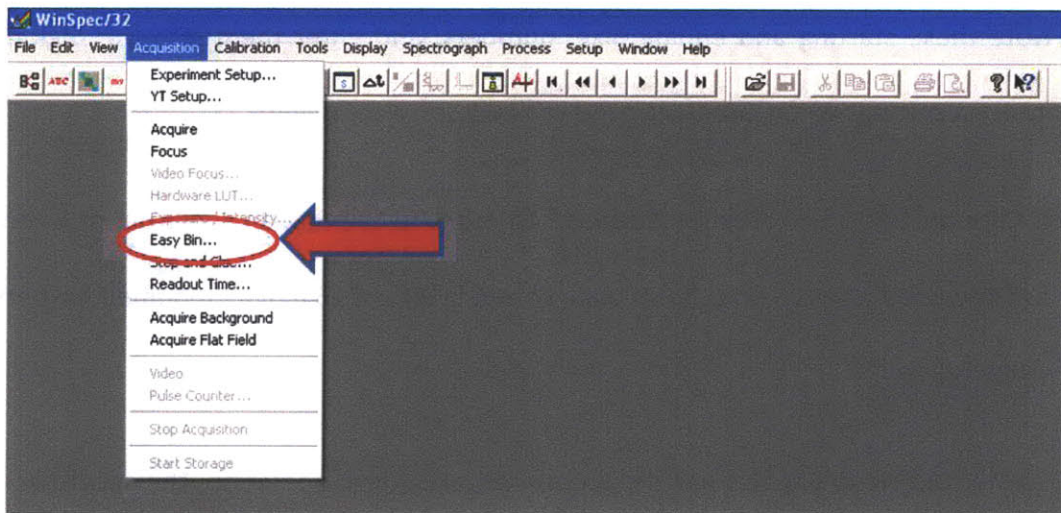
Figure 13 Locating "Easy Bin" command under "Acquisition" menu

e. While the probe is properly positioned over the Tylenol sample (Figure 26A), click on "Acquire Full image" (Figure 14). The acquired image should show several vertical columns of light spots, with high intensity areas corresponding to the Tylenol Raman peaks. By either dragging the pointer on the image or directly entering the pixel numbers, choose the starting and ending pixel numbers so that the red lines cover just enough of the CCD area that contains the spectral data (Figure 14).
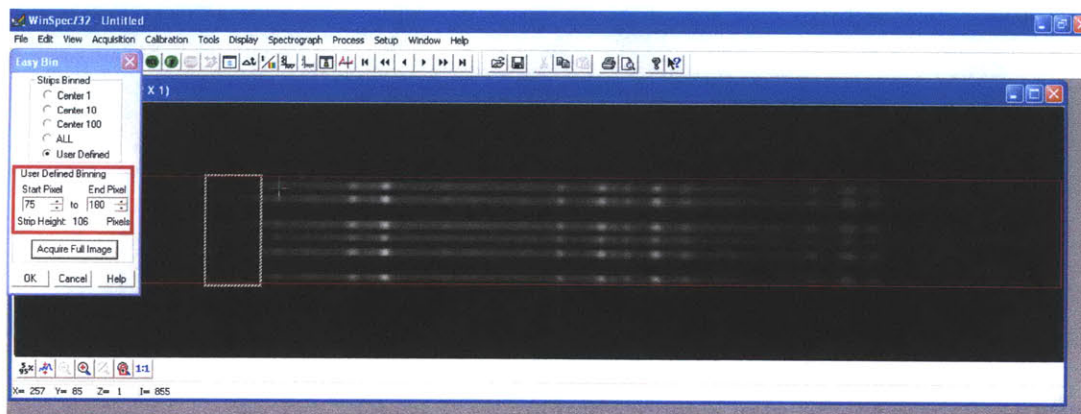
**Figure 14** Using the "Easy Bin" function to define binning pixel ranges (boxed).

Note these starting and ending pixel numbers, and enter them into the region of interest settings when later using the Labview software (Figure 21).

f. Click on "OK", and click on "acquire" to produce the Raman spectrum of Tylenol, as shown in Figure 15 (in original colors), and in Figure 16 (colors modified for better visibility).

(Note: During WinSpec's normal acquisition and focus operation, the spectroscopy mode can also be achieved by navigating to "Acquisition" menu → "Experimental Setup" → "ROI Setup" and selecting "Spectroscopy mode".)
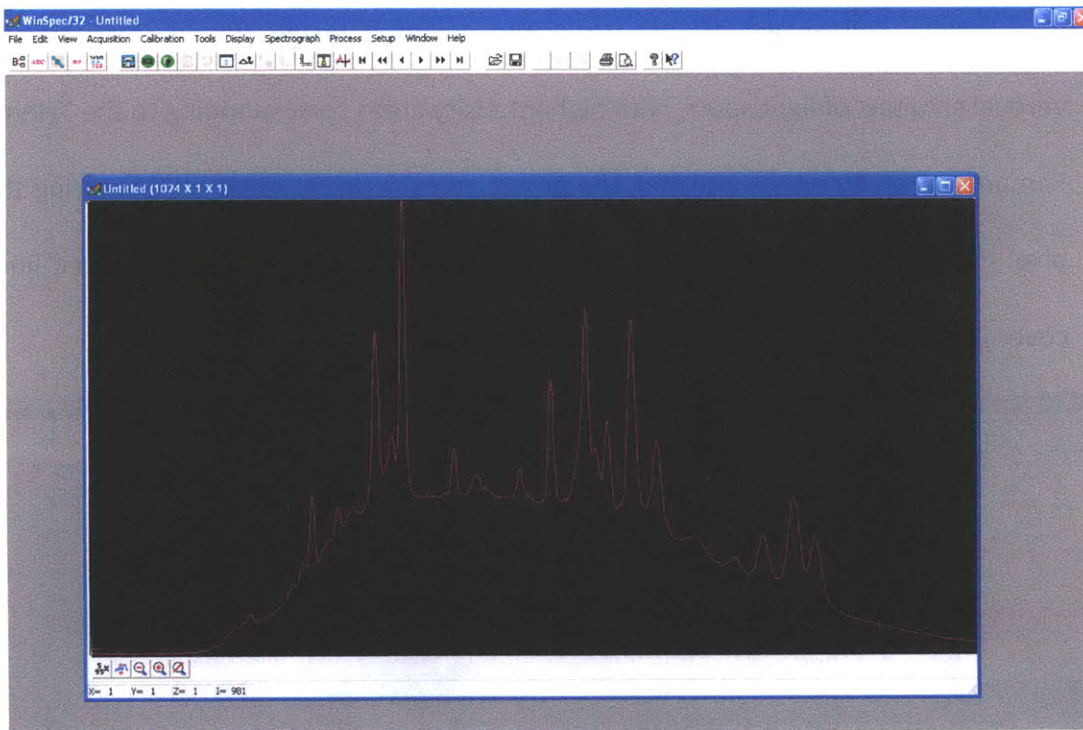
Figure 15 Raman spectrum of Tylenol obtained by "Easy Bin" process.
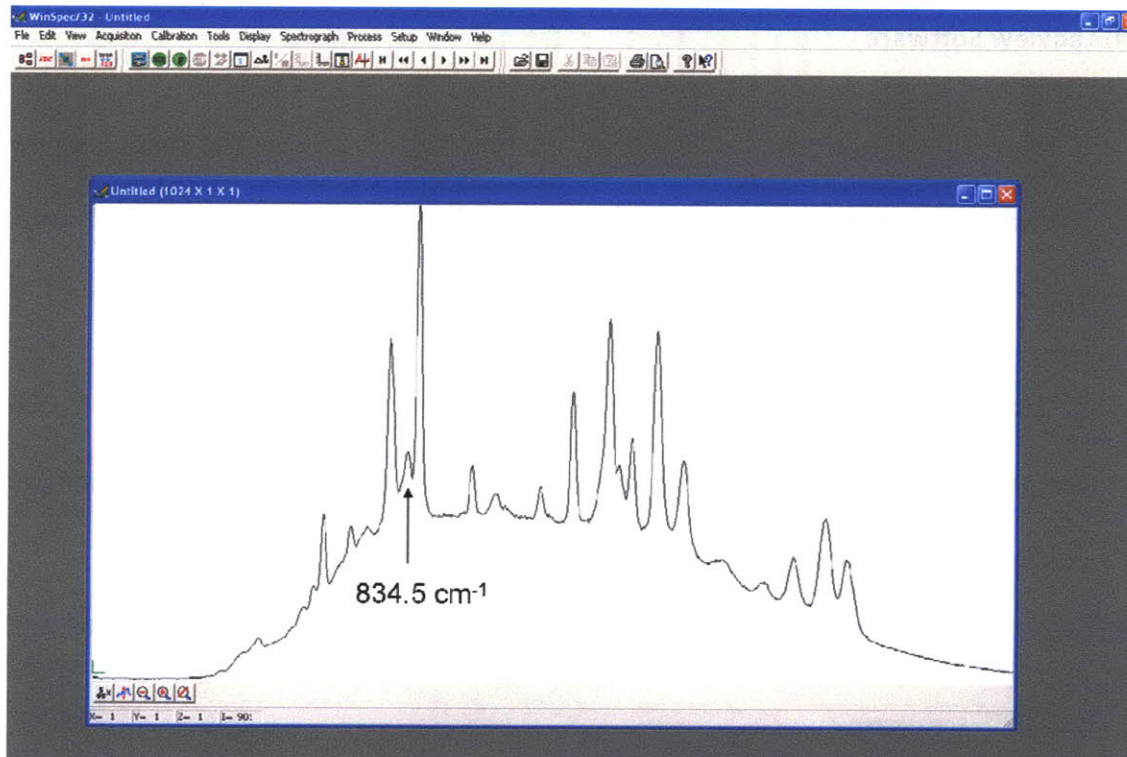
Figure 16 Raman spectrum of Tylenol obtained by "Easy Bin" process, with colors in black and white for visibility.

If the spectrograph is properly aligned and focused, the 834.5cm^{-1} Tylenol peak should be clearly distinguishable from its neighboring peaks (arrow, Figures 33, 16). If this is not the case, adjust the spectrograph focus by turning the camera focus and slit focus knobs located on the outside of the spectrograph.

(ii) Labview Software

a. Make sure the WinSpec software is not running. To initiate the main Labview software, open the shortcut to "Raman_main.vi" on the Desktop and run the code. The main software screen should initially be as shown in Figure 17.

b. Upon initialization, the software will immediately show the current CCD temperature on the upper left corner of the screen (Figure 17, circle) and will initiate cooling to the target temperature.
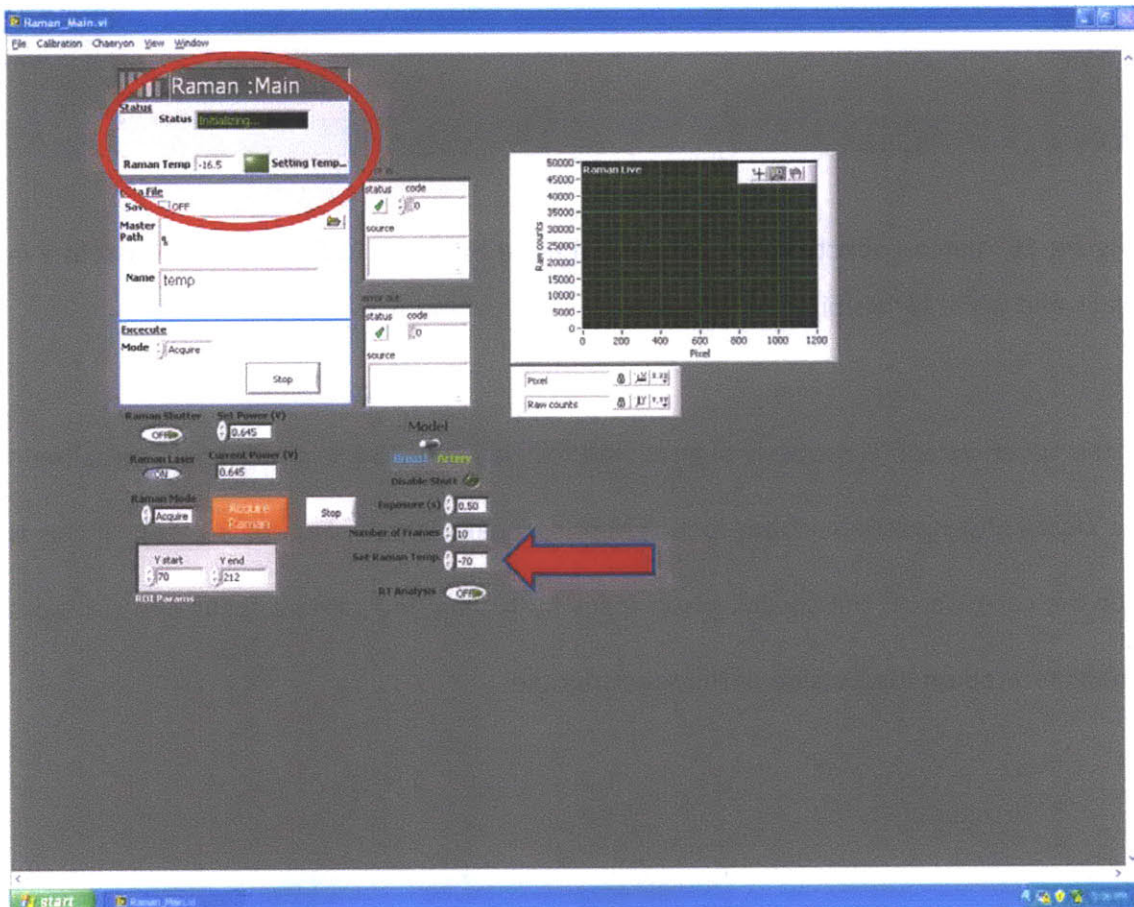

Figure 17 The main Raman spectroscopy software initial screen. Red circle indicates CCD temperature readings, and arrow points to the textbox for entering the target temperature.

The target temperature can be set by typing in the desired temperature at the "Set Raman Temp." box (Figure 17, arrow). Set the target temperature to −70°C. When the target temperature is reached, the green box on the upper left of the screen will light up and it will read "Raman Locked" next to the box (Figure 18).
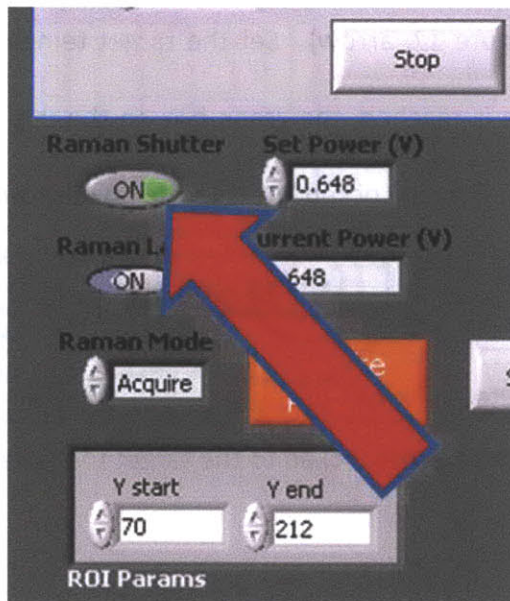

Figure 18 Raman CCD temperature locked to the target temperature

c. Next, the laser should be turned on by clicking on the "Raman laser" switch (Figure 19, arrow). The power level can be controlled by adjusting the "Set Power" setting (Figure 19). This setting should not exceed 1.26V (~440mW at laser output).
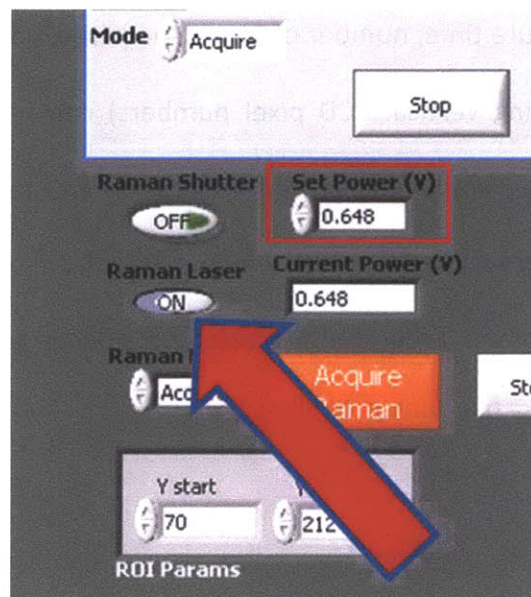

Figure 19 Turning on and setting the power of the laser.

Figure 20 Controlling the laser shutter.

d. For alignment purposes, the laser shutter can be manually opened and closed by clicking on the "Raman Shutter" switch (Figure 20).

e. Also, the CCD exposure time, number of frames acquired, and the region of interest (i.e., starting and ending vertical CCD pixel numbers) can be specified (Figure 21). Exposure time may vary depending on the application and the sample under study. For typical artery and breast tissue measurements, start from exposure time of 0.5 sec and increase as necessary. Enter the starting and ending pixel numbers obtained previously with WinSpec (Figure 14).
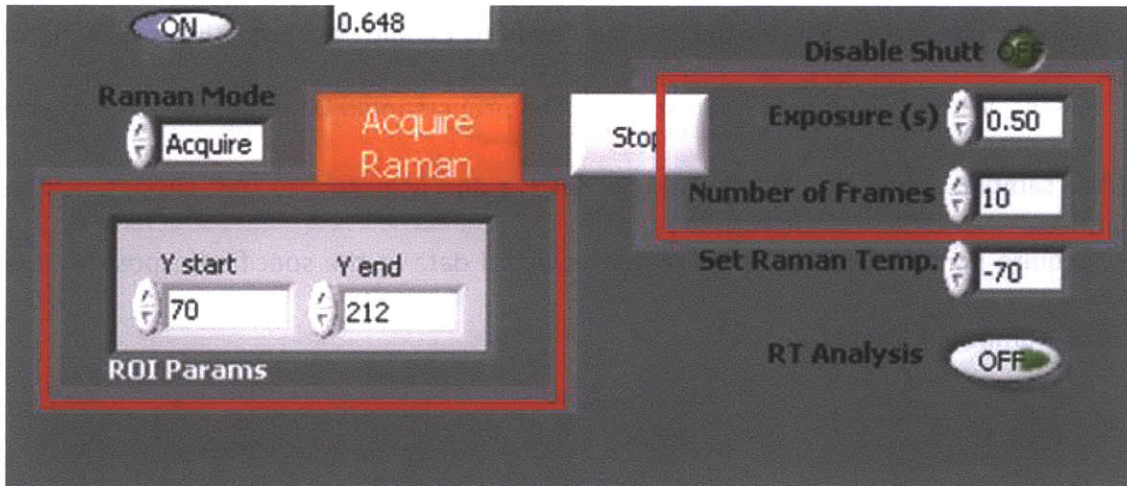
Figure 21 Specifying region of interest, exposure time, and number of frames.

f. To enable saving data, turn on the "Save" option (Figure 22, left). Next, the directory path for storing the data is specified by clicking on the folder button (Figure 22). Navigate to the desired directory and click on "Current Folder" (Figure 22, right). Specify the name of the data files to be stored by changing the content of the "Name" textbox. Each data file will have a date and time stamp in its filename.
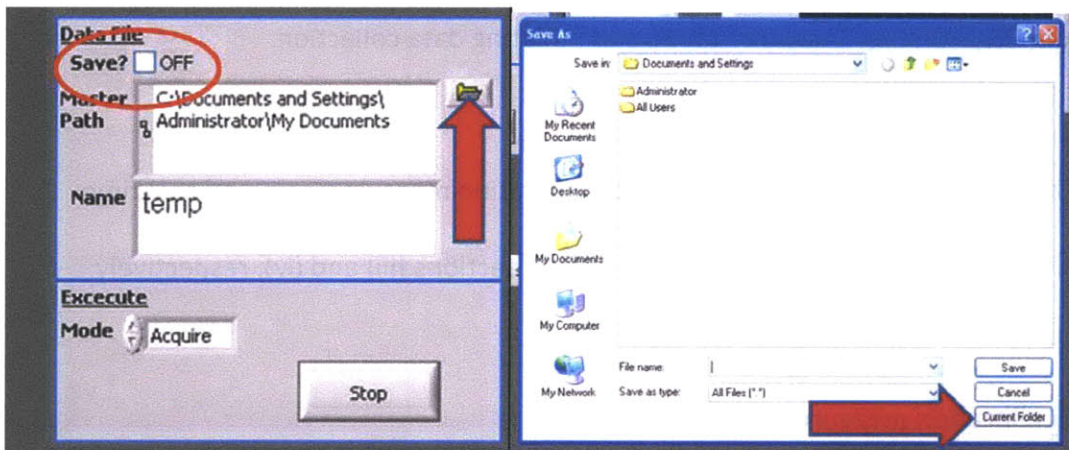
Figure 22 Specifying directory for data storage and selecting save option.

g. To acquire data, click on the orange "Acquire Raman" button. (Figure 23, right, arrow). When collecting Raman spectra, the probe should be in gentle contact with the sample. Keep the "Raman Mode" setting on "Acquire", so that clicking on the "Acquire Raman" button would acquire spectral data at the specified exposure time and number of frames.
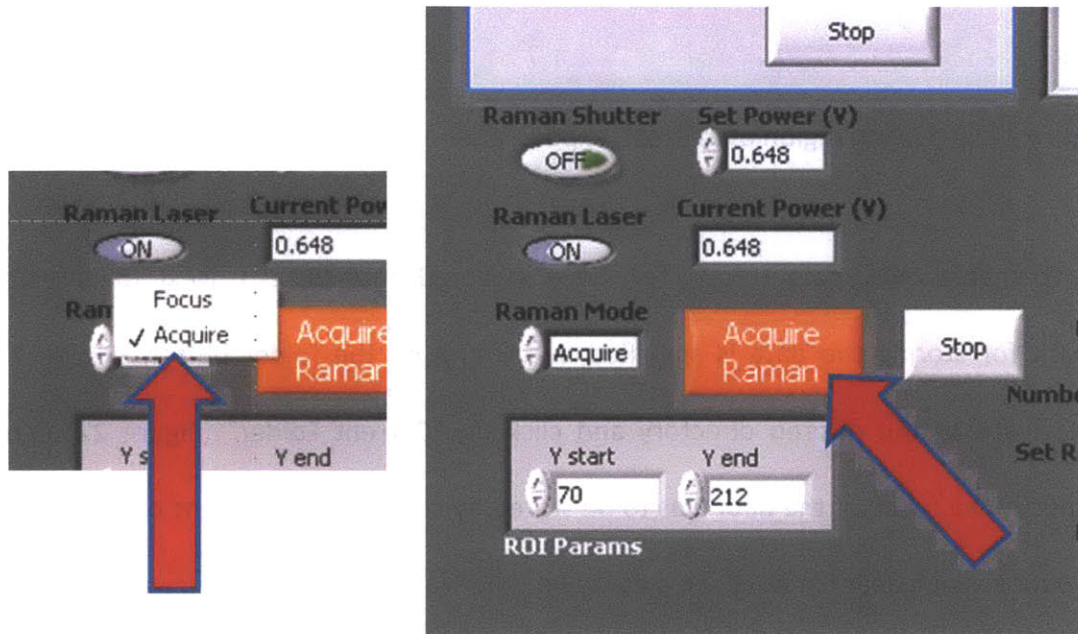
**Figure 23** Selecting "Acquire" mode and initiating data collection.

h. The Labview software is also used for calibration measurements and real-time analysis. These are described in the following sections (iii) and (iv), respectively.

### (iii) Calibration measurements

In order to correct for background Raman scattered light from the optical fiber probe and to accurately measure the Raman shifts, several calibration measurements need to be made. For this purpose, barium sulfate ($BaSO_4$), aluminum and Tylenol

samples, as well as a tungsten halogen lamp light source are required (Figure 24). To help with the calibration measurements, the Labview software has a "calibration" menu with each type of calibration to be selected before taking each measurement (Figure 25).
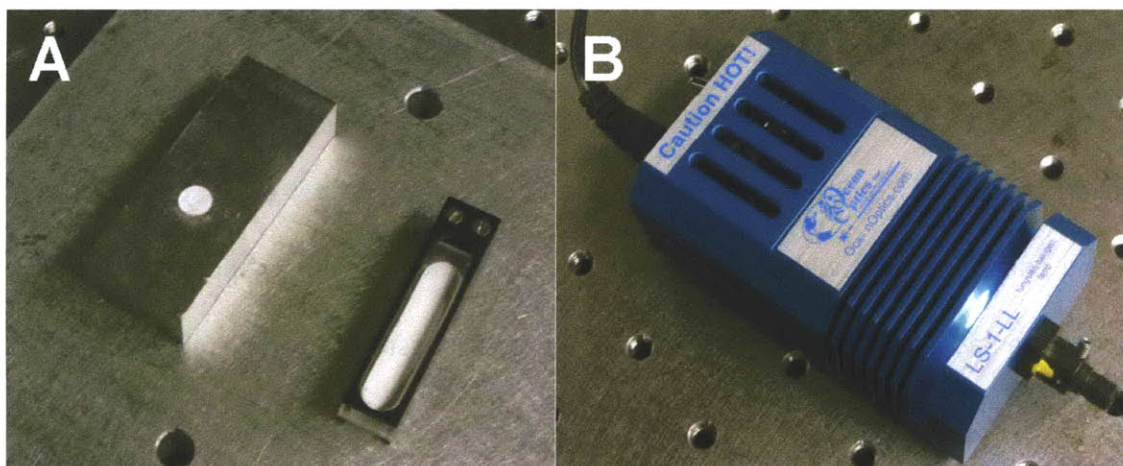

Figure 24 A : BaSO$_4$, aluminum and Tylenol samples **B :** Tungsten halogen lamp
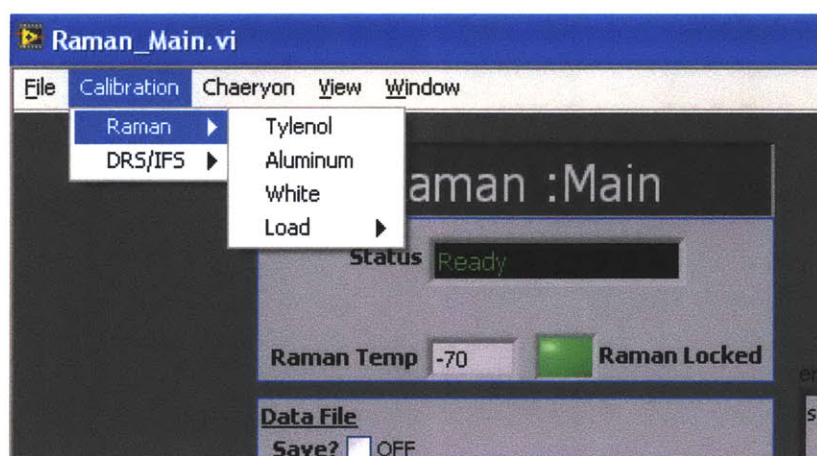
**Figure 25** Selecting type of calibration under "Calibration" menu

First, select "Tylenol" under the calibration menu (Figure 25) and collect the Tylenol Raman spectrum with the probe in gentle contact with the sample (Figure 26). If the tallest peak has less than 20,000 intensity counts, increase the exposure time. Since Tylenol has a well known Raman spectrum with clearly defined peaks (Figure 23), its

Raman spectrum will serve as a standard for calibrating the Raman shift (wavenumber) axis of the spectrum. Next, select "Aluminum" under the calibration menu and collect the aluminum Raman spectrum with the probe in gentle contact with the sample. If the intensity count is less than 8,000, increase the exposure time. The aluminum spectrum will serve as a background spectrum, which will later be subtracted from the Raman spectra collected from the tissue samples. Finally, select "White" under the calibration menu and collect the white light response with the Raman probe approximately 1cm above the $BaSO_4$ sample, while it is illuminated by a tungsten halogen lamp (Figure 28).
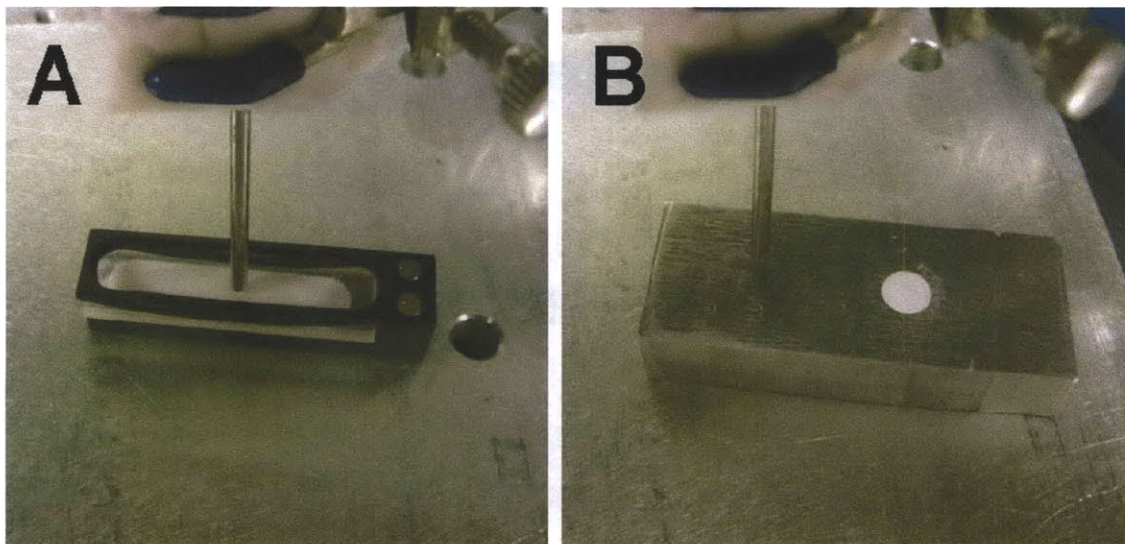
Figure 26 Measuring Raman calibration spectra. **A** : Tylenol, **B** : Aluminum.
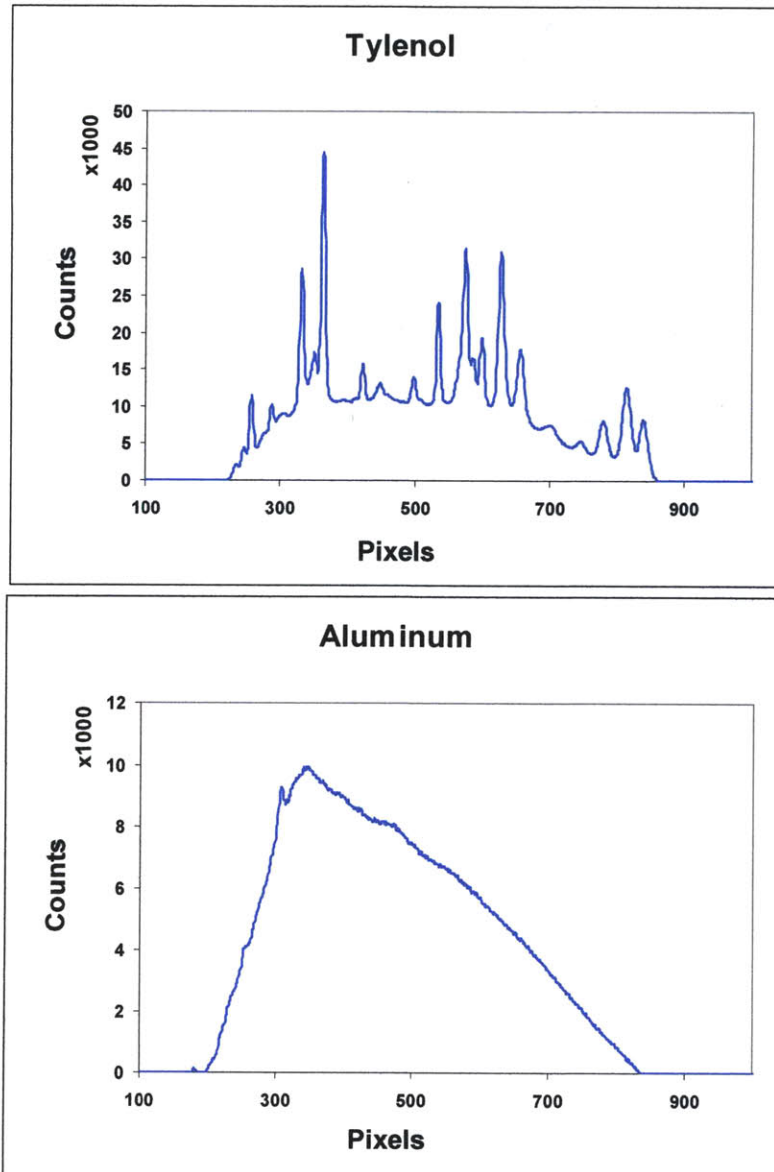
Figure 27 Typical Tylenol and aluminum calibration spectra.

Care must be taken not to saturate the CCD while measuring the white light response. Vary the distance between the probe and the sample until the white light response has an intensity count of about 50,000. For consistent measurements, a probe holder should be used to hold the probe in a vertical position, as shown in Figure 28.
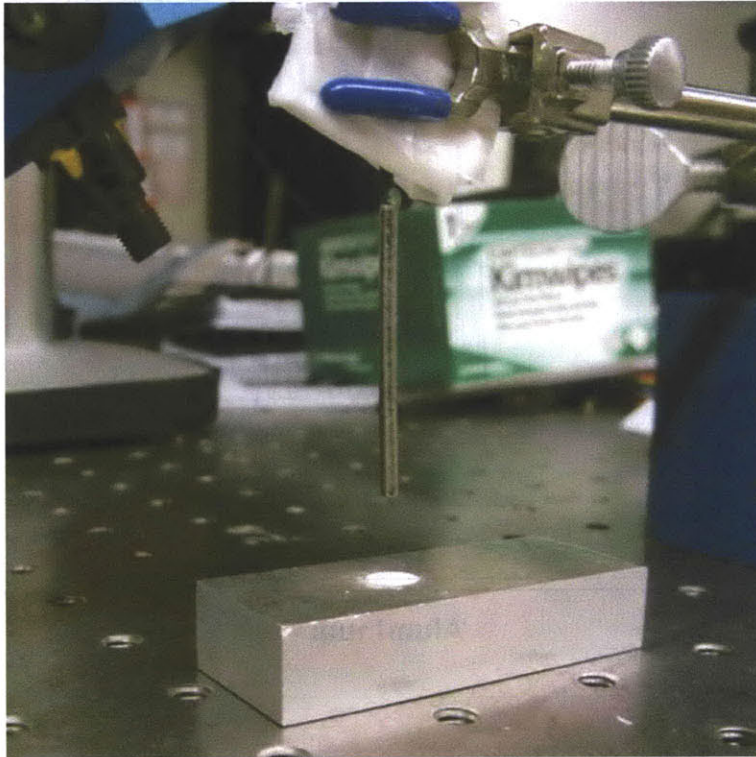
Figure 28 Measuring white light response with a tungsten halogen lamp (upper left) illuminating the BaSO₄ sample, and the Raman probe ~1cm above the sample.
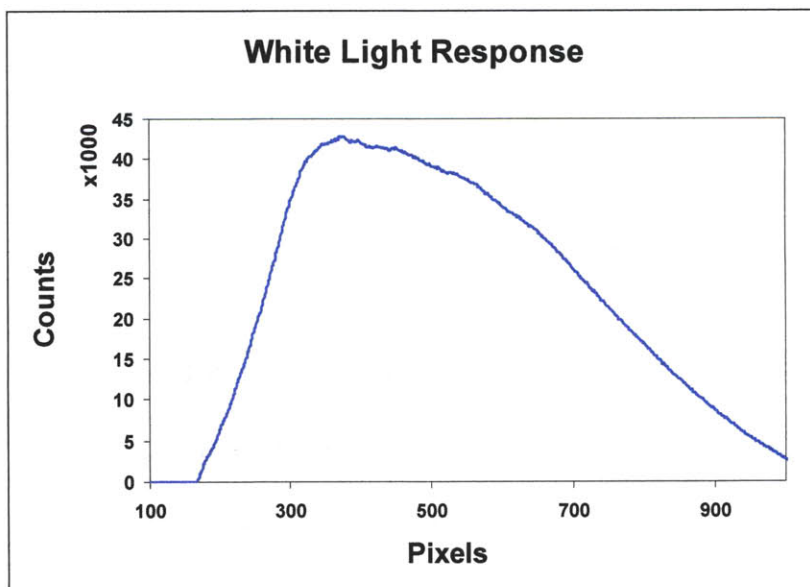
Figure 29 Typical white light response.

(iv) Real-time Analysis

To use the real-time analysis feature of the Raman clinical instrument software, obtain calibration spectra as described in section (iii). Next, load the calibration spectra by 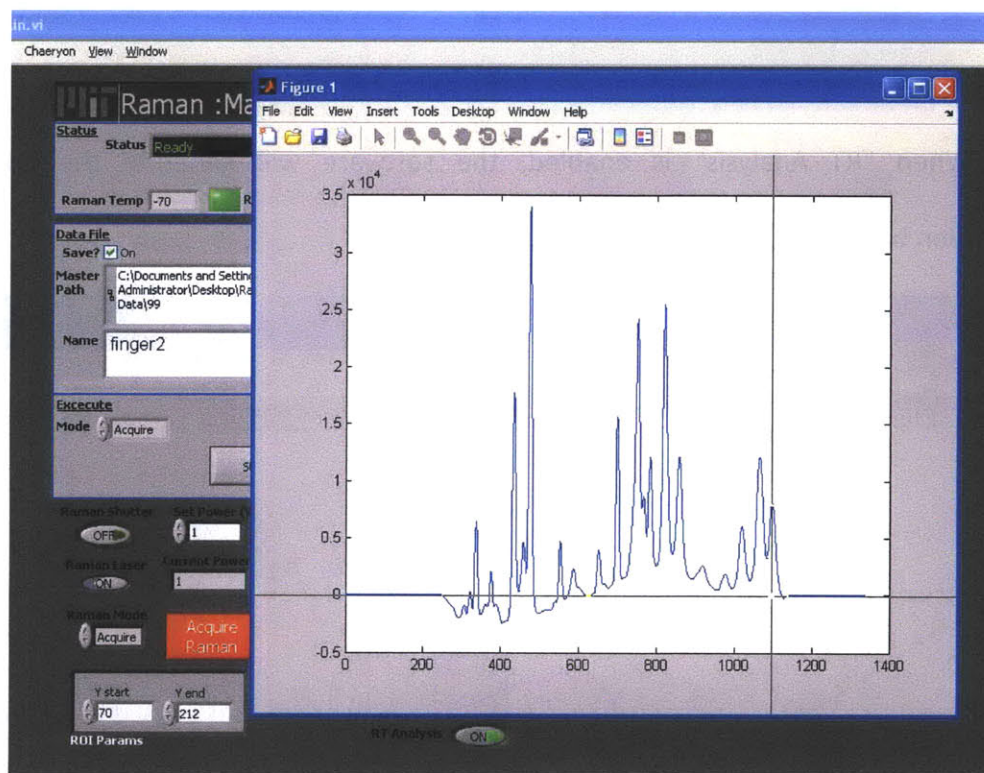choosing "Load" under "Calibration" menu (Figure 25). Select the figure of Tylenol spectrum, and move the mouse pointer over the figure. A crosshair will appear on the figure to help locate the pointer. Choose the calibration pixel points by clicking on the

Figure 30 Selecting Tylenol peaks for calibration.

figure from right to left with a mouse, so that 13 Tylenol peaks are selected as described in section 4A. It is important that these 13 peaks are selected in the proper order of high to low wavenumbers (right to left).

Next, choose between "Breast" and "Artery" model, and enable real-time analysis (Figure 31).
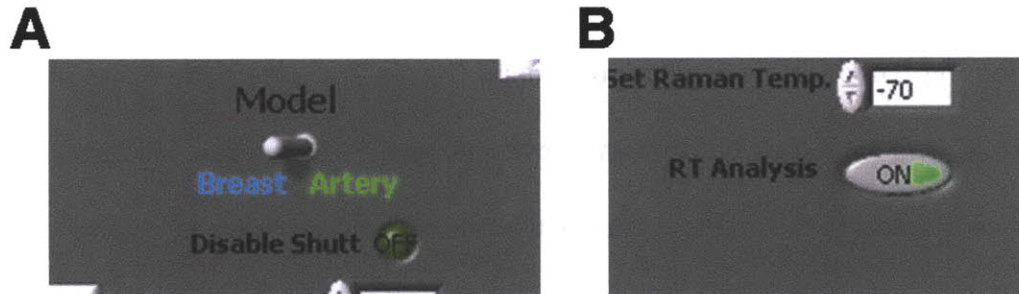
Figure 31 A : Choosing analysis models, **B:** Enabling real-time analysis

When "RT Analysis" is enabled, the software will generate the analysis information based on the model of choice (Figure 32).
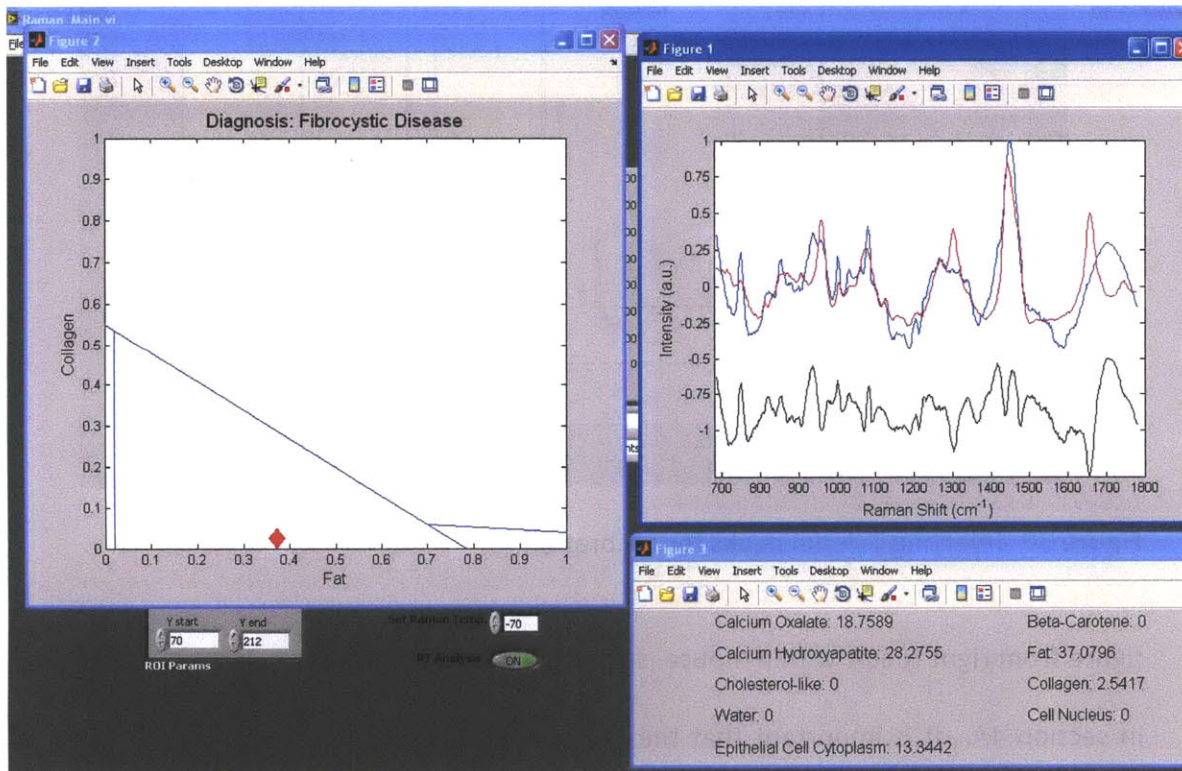
Figure 32 Real-time analysis display.

4. DATA ANALYSIS

A. Extracting Raman spectrum from acquired data

The raw data obtained and stored by the Raman clinical instrument can be processed and analyzed in many different ways. This section describes the data processing methods used by the Raman clinical instrument during its real-time analysis process (section 3(iv)). In order to obtain an accurate representation of the sample's Raman spectrum, the acquired raw spectrum data must first be corrected for the background response. This can be done by dividing the acquired spectrum by the white light response calibration spectrum, which is collected by using the same instrument and probe (section 3(iii)). In addition, the acquired spectrum should also be corrected for probe background. This is achieved by subtracting the aluminum Raman calibration spectrum from the acquired spectrum.
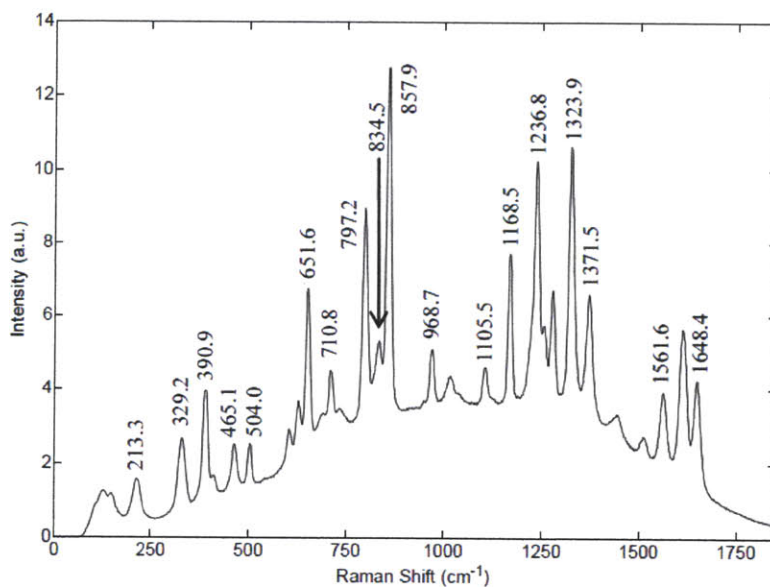
Figure 33 Raman spectrum of Tylenol.

The next step is to remove the fluorescence background in the spectrum, which is achieved by removing a best-fit 6th order polynomial. Finally, the well-known peak locations of the Tylenol calibration Raman spectrum are used to calibrate the Raman shift (wavenumber) axis for displaying the processed Raman spectrum in the proper form (Figure 34 B). This is achieved by using the Matlab codes "calibrateTylenol.m" and "tylenol_ccf.m" (Appendix B), where the appropriate pixel locations corresponding to the following 13 Tylenol peaks in the calibration Raman spectrum are selected from high to low wavenumbers (cm^{-1}) :

1648.4, 1561.6, 1371.5, 1323.9, 1236.8, 1168.5, 1105.5, 968.7, 857.9, 834.5, 797.2, 710.8, 651.6
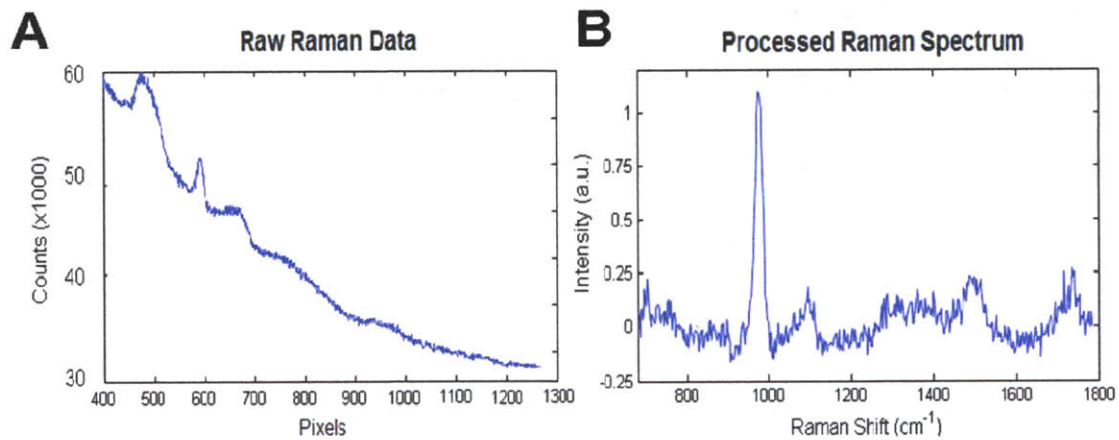
Figure 34 **A :** Raw Raman spectrum of a calcified artery tissue.
B: The same Raman spectrum after spectral response correction, fiber background removal, tissue autofluorescence removal, and Raman shift axis calibration.

After these data processing steps, the raw tissue Raman data (Figure 34 A) is represented in the proper form of Raman spectrum (Figure 34 B). The data processing steps mentioned in this section are described in detail in the commented Matlab files "analysis.m", "calibrateTylenol.m", "tylenol_ccf.m", and "Raman_loadFile.m" (Appendix B).

B. Fitting the Raman spectrum

This section describes the ordinary least squares (OLS) analysis method used by the Raman clinical instrument during its real-time analysis process (section 3(iv)). It should be noted, however, that there are many other ways to analyze the Raman spectrum data, such as principal component analysis (PCA) [1] and partial least squares (PLS) [2].

In the OLS analysis, the tissue Raman spectrum is fitted with linear combinations of Raman spectra collected from tissue constituents [3, 4, 5]. The combination of morphological basis spectra fit coefficients that provide the best fit to the acquired Raman spectrum is a good representation of the tissue composition. In order to generate such fits to the Raman spectrum, the OLS algorithm searches for the best linear combination of fit coefficients with the least amount of error. Figure 35 shows the morphological basis spectra of components known to be present in the artery tissue, and the result of fitting these components into the Raman spectrum of a calcified artery. The detailed analysis steps for Raman spectrum fitting are described in the commented Matlab files "analysis.m", "ffitRaman.m", "nnfit.m", "chopfit.m", and "calibrate2.m" in Appendix B.
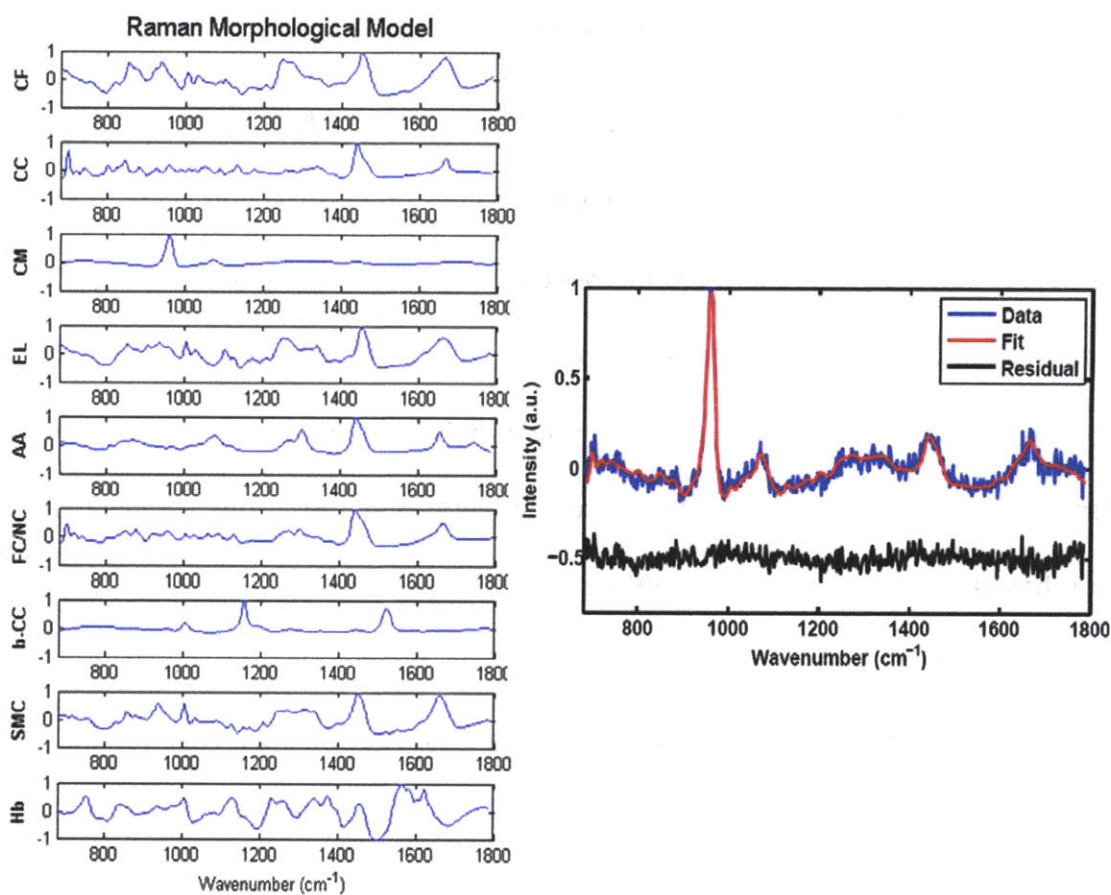
Figure 35 (Left column) Components of artery morphological basis spectra. CF: collagen fibers, CC: cholesterol crystals, CM: calcium mineralization, EL: elastin, AA: adventitial adipocytes, FC/NC: foam cells / necrotic core, b-CC: beta carotene, SMC: smooth muscle cells, Hb : hemoglobin. (Right) Raman spectrum of calcified artery tissue fitted with artery morphological model. The bottom trace is the residual between the Raman spectrum ("Data") and the morphological model ("Fit").

References:

1. G. Deinum, D. Rodriquez, T. J. Romer, M. Fitzmaurice, J. R. Kramer, and M.S. Feld, "Histological classification of Raman spectra of human coronary artery atherosclerosis using principal component analysis," Applied Spectroscopy, 53(8), 938-942, (1999).

2. A. M. K. Enejder, T.-W. Koo, J. Oh, M. Hunter, S. Sasic, and M. S. Feld, "Blood analysis by Raman spectroscopy," Optics Letters, 27(22), 2004-2006 (2002).

3. H. P. Buschman, G. Deinum, J. T. Motz, M. Fitzmaurice, J. R. Kramer, A. van der Laarse, A. V. Bruschke, and M. S. Feld, "Raman microspectroscopy of human coronary atherosclerosis: biochemical assessment of cellular and extracellular morphologic structures in situ," Cardiovasc. Pathol. 10(2), 69–82 (2001).

4. H. P. Buschman, J. T. Motz, G. Deinum, T. J. Romer, M. Fitzmaurice, J. R. Kramer, A. van der Laarse, A. V. Bruschke, and M. S. Feld, "Diagnosis of human coronary atherosclerosis by morphology-based Raman spectroscopy," Cardiovasc. Pathol. 10(2), 59–68 (2001).

5. K. E. Shafer-Peltier, A. S. Haka, M. Fitzmaurice, J. Crowe, J. Myles, R. R. Dasari, M. S. Feld, "Raman microspectroscopic model of human breast tissue: implications for breast cancer diagnosis *in vivo*," Journal of Raman Spectroscopy 33(7), 552–563 (2002).

5. TROUBLESHOOTING

1. Problem : *When attempting to run the Labview program, it displays a message that Matlab license has expired.*

> **Solution :** Renew the Matlab license. If the Matlab license expires, running the Labview code will generate an error message. The Labview code used in the Raman clinical instrument also requires Matlab to be operational.

2. Problem : *Laser shutter does not respond to control software.*

> **Solution :** Check if the shutter control box is turned on. Also, check the back of the shutter control box and make sure the pulse input cable is properly connected to the control box pulse input. Finally, make sure that the shutter control box settings are as described in section 3A and Figure 8 :,

Mode turn key = "STD";   Normally closed ("N.C.");   "REMOTE"

3. Problem : *No laser power, or laser power is not high enough.*

> **Solution :** Check if the shutter is open and the laser power key is switched on. As described in section 3A and 3B, the laser shutter can be opened by clicking on the "Raman laser" button in the Labview control software, and the power is controlled by changing the "Set power(V)" settings, up to a maximum of 1.26 V (Figure 19). If this does not work, check that the control signal (RS-232 serial) cable is properly connected between the computer and laser. If this does not work either, open the shutter manually by switching the shutter control box setting from "N.C." to "N.O.", disconnect the laser control signal cable from the computer and laser, and manually vary the laser power adjustment knob (Figure 9) to confirm that the laser itself is functioning properly.

As described in section 2 and 3A, make sure that the bandpass filter, shutter, coupling lens unit and delivery fiber are properly aligned so that approximately 100mW is delivered at the distal tip of the probe. If necessary, increase the laser power by increasing the value under the "Set power(V)" setting to no more than 1.26V in the Labview control software (Figure 19).

4. Problem : *No Raman spectrum data is saved.*

Solution : Check that the "Save" option is turned on (Figure 22).
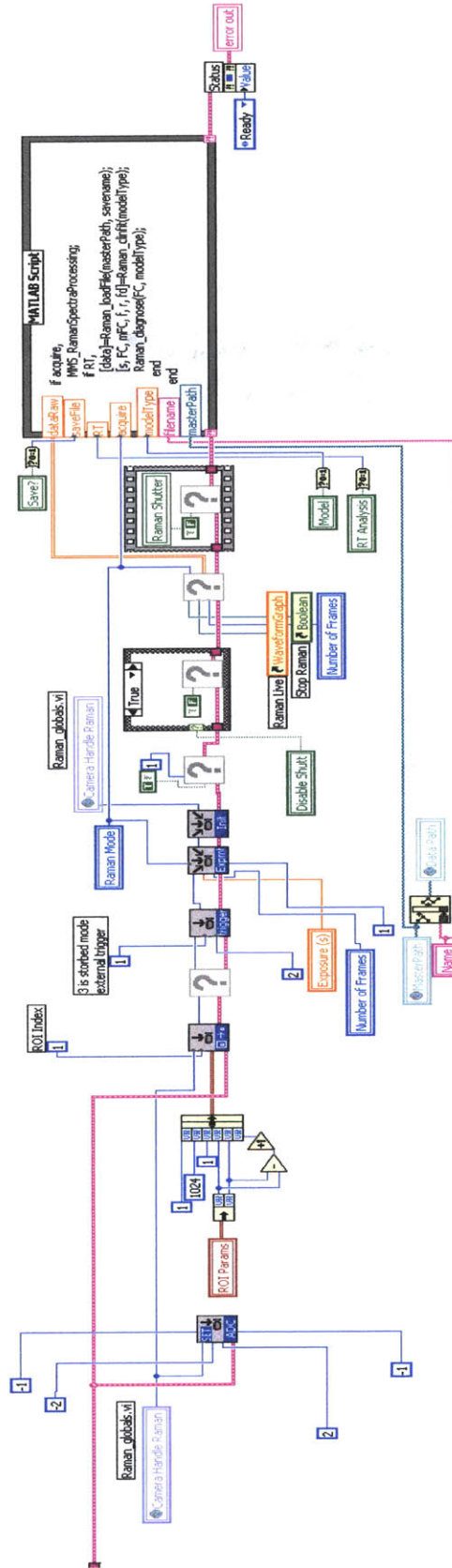
5. Problem : *Raman spectrum intensity is low.*

Solution : Check that at least 100mW is delivered at the distal tip of the probe. If not, refer to troubleshooting number 3. If the problem persists despite proper laser power, try increasing the acquisition exposure time (Figure 21).

APPENDIX A

LABVIEW

Labview VI for Raman spectrum acquisition

APPENDIX B

MATLAB

The following pages in Appendix B describe the Matlab codes used in data acquisition, processing and analysis. These files are created by the researchers at the MIT Spectroscopy Laboratory, and they cannot be found in commercial Matlab packages. Consult with the MIT Spectroscopy Laboratory before distributing in public. Each code can be interpreted with the help of the comments which follow the "%" sign and are shown in green.

File : analysis.m

```matlab
% Specify location of data directory
root = '..\your_data_directory\';

global alum
global data
global white
global minpix
global maxpix


%%%%%%%%%% LOAD Calibration Spectra %%%%%%%%%%%
if exist('wn') ~=1,
   [wn] = calibrateTylenol(root);
end
%%%%%%%%%%%%%% LOAD data %%%%%%%%%%%%%%%%%%%%
tempRam = dir(strcat(root, '\*your_data_file_name*.xls'));

for i=1:length(tempRam),
 [Ram(i,:)]=Raman_loadFile(root,tempRam(i).name(1:end-4));
end

%%%%%%%%%%%%%%%% ANALYZE Data %%%%%%%%%%%%%%%%
% calculate Raman
RamanWn = [686:2:1788];
scalingIn = [48];
for i=1:size(Ram,1),
   if scalingIn(i)~=-1,
      [Raman(i,:), FC, morphFC, Fits, Resids, FullDev] = fitRaman(1, Ram(i,:),
scalingIn(i));
   else
      [Raman(i,:), FC, morphFC, Fits, Resids, FullDev] = fitRaman(1,
Ram(i,:));
   end
end
```

B-1

File : calibrateTylenol.m

```matlab
function [wn] = calibrateTylenol(path);


% This script creates calibrations for clinical Raman data.
% The output is the wavenumber file which is cut to usable range: ("wn")
% The input is the directory where the calibration files are stored: ("path")


% Global variables :
% wn (wavenumber)
% alum (aluminum spectrum)
% white (white light spectrum)
% minpix, maxpix (minimum and maximum pixel numbers)


clf
global wn
wn=[];
acet=[];
global alum
alum=[];
global white
white=[];
global minpix
minpix=[];
global maxpix
maxpix=[];


% Create wavenumber calibration
acetname = dir(strcat(path,'\*Tylenol*.xls'));
acet=load(strcat(path,'\',acetname(1,1).name))';
alumname=dir(strcat(path,'\*Aluminum*.xls'));
alum=load(strcat(path,'\',alumname(1,1).name))';


% Load white light spectrum
whitename=dir(strcat(path,'\*White*.xls'));
white=load(strcat(path,'\',whitename(1,1).name))';
if size(acet,1) > 1,
    acet = mean(acet);
end
```

```matlab
if size(alum,1) > 1,
   alum = mean(alum);
end
if size(white,1) > 1,
   white = mean(white);
end

% Convert 1024 pixels to 1340 pixels
acet_1340 = resample (acet, 335, 256);
alum_1340 = resample (alum, 335, 256);
white_1340 = resample (white, 335, 256);
acet_1024 = acet;
alum_1024 = alum;
white_1024 = white;
acet = acet_1340;
alum = alum_1340;
white = white_1340;
%%%%%%%%%%%%%%%%%%%%%

[wn]= tylenol_ccf(acet-alum);
plot(wn,acet-alum);

% Cut wavenumber calibration to usable range
minpix=max(find(wn<680));
maxpix=min(find(wn>1800));
if isempty(maxpix)
   maxpix = length(wn);
end
wn=wn(minpix:maxpix);
wn=wn';

% Cut white light and aluminmum spectra
alum=alum(minpix:maxpix);
white=white(minpix:maxpix);

% Normalize and correct data for spectral response
white=white/max(white);
alum=alum./white;
alum=alum/max(alum);
alum=smooth(smooth(smooth(smooth(alum))));
```

File : tylenol_ccf.m

```matlab
function [wn] = tylenol_ccf(tyl)


% This program allows one to create tylenol calibration using matlab.


% The input is the Tylenol spectrum : ("tyl")
% The program will ask you to input sixteen peak regions.
% The program will look for the maximum in each region.
% Use the mouse to click on the graph and input the regions.
% Proceed from high to low wavenumbers, in order.
% It is important to make sure there are no cosmic rays in the spectrum.


% The output is a single column of wavenumbers : ("wn")


for i=1:size(tyl,2),
  pixels(i)=i;
end;


spectrum=[pixels;tyl]';


plot(spectrum(:,1),spectrum(:,2));
[x,y]=ginput(13);
z=[];
w=round(x);


%find maxima in peak regions
for i=1:13,
  [z(i,2),out]=max(spectrum(w(i)-5:w(i)+5,2));
  z(i,1)=w(i)+out-6;
end;


c=[1648.4;1561.6;1371.5;1323.9;1236.8;1168.5;1105.5;968.7;857.9;834.5;79
7.2;710.8;651.6];


P=polyfit(z(:,1),c,5);
wn=polyval(P,spectrum(:,1));
```

File : Raman_loadFile.m

```
function [data allFrames] = Raman_loadFile(masterPath, savename,
varargin);
% This program loads data from in vivo Raman procedures.
% It should be preceded by 'calibrateTylenol.m'
% It averages the data from all frames of a given acquisition.
% Then corrects the data for white light spectral response and cuts
% the data into the usable range. It also normalizes the data by
% the maximum intensity.


global data
global minpix
global maxpix
global white


% Load data
data=load(fullfile(masterPath,strcat(savename,'.xls')));
data = data';

% Convert 1024 pixels to 1340 pixels
data_1340 = resample (data, 335, 256);
data_1024 = data;
data = data_1340;
% Average the data
if isempty(varargin)
   if size(data,1)>1
      allFrames = data(1:size(data,1),minpix:maxpix);
      data = mean(data(1:size(data,1),minpix:maxpix));
   else
      data = data(1,minpix:maxpix);
   end
else
   data = mean(data(varargin{1}:varargin{2},minpix:maxpix));
end

% White light division
data=data./white;
% Normalize data
data=data/max(data);
```

B-5

File : fitRaman.m

```
function [allini, FC, morphFC, Fits, Resids, FullDev] = fitRaman(modelType,
data, varargin);

% This program fits the Raman spectrum with the morphological
% basis spectra using OLS, and outputs the fit coefficients, fit spectrum
% and the residual after fitting to the original Raman spectrum data.


global wn
global alum

% Initialize variables
FC=[];
morphFC=[];
Fits=[];
Resids=[];
FullDev=[];
meanFC=[];
stdFC=[];
P=[];
calibwn=[];
calibP=[];
devP=[];
normallFC=[];
allFits=[];
allResids=[];
x=[];
y=[];
iter = 100;

%Subtract various weightings of the aluminum background
if isempty(varargin),
   for j=1:iter,
     P(j,:)=data-alum*(100-j)/100;
   end
else
   P = data - alum*(100-varargin{1})/100;
end
```

```matlab
%Remove the fluorescence background
    P=chopfit(P,6,1);

%Calibrate the data matrix
if modelType,
    load arterymodel.mat;
    Model = arterymodel;
    [calibP,calibwn]=calibrate2(P, wn, 686, 1788, 2);
else
    load breastmodel.mat;
    Model = breastmodel;
    [calibP,calibwn]=calibrate2(P, wn, 686, 1780, 2);
end

%Renormalize the data
    for j=1:size(calibP,1),
        calibP(j,:)=calibP(j,:)/max(calibP(j,:));
    end

%Calulate the fit coefficients
    FC=nnfit(calibP, Model);

%Correct for oversubtraction of the sapphire spectrum,
    oversub = find(FC(:,12) == 0);
    Model2 = Model;
    if ~isempty(oversub),
        Model2(12,:)=-Model(12,:);
        %recalculate fit coefficients with inverted sapphire spectrum
        FC(oversub,:)=nnfit(calibP(oversub,:), Model2);
    end

%Caluculate the fits
    allFits=FC*Model;
    allFits(oversub,:) = FC(oversub,:)*Model2;

%Calculate residuals
allResids=calibP-allFits;
```

```matlab
%Calculate the standard deviation of the residuals
    for j=1:size(allResids,1),
       devP(j)=std(allResids(j,:));
     end

FullDev=devP;


%Find the smallest residual for each exposure
[c,x]=min(devP);
[x, c]


%Normalize the all fit coefficients
    normallFC=FC(x,:);


clear FC

    for j=1:12,
       FC(j)=100*normallFC(j)/sum(normallFC);
    end
    if sum(x == oversub) == 0
       y = 1;
    else
       y = -1;
    end;
    FC(12)=y*FC(12);


%Normalize the morphological model fit coefficients
    for j=1:8,
       morphFC(j)=100*FC(j)/sum(FC(1:8));
    end

clear allini
    allini=calibP(x,:);
    Fits=allFits(x,:);
    Resids=allResids(x,:);


%Plot the data
set(0,'DefaultFigureUnits','normalized');
set(0,'DefaultFigureposition',[0.5 0.4 0.5 0.5]);
```

```
figure(1);
clf;

subplot(1,1,1);
plot(calibwn, allini, 'b');
hold
plot(calibwn, Fits,'r');
plot(calibwn, Resids+2*min(allini),'k');
axis([680 1800 min(Resids)+2*min(allini) max(allini)]);
set(gca,'YTick',-1:.25:1);
set(gca,'YTick',-1:.25:1);
xlabel('Raman Shift (cm^{-1})', 'fontsize', 12);
ylabel('Intensity (a.u.)', 'fontsize', 12);
```

File : nnfit.m

```matlab
function C = nnfit(S,P)

%Uses improved algorithm for non-negative least-squares fitting.
%Based on MATLAB's lsqnonneg command.

%C refers to "concentration", P is the pure spectrum, and S is the mixture
spectrum.
%
itnum=size(S,1);

for i=1:itnum,
  CC(:,i)=lsqnonneg(P',S(i,:)');
end;


C=CC';
```

File : chopfit.m

```matlab
function [outspectrum,fit] = chopfit(S, Pnum, Itnum)


% This function chopfits a spectrum S, returning a spectrum output,
%  "outspectrum".
%  Pnum = order of polynomial
%  Itnum = number of passes through the algorithm


% get size of spectrum
NumofPixels = size(S,2);


% generate polynomial
P = poly2(Pnum, NumofPixels);
PP = P'*inv(P*P')*P;


oldS = S;


for i=1:Itnum,

   fit = S*PP;
   % create residual
   resid = S - fit;
   outspectrum = oldS -fit;   %for plotting

   % flatten residual; get rid of *positives*
   temp = -resid;
   temp = setzero(temp);
   resid = -temp;

   % add fit to the flattened residual; call it S
   S = fit + resid;

end;
```

File : calibrate2.m

```matlab
function [S2, wavenums2] = calibrate2(S, wavenums, wn_start, wn_end, binsize)
%
% This function takes spectral data S and redistributes
% the signal counts into bins of equal wavenumber spacing.
% (This is useful for our CCDs because the dispersion is
% not linear in wavenumber, yet we sometimes want to compare
% data taken at different excitations.  In order to compare two
% such spectra quantitatively, we need to give them a common
% set of bins; otherwise, the data points don't perfectly
% overlap.
%
%  Inputs: spectra: S (each spectrum occupying a ROW)
%          associated wavenumber calibration:  wavenums
%          starting wavenumber for output: wn_start
%          ending wavenumber for output:   wn_end
%          bin size (in cm-1): binsize
%
%  Outputs: spectra S2
%           associated wavenumbers  : wavenums2

% We need to repartition the data into integral wavenumber bins
% of reasonable size and do it in a logical way so the lineshapes aren't
% altered.

% Calculate the width, in wavenumbers, of each pixel :
%      Use the convention that the wavenumbers listed in
%      'wavenums' are at (near) the MIDDLE of each bin;
%      i.e, the wavenumber bin i extends from
%      wavenums(i)-Widths(i-1)/2 to wavenums(i)+Widths(i)/2,
%      except for the first one, which extends from
%      wavenums(1) +/- Widths(1)/2, and the last one, which extends from
%      wavenums(N) +/- Widths(N-1)/2.

sz=size(wavenums,2);

Widths = wavenums(2:sz)-wavenums(1:sz-1);
%% note: for N pixels, there are N-1 widths
%%  --first pixel:
```

```matlab
PixelWidth = Widths(1);
LeftEdgeValue = wavenums(1)-Widths(1)/2;

%% --middle pixels:
PixelWidth = [PixelWidth, Widths(2:sz-1)/2 + Widths(1:sz-2)/2];
LeftEdgeValue = [LeftEdgeValue, wavenums(2:sz-1)-Widths(1:sz-2)/2];

%% --end pixel
PixelWidth = [PixelWidth,  Widths(sz-1)];
LeftEdgeValue = [LeftEdgeValue, wavenums(sz) + Widths(sz-1)/2];

NumofSpectra = size(S,1);

%% set up a loop to create the output spectra
i = 0;
S2 = [];

for CenterValue = wn_start:binsize:wn_end,
  i = i+1; % index for writing new arrays
  LeftValue = CenterValue - binsize/2;
  RightValue =CenterValue + binsize/2;

%% use the whichbin.m function to do the finding of left and right bin....
LeftBin = whichbin(LeftEdgeValue, LeftValue);
RightBin= whichbin(LeftEdgeValue,RightValue);

%% Are the left and right bins the same?
if LeftBin==RightBin
  Counts = (S(:,LeftBin)/PixelWidth(LeftBin)) * binsize;

%% If not, sum left fraction, right fraction, and any middle bins
else
  LeftBinFraction = LeftEdgeValue(LeftBin+1) - LeftValue;
  Counts = (S(:,LeftBin)/PixelWidth(LeftBin)) * LeftBinFraction;

  RightBinFraction = RightValue - LeftEdgeValue(RightBin);
  Counts = Counts + (S(:,RightBin)/PixelWidth(RightBin)) * RightBinFraction;

  for MiddleBin = LeftBin+1:RightBin - 1,
   Counts = Counts + S(:,MiddleBin);
   end; % of for loop
```

```matlab
    end; % of if/else statement

%% append Counts to the reconstituted spectral matrix
S2 = [S2, Counts];

%% loop back
if (rem(i,30)==0)
    fprintf('\nStill working; Nu = %.1f', CenterValue');
    end; %of if statement for user update info
end; %of for CenterValue loop

%% create the corresponding wavenumber calibration for these data
wavenums2 = wn_start:binsize:wn_end;

%% output of this should be the spectral matrix S2, binned according to
%% the desired wavenumber spacing, and the corresponding wavenumber
%% calibration 'wavenums'.
```

Matlab files needed for running Raman clinical instrument Labview program

File : MMS_RamanSpectraProcessing.m (Used by Labview)

```matlab
%This program specifies the date and time stamps used in the filenames
% where data is saved.

data = dataRaw;
indices = [];
for i=1:size(data,1),
  if data(i,:) ~= zeros(1,size(data,2)),
    indices = [indices, i];
  end
end
data = data(indices,:)';
% dataMean = mean(data')';
% dataStd = std(data')';


if ((saveFile || RT) && acquire),
   savename = strcat(datestr(now,'mm.dd.yyyy.HH.MM.SS'),'_',filename);
   save(fullfile(masterPath,strcat(savename,'.xls')),'data','-ascii','-tabs');
%    save(fullfile(masterPath,strcat(savename,'_Stdev.xls')),'dataStd','-ascii','-tabs');
End
```

File : Raman_loadFile.m (Used by Labview)

```matlab
function [data allFrames] = Raman_loadFile(masterPath, savename, varargin);

%This program loads data from in vivo Raman procedures.
%It should be preceeded by calibrateTylenol.m
%It averages the data from all frames of a given acquisition.
%Then corrects the data for white light spectral response and cuts
%the data into the usable range. It also normalizes the data by
%the maximum intensity.

global data
global minpix
global maxpix
global white

%Load in vivo data
data=load(fullfile(masterPath,strcat(savename,'.xls')));
data = data';

%Average the data
if isempty(varargin)
   if size(data,1)>1
      allFrames = data(1:size(data,1),minpix:maxpix);
      data=mean(data(1:size(data,1),minpix:maxpix));
   else
      data=data(1,minpix:maxpix);
   end
else
   data=mean(data(varargin{1}:varargin{2},minpix:maxpix));
end
%White light devision
data=data./white;

%Normalize data
data=data/max(data);
```

File : Raman_clinfit.m (Used by Labview)

```
% This function applies the diagnostic algorithm to the fit coefficients

function [allini, FC, morphFC, Fits, Resids, FullDev] =
Raman_clinfit(modelType);

global wn
global alum
global data
FC=[];
morphFC=[];
Fits=[];
Resids=[];
FullDev=[];
meanFC=[];
stdFC=[];
P=[];
calibwn=[];
calibP=[];
devP=[];
normallFC=[];
allFits=[];
allResids=[];
x=[];
y=[];
iter = 100;

%Subtract various weightings of the aluminum background
   for j=1:iter,
     P(j,:)=data-alum/(2*0.1*j);
   end;

%Remove the fluorescence background
   P=chopfit(P,6,1);

%Calibrate the data matrix
if modelType,
   load arterymodel.mat;
```

```matlab
    Model = arterymodel;
    [calibP,calibwn]=calibrate2(P, wn, 686, 1788, 2);
else
    load breastmodel.mat;
    Model = breastmodel;
    [calibP,calibwn]=calibrate2(P, wn, 686, 1780, 2);
end

%Renormalize the data
    for j=1:iter,
        calibP(j,:)=calibP(j,:)/max(calibP(j,:));
    end

%Calulate the fit coefficients
    FC=nnfit(calibP, Model);

%Correct for oversubtraction of the sapphire spectrum,
    if FC(:,12)==0
        Model(12,:)=-Model(12,:);
        y=-1;
        %recalculate fit coefficients with inverted sapphire spectrum
            FC=nnfit(calibP, Model);
    else
        y=1;
    end

%Caluculate the fits
    allFits=FC*Model;

%Calculate residuals
allResids=calibP-allFits;

%Calculate the standard deviation of the residuals
    for j=1:iter
        devP(j)=std(allResids(j,:));
    end

FullDev=devP;

%Find the smallest residual for each exposure
x=find(devP==min(devP));
```

x

```matlab
%Normalize the all fit coefficients

   normallFC=FC(x,:);

clear FC

   for j=1:12,
      FC(j)=100*normallFC(j)/sum(normallFC);
   end
   FC(12)=y*FC(12);

%Normalize the morphological model fit coefficients

   for j=1:8,
      morphFC(j)=100*normallFC(j)/sum(normallFC(1:8));
   end

clear allini

   allini=calibP(x,:);
   Fits=allFits(x,:);
   Resids=allResids(x,:);

%Plot the data
set(0,'DefaultFigureUnits','normalized');
set(0,'DefaultFigureposition',[0.5 0.4 0.5 0.5]);
figure(1);
clf;

subplot(1,1,1);
plot(calibwn, allini, 'b');
hold
plot(calibwn, Fits,'r');
plot(calibwn, Resids+2*min(allini),'k');
axis([680 1800 min(Resids)+2*min(allini) max(allini)]);
set(gca,'YTick',-1:.25:1);
set(gca,'YTick',-1:.25:1);
xlabel('Raman Shift (cm^{-1})', 'fontsize', 12);
ylabel('Intensity (a.u.)', 'fontsize', 12);
```

File : Raman_diagnose.m (Used by Labview)

```
function [] = Raman_diagnose(FC, modelType)

if modelType,
   sgdiagnose_heme(FC);
else
   diagnose_breast(FC);
end
```

File : sgdiagnose_heme.m (Used by Labview)

```
function f = sgdiagnose_heme(FC);

% This function applies the diagnostic algorithm to the fit coefficients

%
morphFC=[];
morphFC=[FC(1:8)];
morphFC=100*(morphFC/sum(morphFC));
nobetaFC=[];
nocmFC=[];

%Remover beta Carotene and re-normalize the fit coefficients.
nobetaFC=[morphFC(1:6),morphFC(8)];
nobetaFC=nobetaFC/sum(nobetaFC);

%Extract calcium mineralization.
cm=nobetaFC(3);

%Remove calcification and re-normalize the fit coefficients.
nocmFC=[nobetaFC(1:2),nobetaFC(4:7)];
nocmFC=nocmFC/sum(nocmFC);

%Extract cholesterol crystal + foam cell/nacrotic core.
ccfc=nocmFC(2)+nocmFC(5);
```

```matlab
%Plot
set(0,'DefaultFigureUnits','normalized');
set(0,'DefaultFigureposition',[0.01 0.4 0.47 0.5]);
figure(2);
clf;

%Plot the normal or calcified vs. non-calcified plaque line.
plot([(0.07/0.30) 1],[0 0.23]);
hold;

%Plot the normal vs. calcified plaque line.
plot([(0.24/0.79) 0],[(0.17-0.48*(0.24/0.79)) 0.17]);

%Plot diagnosis.
plot(ccfc,cm,'rd','MarkerSize',12,'MarkerFaceColor','r');

if cm<(-0.07+0.30*ccfc)
    title('Diagnosis: Non-Calcified Plaque','fontsize', 14);
elseif cm<(0.17-0.48*ccfc)
    title('Diagnosis: Non-Atherosclerotic Tissue','fontsize', 14);
else
    title('Diagnosis: Calcified Plaque','fontsize', 14);
end

axis([0 1 0 1]);
xlabel('Cholesterol+FCNC', 'fontsize', 12);
ylabel('Calcification', 'fontsize', 12);

%Display fit coefficients
set(0,'DefaultFigureUnits','normalized');
set(0,'DefaultFigureposition',[0.5 0.03 0.49 0.15]);
figure(3);
clf;

axis([0 1 0 1]);
axis off;

text(0,1,['Collagen Fibers:' ' ' num2str(morphFC(1))],'fontsize',12);
text(0,0.75,['Cholesterol Crystals:' ' ' num2str(morphFC(2))],'fontsize',12);
text(0,0.5,['Calcified Minerals:' ' ' num2str(morphFC(3))],'fontsize',12);
text(0,0.25,['Elastic Lamina:' ' ' num2str(morphFC(4))],'fontsize',12);
```

```
text(0.5,1,['Adventitial Adipocytes:' ' ' num2str(morphFC(5))],'fontsize',12);
text(0.5,0.75,['Foam Cells/Necrotic Core:' ' '
num2str(morphFC(6))],'fontsize',12);
text(0.5,0.5,['Beta Carotene:' ' ' num2str(morphFC(7))],'fontsize',12);
text(0.5,0.25,['Smooth Muscle Cells:' ' ' num2str(morphFC(8))],'fontsize',12);
text(0,0,['Hemoglobin:' ' ' num2str(FC(9))],'fontsize',12);

set(0,'DefaultFigureUnits','normalized');
set(0,'DefaultFigureposition',[0.5 0.4 0.5 0.5]);
```

File : diagnose_breast.m (Used by Labview)

```
function f = diagnose_breast(FC);

%Function applies the diagnostic algorithm to the fit coefficients
% and displays the diagnosis on the screen.

morphFC = FC(1:9);
morphFC = morphFC/sum(morphFC);

%Plot
set(0,'DefaultFigureUnits','normalized');
set(0,'DefaultFigureposition',[0.01 0.4 0.47 0.5]);
figure(2);
clf;

%FC(Coll)=-0.70*FC(Fat)+0.55
plot([0 0.55/.7],[0.55 0]);
hold on;

%FC(Coll)=-0.06*FC(Fat)+0.10
plot([0.45/.64 1],[-.06*.45/.64+.1 -.06+.1]);

%FC(Fat)=0.2
plot([0.02 0.02],[0 -.70*.02+.55])

%Plot diagnosis.
plot(morphFC(6),morphFC(7),'rd','MarkerSize',12,'MarkerFaceColor','r');

if FC(6)<0.02
    x=0;
else
    x=1;
end

if FC(7)<(-0.06*FC(6)+0.10)
    y=0;
else
    y=1;
end
```

```matlab
if FC(7)<(-0.70*FC(6)+0.55)
    z=0;
else
    z=1;
end
%checking where point lies on graph relative to all-in-one diagnostic
%algorithm lines

%if point is in fibroendoma region
if and((x==0),(z==0))==1
    title('Diagnosis: Fibroendoma','fontsize', 14);
end

%if point is in fibrocystic region
if and(y,z)==1
    title('Diagnosis: Fibrocystic Disease','fontsize', 14);
end

%if point is in normal region
if and((y==0),(z==1))==1,
    title('Diagnosis: Normal','fontsize', 14);
end

%if point is in infiltrating carcinoma region
if and((x==1),(z==0))==1,
    title('Diagnosis: Infiltrating Carcinoma','fontsize',14);
end

 axis([0 1 0 1]);
xlabel('Fat', 'fontsize', 12);
ylabel('Collagen', 'fontsize', 12);

%Display fit coefficients
set(0,'DefaultFigureUnits','normalized');
set(0,'DefaultFigureposition',[0.5 0.03 0.49 0.15]);
figure(3);
clf;
morphFC = morphFC *100;
axis([0 1 0 1]);
axis off;
text(0,1,['Calcium Oxalate:' ' ' num2str(morphFC(1))],'fontsize',12);
```

```
text(0,0.75,['Calcium Hydroxyapatite:' ' '
num2str(morphFC(2))],'fontsize',12);
text(0,0.5,['Cholesterol-like:' ' ' num2str(morphFC(3))],'fontsize',12);
text(0,0.25,['Water:' ' ' num2str(morphFC(4))],'fontsize',12);
text(0.65,1,['Beta-Carotene:' ' ' num2str(morphFC(5))],'fontsize',12);
text(0.65,0.75,['Fat:' ' ' num2str(morphFC(6))],'fontsize',12);
text(0.65,0.5,['Collagen:' ' ' num2str(morphFC(7))],'fontsize',12);
text(0.65,0.25,['Cell Nucleus:' ' ' num2str(morphFC(8))],'fontsize',12);
text(0,0,['Epithelial Cell Cytoplasm:' ' ' num2str(morphFC(9))],'fontsize',12);
set(0,'DefaultFigureUnits','normalized');
set(0,'DefaultFigureposition',[0.5 0.4 0.5 0.5]);
```